

A Variational Framework for Phase-Field Fracture Modeling with Applications to Fragmentation, Desiccation, Ductile Failure, and Spallation

by

Tianchen Hu

Department of Mechanical Engineering and Materials Science
Duke University

Date: _____

Approved:

John Dolbow, Advisor

Wilkins Aquino

Johann Guilleminot

Manolis Veveakis

Benjamin W. Spencer

Dissertation submitted in partial fulfillment of the requirements for the degree of
Doctor of Philosophy in the Department of Mechanical Engineering and Materials
Science
in the Graduate School of Duke University
2021

ABSTRACT

A Variational Framework for Phase-Field Fracture Modeling with Applications to Fragmentation, Desiccation, Ductile Failure, and Spallation

by

Tianchen Hu

Department of Mechanical Engineering and Materials Science
Duke University

Date: _____
Approved:

John Dolbow, Advisor

Wilkins Aquino

Johann Guilleminot

Manolis Veveakis

Benjamin W. Spencer

An abstract of a dissertation submitted in partial fulfillment of the requirements for
the degree of Doctor of Philosophy in the Department of Mechanical Engineering
and Materials Science
in the Graduate School of Duke University
2021

Copyright © 2021 by Tianchen Hu
All rights reserved

Abstract

Fracture is a common phenomenon in engineering applications. Many types of fracture exist, including, but not limited to, brittle fracture, quasi-brittle fracture, cohesive fracture, and ductile fracture. Predicting fracture has been one of the most challenging research topics in computational mechanics. The variational treatment of fracture and its associated phase-field regularization have been employed with great success for modeling fracture in brittle materials. Extending the variational statement to describe other types of fracture and coupled field phenomena has proven less straightforward. Main challenges that remain include how to best construct a total potential that is both mathematically sound and physically admissible, and how to properly describe the coupling between fracture and other physics.

The research presented in this dissertation aims at addressing the aforementioned challenges. A variational framework is proposed to describe fracture in general dissipative solids. In essence, the variational statement is extended to account for large deformation kinematics, inelastic deformation, dissipation mechanisms, dynamic effects, and thermal effects. The proposed variational framework is shown to be consistent with conservations and laws of thermodynamics, and it provides guidance and imposes restrictions on the construction of models for coupled field problems. Within the proposed variational framework, several models are instantiated to address practical engineering problems. A brittle and quasi-brittle fracture model is used to investigate fracture evolution in polycrystalline materials; a cohesive fracture

model is applied to revisit soil desiccation; a novel ductile fracture model is proposed and successfully applied to simulate some challenging benchmark problems; and a creep fracture model is developed to simulate the spallation of oxide scale on high temperature heat exchangers.

Contents

Abstract	iv
List of Tables	ix
List of Figures	x
Acknowledgements	xviii
1 Introduction	1
1.1 Background	1
1.2 Research contributions	5
1.3 Organization of the dissertation	7
1.4 Notation	7
2 The Variational Framework	9
2.1 Kinematics and Constraints	9
2.2 Thermodynamics	11
2.3 The variational statement	16
2.4 Discretization	21
3 Brittle and Quasi-Brittle Fracture: Intergranular Fracture Evolution in Polycrystalline Materials	25
3.1 Introduction	25
3.2 Theory	27
3.2.1 Constitutive choices	27

3.2.2	Approximation of the pressure boundary condition	30
3.2.3	Governing equations	33
3.3	Verification	34
3.3.1	Uniaxial traction of a bar	34
3.3.2	Pressurized crack propagation	38
3.4	Numerical examples	39
3.4.1	Predicting the critical fracture strength	39
3.4.2	High burnup structure fragmentation	47
4	Cohesive Fracture: Soil desiccation	54
4.1	Introduction	54
4.2	Theory	58
4.2.1	Constitutive choices	58
4.2.2	Enforcing the traction-free boundary condition	60
4.2.3	Stochastic models for fracture properties	62
4.3	Verification	71
4.3.1	Mode I: Edge-Notched Unilateral Tension Test	71
4.3.2	Mode II: Edge-Notched Shear Test	74
4.3.3	Crack Propagation Under Biaxial Tension	77
4.4	Numerical examples	80
4.4.1	One-Dimensional Simplification: Side View	81
4.4.2	Two-Dimensional Simplification: Stochastic Aspects of Fracture	85
4.4.3	Inverse Identification Based on Three-Dimensional Physical Experiments	96
5	Towards Ductile Fracture	102
5.1	Introduction	102

5.2	Theory	106
5.2.1	Constitutive choices	106
5.2.2	A power-law approximation to the yield surface	114
5.2.3	Variational constitutive updates	116
5.3	Verification	118
5.3.1	A homogeneous example: uniaxial constitutive response	120
5.3.2	A nonhomogeneous example: uniaxial load-displacement curves	128
5.3.3	Crack growth resistance curves	131
5.4	Numerical examples	134
5.4.1	Three-point bending	134
5.4.2	The Sandia Fracture Challange	143
5.4.3	Spallation of oxidation scale	146
6	Conclusions	160
A	Code availability	166
B	The flooding algorithm for counting fragments	167
	Bibliography	171
	Biography	185

List of Tables

3.1	Parameters and material properties used in the intergranular fracture simulations	40
3.2	Summary of fracture strength obtained from 15 realizations of 3 porosity values. R denotes the realization index.	47
3.3	Parameters and material properties used in the fission-gas-induced HBS fracture simulations.	48
4.1	Summary of material properties and model parameters for all calculations in Section 4.4.2	86
4.2	Summary of material properties of mining waste and model parameters for all calculations in Section 4.4.3	97
5.1	Summary of the calibrated material properties and model parameters	136
5.2	Summary of the calibrated material properties and model parameters for the Sandia Fracture Challenge specimen	144
5.3	Summary of operation schedule	152
5.4	Summary of material properties and model parameters for the oxide .	153
5.5	Summary of material properties and model parameters for the metal .	153
B.1	Demonstration of classification after the update from time step n to time step n+1. Broken elements are denoted with an underscore. . .	170

List of Figures

3.1	A bar under uniaxial tension.	34
3.2	The apparent traction-separation relations.	35
3.3	Response of the bar with a pressurized crack.	37
3.4	Sneddon benchmark problem.	39
3.5	Comparison between the numerical results and the LEFM solution for the critical pressure values.	40
3.6	Comparison of stress-strain curves for different gas bubble geometries. .	43
3.7	Final configuration (crack surfaces highlighted in blue) for different loading (a) uniaxial (b) biaxial (c) triaxial.	43
3.8	Comparison of stress-strain curves for different loading conditions. .	44
3.9	Crack propagation in REVs with different porosity values.	46
3.10	Comparison of stress-strain curves for different porosity values.	46
3.11	Variation in normalized fracture strength with changing porosity. .	47
3.12	Crack propagation from bubbles with different sizes.	49
3.13	Crack propagation with different external pressure loadings.	51
3.14	Crack propagation from multiple bubbles.	52
3.15	Crack propagation at different recrystallization stages.	53

4.1	Boundary conditions of the plate with a pre-existing crack for (a) a mode I tension test and (d) a mode II shear test. Finite element meshes for the mode I calculations (b - c) and for the mode II calculations (e - f). For (b, e) the meshes have the initial crack geometry “meshed-in” while (c, f) have local refinement around the initial phase field. All meshes are pre-refined along the predicted crack-path with a characteristic element size of 0.005 mm.	72
4.2	Edge-notched specimen loaded in tension with initial crack represented by a geometric notch with a rounded corner. (a) Dimensions of the notched plate. Damage d at (b) $u_y = 0$ mm, (c) $u_y = 0.0048$ mm, (d) $u_y = 0.006$ mm.	72
4.3	Edge-notched specimen loaded in tension with initial crack represented by a phase field. (a) Dimensions of the intact plate. The Damage d at (b) $u_y = 0$ mm (c) $u_y = 0.0048$ mm (d) $u_y = 0.006$ mm.	73
4.4	Mode I force–displacement curves obtained using (a) the spectral decomposition with two representations of the pre-existing crack (b) a spectral decomposition in conjunction with the contact split with different critical damage threshold on two representations of the pre-existing crack.	74
4.5	The crack paths obtained using (a-d) the spectral decomposition on a geometrically notched plate, (e-h) the spectral decomposition with an initial phase field d_0 (4.46) representing the initial crack, and (i-l) the contact split with an initial phase field. Snapshots of crack paths are shown at (b,f,j) $u_x = 0$ mm, (c,g,k) $u_x = 0.0109$ mm, and (d,h,l) $u_x = 0.02$ mm.	75
4.6	Mode II force–displacement curves obtained using (a) spectral decomposition with two representations of the initial crack (b) spectral decomposition in conjunction with the contact split with different critical damage threshold on two representations of the initial crack.	76
4.7	(a) Dimensions and boundary conditions of a thin plate with two parallel initial cracks. (b) The initial cracks are represented by an initial phase field.	78
4.8	Crack paths obtained using (a-c) a no-split technique (d-f) the spectral decomposition (g-i) the contact split.	79

4.9	Contour plot of the normal pressure right before the bridge forms. The pressure is calculated for an orientation that is estimated to be orthogonal to the bridge. Elements within the contour of $d = 0.75$ are removed to indicate the current crack set.	80
4.10	Description of a one-dimensional model for thin-film cracking. (a) Side view (highlighted in yellow) of the geometry (b) schematic representation of the side view. The elasticity solution is derived for the region highlighted with the shaded box, i.e. between the two discontinuities across the thin film. The coordinate system is centered at the middle of the bottom surface of the thin film.	82
4.11	The principal of “super-superposition” applied to the region of interest marked in Figure 4.10b. The analytical solution is derived based on the boundary conditions shown in (c).	82
4.12	Relationship between the dimensionless fracture driving energy and the dimensionless crack spacing: (a) analytical solution using linear elasticity; and (b) numerically generated curves using the phase-field for cohesive model detailed in this work.	84
4.13	Description of a two-dimensional model for thin-film cracking. (a) Top view (highlighted in yellow) (b) schematic representation of the top view. A typical crack is shown to emphasize that fracture is only considered in the film.	87
4.14	phase fields resulting from six pairs of realizations with different correlation models and normalized correlation lengths. The left three pairs (a-b, g-h, m-n) are realizations obtained with a PSE covariance function, while the right three pairs (d-e, j-k, p-q) are samples generated with a PE covariance function. Energy release rate \mathcal{G}_c and the critical fracture energy ψ_c have a coefficient of variation of 0.03, and normalized spatial correlation length L^* of (a-b, d-e) 0.05 (g-h, j-k) 0.1 (m-n, p-q) 0.2 The corresponding phase fields are shown in (c, f, i, l, o, r), respectively. In these results, independent realizations of the underlying Gaussian fields are used.	89
4.15	Three pairs of qualitative comparison of smoothness of the kernel function with the same normalized correlation length $L^* = 0.05$. (a-f) pair 1 (g-l) pair 2 (m-r) pair 3. Each row compares two kernel functions transformed from the same samples of the underlying Gaussian fields.	90

4.16 (a, c) Mean dimensionless crack spacing \underline{l}^* versus dimensionless crack driving force \mathcal{D}^* (b, d) Estimated probability density of dimensionless crack spacing for different values of correlation length when $\mathcal{D}^* = 5.17$ based on (a-b) a PSE kernel (c-d) a PE kernel	91
4.17 Comparisons of (a) mean dimensionless crack spacing \underline{l}^* versus dimensionless crack driving force \mathcal{D}^* and (b) Estimated probability density of dimensionless crack spacing for different values of correlation length when $\mathcal{D}^* = 5.17$ for results obtained using a PSE kernel and a PE kernel	92
4.18 Point-wise correlated material properties: (a-f) normalized fracture toughness \mathcal{G}_c^* and (g-l) normalized critical fracture energy ψ_c^* with (left) PSE covariance function (right) PE covariance function	92
4.19 Comparisons of (a) mean dimensionless crack spacing as a function of dimensionless crack driving force and (b) estimated PDFs of dimensionless fragment size at loading $\mathcal{D}^* = 5.17$ for results with an underlying PSE kernel	93
4.20 Comparisons of (a) mean dimensionless crack spacing and dimensionless crack driving force and (b) estimated PDFs of dimensionless fragment size at loading $\mathcal{D}^* = 5.17$ for results with an underlying PE kernel	94
4.21 Superposition of fracture networks obtained by three samples of different coefficients of correlation, using the PSE kernel. Only the volume within the damage contour of $d = 0.9$ is shown to represent the resulting fracture network. Three samples are sampled (a) by holding \mathcal{G}_c constant and (b) by holding ψ_c constant.	95
4.22 Snapshots of phase field at different loading levels with $d \geq 0.75$ plotted over (a-c) fracture toughness \mathcal{G}_c and (d-f) critical fracture energy ψ_c with an underlying PSE covariance function	96
4.23 Snapshots of phase field at different loading levels with $d \geq 0.75$ plotted over (a-c) fracture toughness \mathcal{G}_c and (d-f) critical fracture energy ψ_c with an underlying PE covariance function	97
4.24 Three sets of experiments and calculations for (a-e) unilateral agitation (f-j) rotational agitation (k-o) point agitation. (b, g, l) snapshots of crack patterns from experiments. postulated spatially correlated (c, h, m) fracture toughness and (d, i, n) critical fracture energy to reproduce experimental observations. (e, j, o) phase fields obtained using corresponding spatially varying material properties.	98

4.25 Procedures of finding the optimal hyperparameter to match the experiment: (a) 12 pairs of fracture properties are sampled to explore the space of admissible spatial correlation lengths; three dimensional energy minimization problems are solved to obtain (b) the resulting fracture morphology; (c) distributions of fragment sizes are extracted from the simulated results, and the log-likelihood values of these distributions at the samples extracted from (d) the experimental fracture morphology are computed.	99
4.26 (a) Estimated PDFs of the dimensionless fragment sizes extracted from the experimental result and the calibrated stochastic model. (b) Fracture morphology obtained using the calibrated fracture properties. (c) Photograph of cracks in the mining waste.	100
4.27 Qualitative comparison between the experiments and the simulations: (a-c) Photographs (modified from [1]) of cracks in mining waste due to desiccation at steady state for three test specimens with thickness (a) 4 mm, (b) 8 mm, and (c) 16 mm. (d-f) Top view and (g-i) panoramic view of corresponding numerical simulation results with different film thickness. Volumes of material with $d \geq 0.75$ were removed to improve the visualization of the crack geometry.	101
5.1 A prototypical stress-strain curve. The critical fracture energy ψ_c is represented by the shaded area. The compositions of the fracture driving energy are different for (a) an E-P-D model and (b) an E-P-PD model.	118
5.2 Characteristic loading and unloading curves of (a) the E-P-D model and (b) the E-P-PD model.	121
5.3 Stress-strain curves obtained with (a) the quadratic crack geometric function $\alpha = d^2$ and the Lorentz-type degradation function $g^e = g^p = g^{\text{Lorentz}}(d; m, p = 1)$, (b) the E-P-PD model with $\xi = 1$, and (c) the E-P-D model with $\xi = 1$	122
5.4 Stress-strain curves obtained with the linear crack geometric function $\alpha = d$ and (a) the quadratic degradation function (b-c) a Lorentz-type degradation function. Both (b) the E-P-PD model ($\psi_c c_0 a / G_c = 0.019$) and (c) the E-P-D model ($\psi_c c_0 a / G_c = 0.039$) show a regularization-length-independent critical fracture strength σ_c	124

5.5 (a, c) the stress strain curve and the degradation for the fracture toughness and (b, d) the corresponding energy conservation. In (a-b), $C = \beta = 1$ and $\frac{\psi_c c_0 a}{\mathcal{G}_c} = 0.0021$. In (c-d), $C = \beta = 0.5$, $\varepsilon_0 = 0.001$, and $\frac{\psi_c c_0 a}{\mathcal{G}_c} = 0.0021$.	125
5.6 (a, c) the stress strain curve and the degradation for the fracture toughness and (b, d) the corresponding energy conservation. In (a-b), $C = 0.3$, $\beta = 0.5$, $\varepsilon_0 = 0.001$, and $\frac{\psi_c c_0 a}{\mathcal{G}_c} = 0.0021$. In (c-d), $C = \beta = 0.5$, $\varepsilon_0 = 0.1$ and $\frac{\psi_c c_0 a}{\mathcal{G}_c} = 0.0012$.	127
5.7 The geometry (black outline) and the final deformed configuration of the bar.	129
5.8 Normalized load-displacement curves obtained for (a) the E-P-PD model and (b-d) the E-P-D model with different values of β . Unit thickness is assumed.	130
5.9 Schematic of domain for calculations. Actual dimensions are $W_0 = 150l$, $H_0 = 72l$, with pre-crack length $a_0 = 0.2W_0$. Symmetry boundary conditions are applied on the dashed line.	131
5.10 J-R curves for different values of l/r_p	134
5.11 The mesh used for calibration and the zoomed-in view of the refined region.	135
5.12 Experimental and calibrated force-displacement curves for the tension test. Experiment data are interpolated from [2]. The calibrated curves correspond to material properties and model parameters summarized in Table 5.1.	136
5.13 (a) schematics of the three-point bending experiment and (b) the mesh. See [3] for a detailed drawing with dimensions. The specimen is assumed to have a fixed support and a roller support on the bottom, and a downward displacement is applied at the location of the top punch.	137
5.14 (a) a picture of the experiment setup [3] and (b) the effective plastic strain prior to crack initiation.	138

5.15 (a-e) Contour plots of the effective fracture toughness $\hat{\mathcal{G}}_c$ with $\beta = 0.1$ and different values of ε_0 , using the E-P-D model. The portion of the domain with $d > 0.8$ is removed to visualize the crack path. (f) Superposition of the damage contours. All contours are plotted on the reference configuration for the purpose of comparison.	139
5.16 (a-e) Contour plots of the effective fracture toughness $\hat{\mathcal{G}}_c$ with $\varepsilon_0 = 0.05$ and different values of β . Domain with $d > 0.8$ is removed to visualize the crack path. (f) Superposition of the damage contours. All contours are plotted on the reference configuration for the purpose of comparision.	140
5.17 Contour of the equivalent plastic strain obtained using the E-P-PD model. Domain with $d > 0.8$ is removed to visualize the crack path. . .	140
5.18 Comparison of load-deflection curves between simulations and experiments [3] for the 3D three-point bend experiment.	141
5.19 Comparison of load-deflection curves between simulations and experiments [3] with tuned β and ε_0	142
5.20 Comparison of crack paths between (a) the experiment [3] and (b-e) the simulation with $\beta = 0.1$ and $\varepsilon_0 = 0.2$. Iso-contours of $d = 0.8$ are highlighted in red.	143
5.21 Comparison of the final crack surfaces between (a) the experiment [3] and (b) the simulation ($\beta = 0.1$ and $\varepsilon_0 = 0.2$). “Shear lips” are circled in red. For comparison purposes, the computational domain is separated into two pieces by removing the domain within the $d \geq 0.8$ contour after complete failure.	144
5.22 Sandia Fracture Challenge problem geometry and mesh, with zoomed-in view of the refined region. The specimen is loaded vertically with displacement control at lines of nodes A and B marked as yellow spheres.	145
5.23 The force displacement curves from the experiment and the numerical simulations for the Sandia Fracture Challenge.	146
5.24 The Sandia Fracture Challenge. Contour plots of (a-c) the phase field d , (d-f) the active part of the strain energy $\psi_{\langle A \rangle}^e$, (g-i) the plastic energy ψ^p , and (j-l) the coalescence degradation function g^c at three different loads. In subfigures (d-i) the domain within the contour of $d > 0.8$ is removed to facilitate crack path visualization.	147
5.25 (a) Top view and (b) side view of the section of the heat exchanger. .	148

5.26	Boundaries of the heat exchanger.	152
5.27	Instantaneous thermal expansion coefficients.	154
5.28	Contour plots of (a-d) the phase field, (e-h) the debonding indicator, and (i-l) the effective creep strain. In the contour plots of the debonding indicator and the effective creep strain, elements within the contour of $d \leq 0.75$ are removed to visualize the pre-existing crack. In all contour plots, the oxide layer is warped according to the debonding indicator to visualize debonding.	156
5.29	The effective plastic strain right after each shut-down event. The region within the contour of $d \leq 0.75$ is removed to visualize in-plane fracture.	157
5.30	The active interface energy density right after each shut-down event. The region within the contour of $c \leq 0.75$ is removed to visualize out-of-plane debonding.	157
5.31	The active strain energy density right after each shut-down event. The region within the contour of $d \leq 0.75$ is removed to visualize in-plane fracture.	158
5.32	The coalescence degradation function right after each shut-down event. The region within the contour of $d \leq 0.75$ is removed to visualize in-plane fracture.	158
5.33	The debonding indicator right after each shut-down event. The region within the contour of $d \leq 0.75$ is removed to visualize in-plane fracture.	159
B.1	(a) Final phase field obtained using a spatially correlated random \mathcal{G}_c and ψ_c . (b) Corresponding clusters labeled by the flooding algorithm. Cluster boundaries are marked in black.	168
B.2	Status change from step n to step n+1. “Broken” elements are labeled in yellow, and “intact” elements are white. The step-by-step reclassification procedure is shown in Table B.1.	170

Acknowledgements

I want to thank Professor Philip Bayly, my undergraduate advisor, for his patient guidance in my first research project, and for telling me Duke is a great place to continue my study and Professor John Dolbow is terrific. I want to thank Professor John Dolbow, my advisor, for his valuable advice, barbeques and Thanksgiving dinners, and for proofreading several poorly written drafts of mine. I want to thank Dr. Benjamin Spencer, my technical advisor at Idaho National Laboratory, and Dr. Wen Jiang for two great summer internship experiences at INL, many helpful conversations, and their time reviewing my pull requests. I want to thank Professors Wilkins Aquino, Johann Guilleminot, Manolis Veveakis for their time and service as my committee members. Most of the work in this dissertation originated from their course projects. I want to thank Dr. Brandon Talamini, Dr. Andrew Stershic, and Dr. Michael Tupek from the Sandia National Laboratories for many enlightening discussions. I want to thank my colleagues Dr. Yingjie Liu and Dr. Rudy Geelen for babysitting me during my first semesters as a graduate student. I want to thank the Dolbow family for their sweet potato pie recipe which helped me navigate through some difficult times during the pandemic. Finally, I am most thankful for my wife Peiyi and my puppy Rudy.

1

Introduction

Fracture can be observed in virtually all engineering applications across several scales. It is important to understand the behavior of materials, components and structures with the presence of fracture. To that end, model-based simulations are widely adopted to help understand fracture-related phenomena. Over the past two decades, variational approaches to fracture have become increasingly popular, among which gradient damage models and phase-field models have received the most attention. On the one hand, these models have been successfully applied to a variety of engineering problems involving brittle/quasi-brittle fracture, cohesive fracture, ductile fracture as well as their coupling with other physics. On the other hand, the development of the theoretical variational framework was mostly confined within the regime of brittle/quasi-brittle fracture. This dissertation is concerned with the gap between the fundamental variational framework and practical engineering applications.

1.1 Background

In this dissertation, four types of fracture are of interest: brittle fracture, quasi-brittle fracture, cohesive fracture, and ductile fracture. Brittle and quasi-brittle fracture

center around the Griffith-type description of fracture, in the sense that the stress field at the crack tip is singular. In particular, brittle fracture is characterized with the complete loss of tensile strength upon crack nucleation. Under displacement-controlled uni-axial tension, a brittle specimen forms a through crack immediately after crack nucleation. Quasi-brittle fracture, in contrast, shows a gradual decay of tensile stress which is often measured in the form of a traction-separation law. Although the celebrated Griffith theory of fracture captures the behavior of a wide range of brittle and quasi-brittle materials, it bears emphasis that most materials are not perfectly brittle in the Griffith sense. Cohesive fracture, for example, describes materials that possess a *fracture process zone* ahead of the crack tip. The fracture process zone (FPZ) is a lumped description of small-scale yielding, void coalescence, and micro-crack merging. Typically, the material inside the FPZ only partially loses its load-carrying capacity, and therefore cohesive fracture also displays a gradual decay of tensile stress after crack initiation. The boundary between the definitions of quasi-brittle fracture and cohesive fracture is inherently vague. In this dissertation, cohesive fracture is assumed to have a substantially larger fracture process zone than quasi-brittle fracture, and at the engineering scale, numerical models for these two types of fracture are often used interchangeably. Lastly, ductile fracture describes the softening due to fracture after a stage of plastic hardening. Most metals and fiber-reinforced cementitious composites are ductile and are subject to ductile failure,

A number of models have been proposed to model fracture. What follows is a brief, non-comprehensive survey of numerical methods to model fracture. Particle-based and mesh-free discretization techniques, such as the discrete element method (DEM), lattice spring methods, and peridynamics, have been developed for fracture simulation. The key advantage of these methods lies in the fact that cracks can nucleate and grow in an unguided manner. However, the computational cost of these methods can be very high and the interface conditions are not straightforward

to apply. Within the context of the finite element method (FEM), linear elastic fracture mechanics models are extensively used, among which the most commonly used methods are the extended finite element method (XFEM) and the cohesive zone method (CZM). In XFEM, cracks are represented as discrete discontinuities and the displacements with discontinuities are enriched using the partition of unity method [4, 5]. Singularities associated with fracture can be represented using XFEM enrichment at relatively low cost. However, tracking the evolution of complex fracture surfaces, particularly in 3D, is quite tedious. In CZM, damage evolution is governed by a traction-separation law at crack surfaces [6, 7]. For polycrystalline material, CZM can explicitly account for grain boundaries and model intergranular crack initiation and evolution [8, 9]. Nonetheless, CZM suffers from mesh dependency because the representation of crack propagation is restricted to element boundaries.

The variational approach to fracture was proposed by Francfort and Marigo [10], and the phase-field implementation is attributed to Bourdin et al. [11]. Bourdin et al. [12] provides an overview. Pham and Marigo [13] used a crack geometric function that is linear in the phase-field variable, resulting in a purely elastic response prior to crack initiation. This fracture energy functional was subsequently referred to as the **AT-1** functional by Bourdin and co-workers (meant to evoke *Ambrosio* and *Tortorelli*, who initially introduced this and related functionals in the context of image segmentation [14]). Wu [15] generalized the *Ambrosio-Tortorelli* functional [14] to a family of second-order polynomials with various phase-field profiles, with specific choices of recovering the widely adopted **AT-1** and **AT-2** models. In the variational approach, crack surfaces are represented by a surface density function in terms of an auxiliary phase-field. This naturally gives rise to a regularization involving a length scale parameter. Recent works have illustrated the potential of phase-field models to be predictive for a wide range of fracture problems. Phase-field for fracture models have succeeded in capturing complex crack patterns, including

branching and merging in both two and three dimensions [16, 17, 18, 19, 20].

The general variational framework was first proposed by Biot [21] in the context of thermoelasticity, followed by extensive investigations in coupled thermoelastic and thermoviscoelastic systems [22, 23, 24, 25, 26, 27]. Well-defined variational principles for dissipative solids with and without heat conduction also exist [7, 28]. However, the case of thermo-mechanical-fracture coupling in dissipative materials has received far less attention.

It is worth noting that there are fundamental differences between variational consistency and thermodynamic consistency. In fact, thermodynamically consistent models are not necessarily variational. To satisfy thermodynamics, the model *must* satisfy mass conservation, linear momentum conservation, angular momentum conservation, as well as the first and the second laws of thermodynamics. Violating any of the aforementioned conservations or thermodynamic laws results in a physically inadmissible model. However, since the second law of thermodynamics is an inequality statement, there are infinitely many ways to satisfy it when modeling a dissipative solid. In contrast, the variational approach (including, but not limited to, variational approaches to fracture) is based on the idea that, upon careful construction of a potential, its variational statements are thermodynamically consistent, implying that the dissipation attains its maximum at the solution corresponding to the variational statements. In other words, the variational approach sets a more restrictive stage for model construction because it places more constraints on the constitutive behavior of the material. For example, if a potential is constructed within the variational framework to account for thermomechanical coupling, the heat generation due to its dissipation is directly predicted by the variational statement and cannot be specified arbitrarily.

The restrictions imposed by the variational approach lead to several beneficial aspects. First, the variational framework enables application of the tools of calcu-

lus of variations to the analysis of the solution. In particular, the direct method of calculus of variations informs conditions for the existence and uniqueness of solutions (e.g. [29]). Second, the localization of the fracture and the plastic zone can be studied within the framework of free-discontinuity problems [30, 31]. Third, in numerical methods, discretization of the variational statement of the problem leads to a symmetric operator, which can save storage and potentially accelerate the assembly process. Furthermore, energy-based line search methods can be directly applied to the system of equations; many powerful numerical optimization algorithms within standard linear algebra packages (e.g. PETSc [32], TAO [33], Trilinos [34], and Matlab [35]) can be utilized out-of-the-box; and the time-discretized variational problem leads to robust and efficient variational constitutive update algorithms [7].

1.2 Research contributions

This dissertation aims to extend the existing variational framework to account for thermal-mechanical-fracture coupling. The proposed framework is able to account for large deformation, inelastic deformation, thermal effects (i.e. heat conduction, heat convection, and heat generation), viscous effects, and potentially dynamic effects. From a fracture mechanics point of view, the framework is flexible enough to model brittle, quasi-brittle, cohesive, and ductile fracture. The applicability to each type of fracture is examined in the following chapters: a brittle/quasi-brittle instantiation is applied to model three-dimensional intergranular fracture and fission-gas-induced fragmentation in microstructures; a cohesive fracture model is applied to revisit the soil desiccation problem with a focus on random fracture properties; and a family of ductile fracture models are developed to simulate quasi-static ductile failure under isothermal conditions as well as thermal-induced oxide spallation.

- In Chapter 3, phase-field for brittle/quasi-brittle fracture models are employed

to simulate intergranular cracking with multiple bubbles on the grain boundaries in 3D and over-pressurized fission-gas-induced fragmentation at the microstructural level. To account for pressurized crack surfaces, we present an extension of the quasi-brittle model by including regularized external work done by pressure into the total energy of the system. The regularized external work is derived based on a phase-field approximation of the sharp interface. We demonstrate that the prediction of the dependence of the critical fracture strength on porosity based on 3D simulations is better than the 2D prediction. The effects of multi-bubble interaction and partial recrystallization in HBS are also investigated.

- In Chapter 4, a phase-field for cohesive fracture model is used to simulate pervasive cracking in thin films. A new strain energy split is proposed to enforce frictionless contact conditions in the vicinity of diffuse fracture surfaces. In contrast to existing splits that have been proposed, our approach completely prevents tractions from being transmitted across fully damaged surfaces that are loaded in tension. We construct a probabilistic model for the critical fracture energy and the fracture toughness, modeled as (potentially correlated) random fields, and demonstrate, through forward analysis and by solving an inverse problem, how crack network morphology can be influenced by stochastic spatially-varying material properties.
- In Chapter 5, we present a variational model for ductile fracture, and demonstrate, through numerical examples, that the model has the following properties: a unperturbed elastic-plastic response can be obtained and the plastic hardening law remain unmodified prior to crack initiation even when the plastic energy is degraded as a function of the phase-field variable; a regularization-length independent critical fracture strength and softening response can be

obtained by a family of rational degradation functions; and a novel dual kinetic potential, termed with *the coalescence dissipation*, can be incorporated to introduce an alternative form of coupling between plasticity and fracture. Thermal effects are then incorporated to model spallation of the oxide scale in a high-temperature heat exchanger.

1.3 Organization of the dissertation

First, the variational framework is presented in Chapter 2. General kinematics and constraints assumed throughout this dissertation are summarized in Section 2.1. Section 2.2 provides a brief review of thermodynamic conservations and laws in their global and local forms. The proposed variational framework is presented in Section 2.3, and discretization of the governing equations is presented in Section 2.4.

The variational framework is applied to solve engineering problems in Chapters 3 to 5. Chapter 3 simulates intergranular fracture and fission-gas-induced fracture in microstructures. Chapter 4 revisits the soil desiccation problem and explores the effect of random fracture properties. Chapter 5 benchmarks the ductile fracture model with a three-point bending experiment and one of the Sandia Fracture Challenges, and models oxide spallation in high-temperature heat exchangers. Each chapter begins with a general introduction to provide context and an overview of state-of-the-art methods and models. Then, specific constitutive choices are made, and the resulting governing equations are presented. Each chapter concludes with verifications of the variational model and some concrete numerical examples.

1.4 Notation

In what follows, deterministic scalar, vectors, second-order tensors, and fourth-order tensors are denoted by a (or A), \mathbf{a} (or \mathbf{A}), \mathbf{A} , and \mathbb{A} , respectively.

Let Ω be a collection of points $\mathbf{X} \in \mathbb{R}^d$, $d \in \{1, 2, 3\}$. Scalar- and vector-valued random fields defined on the probability space (Θ, Σ, P) , indexed by Ω , are denoted as $\{A(\mathbf{X}), \mathbf{X} \in \Omega\}$ and $\{\mathbf{A}(\mathbf{X}), \mathbf{X} \in \Omega\}$, respectively. At any fixed material point $\mathbf{X} \in \Omega$, $a(\mathbf{X})$ and $\mathbf{a}(\mathbf{X})$ are random variables defined on the probability space (Θ, Σ, P) . For any fixed $\theta \in \Theta$, $a(\theta)$ and $\mathbf{a}(\theta)$ are realizations of the random variables. Similarly, $\mathbf{X} \mapsto a(\mathbf{X}; \theta)$ and $\mathbf{X} \mapsto \mathbf{a}(\mathbf{X}; \theta)$ are realizations of the random fields $\{A(\mathbf{X}), \mathbf{X} \in \Omega\}$ and $\{\mathbf{A}(\mathbf{X}), \mathbf{X} \in \Omega\}$.

Einstein summations are assumed wherever applicable unless otherwise stated. For any vectors \mathbf{a} and \mathbf{b} of the same size, the inner product is defined as $\mathbf{a} \cdot \mathbf{b} = a_i b_i$ where a_i and b_i are components of the vectors. The associated vector norm is $\|\mathbf{a}\|^2 = \mathbf{a} \cdot \mathbf{a}$. Similarly, for any second-order tensors \mathbf{A} and \mathbf{B} of the same size, the inner product is defined as $\mathbf{A} : \mathbf{B} = \text{tr}(\mathbf{A}^T \mathbf{B})$. The associated Frobenius norm reads $\|\mathbf{A}\| = \sqrt{\mathbf{A} : \mathbf{A}}$. Other matrix norms will be distinguished by subscripts. The outer (cross) product of two vectors is written as $\mathbf{a} \otimes \mathbf{b} = a_i b_j$. The time derivative is denoted by an over-dot, e.g. \dot{a} .

Macaulay brackets are denoted by triangle brackets $\langle a \rangle_{\pm}$ and are defined as $\langle a \rangle_{\pm} \equiv (a \pm |a|)/2$. Partial derivative is denoted by a subscript starting with a comma, i.e. $a_{,bc} \equiv \partial^2 a / \partial b \partial c$.

2

The Variational Framework

2.1 Kinematics and Constraints

Let us start by defining degrees of freedom in the system. Let Ω be a body consisting of a continuous collection of material points. Let $\Omega_0 \subset \mathbb{R}^d$ be the reference configuration at some time $t = t_0$ whose particles are identified by their position \mathbf{X} , and $\Omega_t \subset \mathbb{R}^d$ be the current configuration at time $t > t_0$, with particles at position \mathbf{x} . The displacement is defined as $\mathbf{u} = \mathbf{x} - \mathbf{X}$. Let $\boldsymbol{\phi} : \Omega_0 \times [t_0, t] \mapsto \mathbb{R}^d$ be the deformation map. The deformation gradient is denoted as $\mathbf{F} = \nabla \boldsymbol{\phi}$, where the operator ∇ denotes differentiation with respect to \mathbf{X} (in the reference configuration Ω_0). The Jacobian determinant of the deformation gradient is written as $J = \det \mathbf{F}$.

Throughout this dissertation, the *local thermodynamic state* of an infinitesimal material neighborhood is defined by:

- the deformation gradient \mathbf{F} from the Lie group of invertible and orientation-preserving linear transformations in \mathbb{R}^d ;
- the collection of internal variables $\mathbf{Z} \in \mathbb{M}$, where the set \mathbb{M} depend on the material;

- the entropy density per unit volume $s \in \mathbb{R}$ in the reference configuration;

Plastic (or creep) deformations are modeled through the framework of multiplicative decomposition

$$\mathbf{F} = \mathbf{F}^e \mathbf{F}^p \mathbf{F}^g, \quad (2.1)$$

where \mathbf{F}^e , \mathbf{F}^p are referred to as the elastic and plastic deformation gradients, respectively. \mathbf{F}^g is the product of eigen deformation gradients.

Example 1. Isotropic thermal expansion can be accounted for by $\mathbf{F}^g = (1 + \bar{\alpha}\Delta T)\mathbf{I}$, where $\bar{\alpha}$ is the thermal expansion coefficient, and $\Delta T = T - T_0$ is the temperature change from the reference temperature T_0 .

Crack surfaces are regularized and modeled using a phase-field d , $0 \leq d \leq 1$, where $d = 0$ represents the intact state of a material point, and $d = 1$ indicates the material point has lost all load-carrying capacity.

For the systems of interest in this contribution, the internal variables are considered to be the plastic deformation \mathbf{F}^p (from the same Lie group of \mathbf{F}), the (scalar) effective plastic strain $\bar{\varepsilon}^p \in \mathbb{R}_+$, and the phase-field d regularizing the crack surfaces, i.e.

$$\mathbf{Z} = \{\mathbf{F}^p, \bar{\varepsilon}^p, d\}. \quad (2.2)$$

In general, internal variables evolve subject to constraints of the following form

$$\mathbf{L}(\mathbf{Z})\dot{\mathbf{Z}} = \mathbf{0}. \quad (2.3)$$

The specific form of the constraint depends on physical requirements and the material class. For isotropic J_2 -plasticity, the Prandtl-Reuss flow rule requires

$$\text{tr} \left(\dot{\mathbf{F}}^p \mathbf{F}^{p-1} \right) = 0, \quad (2.4a)$$

$$\left\| \dot{\mathbf{F}}^p \mathbf{F}^{p-1} \right\|^2 - \frac{3}{2} |\dot{\varepsilon}^p|^2 = 0, \quad (2.4b)$$

where (2.4a) requires the plastic flow to be isochoric, and (2.4b) normalizes the effective plastic strain $\bar{\varepsilon}^p$ to be uniaxial. Furthermore, the plastic flow is assumed to be irreversible in the sense

$$\dot{\bar{\varepsilon}}^p \geq 0. \quad (2.5)$$

Since the phase-field variable d is an approximation to the irreversible crack set, and as will be shown later, the crack geometric function is a monotonically increasing function of d , it is intuitive to impose an irreversibility constraint on the phase-field variable, i.e.

$$\dot{d} \geq 0. \quad (2.6)$$

Note that (2.4a), (2.4b), (2.5), and (2.6) are all of the general form (2.3).

2.2 Thermodynamics

Recall that the motions of the body are described by the deformation mapping $\Phi : \Omega_0 \times [t_0, t] \mapsto \mathbb{R}^d$. Let ρ_0 be the density in the reference configuration, \mathbf{b} be the distributed body force per unit mass, \mathbf{P} be the first Piola-Kirchhoff stress, \mathbf{n}_0 be the outward normal in the reference configuration, u be the internal energy density, $k = \rho_0 \dot{\Phi} \cdot \dot{\Phi}$ be the kinetic energy density, \mathcal{P}^{ext} be the external power expenditure, s be the entropy density, q be the distributed heat source per unit mass, and \mathbf{h} be the heat flux. The densities u , k and s are all defined per unit volume in the reference configuration. The motions of the body must obey the following conservations and thermodynamic laws:

- Conservation of mass:

$$\frac{d}{dt} \int_{\Omega'} \rho_0 \, dV = 0. \quad (2.7)$$

- Conservation of linear momentum:

$$\frac{d}{dt} \int_{\Omega'} \rho_0 \dot{\Phi} dV = \int_{\Omega'} \rho_0 \mathbf{b} dV + \int_{\partial\Omega'} \mathbf{P} \mathbf{n}_0 dA. \quad (2.8)$$

- Conservation of angular momentum:

$$\frac{d}{dt} \int_{\Omega'} \Phi \otimes (\rho_0 \dot{\Phi}) dV = \int_{\Omega'} \Phi \otimes (\rho_0 \mathbf{b}) dV + \int_{\partial\Omega'} \Phi \otimes (\mathbf{P} \mathbf{n}_0) dA. \quad (2.9)$$

- The first law of thermodynamics:

$$\frac{d}{dt} \int_{\Omega'} u dV + \frac{d}{dt} \int_{\Omega'} k dV = \int_{\Omega'} \mathcal{P}^{\text{ext}} dV + \int_{\Omega'} \rho_0 q dV - \int_{\partial\Omega'} \mathbf{h} \cdot \mathbf{n}_0 dA. \quad (2.10)$$

- The second law of thermodynamics:

$$\frac{d}{dt} \int_{\Omega'} s dV - \int_{\Omega'} \frac{\rho_0 q}{T} dV + \int_{\partial\Omega'} \frac{\mathbf{h} \cdot \mathbf{n}_0}{T} dA \geq 0. \quad (2.11)$$

All the above conservation and thermodynamic laws hold for any arbitrary sub-body $\Omega' \subset \Omega$, hence they can be written in the following local forms:

$$\dot{\rho}_0 = 0, \quad (2.12a)$$

$$\rho_0 \mathbf{a} = \nabla \cdot \mathbf{P} + \rho_0 \mathbf{b}, \quad (2.12b)$$

$$\mathbf{P} \mathbf{F} = \mathbf{F} \mathbf{P}^T, \quad (2.12c)$$

$$\dot{u} + \dot{k} = \mathcal{P}^{\text{ext}} + \rho_0 q - \nabla \cdot \mathbf{h}, \quad (2.12d)$$

$$\dot{s}^{\text{int}} = \dot{s} - \frac{\rho_0 q}{T} + \nabla \cdot \frac{\mathbf{h}}{T} \geq 0. \quad (2.12e)$$

Alternatively, the local form of the second law can be written in terms of the internal energy density as

$$\dot{s}^{\text{int}} = \mathcal{P}^{\text{ext}} - \dot{u} - \frac{1}{T} \mathbf{h} \cdot \nabla T. \quad (2.13)$$

For convenience, the collection of thermodynamic state variables (working with the Helmholtz free energy), kinematic degrees of freedom, and internal variables are defined as

$$\mathcal{S} = \{\mathcal{K}, T\}, \quad \mathcal{K} = \{\boldsymbol{\Phi}, \mathbf{Z}\}, \quad \mathbf{Z} = \{\mathbf{F}^p, \bar{\varepsilon}^p, d\}. \quad (2.14)$$

The rates of change of the kinematic variables are denoted as $\mathcal{V} = \{\dot{\boldsymbol{\Phi}}, \dot{\mathbf{F}}^p, \dot{\bar{\varepsilon}}^p, \dot{d}\}$.

The generalized velocities of the kinematic state variables are collected in the set

$$\dot{\Lambda} = \{\dot{\boldsymbol{\Phi}}, \dot{\mathbf{F}}, \dot{\mathbf{F}}^p, \dot{\bar{\varepsilon}}^p, \dot{d}, \nabla \dot{d}\}. \quad (2.15)$$

Recall that the local thermodynamic state is assumed to depend only on $\boldsymbol{\Phi}$, \mathbf{Z} and s , i.e.

$$u = \hat{u}(\Lambda, s), \quad T = \hat{T}(\Lambda, s). \quad (2.16)$$

It is convenient to work with the Helmholtz free energy density (per unit volume) with T as a state variable by introducing the Legendre transformation

$$\psi(\Lambda, T) = \inf_s [u(\Lambda, s) - Ts]. \quad (2.17)$$

The local form of the second law can then be rewritten using the identity $\dot{\psi} = \dot{u} - \dot{T}s$ and the fact that $\mathcal{P}^{\text{ext}} = \mathcal{P}^{\text{int}}$:

$$\dot{s}^{\text{int}} = \delta - \frac{1}{T} \mathbf{h} \cdot \nabla T, \quad \delta = \mathcal{P}^{\text{int}} - \dot{\psi} - \dot{T}s. \quad (2.18)$$

where δ shall be referred to as the internal dissipation density (per unit volume).

Combining (2.12e) and (2.18) yields the energy balance in the *entropy form*:

$$T\dot{s} = \rho_0 q - \nabla \cdot \mathbf{h} + \delta. \quad (2.19)$$

The internal power expenditure \mathcal{P}^{int} can be expressed in terms of generalized forces as

$$\mathcal{P}^{\text{int}} = \mathbf{P} : \dot{\mathbf{F}} + \mathbf{T} : \dot{\mathbf{F}}^p + Y\dot{\bar{\varepsilon}}^p + f\dot{d} + \boldsymbol{\xi} \cdot \nabla \dot{d}. \quad (2.20)$$

It is assumed that each of the generalized forces can be additively decomposed into an equilibrium part, thermodynamically conjugate to the Helmholtz free energy density, and a viscous part, i.e.

$$\mathbf{P} = \mathbf{P}^{\text{eq}}(\Lambda, T) + \mathbf{P}^{\text{vis}}(\dot{\mathbf{F}}, T; \Lambda), \quad (2.21\text{a})$$

$$\mathbf{T} = \mathbf{T}^{\text{eq}}(\Lambda, T) + \mathbf{T}^{\text{vis}}(\dot{\mathbf{F}}^p, T; \Lambda), \quad (2.21\text{b})$$

$$Y = Y^{\text{eq}}(\Lambda, T) + Y^{\text{vis}}(\dot{\varepsilon}^p, T; \Lambda), \quad (2.21\text{c})$$

$$f = f^{\text{eq}}(\Lambda, T) + f^{\text{vis}}(\dot{d}, T; \Lambda), \quad (2.21\text{d})$$

$$\boldsymbol{\xi} = \boldsymbol{\xi}^{\text{eq}}(\Lambda, T) + \boldsymbol{\xi}^{\text{vis}}(\nabla \dot{d}, T; \Lambda), \quad (2.21\text{e})$$

where the viscous forces must vanish as the rate diminishes to preclude viscous dissipation in quasi-static processes, i.e.

$$\lim_{\|\dot{\mathbf{F}}\| \rightarrow 0^+} \mathbf{P}^{\text{vis}} = 0, \quad (2.22\text{a})$$

$$\lim_{\|\dot{\mathbf{F}}^p\| \rightarrow 0^+} \mathbf{T}^{\text{vis}} = 0, \quad (2.22\text{b})$$

$$\lim_{|\dot{\varepsilon}^p| \rightarrow 0^+} Y^{\text{vis}} = 0, \quad (2.22\text{c})$$

$$\lim_{|\dot{d}| \rightarrow 0^+} f^{\text{vis}} = 0, \quad (2.22\text{d})$$

$$\lim_{\|\nabla \dot{d}\| \rightarrow 0^+} \boldsymbol{\xi}^{\text{vis}} = 0. \quad (2.22\text{e})$$

For convenience, the equilibrium forces and the viscous forces are collected in the sets

$$\mathcal{F}^{\text{eq}} = \{\mathbf{P}^{\text{eq}}, \mathbf{T}^{\text{eq}}, Y^{\text{eq}}, f^{\text{eq}}, \boldsymbol{\xi}^{\text{eq}}\}, \quad \mathcal{F}^{\text{vis}} = \{\mathbf{P}^{\text{vis}}, \mathbf{T}^{\text{vis}}, Y^{\text{vis}}, f^{\text{vis}}, \boldsymbol{\xi}^{\text{vis}}\}. \quad (2.23)$$

The rate of the Helmholtz free energy density can be expanded as

$$\dot{\psi} = \psi_{,\mathbf{F}} : \dot{\mathbf{F}} + \psi_{,\mathbf{F}^p} : \dot{\mathbf{F}}^p + \psi_{,\dot{\varepsilon}^p} \dot{\varepsilon}^p + \psi_{,d} \dot{d} + \psi_{,\nabla d} \cdot \nabla \dot{d} + \psi_{,T} \dot{T}. \quad (2.24)$$

Inserting the identity (2.24) into (2.18) and applying the Coleman-Noll procedure

leads to several thermodynamic restrictions on the constitutive relations:

$$\begin{aligned} \mathbf{P}^{\text{eq}} &= \psi_{,\mathbf{F}}, & \mathbf{T}^{\text{eq}} &= \psi_{,\mathbf{F}^p}, & Y^{\text{eq}} &= \psi_{,\bar{\varepsilon}^p}, & f^{\text{eq}} &= \psi_{,d}, & \boldsymbol{\xi}^{\text{eq}} &= \psi_{,\nabla d}, & -s &= \psi_{,T}. \end{aligned} \quad (2.25)$$

Substituting (2.25) and (2.24) into (2.18) simplifies the definition of the internal dissipation density:

$$\delta = \mathbf{P}^{\text{vis}} : \dot{\mathbf{F}} + \mathbf{T}^{\text{vis}} : \dot{\mathbf{F}}^p + Y^{\text{vis}} \dot{\bar{\varepsilon}}^p + f^{\text{vis}} \dot{d} + \boldsymbol{\xi}^{\text{vis}} \cdot \nabla d. \quad (2.26)$$

Using the identities (2.24) and (2.25), the rate of the entropy density can be expanded as

$$\dot{s} = -\dot{\psi}_{,T} = -\mathbf{P}_{,T}^{\text{eq}} : \dot{\mathbf{F}} - \mathbf{T}_{,T}^{\text{eq}} : \dot{\mathbf{F}}^p - Y_{,T}^{\text{eq}} \dot{\bar{\varepsilon}}^p - f_{,T}^{\text{eq}} \dot{d} - \boldsymbol{\xi}_{,T}^{\text{eq}} \cdot \nabla d - \psi_{,TT} \dot{T}. \quad (2.27)$$

By introducing the heat capacity per unit mass at constant Λ :

$$\rho_0 c_v = -T \psi_{,TT}, \quad (2.28)$$

the energy balance (2.19) can be rewritten as

$$\rho_0 c_v \dot{T} = \rho_0 q - \nabla \cdot \mathbf{h} + \delta + \delta_T, \quad (2.29)$$

where δ_T is the dissipation density accounting for the thermal effects in the thermodynamic conjugates:

$$\delta_T = T \left(\mathbf{P}_{,T}^{\text{eq}} : \dot{\mathbf{F}} + \mathbf{T}_{,T}^{\text{eq}} : \dot{\mathbf{F}}^p + Y_{,T}^{\text{eq}} \dot{\bar{\varepsilon}}^p + f_{,T}^{\text{eq}} \dot{d} + \boldsymbol{\xi}_{,T}^{\text{eq}} \cdot \nabla d \right), \quad (2.30)$$

e.g. $T \mathbf{P}_{,T}^{\text{eq}} : \dot{\mathbf{F}}$ accounts for thermoelastic effects, and $T Y_{,T}^{\text{eq}} \dot{\bar{\varepsilon}}^p$ accounts for thermo-plastic softening.

2.3 The variational statement

In this section, we construct a potential such that *all* the conservation and thermodynamic laws can be derived (if not implied by construction) from its variations. First, we assume that the Helmholtz free energy density ψ can be additively decomposed into the strain energy density ψ^e , the plastic energy density ψ^p , the fracture energy density ψ^f , and the thermal energy density ψ^h :

$$\psi = \psi^e(\mathbf{F}, \mathbf{F}^p, d, T) + \psi^p(\bar{\varepsilon}^p, d, T) + \psi^f(d, \nabla d, T) + \psi^h(T). \quad (2.31)$$

To maintain a variational structure, the viscous forces are supposed to be derived from dual kinetic potentials.

Example 2. [The elastic dual kinetic potential] Suppose there exist a potential $\zeta(\mathbf{P}^{\text{vis}})$ such that

$$\dot{\mathbf{F}} = \zeta_{,\mathbf{P}^{\text{vis}}}. \quad (2.32)$$

The dual kinetic potential is introduced by applying the Legendre transformation:

$$\psi^{e*}(\dot{\mathbf{F}}) = \sup_{\mathbf{P}^{\text{vis}}} \left[\mathbf{P}^{\text{vis}} : \dot{\mathbf{F}} - \zeta \right], \quad (2.33)$$

where it follows immediately that

$$\mathbf{P}^{\text{vis}} = \psi^{e*}_{,\dot{\mathbf{F}}}. \quad (2.34)$$

Note that the symbol ψ^{e*} is chosen in line with the energetic counterpart of the potential, not to imply that ψ^{e*} is the Legendre transformation of ψ^e . In fact, ψ^{e*} is the Legendre transformation of ζ .

Following the foregoing example, the viscous forces are defined as

$$\mathbf{P}^{\text{vis}} = \psi^{e*}_{,\dot{\mathbf{F}}}, \quad \mathbf{T}^{\text{vis}} = \psi^{p*}_{,\dot{\mathbf{F}}^p}, \quad \mathbf{Y}^{\text{vis}} = \psi^{p*}_{,\dot{\varepsilon}^p}, \quad \mathbf{f}^{\text{vis}} = \psi^{f*}_{,d}, \quad \boldsymbol{\xi}^{\text{vis}} = \psi^{f*}_{,\nabla d}, \quad (2.35)$$

where ψ^{e*} is the elastic dual kinetic potential describing rate-sensitivity of the deformation, e.g. Newtonian viscosity; ψ^{p*} is the plastic dual kinetic potential describing the rate-sensitivity of cold work, e.g. viscoplasticity; ψ^{f*} is the fracture dual kinetic potential describing viscous regularization of fracture propagation.

To satisfy the second law (2.13), the material is assumed to be *strictly dissipative* in the sense that every thermodynamic process results in an increase in entropy for nonzero rates, i.e. $\mathcal{F}^{\text{dis}} \cdot \dot{\Lambda} > \mathbf{0}, \forall \dot{\Lambda} \neq 0$. These constraints are subject to later verification.

The external power expenditure $\mathcal{P}^{\text{ext}}(\dot{\Phi}, T)$ is defined as

$$\begin{aligned} \mathcal{P}^{\text{ext}} = & \underbrace{\int_{\Omega_0} \rho_0 \mathbf{b} \cdot \dot{\Phi} \, dV}_{\text{body force}} + \underbrace{\int_{\partial_t \Omega_0} \mathbf{t} \cdot \dot{\Phi} \, dA}_{\text{surface traction}} + \underbrace{\int_{\partial_h \Omega_0} \bar{h}_n \ln \left(\frac{T}{T_0} \right) \, dA}_{\text{external heat flux}} \\ & + \underbrace{\int_{\partial_r \Omega_0} h \left[T - T_0 \ln \left(\frac{T}{T_0} \right) \right] \, dA}_{\text{external heat convection}} - \underbrace{\int_{\Omega_0} \rho_0 q \ln \left(\frac{T}{T_0} \right) \, dV}_{\text{heat source}}, \end{aligned} \quad (2.36)$$

where the subscripts in ∂_t , ∂_h and ∂_r denote the corresponding subsets of the surface with the associated Neumann/Robin boundary conditions. \bar{h}_n is the heat flux, h is the heat transfer coefficient, and T_0 is the reference or the ambient temperature.

To account for heat generation due to dissipation (i.e. from dual kinetic potentials), Yang et al. [28] introduced the concept of the *equilibrium temperature* corresponding to the thermodynamic state $\{\Lambda, s\}$ defined as

$$T^{\text{eq}} = u_{,s}(\Lambda, s), \quad (2.37)$$

and the *external temperature* T , along with a dummy integration factor T/T^{eq} . It will be shown later that the equilibrium temperature will be equal to the external temperature at equilibrium, and that the integration factor brings the effect of dissipation mechanisms into heat generation.

The total potential is constructed such that given the current kinematic state variables Λ and the current temperature, the velocities \mathcal{V} and the rate of temperature change can be obtained as a critical point following the first variations, which can then be used to update the state variables. The total potential L is constructed as

$$L(\dot{\Lambda}, \dot{s}, T, \nabla T) = \int_{\Omega_0} \varphi(\dot{\Lambda}, \dot{s}, T) \, dV - \mathcal{P}^{\text{ext}}(\dot{\Lambda}, T), \quad (2.38a)$$

$$\varphi(\dot{\Lambda}, \dot{s}, T, \nabla T) = \dot{k}(\dot{\Phi}) + \dot{u}(\dot{\Lambda}, \dot{s}) + \Delta^* \left(\frac{T}{T^{\text{eq}}} \dot{\Lambda}, T^{\text{eq}} \right) - T \dot{s} - \chi(\mathbf{g}), \quad (2.38b)$$

where \dot{u} is the rate of change in the internal energy, \dot{s} is the rate of change in the entropy, Δ^* is the sum of dual kinetic potentials:

$$\Delta^*(\dot{\Lambda}, T; \Lambda) = \psi^{e*}(\dot{\mathbf{F}}, T; \Lambda) + \psi^{p*}(\dot{\mathbf{F}}^p, \dot{\varepsilon}^p, T; \Lambda) + \psi^{f*}(\dot{d}, \nabla \dot{d}, T; \Lambda), \quad (2.39)$$

and χ is the Fourier potential defined in terms of the normalized temperature gradient $\mathbf{g} = -\frac{1}{T} \nabla T$, with the identity $-\mathbf{h} = \chi_{,\mathbf{g}}$. Finally, the entire problem can be variationally cast into the following inf-sup problem:

$$(\mathcal{V}, \dot{s}, T) = \arg \left[\inf_{\mathcal{V}, \dot{s}} \sup_T L(\dot{\Lambda}, \dot{s}, T, \nabla T) \right]. \quad (2.40)$$

Owing to [29, 28], the solutions of (2.40) have the following properties: Assume Ω_0 is open and bounded with only Dirichlet boundary conditions, and let $\widehat{T} \equiv \ln(T/T_0)$, $\widehat{T} \in \mathbb{R}$. If χ is convex in $\nabla \widehat{T}$ and grows as a power $|\nabla \widehat{T}|^p$, $1 < p < \infty$, then $L(\dot{\Lambda}, \dot{s}, T)$ attains its supremum $L(\dot{\Lambda}, \dot{s})$ in the Sobolev space $W^{1,p}(\Omega_0)$. If χ is *strictly convex* in ∇u , then the solution T is unique. The existence of the solution $\dot{\Lambda}$ is endorsed by the polyconvexity of the potentials $\dot{u}(\dot{\Lambda}, \dot{s})$ and $\Delta^*(\dot{\Lambda})$. In addition, the dissipation inequality (e.g. (2.12e)) is satisfied if $\Delta^*(\dot{\Lambda}, T)$ attains its infimum for every $\dot{\Lambda}$ when the rate is zero.

Remark 1. One may attempt to state the variational inf-sup problem without relying on the concept of the equilibrium temperature, the external temperature, and the integration factor:

$$(\mathcal{V}, \dot{s}, T) = \arg \left[\inf_{\mathcal{V}, \dot{s}} \sup_T L'(\dot{\Lambda}, \dot{s}, T, \nabla T) \right], \quad (2.41a)$$

$$L'(\dot{\Lambda}, \dot{s}, T, \nabla T) = \int_{\Omega_0} \varphi'(\dot{\Lambda}, \dot{s}, T, \nabla T) \, dV - \mathcal{P}^{\text{ext}}(\dot{\Lambda}, T), \quad (2.41b)$$

$$\varphi'(\dot{\Lambda}, \dot{s}, T, \nabla T) = \dot{k}(\dot{\Phi}) + \dot{u}(\dot{\Lambda}, \dot{s}) + \Delta^*(\dot{\Lambda}, T) - T\dot{s} - \chi(\mathbf{g}). \quad (2.41c)$$

However, it immediately follows that the supremum of (2.41a) in T does not include contributions from dissipation mechanisms:

$$\rho_0 c_v \dot{T} = \rho_0 q - \nabla \cdot \mathbf{h}, \quad (2.42)$$

which clearly violates the first law of thermodynamics (2.29).

To find the critical points of the inf-sup problem (2.40), we first isolate the local state variables from the global state variables. That is, (2.40) can be reorganized as

$$(\mathcal{V}, \dot{s}, T) = \arg \left[\inf_{\dot{\Phi}, \dot{d}} \sup_T L \left(\inf_{\dot{\mathbf{F}}^p, \dot{\varepsilon}^p, \dot{s}} \varphi \right) \right], \quad (2.43)$$

since the updates of \mathbf{F}^p , $\dot{\varepsilon}^p$ and s can be performed point-wise. Expanding \dot{u} in (2.38b) and substituting the constitutive restrictions (2.25) yields

$$\begin{aligned} \varphi(\dot{\Lambda}, \dot{s}, T, \nabla T) &= \rho_0 \mathbf{a} \cdot \dot{\Phi} + \mathbf{P}^{\text{eq}} : \dot{\mathbf{F}} + \mathbf{T}^{\text{eq}} : \dot{\mathbf{F}}^p + Y^{\text{eq}} \dot{\varepsilon}^p + f^{\text{eq}} \dot{d} + \boldsymbol{\xi}^{\text{eq}} \cdot \nabla \dot{d} \\ &\quad + T^{\text{eq}} \dot{s} + \Delta^* \left(\frac{T}{T^{\text{eq}}} \dot{\Lambda}, T^{\text{eq}} \right) - T \dot{s} - \chi(\mathbf{g}). \end{aligned} \quad (2.44)$$

The minimizer in \dot{s} follows as

$$T^{\text{eq}} - T = 0. \quad (2.45)$$

The infimum in $\dot{\mathbf{F}}^p$ and $\dot{\bar{\varepsilon}}^p$ shall follow from the joint minimization problem subject to the flow rule (2.3), i.e.

$$\begin{aligned} \left(\dot{\mathbf{F}}^p, \dot{\bar{\varepsilon}}^p \right) = \arg \inf_{\dot{\mathbf{F}}^p, \dot{\bar{\varepsilon}}^p} & \left[\mathbf{T}^{\text{eq}} : \dot{\mathbf{F}}^p + Y^{\text{eq}} \dot{\bar{\varepsilon}}^p + \Delta^* \right] \\ \text{subject to} & \quad \mathbf{L}(\mathbf{Z}) \dot{\mathbf{Z}} = \mathbf{0}. \end{aligned} \quad (2.46)$$

To find the infimum in T , substitute the definition of the free energy (2.31), the definition of the dual kinetic potential (2.39), the definition of the external power (2.36), and the constitutive restrictions (2.25) into (2.38a) to obtain

$$\begin{aligned} L(\dot{\Lambda}, \dot{s}, T, \nabla T) = \int_{\Omega_0} & \left[\rho_0 \mathbf{a} \cdot \dot{\boldsymbol{\phi}} + \mathbf{P}^{\text{eq}} : \dot{\mathbf{F}} + \mathbf{T}^{\text{eq}} : \dot{\mathbf{F}}^p + Y^{\text{eq}} \dot{\bar{\varepsilon}}^p + f^{\text{eq}} \dot{d} \right. \\ & \left. + \boldsymbol{\xi}^{\text{eq}} \cdot \nabla \dot{d} + T^{\text{eq}} \dot{s} + \Delta^* \left(\frac{T^{\text{eq}}}{T} \dot{\Lambda}, T^{\text{eq}} \right) - T \dot{s} - \chi(\mathbf{g}) \right] \, dV \\ & - \int_{\Omega_0} \rho_0 \mathbf{b} \cdot \dot{\boldsymbol{\phi}} \, dV - \int_{\partial_t \Omega_0} \mathbf{t} \cdot \dot{\boldsymbol{\phi}} \, dA - \int_{\partial_h \Omega_0} \bar{h}_n \ln \left(\frac{T}{T_0} \right) \, dA \\ & - \int_{\partial_r \Omega_0} h \left[T - T_0 \ln \left(\frac{T}{T_0} \right) \right] \, dA + \int_{\Omega_0} \rho_0 q \ln \left(\frac{T}{T_0} \right) \, dV \end{aligned} \quad (2.47)$$

The variation of (2.47) in T in the admissible space (admissible with respect to Dirichlet boundary conditions) is

$$T \dot{s} = \rho_0 q - \nabla \cdot \mathbf{h} + \delta, \quad \forall \mathbf{X} \in \Omega_0, \quad (2.48a)$$

$$\mathbf{h} \cdot \mathbf{n}_0 = \bar{h}_n, \quad \forall \mathbf{X} \in \partial_h \Omega_0, \quad (2.48b)$$

$$\mathbf{h} \cdot \mathbf{n}_0 = h(T - T_0), \quad \forall \mathbf{X} \in \partial_r \Omega_0. \quad (2.48c)$$

With the substitution of (2.27) and the definition of heat capacity (2.28), the first law in the form of (2.29) is recovered

$$\rho_0 c_v \dot{T} = \rho_0 q - \nabla \cdot \mathbf{h} + \delta + \delta_T. \quad (2.49)$$

Next, the balance of linear momentum and traction boundary conditions are recovered from variations in the admissible fields of $\dot{\Phi}$:

$$\rho_0 \mathbf{a} = \nabla \cdot \mathbf{P} + \mathbf{b}, \quad \forall \mathbf{X} \in \Omega_0, \quad (2.50a)$$

$$\mathbf{P} \mathbf{n}_0 = \mathbf{t}, \quad \forall \mathbf{X} \in \partial_t \Omega_0. \quad (2.50b)$$

Finally, variation in the admissible space of \dot{d} yields the fracture evolution equation on the inactive set

$$\nabla \cdot \boldsymbol{\xi} - f = 0, \quad \forall \mathbf{X} \in \mathcal{I}(\Omega_0), \quad (2.51)$$

$$\boldsymbol{\xi} \cdot \mathbf{n}_0 = 0, \quad \forall \mathbf{X} \in \mathcal{I}(\partial_d \Omega_0). \quad (2.52)$$

2.4 Discretization

We begin this section by summarizing the strong form of the general initial boundary value problem of interest:

The initial boundary value problem for the time interval $t \in I = [t_0, t_f]$

Linear momentum balance: $\rho_0 \mathbf{a} = \nabla \cdot \mathbf{P} + \rho_0 \mathbf{b},$	$\Omega_0 \times]t_0, t[,$
$\mathbf{P} \mathbf{n}_0 = \mathbf{t},$	$\partial_t \Omega_0 \times]t_0, t[,$
$\mathbf{u} = \mathbf{u}_g,$	$\partial_u \Omega_0 \times]t_0, t[,$
Fracture evolution: $\nabla \cdot \boldsymbol{\xi} - f = 0,$	$\mathcal{I}_t(\Omega_0) \times]t_0, t[,$
$\boldsymbol{\xi} \cdot \mathbf{n}_0 = 0,$	$\mathcal{I}_t(\partial_d \Omega_0) \times]t_0, t[,$
Heat transfer: $\rho_0 c_v \dot{T} = \rho_0 q - \nabla \cdot \mathbf{h} + \delta + \delta_T,$	$\Omega_0 \times]t_0, t[,$
$\mathbf{h} \cdot \mathbf{n}_0 = \bar{h}_n,$	$\partial_h \Omega_0 \times]t_0, t[,$
$\mathbf{h} \cdot \mathbf{n}_0 = h(T - T_0),$	$\partial_r \Omega_0 \times]t_0, t[,$
$T = T_g,$	$\partial_T \Omega_0 \times]t_0, t[,$
Initial conditions: $\mathbf{u} = \mathbf{u}_0,$	$\Omega_0, t = t_0,$
$\dot{\mathbf{u}} = \mathbf{v}_0,$	$\Omega_0, t = t_0,$
$d = d_0,$	$\Omega_0, t = t_0,$
$T = \bar{T}_0,$	$\Omega_0, t = t_0.$

The yield surface and the flow rule (and their corresponding constitutive updates) are defined only after specific constitutive assumptions are made in the following chapters (e.g. Chapter 5).

To derive the weak form, we begin by introducing the trial spaces \mathcal{U}_t , \mathcal{D}_t and \mathcal{T}_t :

$$\mathcal{U}_t = \{\mathbf{u} \in \mathcal{H}^1(\Omega_0)^d \mid \mathbf{u} = \mathbf{u}_g \text{ on } \partial_u \Omega_0\}, \quad (2.53a)$$

$$\mathcal{D}_t = \{d \in \mathcal{H}^1(\Omega_0) \mid \dot{d} > 0 \text{ on } \mathcal{I}_t(\Omega_0)\}, \quad (2.53b)$$

$$\mathcal{T}_t = \{T \in \mathcal{H}^1(\Omega_0) \mid T = T_g \text{ on } \partial_T \Omega_0\}, \quad (2.53c)$$

and the weighting spaces \mathcal{V} , \mathcal{C} and \mathcal{E} :

$$\mathcal{V} = \{\mathbf{w} \in \mathcal{H}^1(\Omega_0)^d \mid \mathbf{w} = \mathbf{0} \text{ on } \partial_u \Omega_0\}, \quad (2.54a)$$

$$\mathcal{C} = \{c \in \mathcal{H}^1(\Omega_0)\}, \quad (2.54b)$$

$$\mathcal{E} = \{e \in \mathcal{H}^1(\Omega_0) \mid T = 0 \text{ on } \partial_T \Omega_0\}. \quad (2.54c)$$

The weak form can be derived as:

The weak form

Given parameters in the IBVP, find $\mathbf{u} \in \mathcal{U}_t$, $d \in \mathcal{D}_t$ and $T \in \mathcal{T}_t$, $t \in [t_0, t_f]$, such that $\forall \mathbf{w} \in \mathcal{V}$, $\forall c \in \mathcal{C}$ and $\forall e \in \mathcal{E}$,

$$(\mathbf{w}, \rho_0 \mathbf{a}) + (\nabla \mathbf{w}, \mathbf{P}) - (\mathbf{w}, \rho_0 \mathbf{b}) - \langle \mathbf{w}, \mathbf{t} \rangle_{\partial_t \Omega_0} = 0, \quad (2.55a)$$

$$(\nabla c, \boldsymbol{\xi}) + (c, f) = 0, \quad (2.55b)$$

$$\begin{aligned} - \left(e, \rho_0 c_v \dot{T} \right) + (e, \rho_0 q) + (\nabla e, \mathbf{h}) + (e, \delta + \delta_T) \\ - \langle e, \bar{h}_n \rangle_{\partial_h \Omega_0} - \langle e, h(T - T_0) \rangle_{\partial_r \Omega_0} = 0, \end{aligned} \quad (2.55c)$$

with projections of initial conditions

$$(\mathbf{w}, \mathbf{u} - \mathbf{u}_0) = 0, \quad (2.56a)$$

$$(\mathbf{w}, \dot{\mathbf{u}} - \mathbf{v}_0) = 0, \quad (2.56b)$$

$$(c, d - d_0) = 0, \quad (2.56c)$$

$$(e, T - \bar{T}_0) = 0. \quad (2.56d)$$

Using the Galerkin method, with finite dimensional function spaces $\tilde{\mathcal{U}}_t \subset \mathcal{U}_t$, $\tilde{\mathcal{V}} \subset \mathcal{V}$, $\tilde{\mathcal{D}}_t \subset \mathcal{D}_t$, $\tilde{\mathcal{C}} \subset \mathcal{C}$, $\tilde{\mathcal{T}}_t \subset \mathcal{T}_t$, $\tilde{\mathcal{E}} \subset \mathcal{E}$, we arrive at the spatially discrete form of the problem:

The semidiscrete Galerkin form

Given parameters in the IVP, find $\mathbf{u}^h \in \tilde{\mathcal{U}}_t$, $d^h \in \tilde{\mathcal{D}}_t$ and $T^h \in \tilde{\mathcal{T}}_t$, $t \in [t_0, t_f]$, such that $\forall \mathbf{w}^h \in \tilde{\mathcal{V}}$, $\forall q^h \in \tilde{\mathcal{C}}$ and $\forall e^h \in \tilde{\mathcal{E}}$,

$$(\mathbf{w}^h, \rho_0 \mathbf{a}) + (\nabla \mathbf{w}^h, \mathbf{P}) - (\mathbf{w}^h, \rho_0 \mathbf{b}) - \langle \mathbf{w}^h, \mathbf{t} \rangle_{\partial_t \Omega_0} = 0, \quad (2.57a)$$

$$(\nabla c^h, \boldsymbol{\xi}) + (c^h, f) = 0, \quad (2.57b)$$

$$\begin{aligned} & - \left(e^h, \rho_0 c_v \dot{T} \right) + (e^h, \rho_0 q) + (\nabla e^h, \mathbf{h}) + (e^h, \delta + \delta_T) \\ & - \langle e^h, \bar{h}_n \rangle_{\partial_h \Omega_0} - \langle e^h, h(T^h - T_0) \rangle_{\partial_r \Omega_0} = 0, \end{aligned} \quad (2.57c)$$

with projections of initial conditions

$$(\mathbf{w}^h, \mathbf{u}^h - \mathbf{u}_0) = 0, \quad (2.58a)$$

$$(\mathbf{w}^h, \dot{\mathbf{u}}^h - \mathbf{v}_0) = 0, \quad (2.58b)$$

$$(c^h, d^h - d_0) = 0, \quad (2.58c)$$

$$(e^h, T^h - \bar{T}_0) = 0. \quad (2.58d)$$

The semidiscrete momentum balance equation (2.57a) is discretized using the generalized- α method. The semidiscrete fracture evolution equation (2.57b) and the heat conduction equation (2.57c) are discretized using the backward-Euler time integration. Discretizations of the plasticity constitutive updates are discussed in Chapter 5. The discrete inequality for crack irreversibility is satisfied node-wise with a primal-dual active set (PDAS) strategy. See e.g. Heister et al. [36] for implementational details of such a solver. The solver is also generally available in numerical toolboxes, e.g. PETSc [32]. The discrete approximation is calculated using a fixed-point iterative solution scheme outlined from [37]. A simple fixed-point iterative Newton-based PDAS solution algorithm is outlined in Algorithm 1. The algorithm is observed to be effective for all numerical examples included in this dissertation. Note that notation is slightly abused in the algorithm for simplicity: all state variables with subscripts or superscripts represent their discrete counterpart; the time step is indexed by the counter n in the subscript; the fixed-point iteration is indexed by the counter a in the

subscript; the Newton iteration is indexed by the counter k in the superscript; the constant mass matrix is denoted by M ; and c is the numerical parameter controlling the update of the active set.

Algorithm 1 A fixed-point iterative PDAS-Newton solution algorithm.

- 1: Given \mathbf{u}_n , T_n , d_n , \mathbf{F}^p_n , $\bar{\varepsilon}^p_n$.
 - 2: Set $a \leftarrow 0$.
 - 3: Set $\mathbf{u}_{n+1,a} \leftarrow \mathbf{u}_n$, $T_{n+1,a} \leftarrow T_n$, $d_{n+1,a} \leftarrow d_n$, $\mathbf{F}^p_{n+1,a} \leftarrow \mathbf{F}^p_n$, $\bar{\varepsilon}^p_{n+1,a} \leftarrow \bar{\varepsilon}^p_n$.
 - 4: **repeat**
 - 5: Compute \dot{d} using $d_{n+1,a}$ and d_n with the appropriate time integrator.
 - 6: Solve for $\mathbf{u}_{n+1,a+1}$, $\mathbf{F}^p_{n+1,a+1}$, $\bar{\varepsilon}^p_{n+1,a+1}$, and $T_{n+1,a+1}$ using the discretized incremental variational (sub-) problem
- $$\inf_{\mathbf{u}_{n+1,a+1}} \sup_{T_{n+1,a+1}} L_n \left(\inf_{\mathbf{F}^p_{n+1,a+1}, \bar{\varepsilon}^p_{n+1,a+1}} \varphi_n \right).$$
- 7: Compute $\dot{\mathbf{u}}$ using $\mathbf{u}_{n+1,a+1}$ and \mathbf{u}_n with the appropriate time integrator.
 - 8: Set $k \leftarrow 0$.
 - 9: Set $d_{n+1,a+1}^k \leftarrow d_{n+1,a}$.
 - 10: Assemble the gradient g and the hessian H for the discretized incremental variational (sub-) problem
- $$\inf_{d_{n+1,a+1}^k} L_n.$$
- 11: Compute the initial Lagrange multiplier $\lambda = -M^{-1}g$.
 - 12: Identify the initial active/inactive as $\mathcal{A} = \{i | \lambda_i > 0\}$, $\mathcal{I} = \{i | \lambda_i \leq 0\}$.
 - 13: **repeat**
 - 14: Eliminate dofs on \mathcal{A} and \mathcal{I} to obtain the reduced gradient \hat{g} and reduced Hessian \hat{H} .
 - 15: Compute the Newton update on the inactive set as $\hat{p} = -\hat{H}^{-1}\hat{g}$.
 - 16: Update the solution on the inactive set to obtain $d_{n+1,a+1}^{k+1}$.
 - 17: Update g and H .
 - 18: Update $\lambda = -M^{-1}(g + Hp)$.
 - 19: Update $\mathcal{A} = \{i | (\lambda - cp)_i > 0\}$, $\mathcal{I} = \{i | (\lambda - cp)_i \leq 0\}$.
 - 20: Update $k \leftarrow k + 1$.
 - 21: **until** $d_{n+1,a+1}$ and \mathcal{A} have converged.
 - 22: Update $d_{n+1,a+1} \leftarrow d_{n+1,a+1}^k$.
 - 23: Update $a \leftarrow a + 1$.
 - 24: **until** \mathbf{u}_{n+1} , T_{n+1} and d_{n+1} have converged.
 - 25: Update $\mathbf{u}_{n+1} \leftarrow \mathbf{u}_{n+1,a}$, $T_{n+1} \leftarrow T_{n+1,a}$, $d_{n+1} \leftarrow d_{n+1,a}$.
-

3

Brittle and Quasi-Brittle Fracture: Intergranular Fracture Evolution in Polycrystalline Materials

3.1 Introduction

During the operation of commercial light water reactors, fission of uranium dioxide (UO_2) produces a variety of fission products within the fuel matrix. The fracture behavior of brittle materials is strongly influenced by their underlying microstructural features such as gas bubbles, second-phase particles, pre-existing micro-cracks, grains, grain boundaries, and etc. For example, the bubbles at the grain boundaries alter the fracture properties, and subsequently affects the pellet-cladding mechanical interaction (PCMI), fission gas release and swelling. Therefore, it is important to develop a fracture model that incorporates the effects of microstructural features to better understand how fission changes the fracture response of the nuclear fuel.

On the other hand, to improve the economics of commercial nuclear power production, utilities are seeking to increase the allowable burnup limit for UO_2 fuel. A main factor contributing to the current burnup limit in commercial light water reactors is the risk of fragmentation during a loss-of-coolant accident (LOCA). To allow

the industry to pursue an increased burnup limit and develop mitigation strategies, an improved capability for predicting the onset of fragmentation is essential.

A thorough review of fuel fracture and high-burnup fuel fragmentation is provided in [38]. In this chapter, we focus on the fine fragmentation that results in fuel fragments typically less than 0.1 mm in size. It has been reported that fine fragmentation primarily occurs at high burnups – especially when the high-burnup structure (HBS) has formed. The HBS is typically characterized by small newly formed grains with sizes of 100–300 nm and round fission gas pores of micrometric size [39]. It is hypothesized that over-pressurization of fission gas bubbles in the UO₂ HBS could result in fine fragmentation during typical LOCA transients.

In general, fuel fracture can be modeled using phenomenological [40] and mechanical models [41]. Various criteria have been used to determine whether fine fragmentation will occur during a LOCA, but such criteria are all based on simple analytical models [42, 43]. For additional insight into gas-bubble-induced fracture in polycrystalline materials and HBS fine fragmentation (including crack topology, fragment morphology, and fragment topography), a physics-based model is needed to simulate over-pressurization of fission gas bubbles.

Recently, the phase-field fracture models have been applied to study gas-bubble-induced fracture in polycrystalline materials. Chakraborty et al. [44] developed a hierarchical multi-scale approach to model microstructure-sensitive brittle fracture, and 2D simulations were performed to relate fracture strength to porosity. A 2D approximation often over-simplifies the actual microstructure and results in an inaccurate measurement of porosity. Diehl et al. [45] proposed 3D models of damage evolution around a single bubble and investigated the influence of the bubble geometry on the fracture response. 3D simulations provide important insights into the influence of porosity on fracture. In this chapter, a phase-field for fracture model is employed to address intergranular cracking with multiple bubbles on the grain

boundaries in 3D and is used to model over-pressurized fission-gas-induced fragmentation at the microstructural level.

In HBS, following crack initiation, the cracks will be filled with fission gas, and the crack surfaces will become pressurized. To account for pressurized crack surfaces, we present an extension of the brittle/quasi-brittle fracture model by including regularized external work done by pressure. The regularized external work can be derived either based on a phase-field approximation of the sharp interface [46], or by modifying the free energy in a Biot system via an indicator function based on the phase-field [47]. In this chapter, the former approach is used to derive the phase-field model for brittle and quasi-brittle fracture with pressurized cracks.

This chapter is organized as follows. Constitutive choices for the strain energy density and the fracture energy density are presented in Section 3.2.1. The phase-field approximation of the external pressure and its derivation are provided in Section 3.2.2. Governing equations are summarized in Section 3.2.3. The theory is followed by numerical verification and examples. The traction-separation behavior with the presence of pressure is studied in Section 3.3.1. The numerical critical pressure associated with crack propagation is compared with the linear elastic fracture mechanics solution in Section 3.3.2. Finally, Section 3.4 applies the model to investigate the relationship between the critical fracture strength and porosity, and to model fracture evolution in HBS.

3.2 Theory

3.2.1 Constitutive choices

Following the variational framework presented in Chapter 2, to account for elastic deformation and fracture in polycrystalline materials, the Helmholtz free energy

density is decomposed as

$$\psi = \psi^e + \psi^f. \quad (3.1)$$

Recall that ψ^e is the strain energy density, and ψ^f is the fracture energy density.

3.2.1.1 strain energy density

For small deformation elasticity considered in this chapter, the state variable $\mathbf{u} = \Phi - \mathbf{X}$ enters the strain energy density only through the infinitesimal strain tensor

$$\boldsymbol{\varepsilon} = \frac{1}{2} (\boldsymbol{\nabla} \mathbf{u} + \boldsymbol{\nabla}^T \mathbf{u}). \quad (3.2)$$

The material is assumed to be isotropic, characterized by the Lamé parameter λ and the shear modulus G . The strain energy density (with the spectral split [48, 49]) is defined as

$$\psi^e = g\psi_{\langle A \rangle}^e + \psi_{\langle I \rangle}^e, \quad (3.3a)$$

$$\psi_{\langle A \rangle}^e = \frac{1}{2}\lambda \langle \text{tr}(\boldsymbol{\varepsilon}) \rangle_+^2 + G\boldsymbol{\varepsilon}^+ : \boldsymbol{\varepsilon}^+, \quad (3.3b)$$

$$\psi_{\langle I \rangle}^e = \frac{1}{2}\lambda \langle \text{tr}(\boldsymbol{\varepsilon}) \rangle_-^2 + G\boldsymbol{\varepsilon}^- : \boldsymbol{\varepsilon}^-, \quad (3.3c)$$

where $g = \hat{g}(d)$ is the degradation function to be defined in Section 3.2.1.2, and $\boldsymbol{\varepsilon}^\pm$ denotes the positive or the negative part of the strain projected onto the spectrum associated with positive or negative eigenvalues. In the context of small deformation, the Cauchy stress $\boldsymbol{\sigma}$ can be viewed as the thermodynamic conjugate to the infinitesimal strain $\boldsymbol{\varepsilon}$, and can be written as

$$\boldsymbol{\sigma} = \psi_{,\boldsymbol{\varepsilon}}^e = g\boldsymbol{\sigma}_{\langle A \rangle} + \boldsymbol{\sigma}_{\langle I \rangle}, \quad (3.4a)$$

$$\boldsymbol{\sigma}_{\langle A \rangle} = \lambda \langle \text{tr}(\boldsymbol{\varepsilon}) \rangle_+ \mathbf{I} + 2G\boldsymbol{\varepsilon}^+, \quad (3.4b)$$

$$\boldsymbol{\sigma}_{\langle I \rangle} = \lambda \langle \text{tr}(\boldsymbol{\varepsilon}) \rangle_- \mathbf{I} + 2G\boldsymbol{\varepsilon}^-. \quad (3.4c)$$

3.2.1.2 Fracture energy density

With a sharp crack set Γ , the fracture energy is defined as $\Psi^f = \int_{\Gamma} \mathcal{G}_c \, dA$, where \mathcal{G}_c is

the fracture toughness. An approximation of the sharp crack set using a phase-field can be written as

$$\Psi^f \approx \int_{\Omega_0} \psi^f \, dV = \int_{\Omega_0} \mathcal{G}_c \gamma_l(d, \nabla d) \, dV, \quad (3.5)$$

where γ_l is often referred to as the crack surface density parameterized by a regularization length l . An Allen-Cahn type approximation can be expressed as

$$\gamma_l(d, \nabla d) = \frac{1}{c_0 l} (\alpha + l^2 \nabla d \cdot \nabla d), \quad (3.6)$$

where $\alpha = \hat{\alpha}(d)$ is the crack geometric function. According to the discussion in Chapter 2, existence requires $\hat{\alpha}(d)$ to be convex in d , and the phase-field irreversibility condition (2.6) assumes $\hat{\alpha}(d)$ attains its minimum at $d = 0$.

In the current variational framework, the fracture response, e.g. the critical fracture strength and the softening behavior, is determined by the crack geometric function and the degradation function. In this chapter, to model brittle fracture, where crack only nucleates at stress singularities, i.e. $\psi_c \rightarrow \infty$, the following combination of crack geometric function and degradation function is used,

$$\alpha = d^2, \quad g = (1 - d)^2. \quad (3.7)$$

To model quasi-brittle fracture in polycrystalline materials, where the post-fracture behavior can be characterized by a certain softening law, the following combination is used,

$$\alpha = \xi d - (1 - \xi)d^2, \quad g = \frac{1}{1 + \phi}, \quad \phi = \frac{a_1 d + a_1 a_2 d^2 + a_1 a_2 a_3 d^3}{(1 - d)^p}, \quad (3.8)$$

where ψ_c is the critical fracture energy density, α is parameterized by ξ (ξ is conveniently the derivative of α at $d = 0$), and the degradation function g is parameterized by p , a_1 , a_2 and a_3 . Based on some 1-D analyses [15], the optimal profile of the phase-field is controlled by ξ . For a given ξ , the approximated traction-separation law is determined by p , a_1 , a_2 and a_3 . In this chapter, the following parameters are chosen:

$$\xi = 2, \quad p = 2, \quad a_1 = \frac{\mathcal{G}_c}{c_0 l \psi_c}, \quad a_2 = -\frac{1}{2}, \quad a_3 = 0, \quad (3.9)$$

such that the phase-field is compactly supported by a constant half interfacial width of $D_u = \frac{\pi}{2}l$, and a linear traction-separation law is approximated with a slope of $-\frac{E\psi_c}{\mathcal{G}_c}$ (in the 1D setting).

Remark 2. For most materials, instead of the critical fracture energy, the critical fracture strength (or sometimes referred to as the ultimate strength) is measured. The critical fracture energy and the critical fracture strength can be related using the following approximation:

$$\sigma_c \approx \sqrt{(2E\psi_c)}. \quad (3.10)$$

This approximation is made under the assumption of 1D uniaxial tension, and will be inaccurate in multi-axial loading or due to Poisson's effect.

3.2.2 Approximation of the pressure boundary condition

Starting from the sharp representation of the crack set, the external power expenditure on the crack set due to pressure can be written as

$$\mathcal{P}^{\text{ext}} = \int_{\Gamma} \bar{p} \mathbf{n}_0 \cdot \dot{\boldsymbol{\phi}} \, dA, \quad (3.11)$$

where \bar{p} is the magnitude of the pressure. Following [46], the external work is approximated as:

$$\begin{aligned}\mathcal{P}^{\text{ext}} &= \int_{\Omega_0} \rho^{\text{ext}} \, dV = \int_{\Omega_0} \bar{p} \left(-\frac{\nabla d}{\|\nabla d\|} \right) \cdot \dot{\Phi} \|\nabla I\| \, dV \\ &= \int_{\Omega_0} \bar{p} \left(-\frac{\nabla d}{\|\nabla d\|} \right) \cdot \dot{\Phi} \|\nabla d\| I_{,d} \, dV = - \int_{\Omega_0} \bar{p} \nabla d \cdot \dot{\Phi} I_{,d} \, dV,\end{aligned}\tag{3.12}$$

where the surface normal \mathbf{n} is approximated using the gradient of the phase-field, and a crack indicator function $I(d) \in C^1([0, 1])$ is introduced so that the approximation respects the Γ -convergence properties.

Remark 3. Based on (3.12), the effective pressure approximated by the phase field can be defined as:

$$\tilde{p} = \int_{\Omega_0} \frac{\partial \rho^{\text{ext}}}{\partial \dot{\Phi}} \cdot \left(-\frac{\nabla d}{\|\nabla d\|} \right) \, dV = \int_{\Omega_0} \bar{p} \|\nabla I\| \, dV.\tag{3.13}$$

Assuming that $I(0) = 0$ and $I(1) = 1$, the proof of Γ -convergence can be sketched via the following method. Consider the approximated external power expenditure due to pressure (parameterized by the phase-field regularization length l). The phase-field profile can always be expressed by $d = \bar{d}(d_\Gamma(\mathbf{X})/l)$, where $d_\Gamma(\mathbf{X})$ is the unsigned distance function for the crack set Γ [50]. Substituting the phase-field profile into (3.12) yields:

$$\begin{aligned}\mathcal{P}^{\text{ext}} &= - \int_{\Omega_0} \bar{p} \nabla \tilde{d} \cdot \dot{\Phi} I_{,d}(\tilde{d}) \, dV = - \int_{\Omega_0} \bar{p} \nabla I \cdot \dot{\Phi} \, dV \\ &= - \int_{\Omega_0} \bar{p} \frac{dI}{d(d_\Gamma/l)} \frac{1}{l} \nabla d_\Gamma(\mathbf{X}) \cdot \dot{\Phi} \, dV.\end{aligned}\tag{3.14}$$

The domain integral can be converted to a set of path integrals along the level set

(phase-field), using the co-area formula, as follows:

$$\mathcal{P}^{\text{ext}} = - \int_0^\infty \int_{\{\mathbf{X} \in \Omega_0, d_\Gamma(\mathbf{X})=r\}} \bar{p} \frac{dI}{d(r/l)} \frac{1}{l} \nabla d_\Gamma(\mathbf{X}) \cdot \dot{\Phi} \, ds \, dr. \quad (3.15)$$

A simple change of variables with $\tilde{r} = r/l$ yields:

$$\begin{aligned} \mathcal{P}^{\text{ext}} &= - \int_0^\infty \left(\int_{\{\mathbf{X} \in \Omega_0, d_\Gamma(\mathbf{X})=r\}} \bar{p} \nabla d_\Gamma(\mathbf{X}) \cdot \dot{\Phi} \, ds \right) \frac{dI}{d(r/l)} \frac{1}{l} \, dr \\ &= - \int_0^\infty \left(\int_{\{\mathbf{X} \in \Omega_0, d_\Gamma(\mathbf{X})=l\tilde{r}\}} \bar{p} \nabla d_\Gamma(\mathbf{X}) \cdot \dot{\Phi} \, ds \right) \frac{dI}{d\tilde{r}} \, d\tilde{r}. \end{aligned} \quad (3.16)$$

Next, as the phase-field regularization length diminishes (i.e., $l \rightarrow 0$), the approximation of the pressure power expenditure converges to:

$$\lim_{l \rightarrow 0} \mathcal{P}^{\text{ext}} = - \int_0^\infty \frac{dI}{d\tilde{r}} \, d\tilde{r} \left[\int_{\Gamma^+} \bar{p}(-\mathbf{n}_0) \cdot \dot{\Phi} \, dA + \int_{\Gamma^-} \bar{p}(-\mathbf{n}_0) \cdot \dot{\Phi} \, dA \right], \quad (3.17a)$$

where it is apparent that the path integral along the level set converges to the surface integral on two opposite sides of the crack surface, while the gradient of the unsigned distance function converges to the normal on the crack surfaces Γ , i.e., $\lim_{l \rightarrow 0} \nabla d_\Gamma(\mathbf{X}) = -\mathbf{n}_0(\mathbf{X})$. Recall that the support of the phase-field depends on the form of the crack geometric function α [50]; the integral shall be split according

to the the ultimate phase-field half interfacial width D_u :

$$\begin{aligned}
& \lim_{l \rightarrow 0} \mathcal{P}^{\text{ext}} \\
&= - \left(\int_0^{D_u/l} \frac{dI}{d\tilde{r}} d\tilde{r} + \int_{D_u/l}^{\infty} \frac{dI}{d\tilde{r}} d\tilde{r} \right) \left[\int_{\Gamma^+} \bar{p}(-\mathbf{n}_0) \cdot \dot{\boldsymbol{\Phi}} dA + \int_{\Gamma^-} \bar{p}(-\mathbf{n}_0) \cdot \dot{\boldsymbol{\Phi}} dA \right] \\
&= - \left[I\left(\tilde{r} = \frac{D_u}{l}\right) - I(\tilde{r} = 0) \right] \left[\int_{\Gamma^+} \bar{p}(-\mathbf{n}_0) \cdot \dot{\boldsymbol{\Phi}} dA + \int_{\Gamma^-} \bar{p}(-\mathbf{n}_0) \cdot \dot{\boldsymbol{\Phi}} dA \right] \quad (3.18) \\
&= - [I(0) - I(1)] \left[\int_{\Gamma^+} \bar{p}(-\mathbf{n}_0) \cdot \dot{\boldsymbol{\Phi}} dA + \int_{\Gamma^-} \bar{p}(-\mathbf{n}_0) \cdot \dot{\boldsymbol{\Phi}} dA \right].
\end{aligned}$$

Finally, recall our previous restrictions on the indicator function $I(c)$; this limit reduces to:

$$\lim_{l \rightarrow 0} \mathcal{P}^{\text{ext}} = \int_{\Gamma^+} \bar{p}(-\mathbf{n}_0) \cdot \dot{\boldsymbol{\Phi}} dA + \int_{\Gamma^-} \bar{p}(-\mathbf{n}_0) \cdot \dot{\boldsymbol{\Phi}} dA. \quad (3.19)$$

3.2.3 Governing equations

Following the variational framework, substituting (3.1), (3.3a), (3.5), (3.6), and (3.12) into the problem statement (2.40), under quasi-static and isothermal conditions, the governing equations can be obtained as

$$\nabla \cdot \boldsymbol{\sigma} - \bar{p} \nabla d I_{d,d} = \mathbf{0}, \quad (3.20a)$$

$$\nabla \cdot \boldsymbol{\xi} - f = 0, \quad (3.20b)$$

supplemented by the constitutive relations (3.4a) and

$$\boldsymbol{\xi} = \frac{2\mathcal{G}_c l}{c_0} \nabla d, \quad f = g_{,d} \psi_{\langle A \rangle}^e + \frac{\mathcal{G}_c}{c_0 l} \alpha_{,d}. \quad (3.21)$$

3.3 Verification

3.3.1 Uniaxial traction of a bar

We first verify the uniaxial response of the quasi-brittle fracture model with a pressurized crack. Consider a bar of length $2L = 400$ mm and width $2W = 2$ mm that is subject to uniaxial tension. Plane strain conditions are assumed to hold. A similar example without crack pressurization can be found in [50]. Boundary conditions are shown in Figure 3.1. Both ends of the bar are subject to monotonically increasing horizontal displacements. Only a quarter of the domain is simulated utilizing the two symmetry conditions. The domain is uniformly discretized using QUAD4 elements, with 200 elements along the length and 1 element along the width. The material and model parameters are Young's modulus $E = 3 \times 10^4$ MPa, Poisson's ratio $\nu = 0.2$, critical fracture strength $\psi_c = 1.5 \times 10^{-4}$ mJ mm $^{-3}$, fracture toughness $\mathcal{G}_c = 0.12$ mJ mm $^{-2}$, and the characteristic length $l_{ch} = \frac{\mathcal{G}_c}{2\psi_c} = 400$ mm.

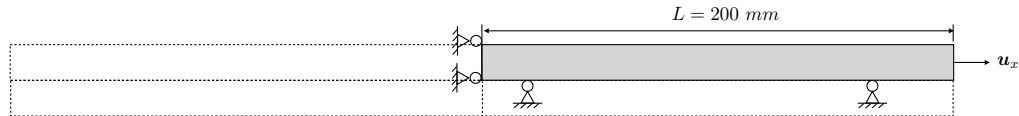
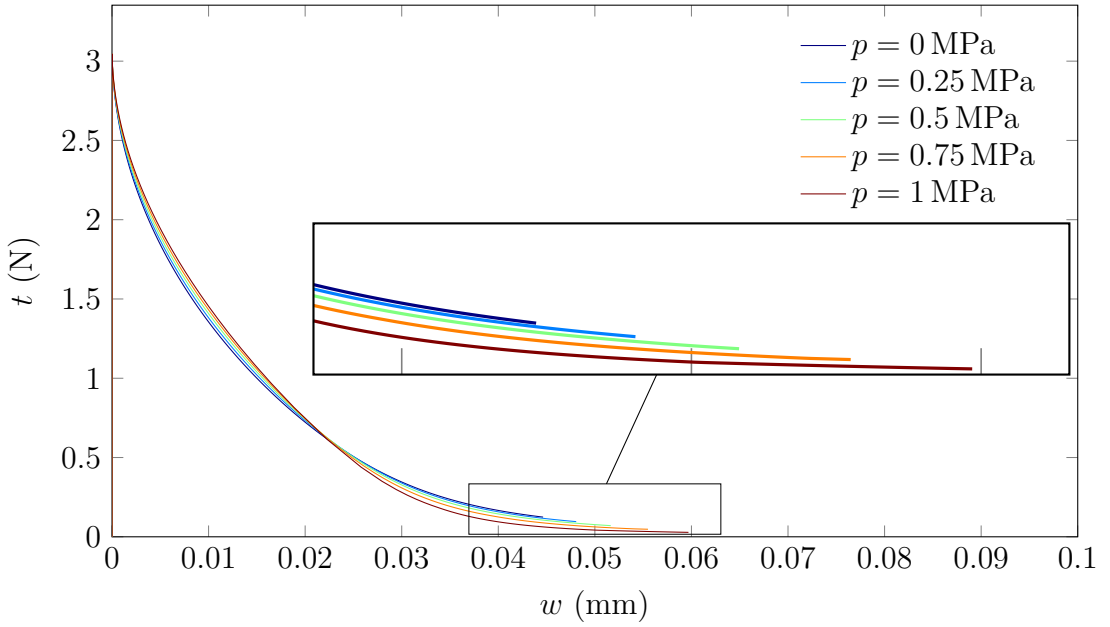


FIGURE 3.1. A bar under uniaxial tension.

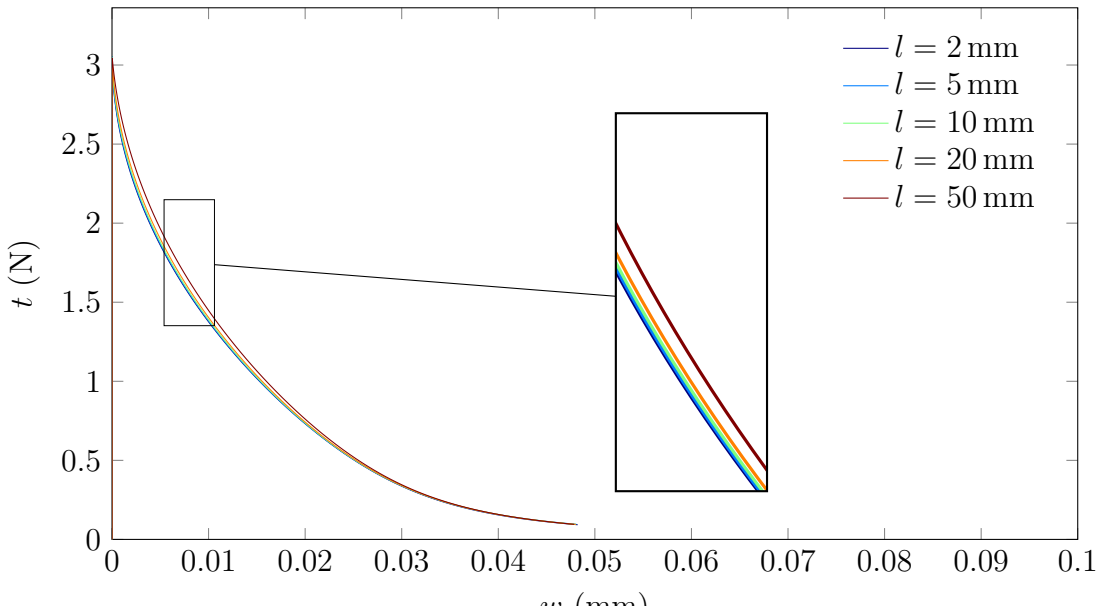
An arbitrarily small imperfection, $d_0 = \mathcal{O}(\epsilon)$, is introduced on the left side of the computational domain to induce localization. To study the effect of the pressure, different pressure values

$$\bar{p} \in \{0 \text{ MPa}, 0.25 \text{ MPa}, 0.5 \text{ MPa}, 0.75 \text{ MPa}, 1 \text{ MPa}\}$$

are considered. In the context of fuel fracture, the pressure on the crack surfaces can result from a pressurized gas environment.



(a)



(b)

FIGURE 3.2. The apparent traction-separation relations (a) for different values of pressure with a fixed regularization length $l = 5$ mm and (b) for different values of regularization length with a fixed pressure $p = 0.25$ MPa. The level of mesh refinement is chosen to be $l/h^e = 5$.

Figure 3.2a plots the apparent traction-separation law. The traction t and the separation w are approximated as $t = -R_x^{\text{left}}$ and $w = -\int_{\Omega_0} \mathbf{u} \cdot \nabla I \, dV$, respectively.

The apparent traction separation relations for different values of pressure are virtually indistinguishable.

Remark 4. In similar formulations of pressurized crack using phase-field (e.g. [46, 47, 51]), the fact that the pressure work (or the pressure power in the current variational framework) is independent of the velocities of the phase-field, i.e. $\dot{d}, \nabla \dot{d}$, is not respected. Leading to formulations of the following form:

$$\nabla \cdot \boldsymbol{\sigma} - \bar{p} \nabla d I_{,d} = \mathbf{0}, \quad (3.22a)$$

$$\nabla \cdot \boldsymbol{\xi} - f = 0, \quad (3.22b)$$

where

$$\boldsymbol{\xi} = \frac{2G_c l}{c_0} \nabla d, \quad f = g_{,d} \psi_{(A)}^e - \bar{p} \nabla \cdot \mathbf{u} + \frac{G_c}{c_0 l} \alpha_{,d}. \quad (3.23)$$

Note that an additional contribution from the pressure arises in f , which leads to pressure-dependent traction-separation relations and critical fracture strength.

At a given load (prescribed displacement), with a larger pressure, the separation between the crack surfaces is larger, resulting in a smaller traction. Figure 3.2b shows the convergence of the apparent traction-separation law as $l \rightarrow 0$.

The reaction force on the left symmetry plane (Figures 3.3a, 3.3d, 3.3g and 3.3j) shows that softening occurs at the same loading for different pressure values.

As is seen in Figures 3.3b, 3.3e, 3.3h and 3.3k, the reaction force on the right boundary is balanced by the prescribed pressure once the crack has fully developed. The approximated effective pressure \tilde{p} (3.13) (Figures 3.3c, 3.3f, 3.3i and 3.3l) also shows good agreement with the prescribed values \bar{p} .

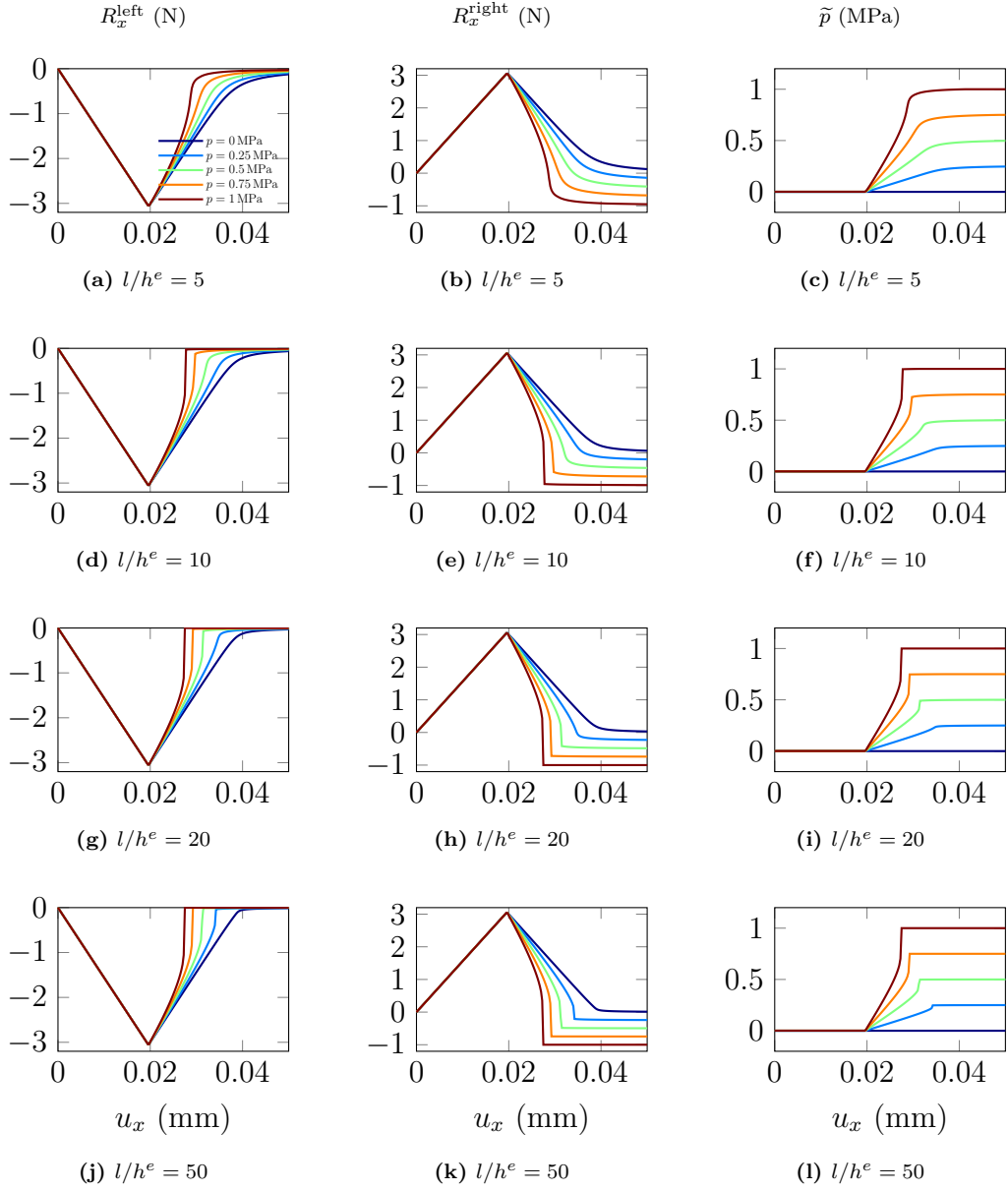


FIGURE 3.3. Response of the bar with a pressurized crack. The phase-field regularization length is fixed to be 5 mm. Different levels of mesh refinement are considered: (a-c) $l/h^e = 5$, (d-f) $l/h^e = 10$, (g-i) $l/h^e = 20$, (j-l) $l/h^e = 50$. The first column (a, d, g, j) shows the reaction force on the left symmetry plane; the second column (b, e, h, k) shows the reaction force on the right boundary where the displacement control is applied; the third column (c, f, i, l) shows the approximated pressure applied on the crack. For comparison purposes, all responses are plotted as a function of the prescribed displacement.

3.3.2 Pressurized crack propagation

Next, we verify fracture propagation conditions predicted by the quasi-brittle fracture model using a benchmark problem proposed by Wilson and Landis [51]. This problem serves to verify the propagation conditions once a critical pressure is attained. In Figure 3.4d, an initial crack is prescribed in the center with a length of $2a$. As shown in Figure 3.4a, the phase-field is initialized to be 1 only for those nodes on the bottom boundary belonging to the crack set. The phase-field variable is then regularized to satisfy the governing equations, as shown in Figure 3.4b. Note that this differs from the approach suggested in [51, 52] which involves imposing initial values for a set of elements. Utilizing the symmetry, only half of the domain with size $L \times L/2$ is used (Figure 3.4c). The ratio L/a is taken to be 20. All outer surfaces are fixed. The prescribed pressure is increased until the crack starts to propagate. The propagation of the crack right after the critical pressure is attained is unstable. According to the linear elastic fracture mechanics (LEFM) solution, the normalized critical pressure is given as:

$$\frac{p_c}{\sigma_0} = \sqrt{\frac{l}{\pi a}}, \quad \sigma_0 = \sqrt{\frac{E}{(1 - \nu^2)} \frac{\mathcal{G}_c^{\text{eff}}}{l}}, \quad (3.24)$$

where $\mathcal{G}_c^{\text{eff}}$ is the effective fracture toughness (considering the phase-field regularization) [53, 52] and is given as:

$$\mathcal{G}_c^{\text{eff}} = \mathcal{G}_c \left(\frac{h}{4c_0 l} + 1 \right). \quad (3.25)$$

Note that the LEFM solution is based on a brittle fracture model. A comparison between the numerical results and the LEFM solution for the critical pressure values is shown in Figure 3.5. The phase-field solution converges as ψ_c increases, and shows good agreement with the LEFM solution.

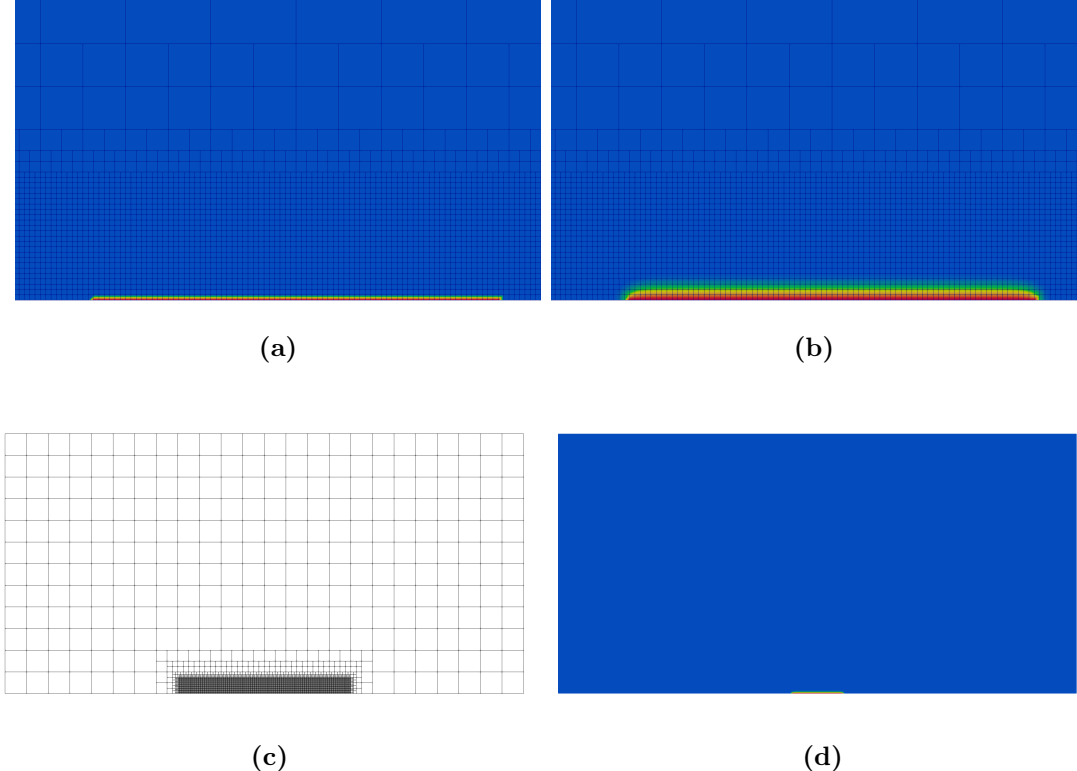


FIGURE 3.4. Pressurized crack propagation problem: (a) Initial values are imposed on crack surface nodes (zoomed view). (b) Regularized phase-field variable after one time step (zoomed view). (c) Mesh with five levels of local refinement. (d) Pre-existing crack. The red and blue color correspond to value of 1 and 0, respectively.

3.4 Numerical examples

3.4.1 Predicting the critical fracture strength

This phase-field for brittle fracture model is readily applicable to three dimensional intergranular fracture. In this section, as an example, we simulate UO₂ intergranular fracture and compare with experimental results. Material properties and model parameters are summarized in Table 3.1. We show how the presence of gas bubbles can alter the critical fracture strength of the specimen. The fracture toughness $\mathcal{G}_c^b = 2 \times 10^{-3} \text{ mJ mm}^{-2}$ is calibrated based on molecular dynamics simulations [44], and is assumed to be homogeneous over the grain boundaries.

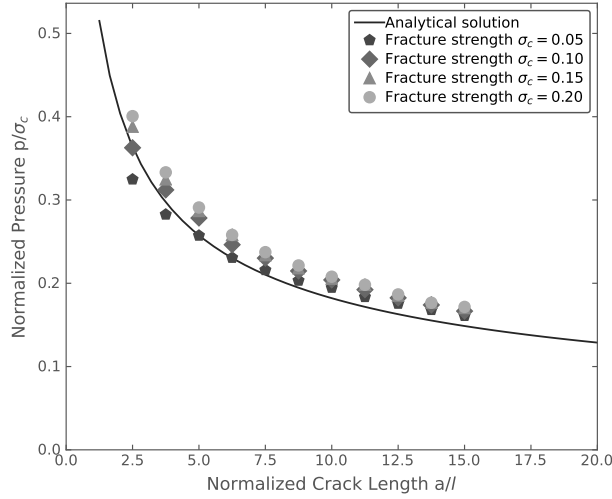


FIGURE 3.5. Comparison between the numerical results and the LEFM solution for the critical pressure values.

Table 3.1. Parameters and material properties used in the intergranular fracture simulations

Property	Symbol	Value	Unit	Reference
Young's modulus	E	385	GPa	[54]
Grain boundary fracture toughness	\mathcal{G}_c^b	0.002	mJ mm^{-2}	[44]
Grain fracture toughness	\mathcal{G}_c^g	0.01	mJ mm^{-2}	
Phase-field regularization length	l	0.5	μm	

Without further calibration, to facilitate intergranular crack propagation, the fracture toughness of grains need to satisfy $\mathcal{G}_c^g \gg \mathcal{G}_c^b$ so that crack propagation is predominately driven by intergranular strain energy. The polycrystalline microstructure is described by a set of non-conserved variables in a diffuse manner, obtained from a phase-field grain growth model [55]. The phase field $\phi_i = 1$ within the i -th grain, and $\phi_i = 0$ elsewhere. Regions where ϕ_i varies between 0 and 1 correspond to grain boundaries. The grain boundary indicator is computed as $B = \sum \phi_i^2$. The

fracture toughness \mathcal{G}_c is then defined as

$$\mathcal{G}_c(\mathbf{X}) = \begin{cases} \mathcal{G}_c^b, & B(\mathbf{X}) < \bar{B}, \\ \mathcal{G}_c^g, & B(\mathbf{X}) \geq \bar{B}, \end{cases} \quad (3.26)$$

where \bar{B} is the threshold to distinguish between grains and grain boundaries. For simulations considered in this chapter, $\bar{B} = 0.75$ has been observed to be an appropriate choice. The elastic properties for the grain is assumed to be isotropic, e.g. independent of the crystal orientations. The bubbles are modeled as elastic solid with an arbitrarily small stiffness. The domain is uniformly discretized with `HEX8` elements with element size of 0.25 μm .

3.4.1.1 Effect of gas bubble geometry

Gas bubbles on the grain boundaries act as crack initiators, and an accurate representation of their geometry is necessary to capture the stress concentration at the interface between the bubbles and the grain boundaries.

At equilibrium, gas bubbles on the grain boundaries have a lenticular shape. A 2D schematic of the lenticular bubble is shown in Figure 3.6a. The lenticular geometry is characterized by its length L , thickness S and dihedral angle ϕ . The dihedral angle is determined by the ratio of grain boundary energy to surface energy and it can vary over a wide range for UO_2 [56, 57].

To study the effect of gas bubble geometry on the critical fracture strength, three frequently adopted geometries are considered:

- (i) A lenticular gas bubble with length $L = 22.4 \mu\text{m}$, thickness $S = 16 \mu\text{m}$ and dihedral angle $\phi = 142.6^\circ$.
- (ii) A lenticular gas bubble with length $L = 22.4 \mu\text{m}$, thickness $S = 10 \mu\text{m}$ and dihedral angle $\phi = 96.6^\circ$.

- (iii) A spherical gas bubble with radius $7.9\text{ }\mu\text{m}$ which has the same volume as the lenticular gas bubble.

Consider a representative elementary volume (REV) with side length $120\text{ }\mu\text{m}$. The gas bubbles are placed over the grain boundaries such that the middle plane of the lenticular- or spherical- shaped bubbles are tangent to the grain boundaries. Symmetric boundary conditions are prescribed and a uniform displacement is applied on the top of the REV.

The variations in the critical fracture strength (Figure 3.6c) suggest that the shape of the gas bubbles affects the predicted fracture properties. A lenticular-shaped bubble has higher stress concentration at the edges of grain boundary bubbles, which lowers the critical fracture strength.

3.4.1.2 Effect of loading

Next, we study the effect of different loading conditions. Uniaxial, biaxial and triaxial loading conditions are considered. The final crack configurations are shown in Figure 3.7. A change in crack path due to a different loading condition is evident from the figure. For uniaxial loading, cracks propagate along the grain boundaries that are mainly perpendicular to the loading direction. For biaxial loading, crack branching occurs because biaxial loading results in two positive principal components of the strain tensor of the same order of magnitude. For triaxial loading, cracks propagate along all three directions.

The stress-strain curves are shown in Figure 3.8. The difference in the slopes during loading is due to the Poisson's effect. The sample under the biaxial and triaxial loading conditions manifests a lower critical fracture strength compared to that under uniaxial loading conditions. The critical strain corresponding to the critical fracture strength under triaxial loading is about half that under uniaxial loading.

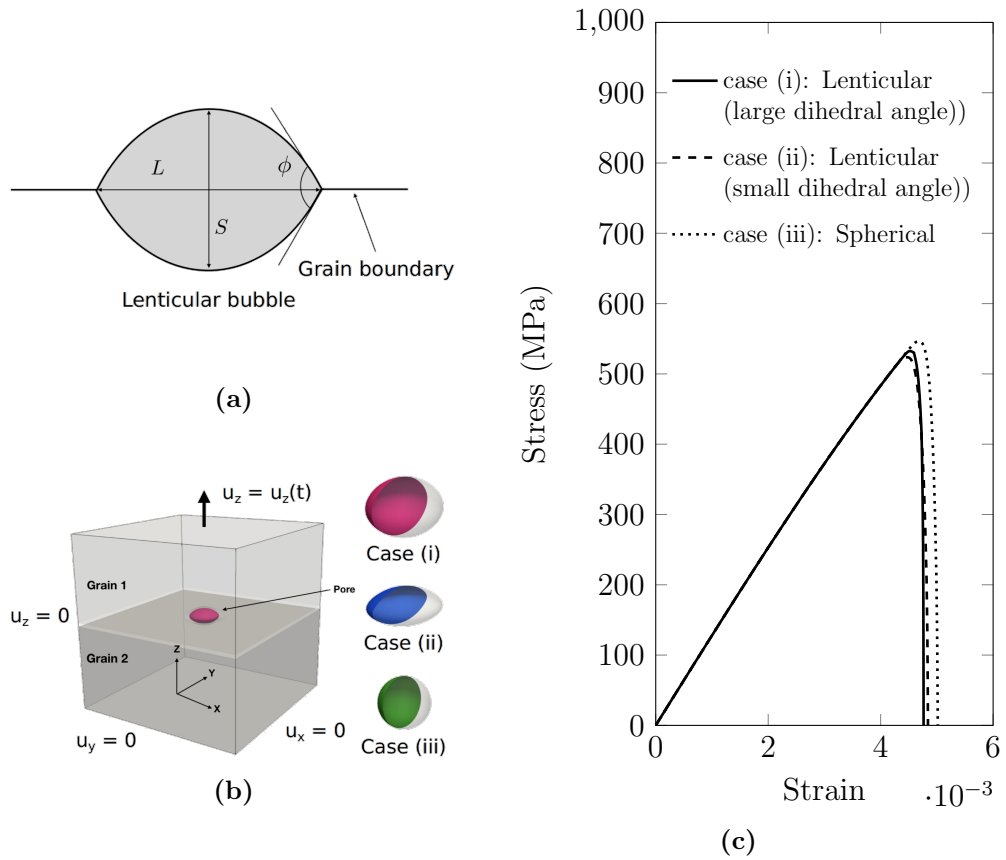


FIGURE 3.6. (a) The lenticular geometry is described by the length L , the thickness S and the dihedral angle ϕ . (b) Gas bubble geometry and boundary conditions. (c) Comparison of stress-strain curves for different gas bubble geometries.

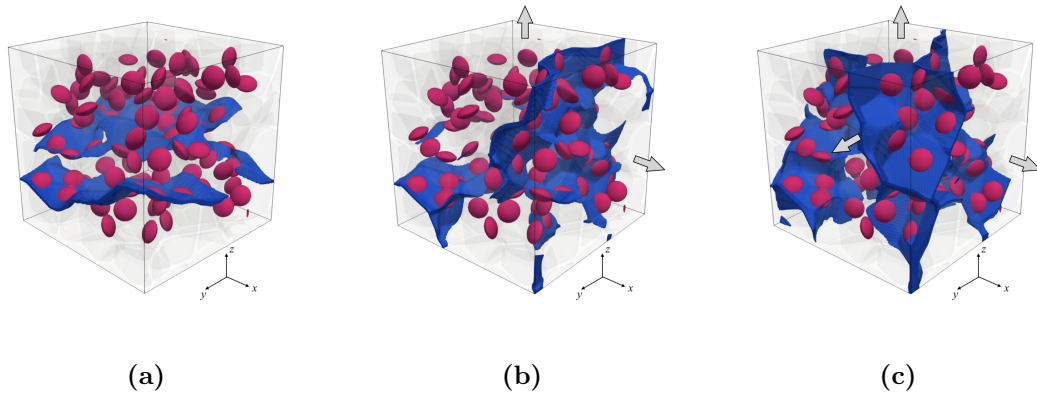


FIGURE 3.7. Final configuration (crack surfaces highlighted in blue) for different loading (a) uniaxial (b) biaxial (c) triaxial.

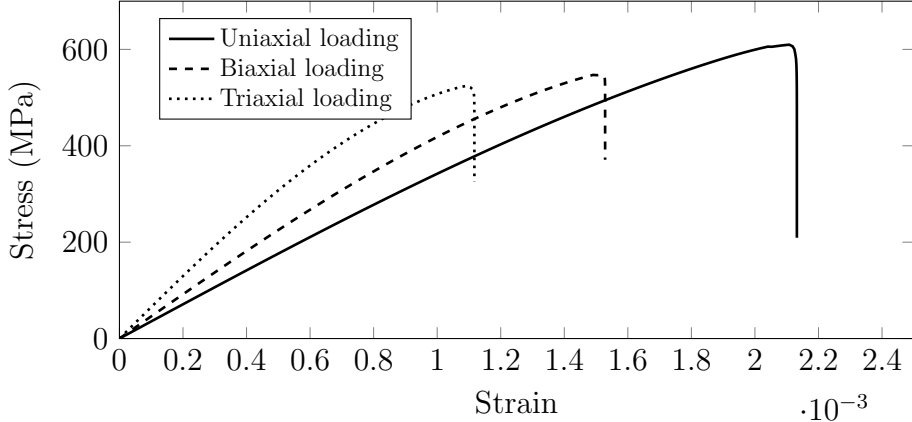


FIGURE 3.8. Comparison of stress-strain curves for different loading conditions.

3.4.1.3 Effect of porosity

In 2D, under plane-strain assumptions, the porosity represented by a planar bubble is computed by extruding it along the out-of-plane direction, which overestimates the actual porosity. In order to obtain a reasonable correlation between the critical fracture strength and the porosity, a 3D model is necessary.

To study the effect of porosity, consider an REV with side length of 40 μm . Grain centroids are generated from a random close-packing (RCP) voronoi structure. The RCP structures can be realized by a spatial sampling process known as Maximal Poisson-disk Sampling (MPS) [58]. For the RCP voronoi structure, the average aspect ratio of each voronoi cell is approximately 1 and an equiaxed grain structure is provided.

The influence of the voronoi structure on fracture properties can be isolated by considering a specific realization of RCP. The realization under consideration consists of 77 grains and the average radius of grains is 9.4 μm . As shown in Figure 3.9, 50, 100 and 150 gas bubbles are randomly distributed over the grain boundaries, with corresponding porosity values 2.02%, 4.04% and 6.06%, respectively. All gas bubbles have a lenticular shape with $L = 6.4 \mu\text{m}$, $S = 4 \mu\text{m}$, and $\phi = 128^\circ$. Symmetric boundary conditions are prescribed and a uniform displacement is applied on the

top of the REV.

Final configurations of the approximated crack surfaces are shown in Figure 3.9, where, in general, cracks propagate perpendicular to the direction of the applied load. It is worth noting that cracks keep propagating after initiation without any increase in the applied stress, which suggests that a snap-back is likely to take place after crack initiation and a mixed force-displacement control is necessary to follow the actual stress-strain curve without loss of information. However, we argue that the simple displacement control suffices to obtain the critical fracture strength – the maximum stress value along the stress-strain curve. From Figure 3.10, we conclude that an increase in porosity leads to a higher probability of crack initiation at a lower stress state and consequently a decrease in the critical fracture strength.

To describe the porosity, average gas bubble and grain size effect on fracture strength, an exponential functional form obtained from a biaxial flexure test has been reported in [59]:

$$\frac{\sigma_c}{\sigma_0} = \exp(-ar), \quad (3.27)$$

where r is the porosity. The critical fracture strength is normalized with respect to σ_0 . To benchmark with experiments, σ_0 is obtained by substituting the average grain and bubble size of 9.4 μm and 5.2 μm . To give proper error bounds on our numerical predictions, five trial calculations were performed on five different realizations of the spatial distribution of bubbles for each porosity level. The fracture strength values obtained from 15 realizations of 3 porosity levels are summarized in Table 3.2. The fitted σ_0 is 198 MPa, 693 MPa and 697.8 MPa and the coefficient a is 0.057, 0.14 and 0.04, for experiment, 2D simulations and 3D simulations, respectively. A comparison of the experimental model, previous 2D simulations [44] and current 3D simulations is shown in Figure 3.11. In particular, the 95% confidence interval for the 3D simulations is shown in stripes. It shows that the 3D simulation has

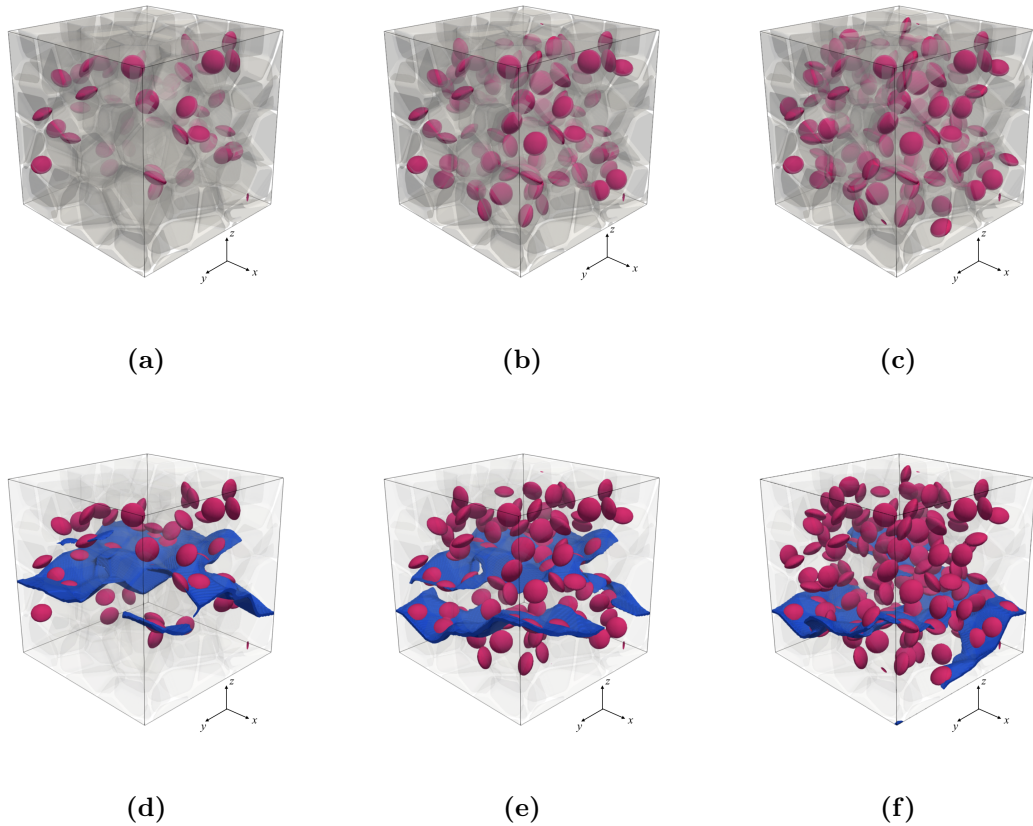


FIGURE 3.9. (a-c) Initial configuration of REVs with an average grain size of 9.4 μm . (d-f) Final configuration (crack surfaces highlighted in blue) for REVs. Different porosity values are considered: (a, d) 2.02%, (b, e) 4.04%, (c, f) 6.06%.

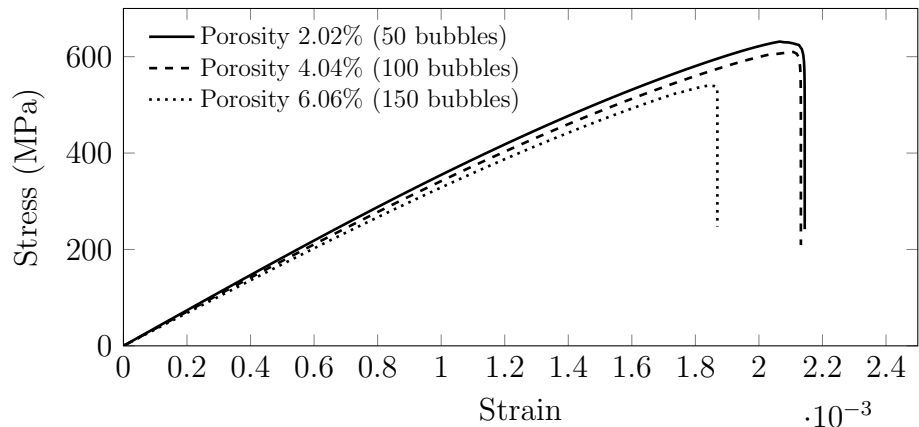


FIGURE 3.10. Comparison of stress-strain curves for different porosity values.

significant improvement towards the prediction of the dependence of the critical fracture strength on porosity. It is worth mentioning that the difference between simulation predictions of σ_0 and experimental values could be due to the fact that the transgranular fracture observed in experiments [60] has not been incorporated into the current numerical model.

Table 3.2. Summary of fracture strength obtained from 15 realizations of 3 porosity values. R denotes the realization index.

Porosity (%)	Critical fracture strength (MPa)				
	R1	R2	R3	R4	R5
2.02	631.4	657.4	645.6	663.4	630.7
4.04	609.8	555.6	605.5	611.2	589.2
6.06	540.0	530.8	557.0	563.2	567.9

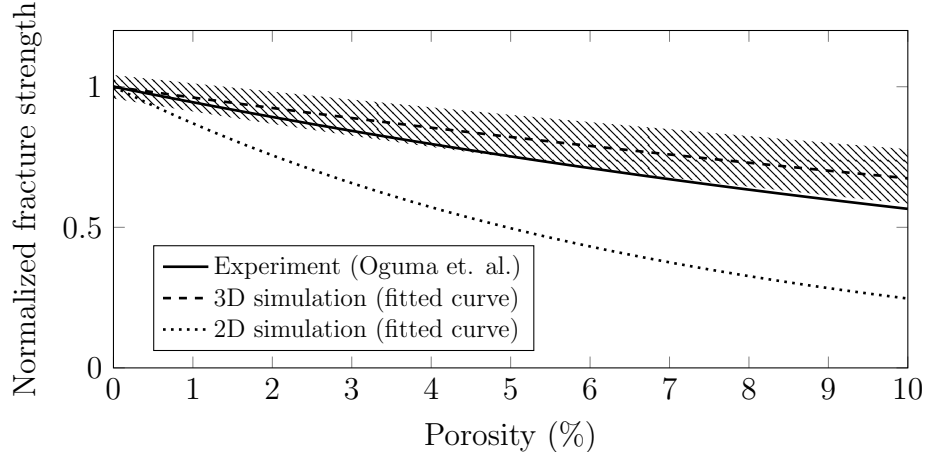


FIGURE 3.11. Variation in normalized fracture strength with changing porosity. Five trial calculations were performed for each porosity level, and each calculation was based on one realization of the spatial distribution of bubbles. The 95% confidence interval is shown in stripes.

3.4.2 High burnup structure fragmentation

Next, we adopt the quasi-brittle fracture model to simulate fission-gas-induced intergranular fracture of UO₂ HBS. A two-dimensional REV with side length $L = 3\text{ }\mu\text{m}$ is

considered, and plane-strain conditions are assumed to hold. The material properties and model parameters are summarized in Table 3.3. The critical fracture energy of UO_2 is taken to be 0.022 mJ mm^{-3} [59]. Due to the lack of experimental data, the fracture toughness \mathcal{G}_c^g is assumed to be $1.2 \times 10^{-6} \text{ mJ mm}^{-3}$ and the characteristic length $l_{\text{ch}} = \frac{\mathcal{G}_c}{2\psi_c} \approx 22.78 \text{ nm}$. The domain is uniformly discretized with QUAD4 elements with element size of $0.005 \mu\text{m}$.

Table 3.3. Parameters and material properties used in the fission-gas-induced HBS fracture simulations.

Property	Symbol	Value	Unit	Reference
Young's modulus	E	385	GPa	[54]
Critical fracture energy	ψ_c	0.022	mJ mm^{-3}	[59]
Grain boundary fracture toughness	\mathcal{G}_c^g	1.2×10^{-6}	mJ mm^{-3}	
Grain fracture toughness	\mathcal{G}_c^b	1.2×10^{-5}	mJ mm^{-3}	
Phase-field regularization length	l	0.01	μm	

3.4.2.1 LOCA pressure transients

We begin by investigating gas-pressure-induced fracture during LOCA-driven temperature transients. During a LOCA transient, temperatures in the fuel rod increase rapidly, leading to increased pressure in the gas contained within the bubbles. The temperature as a function of time at the edge of a representative pellet for each rod is obtained from simulation of the Studsvik Rod 196 experiment [61] using the engineering-scale fuel performance code BISON [62]. The temperature transient is used as an input to the Kim-Kim-Suzuki (KKS) phase-field model [63] to determine the pressure as a function of time. In the KKS model, the gas pressure is assumed to be 100 MPa during steady-state reactor operation at 700 K. The Studsvik experiment is initialized with a fixed temperature $T = 572.6 \text{ K}$ at the outer surface prior to the transient, resulting in a decrease in the pressure from 100 MPa to below 80 MPa. The pressure is assumed to be known in the quasi-brittle fracture model to simu-

late crack nucleation and propagation in the surrounding regions of the individual bubbles.

Two bubble radii ($0.25\text{ }\mu\text{m}$ and $0.5\text{ }\mu\text{m}$) are considered, and no loading is applied on the exterior. The resulting fracture patterns are shown in Figure 3.12. With the smaller bubble, two cracks propagate from the bubble towards the outer surface. With a larger bubble, only one major crack propagates to the free surface, and other minor cracks are arrested. Cracks nucleate when the tensile stress on the bubble-matrix interface reaches the critical fracture strength. The critical pressures are 120.17 MPa and 89.69 MPa for the small and large bubbles, respectively. The critical pressure is significantly lower for the larger bubble.

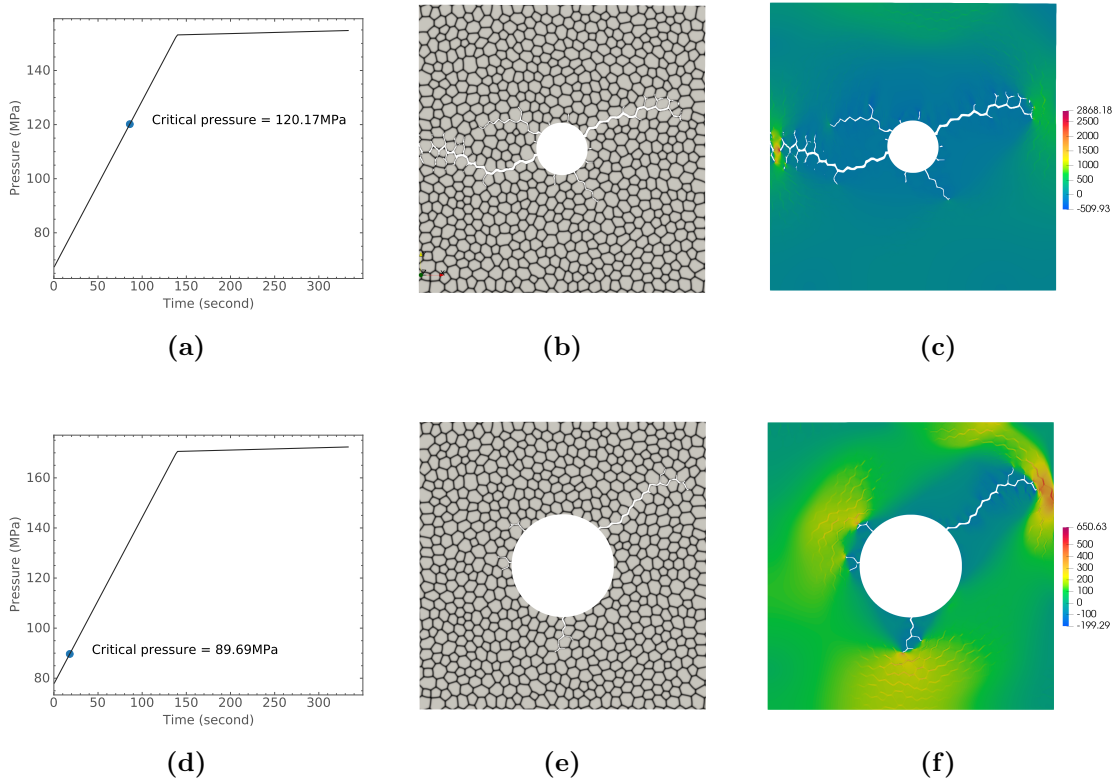


FIGURE 3.12. Results for (a-c) the small bubble with radius $0.25\text{ }\mu\text{m}$ and (d-f) the large bubble with radius $0.25\text{ }\mu\text{m}$ (a, d) Pressure history. (b, e) Crack paths superimposed on the voronoi structure. (c, f) Contour plot of the maximum principal stress.

In a fuel pellet system, external pressure can arise from fuel-cladding mechanical interaction. To study the effect of external pressure, different external pressures are applied on the top and right boundaries. The results obtained from using three different external pressures, 0, 30 MPa, and 60 MPa, are shown in Figure 3.13. The critical pressure is significantly higher for larger external pressure values, while there is no qualitative change in the crack pattern.

3.4.2.2 Multi-bubble interaction

We next investigate the effect of the spatial distribution of the gas bubbles on fragment size. To that end, dimensions are expressed in dimensionless form in this section. With the origin of the coordinate system placed at the lower left corner of the REV, two cases are considered:

- Two bubbles with centers at $\left(\frac{2}{15}L, \frac{7}{15}L\right)$ and $\left(\frac{7}{15}L, \frac{2}{15}L\right)$.
- Three bubbles with centers at $\left(\frac{1}{6}L, \frac{8}{15}L\right)$, $\left(\frac{8}{15}L, \frac{1}{6}L\right)$, and $\left(\frac{8}{15}L, \frac{8}{15}L\right)$.

All bubbles have a radius of $\frac{1}{12}L$. Results are shown in Figure 3.14. It is observed that the crack paths in cases involving multiple bubbles is strongly affected by the positions of the bubbles relative to each other: Cracks prefer to connect neighboring bubbles. Fully developed cracks and bubbles form a fragment at the lower-left corner in both cases. These fragments consist of multiple grains, and their sizes are affected by the spatial distribution of bubbles.

3.4.2.3 Partial HBS

Lastly, we incorporate defect evolution and recrystallization into the quasi-brittle fracture model. A phase-field model is used to simulate the defect evolution and the recrystallization behavior leading to HBS formation. A detailed description of

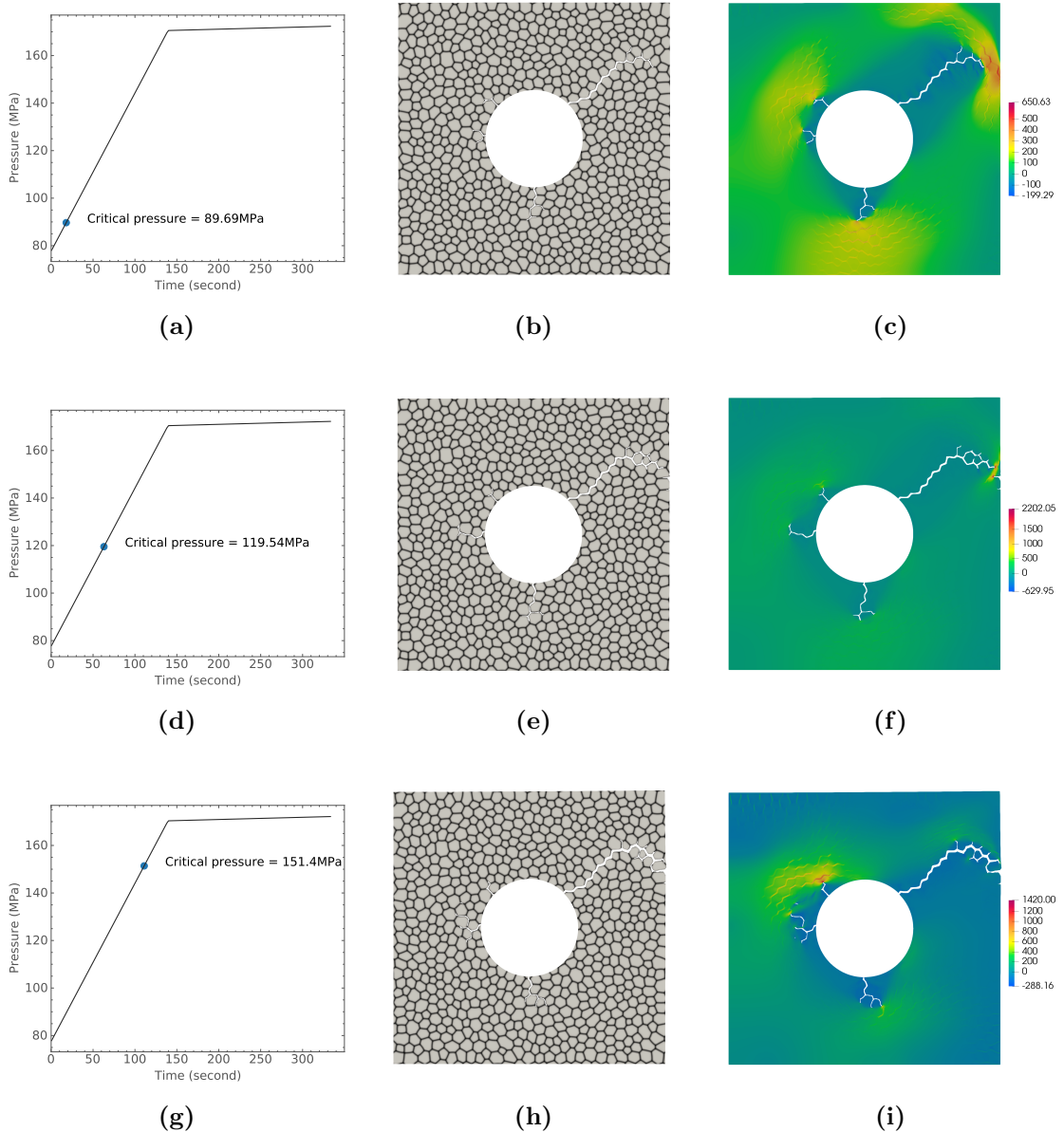


FIGURE 3.13. Results for bubble radius $0.5 \mu\text{m}$ and external pressure (a-c) 0 MPa, (d-f) 30 MPa, (g-i) 60 MPa. (a, d, g) Pressure history. (b, e, h) Crack paths superimposed on the voronoi structure. (c, f, i) Contour plot of the maximum principal stress.

the phase-field model is available in [63]. The quasi-brittle fracture model is applied directly on the microstructure resulting from simulations of the HBS formation process. Considering the fact that fragmentation can be observed in partially re-

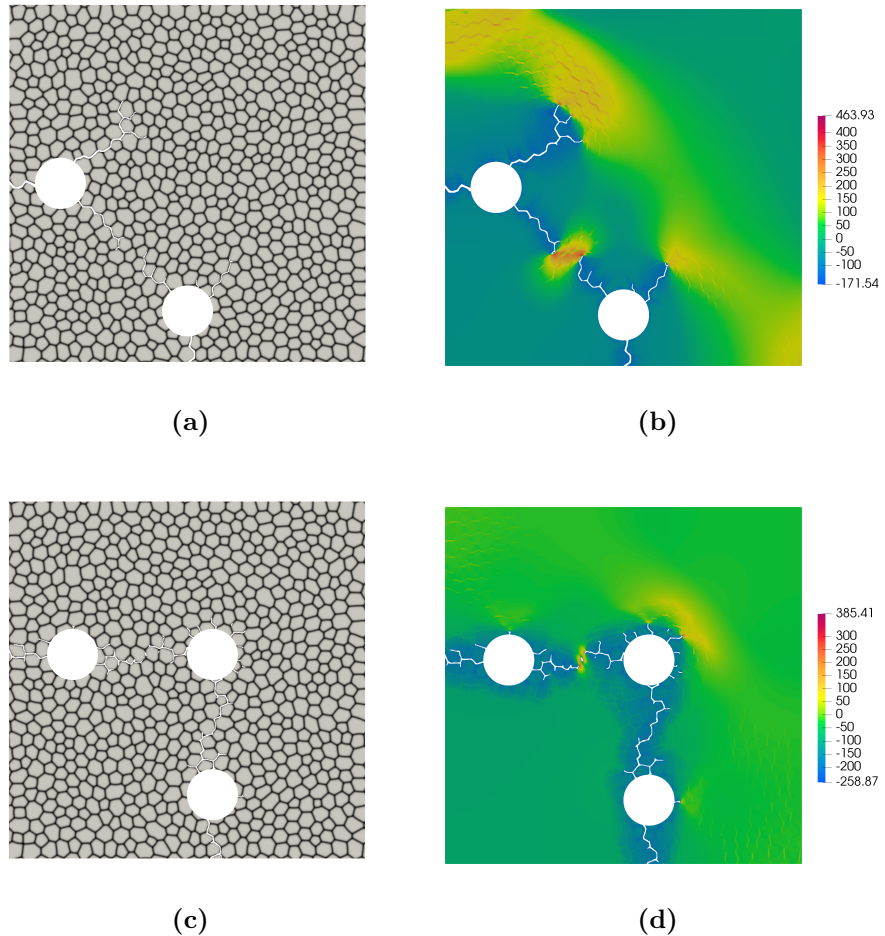


FIGURE 3.14. Results for (a-b) the two-bubble case and (c-d) the three-bubble case. (a, c) Crack paths superimposed on the voronoi structure. (b, d) Contour plot of the maximum principal stress.

crystallized zones, we focus on the fracture behavior of partial HBS. Three HBS at different recrystallization stages with 25%, 60%, and 100% recrystallization fraction are considered. A linearly increasing gas pressure is applied. Results are shown in Figure 3.15. In all three cases, cracks nucleate at around 60 MPa, owing to their similar defect sizes. Crack nucleation locations vary among the three cases, as more grains form around the defect during recrystallization and their intersections with the defect become possible nucleation sites. Furthermore, recrystallization changes the grain morphology, leading to different crack paths.

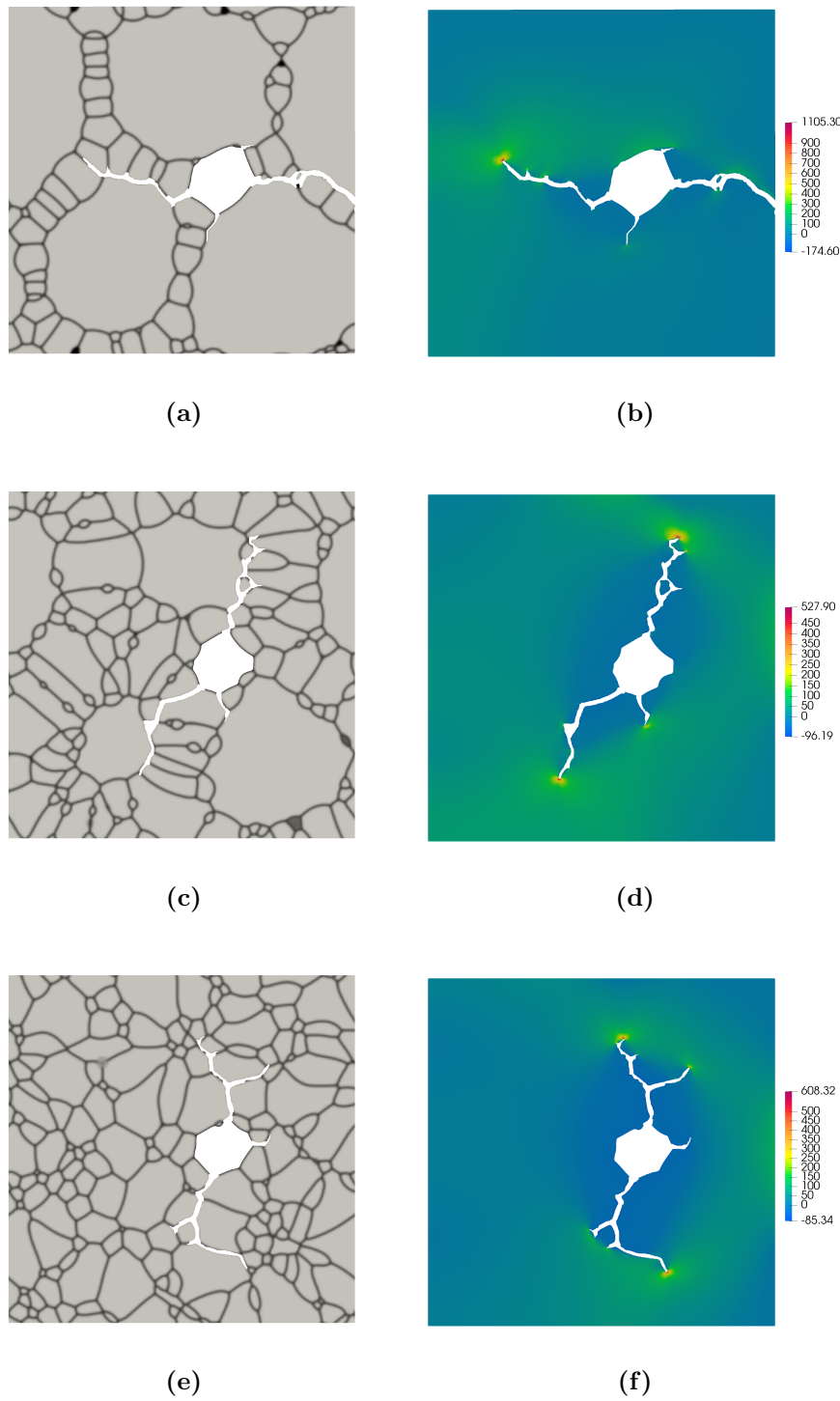


FIGURE 3.15. (a, c, e) Crack paths superimposed on the microstructure and (b, d, f) contour plots of the maximum principal stress assuming different recrystallization stages: (a-b) 25% recrystallization, (c-d) 60% recrystallization, (e-f) 100% recrystallization.

4

Cohesive Fracture: Soil desiccation

4.1 Introduction

In this chapter, a phase-field for cohesive fracture model is used to simulate pervasive cracking in thin films. A new strain energy split is proposed to enforce frictionless contact conditions in the vicinity of diffuse fracture surfaces. In contrast to existing splits that have been proposed, our approach completely prevents tractions from being transmitted across fully damaged surfaces that are loaded in tension. Spatial variations of material properties are incorporated into our model, and we demonstrate, through forward analysis and by solving an inverse problem, how crack network morphology can be influenced by stochastic spatially-varying material properties.

To prevent crack growth under compression, phase-field models of fracture typically employ some form of tension-compression asymmetric split in the strain energy. Two popular approaches are the spectral decomposition [48, 49] and the volumetric-deviatoric decomposition [64]. Both the spectral decomposition and the volumetric-deviatoric decomposition are variational and can be fit within the current variational

framework. Although these variational approaches represent crack growth reasonably well for a broad range of problems, they do not completely preclude the transmission of tractions across fully damaged surfaces. In part, this is by design. The decompositions are designed to allow compressive tractions to be transmitted across fully damaged surfaces. But since they are developed from the full stress or strain as opposed to the surface tractions, they can also allow unwanted tensile or shear tractions to be transmitted. This can give rise to spurious macro-scale responses in some situations. Strobl and Seelig [65] proposed constitutive relations that satisfy the boundary conditions on diffuse crack surfaces by taking into account the crack orientation. Although the use of such a constitutive model violated the fundamental variational structure of phase-field models, it was shown to yield better results in some fracture problems [66]. A similar approach was presented by Fei and Choo [67, 68] to extend the model to better account for frictional contact conditions at crack surfaces. Finally, we mention the recent work of Lo et al. [69], in which the standard spectral split was modified to better guard against crack growth in compression.

In this chapter, we propose a variational strain energy split that enforces frictionless contact conditions. Importantly, the split effectively prevents the transmission of tractions across fully-damaged surfaces that are loaded in tension. The proposed split leads to a decomposition that is shown to be important in mode II and mixed-mode fracture problems. The new phase-field model is then applied to study the classical problem of the fracture of thin films bonded to thick substrates. Due to the accumulation of inelastic strain and the stiffness mismatch between the film and the substrate, cracks form either transversely through the thickness of the film, referred to as “channeling”, or at the interface, referred to as “debonding”. Film-substrate systems exist across a wide span of application problems, from technological systems such as nuclear fuel pellet–cladding interactions (PCI) [70, 71, 72, 73, 74] to more

common civil infrastructure examples such as pavement asphalts [75, 76, 77, 78, 79]. The study of fracture in these systems is driven by an interest in both understanding the underlying mechanisms and in preventing crack nucleation and evolution. In the current work, we confine attention to transverse channeling cracks in the film. When a system of cracks nucleate, branch and coalesce, complicated crack networks appear in the thin films. Hutchinson and Suo [80] provides a comprehensive review of crack patterns in film-substrate systems.

The fracture of thin films bonded to substrates has been studied using model-based simulations based on a wide range of methodologies. These problems are challenging to simulate because they involve pervasive crack nucleation, branching, and coalescence. Phenomenological spring models were developed and employed by Crosby and Bradley [81], Leung and Néda [82] and Sadhukhan et al. [83]. Zhang et al. [84] applied a cohesive zone method to study the film-substrate interface debonding, and Sánchez et al. [85] proposed a mesh fragmentation technique to simulate three-dimensional crack morphologies. Although such techniques are known to produce mesh-dependent results, the resulting crack networks were found to be satisfactory. Liang et al. [86], Sukumar and Prévost [87] and Huang et al. [88] modeled thin film cracking using the eXtended Finite Element Method (XFEM) which allowed for the cracks to evolve independently of the finite-element mesh.

The aforementioned analytical and numerical efforts have provided a great deal of insight into the factors controlling the fracture of thin films. In particular, the mechanical properties that govern the spacing between cracks have been studied by Hutchinson and Suo [80], Xia and Hutchinson [89] and most recently by Yin et al. [90]. In contrast, the connection between spatial variations in material properties and the morphology of the resulting crack patterns has received fairly little attention. This is despite experimental evidence that crack morphologies are sensitive to spatial variations in material properties, see, e.g. Kitsunezaki et al. [91, 92], Halász

et al. [93], Kitsunezaki et al. [94] and Nakahara et al. [95]. To our knowledge, while some previous model-based simulations of thin-film fracture have incorporated random material properties, they have not specifically considered spatial fluctuations and the construction of proper stochastic models. More broadly, the literature on probabilistic modeling for fracture simulations remains scarce. In [96], variability in fracture strength was estimated from multiscale simulations, and spatially-varying mesoscale properties were subsequently integrated into an asynchronous spacetime discontinuous Galerkin finite element based fracture model to study the impact on fragmentation. The integration of apparent elasticity coefficients in a multiscale-informed phase-field formulation was investigated in [97], with the aim of reproducing variability in the macroscopic response. The fracture toughness was modeled as deterministic and homogeneous, and was identified by solving an inverse problem. In [98], a continuum mapping of the meso-scale structure to the packing fraction at the macro-scale was employed to introduce a random component to phase-field simulations of surfactant-induced fracture of particle rafts. In this chapter, we construct a probabilistic model for the critical fracture energy and the fracture toughness, modeled as (potentially correlated) random fields, and examine their influence on the random morphology of the resulting fracture patterns.

Our model-based simulations of thin-film fracture for systems with spatially-variable material properties are facilitated in this work through the adoption of an extension of phase-field models to cohesive fracture [99, 15, 100]. Phase-field for cohesive fracture models incorporate the original proposition by Xia and Hutchinson [89] regarding a “critical fracture energy”. The regularization length is decoupled from the material properties in these approaches, and the critical strength and the fracture toughness of the material are no longer strongly correlated. This independence permits simulations of drying in systems with realistic material properties for typical clays or soils, for example, without compromising the magnitude of the

critical strength or requiring regularization lengths that are larger than the specimen dimensions. It also allows systems with spatially-variable fracture properties to be studied using a spatially-constant regularization length, greatly improving the fidelity of the numerical calculations.

This chapter is organized as follows. Section 4.2 the constitutive choices and stochastic models for fracture properties. In Section 4.3, several numerical examples of benchmark problems in quasi-static fracture mechanics are provided to illustrate the efficacy of the new approach to enforcing frictionless contact conditions. The main results of this work are provided in Section 4.4, where the new model is used to study the formation of crack networks in thin films and in soil desiccation problems. In particular, model-based simulations are used to examine how the fragment statistics and fracture morphologies are influenced by spatial variations in the fracture properties. Comparisons with both theory and experimental observations are provided.

4.2 Theory

4.2.1 Constitutive choices

In this chapter, the material is assumed to be isotropic while not necessarily homogeneous. Quasi-static and isothermal conditions are assumed to hold. No viscous regularization is incorporated, i.e. the dual kinetic potentials are zero. Following the variational framework (Chapter 2), the Helmholtz free energy density is decomposed as

$$\psi = \psi^e + \psi^f + \psi^i, \quad (4.1)$$

where ψ^e is the strain energy density and ψ^f is the fracture energy density. In the two dimensional simplification of the film-substrate system, ψ^i represents the interfacial energy density that arises from the stiffness mismatch between the film

and the substrate at the interface.

The same definition of the strain energy density as in (3.3a) and consequently the same stress-strain relation (3.4a) are used. The following crack geometric function and degradation function are used to model cohesive fracture:

$$\alpha = d, \quad g = \frac{(1-d)^2}{(1-d)^2 + md(1+pd)}, \quad m = \frac{3\mathcal{G}_c}{8l\psi_c}. \quad (4.2)$$

This degradation function is hereinafter referred to as the Lorentz (or in general the Lorentz-type) degradation function¹.

Remark 5. With a view towards the following stochastic analysis of fracture properties, the use of a Lorentz-type degradation function is necessary. According to one-dimensional analyses in [100, 15], the use of Lorentz-type degradation functions decouples the phase-field regularization length from the critical fracture energy, in the sense that the critical fracture energy ψ_c may now be treated as a separate material property and later on as a *marginally independent* random field, and the phase-field regularization length can truly be a numerical regularization parameter which the Γ -convergence properties of the model depend upon.

The interfacial energy density describes the stiffness mismatch between the film and the substrate at the interface. The interfacial energy density and its thermodynamic conjugates are defined as

$$\psi^i = \frac{1}{2}g \frac{G}{hH} \boldsymbol{\Phi} \cdot \boldsymbol{\Phi}, \quad (4.3a)$$

$$\psi_{,\boldsymbol{\Phi}}^i = g \frac{G}{hH} \boldsymbol{\Phi}, \quad (4.3b)$$

$$\psi_{,d}^i = \frac{1}{2}g_{,d} \frac{G}{hH} \boldsymbol{\Phi} \cdot \boldsymbol{\Phi}. \quad (4.3c)$$

¹ Later on, the Lorentz-type degradation function may be denoted as g^{Lorentz} to distinguish from the quadratic degradation function $g^{\text{Quadratic}} = (1-d)^2$.

The governing equations can be summarized as

$$\nabla \cdot \boldsymbol{\sigma} - g \frac{G}{hH} \boldsymbol{\Phi} = \mathbf{0}, \quad (4.4)$$

$$\nabla \cdot \boldsymbol{\xi} - f = 0, \quad (4.5)$$

supplemented by the constitutive relations (3.4a) and

$$\boldsymbol{\xi} = \frac{3\mathcal{G}_c l}{4} \nabla d + \psi_{,\nabla d}^e, \quad f = \frac{3\mathcal{G}_c}{8l} \alpha_{,d} + \psi_{,d}^e + \frac{1}{2} g_{,d} \frac{G}{hH} \boldsymbol{\Phi} \cdot \boldsymbol{\Phi}. \quad (4.6)$$

Note that (4.4) resembles a shear-lag model. The additional term in $\boldsymbol{\xi}$ comes from the contact split to be introduced in Section 4.2.2.

4.2.2 Enforcing the traction-free boundary condition

Widely used strain energy splits are spectral split [48, 49] and volumetric-deviatoric split [20]. Unfortunately, neither the spectral split nor the volumetric-deviatoric split completely prevent tensile or shear tractions from being transmitted across fully-damaged surfaces. Accordingly, we now develop a split that is motivated by the consideration of frictionless contact conditions along fully damaged surfaces.

We begin by recalling the standard Kuhn-Tucker optimality conditions for frictionless contact under small deformation, which can be written as

$$t_N \geq 0, \quad u_I \leq 0, \quad t_N u_I = 0, \quad (4.7)$$

where t_N is the contact pressure and u_I denotes the interpenetration between the contact surfaces. The contact pressure is typically obtained from the stress and the exterior normal of the contact surface. In regularized models of fracture, however, it can be difficult to identify a unique surface based on the phase field. Accordingly, we rely on the gradient of the phase field to construct an approximate normal $\tilde{\mathbf{n}}$, viz.

$$\tilde{\mathbf{n}} = \frac{\nabla d}{\|\nabla d\|}, \quad (4.8)$$

and calculate the normal pressure as

$$t_N = -\tilde{\mathbf{n}} \cdot \boldsymbol{\sigma} \tilde{\mathbf{n}}. \quad (4.9)$$

Our split keys off the sign of the normal pressure, by isolating the cases of a positive pressure (for contact) from a negative pressure (for opening). In particular, we construct a “normal-tangential” stress decomposition of the form

$$\boldsymbol{\sigma} = \boldsymbol{\sigma}_n^+ + \boldsymbol{\sigma}_n^- + \boldsymbol{\sigma}_t, \quad (4.10)$$

where

$$\boldsymbol{\sigma}_n^\pm = \langle -t_N \rangle_\pm \tilde{\mathbf{n}} \otimes \tilde{\mathbf{n}}, \quad \boldsymbol{\sigma}_t = \boldsymbol{\sigma} - \boldsymbol{\sigma}_n^+ - \boldsymbol{\sigma}_n^-, \quad (4.11)$$

In the vicinity of the regularized crack surface, we then propose the use of a stress-based strain energy split, hereafter referred to as the *contact split*, that takes the form:

$$\psi^e = g\psi_{\langle A \rangle}^e + \psi_{\langle I \rangle}^e, \quad (4.12a)$$

$$\psi_{\langle A \rangle}^e = \frac{1}{2} \boldsymbol{\sigma}_{\langle A \rangle} : \boldsymbol{\varepsilon}, \quad \psi_{\langle I \rangle}^e = \frac{1}{2} \boldsymbol{\sigma}_{\langle I \rangle} : \boldsymbol{\varepsilon}, \quad (4.12b)$$

$$\boldsymbol{\sigma}_{\langle A \rangle} = \boldsymbol{\sigma}_n^+ + \boldsymbol{\sigma}_t, \quad \boldsymbol{\sigma}_{\langle I \rangle} = \boldsymbol{\sigma}_n^-. \quad (4.12c)$$

After a lengthy but straight-forward derivation, the corresponding constitutive relation follows as:

$$\boldsymbol{\sigma} = g(d)\boldsymbol{\sigma}_{\langle A \rangle} + \boldsymbol{\sigma}_{\langle I \rangle}, \quad (4.13)$$

and

$$\psi_{\langle A \rangle, \nabla d}^e = \frac{1}{\|\nabla d\|} [2 \langle -t_N \rangle_- \boldsymbol{\varepsilon}_N \tilde{\mathbf{n}} - H(t_N) \boldsymbol{\varepsilon}_N \boldsymbol{\sigma} \tilde{\mathbf{n}} - \langle -t_N \rangle_- \boldsymbol{\varepsilon} \tilde{\mathbf{n}}], \quad (4.14a)$$

$$\psi_{\langle I \rangle, \nabla d}^e = -\psi_{\langle A \rangle, \nabla d}^e, \quad (4.14b)$$

with $\boldsymbol{\varepsilon}_N = \tilde{\mathbf{n}} \cdot \boldsymbol{\varepsilon} \tilde{\mathbf{n}}$.

It bears emphasis that the proposed strain energy split only serves to enforce the crack surface traction free boundary condition, and it is not reasonable to expect it to reliably govern crack nucleation and growth. In this chapter, to ensure that the contact split is applied only in the vicinity of the crack surface, we impose a simple threshold d_c such that we apply

$$\begin{cases} \text{the contact split (4.12a) to (4.13), } d \geq d_c \\ \text{the strain-based spectral split [48, 49], } d < d_c. \end{cases}$$

Alternative. In principle a total energy could be constructed using a blending function that transitions between a standard split and the contact split.

It can be shown that the definition of the contact pressure (4.9) follows by relaxing the frictionless constraint into a minimization problem, and t_N is therefore the best scalar quantity one can choose to approximate the traction-free boundary condition:

$$\min_{t_N} \|\boldsymbol{\sigma}_t(t_N)\tilde{\mathbf{n}}\|^2 \quad (4.15a)$$

$$= \|(\boldsymbol{\sigma} - \langle -t_N \rangle_+ \tilde{\mathbf{n}} \otimes \tilde{\mathbf{n}} - \langle -t_N \rangle_- \tilde{\mathbf{n}} \otimes \tilde{\mathbf{n}}) \cdot \tilde{\mathbf{n}}\|^2 \quad (4.15b)$$

$$= \|(\boldsymbol{\sigma} + t_N \tilde{\mathbf{n}} \otimes \tilde{\mathbf{n}}) \cdot \tilde{\mathbf{n}}\|^2 \quad (4.15c)$$

$$= t_N^2 + 2t_N \tilde{\mathbf{n}} \cdot \boldsymbol{\sigma} \tilde{\mathbf{n}} + \|\boldsymbol{\sigma} \tilde{\mathbf{n}}\|^2, \quad (4.15d)$$

and the minimizer is

$$t_N = \arg \min_{t_N} (t_N^2 + 2t_N \tilde{\mathbf{n}} \cdot \boldsymbol{\sigma} \tilde{\mathbf{n}} + \|\boldsymbol{\sigma} \tilde{\mathbf{n}}\|^2) = -\tilde{\mathbf{n}} \cdot \boldsymbol{\sigma} \tilde{\mathbf{n}}. \quad (4.16)$$

4.2.3 Stochastic models for fracture properties

In this chapter, we allow for material property inhomogeneity in the macroscopic continuum model. Specifically, we introduce the random field

$$\{\boldsymbol{P}(\mathbf{X}) = (P_1(\mathbf{X}), P_2(\mathbf{X})), \mathbf{X} \in \Omega\} \quad (4.17)$$

defined on the probability space (Θ, Σ, P) , indexed by Ω and with values in $\mathbb{R}_{>0} \times \mathbb{R}_{>0}$, such that $\{P_1(\mathbf{X}), \mathbf{X} \in \Omega\}$ (respectively $\{P_2(\mathbf{X}), \mathbf{X} \in \Omega\}$) is a prior representation of $\{\mathcal{G}_c(\mathbf{X}), \mathbf{X} \in \Omega\}$ (respectively $\{\psi_c(\mathbf{X}), \mathbf{X} \in \Omega\}$). Due to the restrictions on the state space, the bivariate random field $\{\mathbf{P}(\mathbf{X}), \mathbf{X} \in \Omega\}$ is non-Gaussian. In order to model nongaussianity, the random field $\{\mathbf{P}(\mathbf{X}), \mathbf{X} \in \Omega\}$ is *defined* as

$$\mathbf{P}(\mathbf{X}) := \mathcal{T}(\boldsymbol{\Xi}(\mathbf{X}), \mathbf{X}) , \quad \forall \mathbf{X} \in \Omega , \quad (4.18)$$

where \mathcal{T} is a measurable, nonlinear mapping and $\{\boldsymbol{\Xi}(\mathbf{X}), \mathbf{X} \in \Omega\}$ is a centered Gaussian random field with values in \mathbb{R}^2 to be defined momentarily. From a methodological standpoint, it should be noticed that the transformation \mathcal{T} is constructed *a priori* and used to define $\{\mathbf{P}(\mathbf{X}), \mathbf{X} \in \Omega\}$ such that the latter constitutes a surrogate capturing some essential features of $\{(\mathcal{G}_c(\mathbf{X}), \psi_c(\mathbf{X})), \mathbf{X} \in \Omega\}$ (while exhibiting a low dimensional parameterization). In general, the existence of a nonlinear mapping \mathcal{T} such that (4.18) holds for a *given* non-Gaussian field is not guaranteed; see, e.g., [101].

4.2.3.1 Construction of the Non-Gaussian Model

In this work, the transformation \mathcal{T} is constructed by imposing the family $\{f_{\mathbf{X}}\}_{\mathbf{X} \in \Omega}$ of first-order marginal distributions:

$$P_{\mathbf{P}(\mathbf{X})}(d\mathbf{p}) = f_{\mathbf{X}}(\mathbf{p})d\mathbf{p} , \quad \forall \mathbf{X} \in \Omega , \quad (4.19)$$

where $f_{\mathbf{X}}$ is the probability density function of $\mathbf{P}(\mathbf{X})$, \mathbf{X} being fixed in Ω , and $d\mathbf{p} = dp_1 dp_2$ is the Lebesgue measure in \mathbb{R}^2 . It is assumed that $f_{\mathbf{X}}(\cdot) = f(\cdot; \mathbf{w}_{\mathbf{X}})$, where $\mathbf{w}_{\mathbf{X}}$ is a vector-valued hyperparameter indexed by $\mathbf{X} \in \Omega$. In order to simplify the analysis, we assume from now on that the aforementioned hyperparameter does not depend on location, and we write $f_{\mathbf{X}}(\cdot) = f(\cdot; \mathbf{w})$ using a slight abuse of notation.

The construction of f can be achieved in many different ways. In what follows, the construction is performed by assuming that (i) \mathcal{G}_c and ψ_c (together with their inverses) are positive and have finite variance, for physical consistency, and (ii) the two fracture properties can exhibit some level of correlation. In accordance with information theory [102, 103] and more precisely, with the principle of maximum entropy [104, 105], the first assumption leads to the consideration of Gamma marginal distributions. Following the notation introduced above, we shall impose that

$$P_{P_1(\mathbf{X})}(dp_1) = f_{\mathcal{G}}(p_1; (\underline{p}_1, \delta_1))dp_1 , \quad \forall \mathbf{X} \in \Omega , \quad (4.20)$$

and

$$P_{P_2(\mathbf{X})}(dp_2) = f_{\mathcal{G}}(p_2; (\underline{p}_2, \delta_2))dp_2 , \quad \forall \mathbf{X} \in \Omega , \quad (4.21)$$

where $f_{\mathcal{G}}(\cdot; (\underline{p}, \delta))$ denotes the univariate Gamma probability density function with mean \underline{p} and coefficient of variation δ . In this setting, the joint distribution of $\mathbf{P}(\mathbf{X})$ must be constructed from the knowledge of the marginal laws associated with $P_1(\mathbf{X})$ and $P_2(\mathbf{X})$. This ill-posed problem does not admit a unique solution, and many possible forms were proposed in the case of a bivariate Gamma distribution (see, e.g., Chapter 8 in [106] for a review). Here, we use the bivariate Gamma distribution derived by Moran using a copula [107]:

$$\begin{aligned} f(\mathbf{p}) &= \frac{1}{\sqrt{1-\rho^2}} \exp \left\{ -\frac{1}{2(1-\rho^2)} [(\rho \tilde{p}_1)^2 - 2\rho \tilde{p}_1 \tilde{p}_2 + (\rho \tilde{p}_2)^2] \right\} \\ &\quad \cdot f_{\mathcal{G}}(p_1; (\underline{p}_1, \delta_1)) f_{\mathcal{G}}(p_2; (\underline{p}_2, \delta_2)), \end{aligned} \quad (4.22)$$

where $\rho \in (-1, 1)$ is the (Pearson) correlation coefficient between $P_1(\mathbf{X})$ and $P_2(\mathbf{X})$ (\mathbf{X} being fixed), and

$$\tilde{p}_i = \Phi^{-1}(F_{\mathcal{G}}(p_i; (\underline{p}_i, \delta_i))) , \quad i \in \{1, 2\} , \quad (4.23)$$

where Φ^{-1} is the inverse of the univariate Gaussian distribution function and $F_{\mathcal{G}}(\cdot; (\underline{p}_i, \delta_i))$ is the univariate Gamma distribution function with mean \underline{p}_i and coefficient of variation δ_i (which is associated with $f_{\mathcal{G}}(\cdot; (\underline{p}_i, \delta_i))$), and that the extreme cases $\rho = \pm 1$ are also well defined; see [107]. Notice that the vector of hyperparameters then reads as $\mathbf{w} = (\underline{p}_1, \delta_1, \underline{p}_2, \delta_2, \rho)$. It follows that

$$P_1(\mathbf{X}) = F_{\mathcal{G}}^{-1}(\Phi(\Upsilon_1(\mathbf{X})); (\underline{p}_1, \delta_1)) \quad (4.24)$$

and

$$P_2(\mathbf{X}) = F_{\mathcal{G}}^{-1}(\Phi(\Upsilon_2(\mathbf{X})); (\underline{p}_2, \delta_2)) \quad (4.25)$$

for any \mathbf{X} fixed in Ω , where $\Upsilon(\mathbf{X}) = (\Upsilon_1(\mathbf{X}), \Upsilon_2(\mathbf{X}))$ is a centered Gaussian random variable with covariance matrix [107]:

$$[C_{\Upsilon}] = \begin{bmatrix} 1 & \rho \\ \rho & 1 \end{bmatrix} . \quad (4.26)$$

Upon using the Cholesky factorization $[C_{\Upsilon}] = [L_{\Upsilon}]^T [L_{\Upsilon}]$, it can be deduced that $\{\mathbf{P}(\mathbf{X}), \mathbf{X} \in \Omega\}$ can be defined through

$$P_1(\mathbf{X}) = F_{\mathcal{G}}^{-1}(\Phi(\Xi_1(\mathbf{X})); (\underline{p}_1, \delta_1)) , \quad \forall \mathbf{X} \in \Omega , \quad (4.27)$$

and

$$P_2(\mathbf{X}) = F_{\mathcal{G}}^{-1}(\Phi(\rho \Xi_1(\mathbf{X}) + \sqrt{1 - \rho^2} \Xi_2(\mathbf{X})); (\underline{p}_2, \delta_2)) , \quad \forall \mathbf{X} \in \Omega , \quad (4.28)$$

where $\{\Xi(\mathbf{X}) = (\Xi_1(\mathbf{X}), \Xi_2(\mathbf{X})), \mathbf{X} \in \mathbb{R}^n\}$ is a centered Gaussian random field with statistically independent, centered Gaussian components such that $\Upsilon(\mathbf{X}) = [L_{\Upsilon}]^T \Xi(\mathbf{X})$, $\forall \mathbf{X} \in \Omega$. Equations (4.27) and (4.28) define the nonlinear mapping \mathcal{T} introduced in Equation (4.18) such that $\mathbf{P}(\mathbf{X}) = \mathcal{T}(\Xi(\mathbf{X}))$, for all $\mathbf{X} \in \Omega$ (note that

the spatial dependence of the transformation was dropped given the retained modeling assumptions). This relation can equivalently be stated as $\mathbf{P}(\mathbf{X}) = \mathcal{T}^*(\mathbf{\Upsilon}(\mathbf{X}))$, with obvious notation. The Gaussian random fields are defined in the next section.

4.2.3.2 Construction of the Underlying Gaussian Models

In accordance with the periodic assumption retained in the mechanical modeling framework, it is assumed that each random field $\{\Xi_i(\mathbf{X}), \mathbf{X} \in \mathbb{R}^n\}$, $i \in \{1, 2\}$, satisfies the invariance property $\Xi_i(\mathbf{X}) = \Xi_i(\mathbf{X} + p\mathbf{X}')$ for all $\mathbf{X} \in \Omega$ and $\mathbf{X}' \in \mathbb{Z}^n$ P -almost surely, where it is assumed (without loss of generality) that $\Omega = ([0, p])^n$. Consequently, the centered random field $\{\Xi(\mathbf{X}), \mathbf{X} \in \mathbb{R}^n\}$ is uniquely defined by its restriction to Ω . Assuming the stationary of this restriction in Ω , the underlying Gaussian field is defined through the matrix-valued covariance function $\boldsymbol{\tau} \mapsto [\mathbf{R}_\Xi(\boldsymbol{\tau})] = \mathbb{E}\{\Xi(\mathbf{X} + \boldsymbol{\tau}) \otimes \Xi(\mathbf{X})\}$ such that

$$[\mathbf{R}_\Xi(\boldsymbol{\tau})] = \begin{bmatrix} R_1(\boldsymbol{\tau}) & 0 \\ 0 & R_2(\boldsymbol{\tau}) \end{bmatrix}, \quad \forall \boldsymbol{\tau} \in ([0, p])^n, \quad (4.29)$$

where R_1 and R_2 are the p -periodic covariance functions defining (the restrictions of) $\{\Xi_1(\mathbf{X}), \mathbf{X} \in \mathbb{R}^n\}$ and $\{\Xi_2(\mathbf{X}), \mathbf{X} \in \mathbb{R}^n\}$ (to Ω), respectively. For the sake of illustration, we assume similar covariance functions for the two Gaussian components, setting $R_1 = R_2 = R$, and we consider the case of a separable covariance function in \mathbb{R}^2 :

$$R(\boldsymbol{\tau}) = R_1(\tau_1) \times R_2(\tau_2). \quad (4.30)$$

We further assume that R_1 and R_2 only differ in the choice of hyperparameters, so that the above equation can be written, using an abuse of notation, as

$$R(\boldsymbol{\tau}) = R(\tau_1; L_1) \times R(\tau_2; L_2), \quad (4.31)$$

where $L_1 > 0$ and $L_2 > 0$ are model parameters controlling the correlation ranges of the fields along the directions defined by the canonical basis in \mathbb{R}^2 . The univariate

covariance function R is assumed to take the generic form

$$R_\phi(\tau; L) = \exp(-c\phi(\tau; L)) , \quad \forall \tau \in [0, p] , \quad (4.32)$$

where c is a positive constant (that depends on both ϕ and L) to be defined and ϕ is a p -periodic function taken as

$$\phi(\tau; L) = \frac{|\sin(\pi\tau/p)|}{L} \quad (\text{Periodic Exponential, PE}), \quad (4.33)$$

or

$$\phi(\tau; L) = \frac{\sin(\pi\tau/p)^2}{L^2} \quad (\text{Periodic Squared-Exponential, PSE}) . \quad (4.34)$$

The subscript in the notation R_ϕ underlines the choice of a particular periodic function. The two functions defined by (4.33) and (4.34) are specifically chosen so as to investigate the impact of sample path regularity on fracture simulation outcomes. In particular, and while both functions yield random fields of fracture properties that are mean-square continuous, the periodic squared-exponential covariance function obtained by combining (4.32) and (4.34) leads to mean-square differentiable fields which exhibit “smooth” realizations. On the contrary, the periodic exponential function defined by considering (4.33) yields random fields that are not mean-square differentiable and thus have much rougher realizations.

In order to ensure meaningful comparison between the covariance models, the normalization constants are determined such that the spatial correlation length along the direction of one main direction is equal to L , that is:

$$\int_0^{p/2} |R_\phi(\tau; L)| d\tau = L . \quad (4.35)$$

For later use, we introduce the normalized correlation length $L^* = L/p$. For the squared exponential model, the constant c_{PSE} is hence required to satisfy the non-

linear equation

$$\frac{1}{2}p \exp\left(-\frac{c_{\text{PSE}}}{2L^2}\right) I_0\left(\frac{c_{\text{PSE}}}{2L^2}\right) = L , \quad (4.36)$$

where I_0 is the 0th order modified Bessel's function, whereas the constant c_{PE} associated with the exponential covariance kernel must satisfy

$$\frac{1}{2}p \left[I_0\left(\frac{c_{\text{PE}}}{L}\right) - S_0\left(\frac{c_{\text{PE}}}{L}\right) \right] = L , \quad (4.37)$$

where S_0 is the 0th order modified Struve's function. In this work, these equations are solved numerically using a Newton-Raphson solver.

It should be noticed that the covariance function $\boldsymbol{\tau} \mapsto [\mathbf{R}_{\mathbf{Y}}(\boldsymbol{\tau})]$ defining the restriction of the Gaussian random field $\{\mathbf{Y}(\mathbf{X}), \mathbf{X} \in \mathbb{R}^n\}$ to Ω is given by

$$[\mathbf{R}_{\mathbf{Y}}(\boldsymbol{\tau})] = \begin{bmatrix} R_1(\boldsymbol{\tau}) & \rho R_1(\boldsymbol{\tau}) \\ \rho R_1(\boldsymbol{\tau}) & \rho^2 R_1(\boldsymbol{\tau}) + (1 - \rho^2) R_2(\boldsymbol{\tau}) \end{bmatrix} , \quad \forall \boldsymbol{\tau} \in ([0, p])^n , \quad (4.38)$$

which shows the role played by the parameter ρ on the covariance function of $\{P_2(\mathbf{X}), \mathbf{X} \in \Omega\}$ (after the action of \mathcal{T}^*).

4.2.3.3 Fundamental Properties of the Random Field of Fracture Properties

Based on the construction proposed in Sections 4.2.3.1 and 4.2.3.2, the non-Gaussian random field $\{\mathbf{P}(\mathbf{X}), \mathbf{X} \in \Omega\}$ modeling the fracture properties satisfies the following properties:

1. $P_i(\mathbf{X}) > 0$ for all $\mathbf{X} \in \Omega$ and $i \in \{1, 2\}$, almost surely.
2. $\{\mathbf{P}(\mathbf{X}), \mathbf{X} \in \Omega\}$ is of second order, $\mathbb{E}\{|0\mathbf{P}(\mathbf{X})|^0\} < +\infty \quad \forall \mathbf{X} \in \Omega$.
3. The field satisfies $\mathbf{P}((0, x_2)) = \mathbf{P}((p, x_2))$ and $\mathbf{P}((x_1, 0)) = \mathbf{P}((x_1, p))$, almost surely.

4. The mean function $\mathbf{X} \mapsto \underline{\mathbf{p}}(\mathbf{X}) = \mathbb{E}\{\mathbf{P}(\mathbf{X})\}$ is given by $\underline{\mathbf{p}}(\mathbf{X}) = \underline{\mathbf{p}} = (\underline{p}_1, \underline{p}_2)$ for all $\mathbf{X} \in \Omega$.

5. The covariance matrix at any location $\mathbf{X} \in \Omega$ reads as

$$\mathbb{E}\{(\mathbf{P}(\mathbf{X}) - \underline{\mathbf{p}}) \otimes (\mathbf{P}(\mathbf{X}) - \underline{\mathbf{p}})\} = \begin{bmatrix} \underline{p}_1^2 \delta_1^2 & \underline{p}_1 \underline{p}_2 \delta_1 \delta_2 \rho \\ \underline{p}_1 \underline{p}_2 \delta_1 \delta_2 \rho & \underline{p}_2^2 \delta_2^2 \end{bmatrix}. \quad (4.39)$$

It can also be deduced that the random field $\{\mathbf{P}(\mathbf{X}), \mathbf{X} \in \Omega\}$ is mean-square continuous for the PE and PSE correlation functions introduced in Section 4.2.3.2. Finally, the field is mean-square differentiable for the PSE covariance function.

Recall that in the properties above, \underline{p}_1 and \underline{p}_2 correspond to the desired mean values for the fracture toughness \mathcal{G}_c and energy threshold ψ_c , and δ_1 and δ_2 are the coefficients of variation that control the statistical dispersions of these parameters. The parameter ρ measures the level of correlation between the fracture properties.

4.2.3.4 Stochastic Simulation Aspects

Simulating realizations of the random field of fracture properties requires (i) drawing realizations of the underlying Gaussian random fields defined in Section 4.2.3.2, and (ii) evaluating the nonlinear transformations defined by (4.27) and (4.28). Routines to compute the latter mappings are readily available in many scientific computing environments. Regarding the generation of the Gaussian fields, we presently resort to truncated Karhunen-Loève expansions. Each (mean-square continuous) random field $\{\Xi_i(\mathbf{X}), \mathbf{X} \in \mathbb{R}^n\}$, $i \in \{1, 2\}$, is thus expanded as

$$\Xi_i(\mathbf{X}) = \sum_{k=1}^{q_i} \sqrt{\lambda_k} \eta_k \varphi_k(\mathbf{X}), \quad (4.40)$$

where $\{\eta_k\}_{k \geq 1}$ is a set of independent normalized Gaussian random variables, and $\{\lambda_k\}_{k \geq 1}$ and $\{\varphi_k\}_{k \geq 1}$ are the nonnegative eigenvalues (ordered as a nonincreasing

sequence) and the associated orthonormal eigenfunctions of the covariance function that satisfy the following integral equation (which is a Fredholm integral equation of the second kind):

$$\int_{\Omega} R(\mathbf{X}, \mathbf{X}') \varphi_k(\mathbf{X}') d\mathbf{X}' = \lambda_k \varphi_k(\mathbf{X}) , \quad \forall \mathbf{X} \in \Omega , \quad (4.41)$$

where R is the covariance kernel introduced in Section 4.2.3.2 (note the abuse of notation, with $\tau = \mathbf{X} - \mathbf{X}'$). For arbitrary covariance functions, this integral equation can be solved by using a standard Galerkin formulation [108, 109]: given a finite set of basis functions $\{\phi_j\}_{j=1}^{N_{\text{node}}} \subset L_2(\Omega)$, each eigenfunction is approximated as

$$\varphi_k(\mathbf{X}) \approx \sum_{j=1}^{N_{\text{node}}} \alpha_j^{(k)} \phi_j(\mathbf{X}) . \quad (4.42)$$

Substituting this approximation in the integral equation and enforcing the residual to be orthogonal to $\text{span}(\{\phi_j\}_{j=1}^{N_{\text{node}}})$, we obtain

$$\sum_{j=1}^{N_{\text{node}}} \alpha_j^{(k)} \int_{\Omega} \int_{\Omega} R(\mathbf{X}, \mathbf{X}') \phi_j(\mathbf{X}') \phi_\ell(\mathbf{X}) d\mathbf{X}' d\mathbf{X} = \sum_{j=1}^{N_{\text{node}}} \alpha_j^{(k)} \int_{\Omega} \lambda_k \phi_j(\mathbf{X}) \phi_\ell(\mathbf{X}) d\mathbf{X} . \quad (4.43)$$

Considering the above equation for all eigenfunctions leads to the generalized eigenvalue problem $[K][A] = [\Lambda][M][A]$, where $[A]_{j\ell} = \alpha_j^{(\ell)}$, $[\Lambda]_{j\ell} = \lambda_j \delta_{j\ell}$ (with $\delta_{j\ell}$ the Kronecker delta), and $[K]$ and $[M]$ are the matrices with entries

$$[K]_{j\ell} = \int_{\Omega} \int_{\Omega} R(\mathbf{X}, \mathbf{X}') \phi_j(\mathbf{X}') \phi_\ell(\mathbf{X}) d\mathbf{X}' d\mathbf{X} , \quad [M]_{j\ell} = \int_{\Omega} \phi_j(\mathbf{X}) \phi_\ell(\mathbf{X}) d\mathbf{X} . \quad (4.44)$$

For each Gaussian field $\{\Xi_i(\mathbf{X}), \mathbf{X} \in \mathbb{R}^n\}$, the truncation order $q_i \leq N_{\text{node}}$ can be determined by analyzing the convergence of the error function

$$\varepsilon_{\text{KL}}(q) = 1 - \left(\sum_{k=1}^q \lambda_k \middle/ \sum_{k=1}^{N_{\text{node}}} \lambda_k \right), \quad (4.45)$$

and by selecting q_i such that $\varepsilon_{\text{KL}}(q_i) \leq \varepsilon_0$ for some given tolerance $0 < \varepsilon_0 \ll 1$.

4.3 Verification

4.3.1 Mode I: Edge-Notched Unilateral Tension Test

Consider a $1 \text{ mm} \times 1 \text{ mm}$ plate with a pre-existing crack on the left side, loaded in uniaxial tension, as shown in Figure 4.1a. We assume the plate to be composed of an isotropic material with Young's modulus $E = 2.1 \times 10^5 \text{ MPa}$, Poisson's ratio $\nu = 0.3$, fracture toughness $\mathcal{G}_c = 2.7 \text{ mJ mm}^{-2}$, and critical strength $\sigma_c = 2.5 \times 10^3 \text{ MPa}$. The plate is fixed along the bottom, and the top surface is displaced in the vertical direction. Roller supports are also assumed to be in place, such that the horizontal displacement vanishes along the top surface. The plate is assumed to be sufficiently thick such that plane strain conditions hold.

The domain is meshed with linear triangular elements. The maximum/minimum element characteristic lengths are 0.05 mm and 0.005 mm, respectively, corresponding to a mesh with 7845 elements. The crack surface density is approximated with a regularization length $l = 0.015 \text{ mm}$, such that the half phase-field bandwidth is resolved by approximately 6 elements.

We examine two representations of the pre-existing crack. First, we use a “geometric notch” to represent the crack as shown in Figures 4.1b and 4.2a. In this case, the traction-free boundary condition on the notch surfaces is satisfied in a weak sense. The resulting phase fields as a function of boundary displacement are shown in Figures 4.2b to 4.2d. Only the phase fields obtained using the spectral

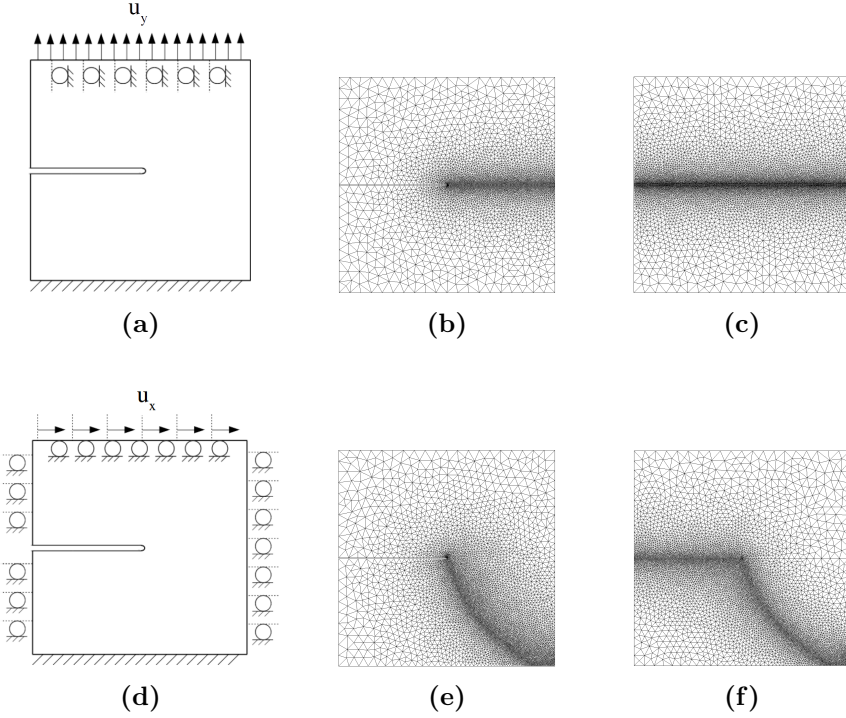


FIGURE 4.1. Boundary conditions of the plate with a pre-existing crack for (a) a mode I tension test and (d) a mode II shear test. Finite element meshes for the mode I calculations (b - c) and for the mode II calculations (e - f). For (b, e) the meshes have the initial crack geometry “meshed-in” while (c, f) have local refinement around the initial phase field. All meshes are pre-refined along the predicted crack-path with a characteristic element size of 0.005 mm.

decomposition are shown in the Figures. Contours of the phase field obtained using the contact split with a threshold were found to be indistinguishable.

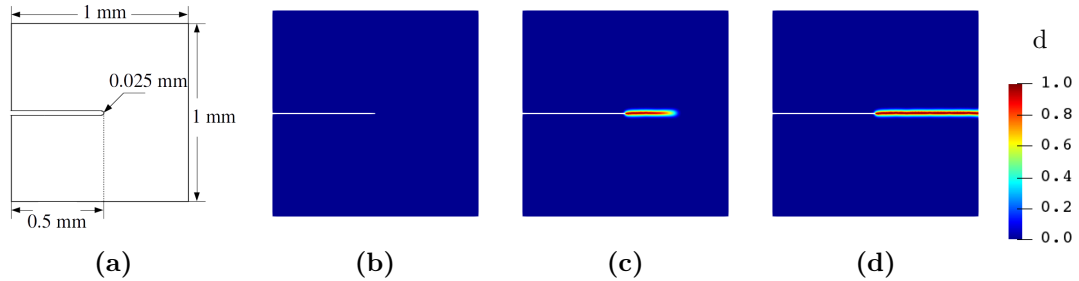


FIGURE 4.2. Edge-notched specimen loaded in tension with initial crack represented by a geometric notch with a rounded corner. (a) Dimensions of the notched plate. Damage d at (b) $u_y = 0$ mm, (c) $u_y = 0.0048$ mm, (d) $u_y = 0.006$ mm.

Secondly, we use an initial phase field $d(t = 0) = d_0$ to represent the initial crack, where d_0 is given by:

$$d_0(\mathbf{X}) = \begin{cases} \left(1 - \frac{\tau(\mathbf{X})}{2l}\right)^2, & \tau(\mathbf{X}) \leqslant 2l \\ 0, & \tau(\mathbf{X}) > 2l \end{cases} \quad (4.46)$$

$$\text{with} \quad (4.47)$$

$$\tau(\mathbf{X}) = \begin{cases} |\mathbf{X} \cdot \mathbf{e}_2|, & \mathbf{X} \cdot \mathbf{e}_1 \leqslant 0, \\ \|\mathbf{X}\|, & \mathbf{X} \cdot \mathbf{e}_1 > 0, \end{cases} \quad (4.48)$$

with an origin for the coordinate system at the center of the plate. The initial phase field is resolved using the locally refined mesh of linear triangular elements shown in Figure 4.1c. The resulting initial phase field is shown in Figure 4.3b. Once again, the contour plots of the phase field obtained using a spectral decomposition and the contact split were found to be indistinguishable.

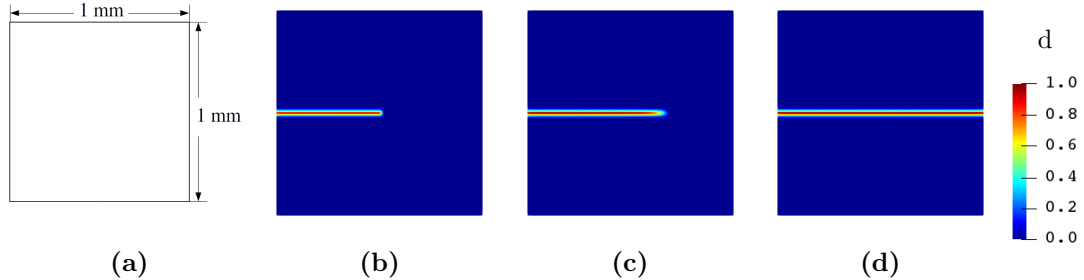


FIGURE 4.3. Edge-notched specimen loaded in tension with initial crack represented by a phase field. (a) Dimensions of the intact plate. The Damage d at (b) $u_y = 0$ mm (c) $u_y = 0.0048$ mm (d) $u_y = 0.006$ mm.

Plots of the vertical component of the reaction force at the top boundary of the plate versus the prescribed y -displacement are shown in Figure 4.4, for both representations of the initial crack and split strategies. The reaction force is nondimensionalized with respect to the critical strength and the plate thickness, i.e. $f_y^* = f_y/(\sigma_c t)$, and the displacement is nondimensionalized by $u_y^* = u_y/a$, where a is the side length of the square plate. As expected, the contact split does not affect the material

response in the uniaxial loading case (Figure 4.4a), and the results appear to be relatively insensitive to the choice of threshold for switching between the spectral split and the contact split (Figure 4.4b).

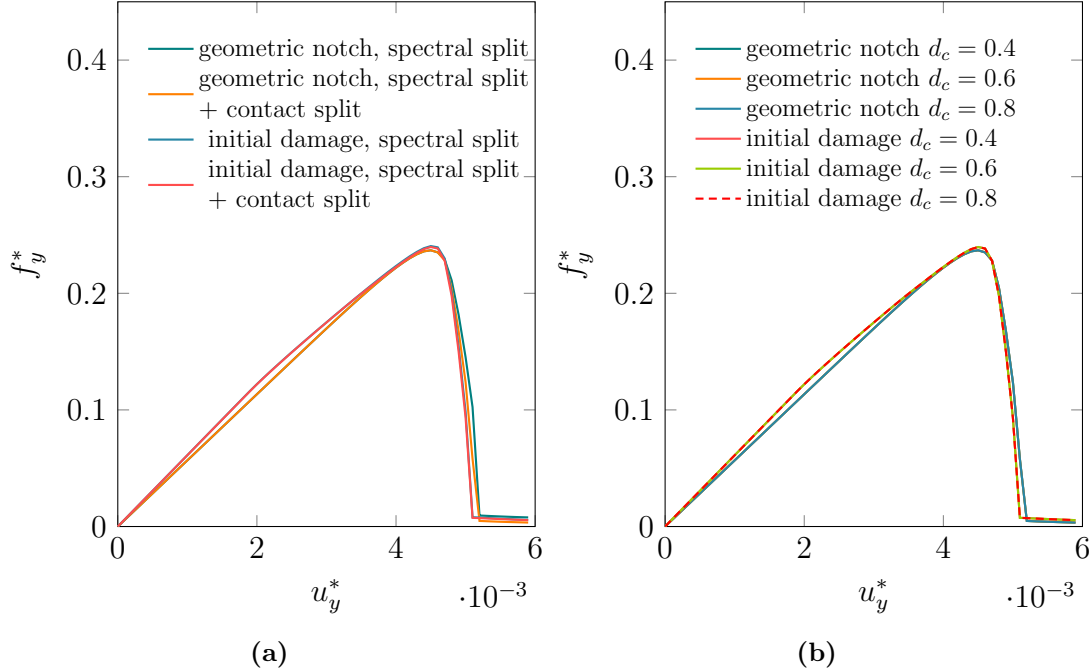


FIGURE 4.4. Mode I force–displacement curves obtained using (a) the spectral decomposition with two representations of the pre-existing crack (b) a spectral decomposition in conjunction with the contact split with different critical damage threshold on two representations of the pre-existing crack.

4.3.2 Mode II: Edge-Notched Shear Test

The effect of the proposed energy split becomes readily apparent when the loading case is dominated by in-plane or out-of-plane shear. Let us consider the same edge-notched thick plate as in the last section, but subjected to a different loading. A schematic of the boundary conditions for this case and the corresponding meshes are shown in Figures 4.1d to 4.1f.

Once again, the effect of the contact split is examined by comparing the results using two different representations of the initial crack, as shown in Figure 4.5 and

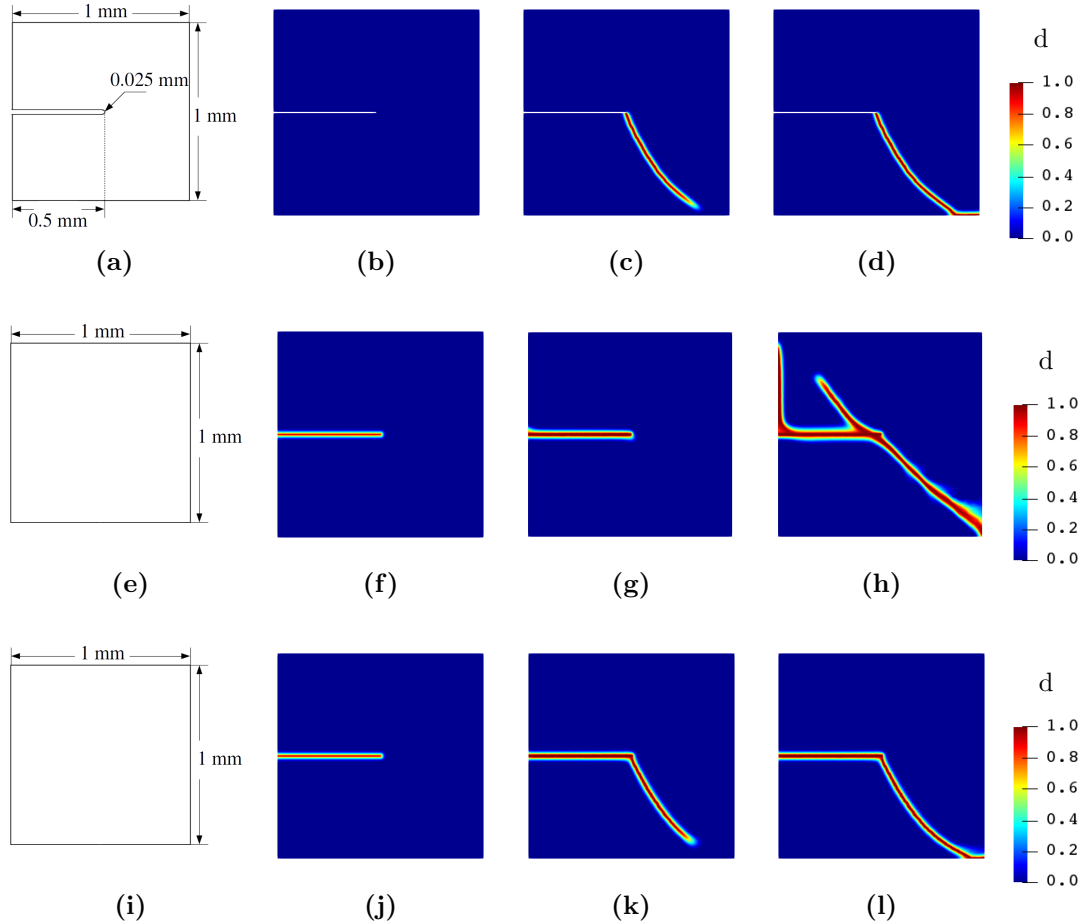


FIGURE 4.5. The crack paths obtained using (a-d) the spectral decomposition on a geometrically notched plate, (e-h) the spectral decomposition with an initial phase field d_0 (4.46) representing the initial crack, and (i-l) the contact split with an initial phase field. Snapshots of crack paths are shown at (b,f,j) $u_x = 0 \text{ mm}$, (c,g,k) $u_x = 0.0109 \text{ mm}$, and (d,h,l) $u_x = 0.02 \text{ mm}$.

Figure 4.6a. Simulations that rely solely on the spectral decomposition result in dramatically different crack paths (Figures 4.5c, 4.5d, 4.5g and 4.5h) and force-displacement responses (Figure 4.6a). We note that after the initial decay following a horizontal displacement of $u_x = 1.0 \times 10^{-2} \text{ mm}$, the force for the geometric notch with the spectral decomposition begins to rise. Even though the phase field completely separates the plate into two sections, the force continues to increase. This is because the spectral decomposition does not prevent all traction from being transmitted

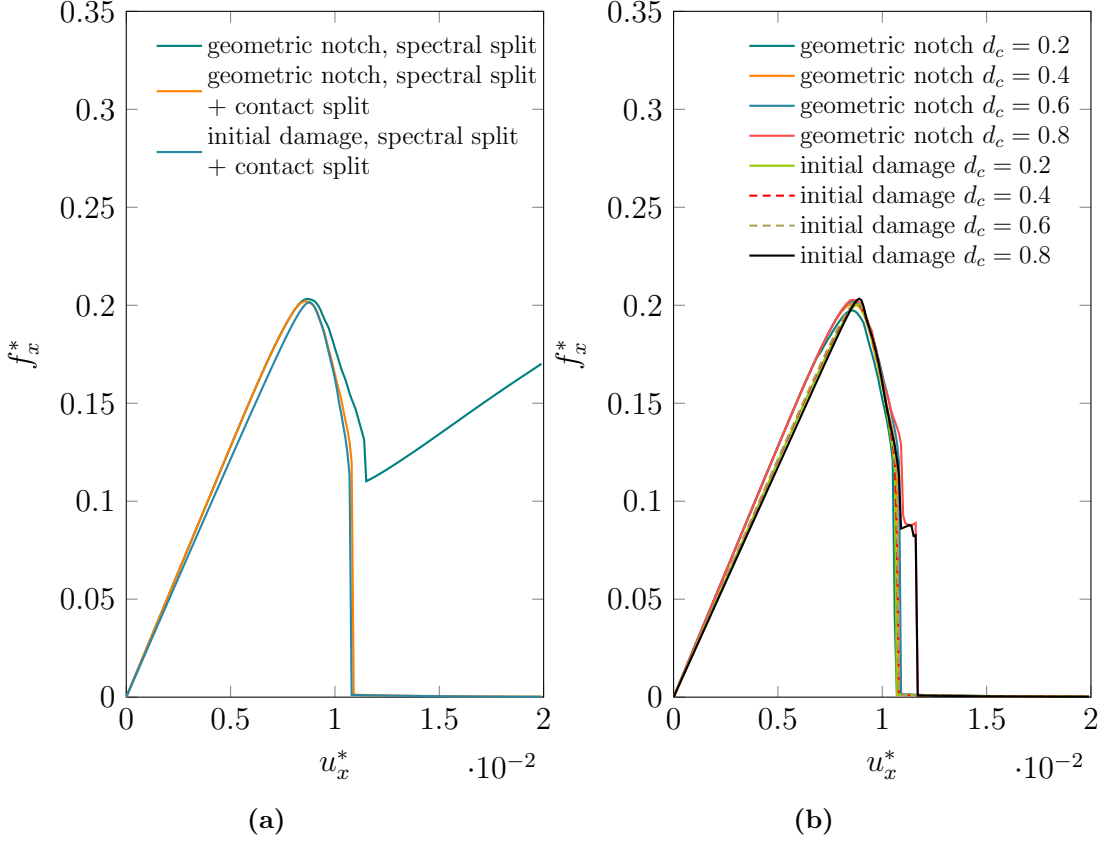


FIGURE 4.6. Mode II force–displacement curves obtained using (a) spectral decomposition with two representations of the initial crack (b) spectral decomposition in conjunction with the contact split with different critical damage threshold on two representations of the initial crack.

across a fully damaged surface.

In contrast, when the traction-free condition is enforced using the contact split, the crack paths (Figures 4.5c, 4.5d, 4.5k and 4.5l) as well as the force-displacement curves (Figure 4.6b) are similar for both representations of the pre-existing crack. Notably in this case, the force at the boundary decays completely to zero as the plate is separated in two by the phase field. As shown in Figure 4.6b, the results are also relatively insensitive to the particular choice of threshold for the contact split.

We note that if the threshold is selected to be too high (e.g. $d_{\text{critical}} \geq 0.8$) a small upward perturbation in the force-displacement curve can be observed, shortly after a

horizontal displacement of $u_x = 1.0 \times 10^{-2}$ mm. The brief increase is due to the fact that the band of damage wherein the contact split is applied is too small, and some traction can still be transmitted across the fully damaged band. Essentially, there are elements capturing the peak phase field wherein some quadrature points are below the threshold while others are above it. While further mesh refinement can remove this artifact, in practice we employ meshes that sufficiently capture the phase-field regularization, wherein $2l/h^e = 5$. Given this level of mesh refinement and typical damage profiles, we anticipate that a threshold of $d_{\text{critical}} = 0.6$ is sufficient to prevent any such artifacts. As such, we employ a threshold of $d_{\text{critical}} = 0.6$ for all subsequent problems.

4.3.3 Crack Propagation Under Biaxial Tension

We now examine a problem in which a thin plate with initial imperfections is subject to biaxial tension. Plane-stress conditions are assumed to hold. The plate geometry and boundary conditions are summarized in Figure 4.7a, and the initial phase field representing two imperfections is shown in Figure 4.7b. Periodic boundary conditions are assumed on all sides.

Using property values that are representative of a typical clay specimen, the plate is assumed to be composed of a material with a Young's modulus E of 4 MPa, a Poisson's ratio ν of 0.2, a fracture toughness \mathcal{G}_c of 27 kJ m^{-2} , and a critical fracture energy ψ_c of 30 J m^{-2} .

The governing equation for the mechanical problem in this case is given by:

$$\nabla \cdot (\tilde{\boldsymbol{\sigma}} + \sigma_0 \mathbf{I}) = 0, \quad (4.49)$$

where σ_0 is a scalar-valued function that varies temporally and serves to model the drying process. The initial stress $\sigma_0 \mathbf{I}$ is equivalent to an inelastic eigen-strain, i.e. $\boldsymbol{\varepsilon}_0 = \mathbb{S} : (\sigma_0 \mathbf{I})$, where \mathbb{S} is the compliance tensor.

With a view towards nondimensionalization, as will be discussed in Section 4.4.1, the fracture driving force may be nondimensionalized as

$$\mathcal{D}^* = \sqrt{\frac{(1 - \nu^2)a}{EG_c}}\sigma_0, \quad (4.50)$$

where a is a characteristic size for the domain. Here, we choose it to be the width of the plate.

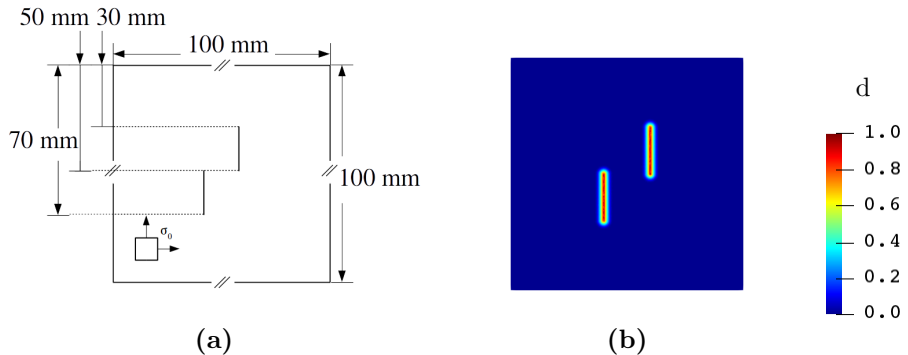


FIGURE 4.7. (a) Dimensions and boundary conditions of a thin plate with two parallel initial cracks. (b) The initial cracks are represented by an initial phase field.

We now compare simulation results obtained using three strain energy split techniques: a no-split approach, the spectral split, and the contact split. The phase fields obtained using the three different split techniques are shown in Figure 4.8 at representative magnitudes of the dimensionless driving force.

The no-split approach treats the entire strain energy as an active potential to be degraded, neglecting the tension-compression asymmetry. It is widely used in calculations of drying processes because the effective loading condition is assumed to be tensile: biaxial tension in 2D and triaxial tension in 3D. However, we note that tensile loading conditions do not necessarily lead to a tensile local stress/strain state everywhere in the domain, hence it is possible to have crack propagation under compression, as can be observed in this example. We will return to this issue

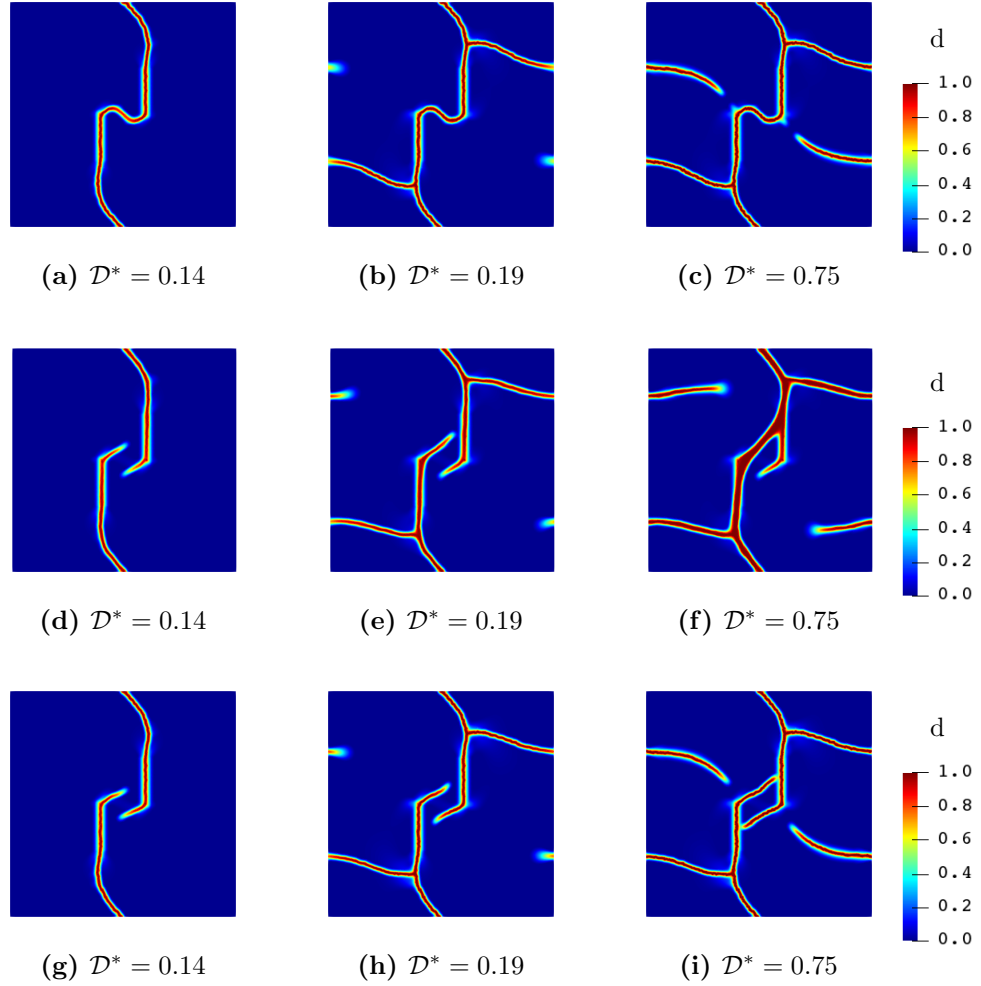


FIGURE 4.8. Crack paths obtained using (a-c) a no-split technique (d-f) the spectral decomposition (g-i) the contact split.

after examining the results obtained using a spectral decomposition and a spectral decomposition with the contact split.

The spectral decomposition prevents crack propagation under compression (Figure 4.8d), but without enforcing the traction-free condition on the crack surfaces represented by the phase field, which may affect secondary crack paths that emerge from existing crack surfaces (Figure 4.8e). Such artifacts can be removed by enforcing the traction-free condition on the regularized crack surfaces using the contact split (Figures 4.8g to 4.8i).

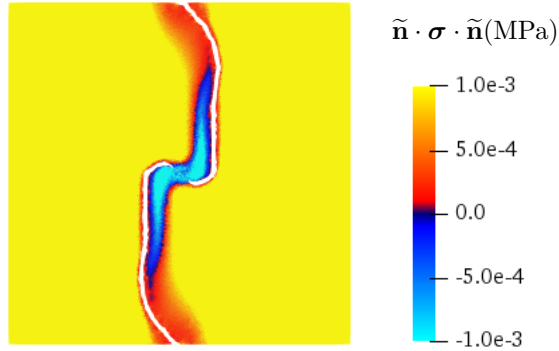


FIGURE 4.9. Contour plot of the normal pressure right before the bridge forms. The pressure is calculated for an orientation that is estimated to be orthogonal to the bridge. Elements within the contour of $d = 0.75$ are removed to indicate the current crack set.

We now return to the issue of the possibility of crack growth under compression with a no-split approach. Comparing the damage profiles shown in Figures 4.8a, 4.8d and 4.8g one can observe that a damage bridge forms between the two vertical initial cracks only for the case of a no-split method. To explore this region more precisely, we consider the fields immediately before the bridge forms, and examine contour plots of the normal pressure for an orientation that is orthogonal to the bridge (Figure 4.9). The contour plots clearly indicate that the region is loaded in compression immediately before the bridge forms.

As a final observation in this section, we note that the crack-paths obtained using the spectral decomposition exhibit a broadening of the phase field at late stages of growth (Figure 4.8f). By contrast, the contact decomposition results in damage profiles that remain relatively thin compared to the specimen dimensions (Figure 4.8i).

4.4 Numerical examples

In this section, we study in detail the formation of crack networks in thin films and soil desiccation. We begin in Section 4.4.1 with a deterministic benchmark problem

under quasi-one-dimensional conditions. The spacing between fractures is calculated as a function of the driving force with the cohesive fracture model and compared against a linear elasticity solution. Attention is then turned to an investigation of the stochastic aspects of fracture with a two-dimensional plane stress model in Section 4.4.2, wherein the fracture toughness and critical fracture energy are modeled as random fields. Finally, in Section 4.4.3 we present stochastic simulations of a soil desiccation process in three dimensions.

4.4.1 One-Dimensional Simplification: Side View

We begin by deriving an analytical solution for the fracture of a thin film bonded to a thick substrate, as shown in Figure 4.10. Assuming that the planar dimensions of the film are much larger than its thickness, we first simplify the problem into a two-dimensional (or quasi 1D) plane-strain problem. The film is assumed to have Young's modulus E_1 , Poisson's ratio ν_1 , and thickness h . The substrate has Young's modulus E_0 , Poisson's ratio ν_0 , and thickness H . The fracture of the film is driven by the underlying substrate being stretched an amount ε_x . The problem with these simplifications and assumptions has been studied by many researchers, and analytical solutions from elasticity theory have been derived in several different ways. The derivation presented herein most closely follows that provided in Yin et al. [90].

With the increase of the tensile strain in the substrate, some uniformly distributed discontinuities with spacing 2λ form across the thickness of the film. We assume that no debonding occurs and that the vertical component of the displacement does not vary in the horizontal direction, i.e.

$$u_y(x, y) = u_y(y). \quad (4.51)$$

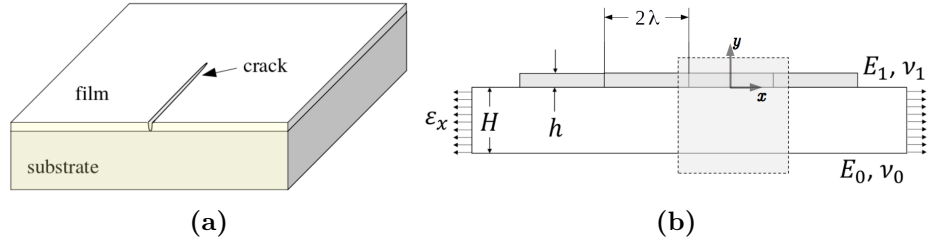


FIGURE 4.10. Description of a one-dimensional model for thin-film cracking. (a) Side view (highlighted in yellow) of the geometry (b) schematic representation of the side view. The elasticity solution is derived for the region highlighted with the shaded box, i.e. between the two discontinuities across the thin film. The coordinate system is centered at the middle of the bottom surface of the thin film.

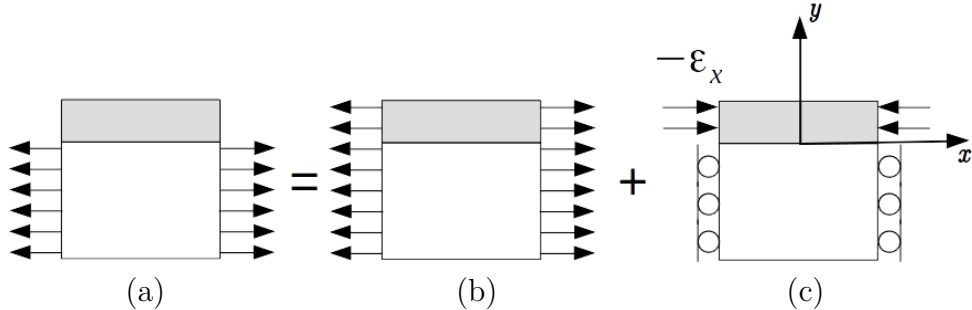


FIGURE 4.11. The principle of “super-superposition” applied to the region of interest marked in Figure 4.10b. The analytical solution is derived based on the boundary conditions shown in (c).

The plane-strain equilibrium equation in the x-direction is written as

$$\frac{E_1}{1 - \nu_1^2} u_{x,xx} + \mu_1 u_{x,yy} = 0, \quad (4.52)$$

where μ_1 denotes the shear modulus of the film. This is supplemented by appropriate boundary conditions (Figure 4.11)

$$u_x(0, y) = 0, \quad (4.53)$$

$$u_{x,y}(x,h) = 0, \quad (4.54)$$

$$\frac{1}{h} \int_0^h \sigma_x(\lambda, y) \, dy = -\frac{E_1}{1 - \nu_1^2} \varepsilon_x. \quad (4.55)$$

We obtain the closed-form solution to the displacement field

$$u_x(x, y) = \varepsilon_x x - \frac{\sinh(cx/h)}{\cosh(c\lambda/h)} \frac{\cos(d(1-y/h))}{\sin(d)} \sqrt{\frac{E_1}{\mu_1(1-\nu_1^2)}} h \varepsilon_x, \quad (4.56)$$

where c and d are functions of Dundur's parameters α and β . Following [110, 89, 90], c and d can be computed as:

$$c = \frac{2}{\pi k(\alpha, \beta)}, \quad d = \sqrt{\frac{2}{1-\nu_1}} c, \quad (4.57)$$

$$\alpha = \frac{\bar{E}_1 - \bar{E}_0}{\bar{E}_1 + \bar{E}_0}, \quad \beta = \frac{\mu_1(1-2\nu_0) - \mu_0(1-2\nu_1)}{2\mu_1(1-\nu_0) + 2\mu_0(1-\nu_1)}, \quad (4.58)$$

$$k(\alpha, \beta) \approx k(\alpha) = \frac{1.258 - 0.4\alpha - 0.26\alpha^3 - 0.3\alpha^4}{1-\alpha}, \quad (4.59)$$

with $\bar{E}_0 = \frac{E_0}{(1-\nu_0^2)}$, and $\bar{E}_1 = \frac{E_1}{(1-\nu_1^2)}$. By replacing λ with $\lambda/2$, the crack opening displacement can be written as

$$\delta(0, y) = 2 \tanh\left(\frac{c\lambda}{2h}\right) \frac{\cos(d(1-y/h))}{\sin(d)} \sqrt{\frac{E_1}{\mu_1(1-\nu_1^2)}} h \varepsilon_x. \quad (4.60)$$

Then the fracture toughness can be obtained as the work done to close the crack, i.e.

$$\mathcal{G}_c \cdot 2h = \int_0^h \sigma_x(0, y) \delta(0, y) \, dy, \quad (4.61)$$

$$\mathcal{G}_c = \frac{(1-\nu_1^2)\sigma_x^2 h}{E_1 c} \left[2 \tanh\left(\frac{c\lambda}{2h}\right) - \tanh(c\lambda/h) \right]. \quad (4.62)$$

The amount of energy released by opening a transverse crack is governed by two dimensionless parameters:

$$\mathcal{D}^* = \sqrt{\frac{(1-\nu_1^2)h}{E_1 \mathcal{G}_c}} \sigma_x, \quad l^* = \frac{\lambda}{h}. \quad (4.63)$$

It is then convenient to interpret the parameter \mathcal{D}^* as the dimensionless fracture driving energy and l^* as the dimensionless crack spacing. (4.62) can be rendered dimensionless following (4.63), and the relation between the dimensionless fracture driving energy and the dimensionless crack spacing can be written as

$$\mathcal{D}^* \mathcal{C}(l^*; c) = 1, \quad \mathcal{C}(l^*; c) = \frac{1}{c} \left[2 \tanh\left(\frac{1}{2} cl^*\right) - \tanh(cl^*) \right]. \quad (4.64)$$

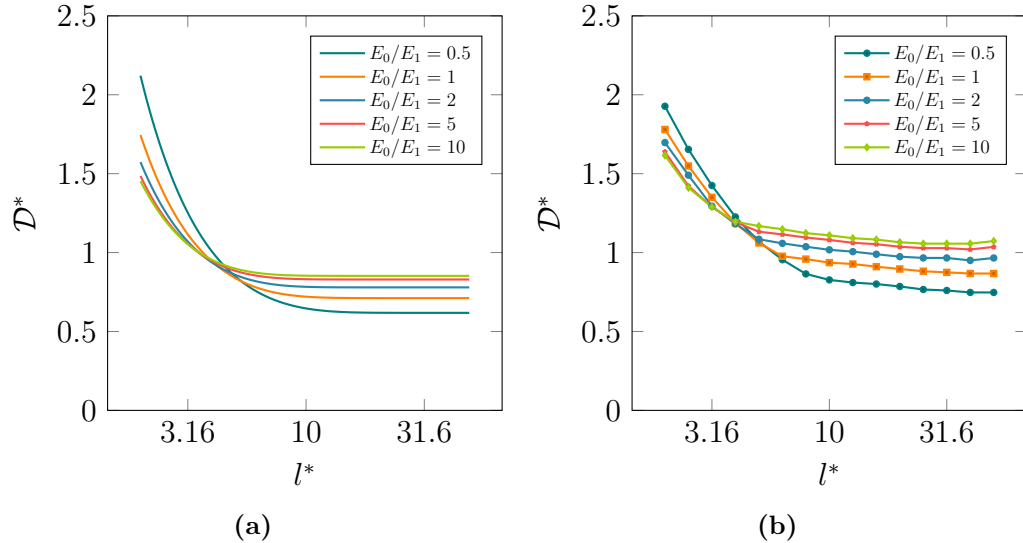


FIGURE 4.12. Relationship between the dimensionless fracture driving energy and the dimensionless crack spacing: (a) analytical solution using linear elasticity; and (b) numerically generated curves using the phase-field for cohesive model detailed in this work.

In Figure 4.12a, we set the Poisson's ratio of both the film and the substrate to be $\nu_0 = \nu_1 = 0.2$, and plot the dimensionless fracture driving energy versus the dimensionless crack spacing for different combinations of the mismatch in the Young's modulus between the film and the substrate.

Next, we performed a series of numerical simulations using the phase-field for cohesive fracture model following the setup described in Figure 4.10b. Specifically, we examine the amount of driving energy required to propagate one transverse crack

through the thickness of the film. The substrate and the film are represented by two rectangular domains $\Omega_s = [-\lambda, \lambda] \times [-5 \text{ mm}, 0]$ and $\Omega_f = [-\lambda, \lambda] \times [0, 1 \text{ mm}]$, respectively. The film-substrate system is the union of the two, i.e. $\Omega_0 = \Omega_s \cup \Omega_f$, and left-right periodicity is enforced. The substrate and the film are discretized with linear triangular elements with characteristic lengths of $h_s^e = \lambda/10$ and $h_f^e = \lambda/100$, respectively. The numerical results (Figure 4.12b) show a good agreement with the analytical solution.

4.4.2 Two-Dimensional Simplification: Stochastic Aspects of Fracture

We now consider a two-dimensional model of a thin film on a substrate wherein the geometry of the resulting fracture patterns is considerably more complex. For the bulk material properties, we adopt values that are representative of clay. The material properties and model parameters are summarized in Table 4.1.

We focus attention on the sensitivity of the resulting fracture patterns to stochastic spatial variations in the fracture properties. The random field of fracture properties $\{(\mathcal{G}_c(\mathbf{X}), \psi_c(\mathbf{X})), \mathbf{X} \in \Omega_0\}$ is defined and sampled following the model and procedures presented in Section 4.2.3. For all cases, the spatial correlation length L is larger than the regularization length l of the phase-field model. A tolerance of 1×10^{-3} is chosen for the truncation error in the Karhunen-Loëve expansion (4.45). The mean values of \mathcal{G}_c and ψ_c are chosen in accordance with reported values for clay as listed in Table 4.1. Coefficients of variation are chosen to be 0.03, leading to a variation of about $\pm 10\%$ around the mean value for the two random fracture parameters. All realizations shown in figures are normalized with respect to the corresponding stationary mean function, and the normalized quantities are denoted by \mathcal{G}_c^* and ψ_c^* .

Table 4.1. Summary of material properties and model parameters for all calculations in Section 4.4.2

Property/Parameter	Symbol	Value	Unit	Comment
Young's modulus	E	4	MPa	See [111, 1]
Poisson's ratio	ν	0.2	nondim.	See [111, 1]
Mean fracture toughness	\mathcal{G}_c	27	kJ m^{-2}	See [112]
Mean critical fracture energy	ψ_c	30	J m^{-2}	See [112]
Regularization length	l	0.5	mm	Such that $2l/h^e \approx 5$
Degradation shape parameter	p	1	nondim.	

4.4.2.1 A Plane-Stress Model

We now consider the problem of a thin film of thickness h that is bonded to an elastic underlayer of thickness H , as shown in Figure 4.13. The entire structure is assumed to be bonded to a rigid substrate. For this case, we employ the shear-lag model that is detailed in [86]. The square domain is discretized using linear triangular elements with a characteristic length of $h^e = a/500$. This mesh is used for the displacement subproblem, the phase-field subproblem for fracture, and the generalized eigenvalue problem for the random fields. The displacement field and the phase field are constrained to be a -periodic, and the random fields are constructed to be a -periodic as well.

4.4.2.2 Effect of Correlation Length and Smoothness

To study the effect of the correlation length, crack patterns for four different values of L are compared. Ten calculations, corresponding to ten samples of the stochastic fields, are carried out for each value of L . Representative random fields and their corresponding phase fields are shown in Figure 4.14. A Flooding algorithm (described in Appendix B) is used to group elements into clusters in a volume-preserving way, to facilitate the counting of distinct fragments. Following the one-dimensional deriva-

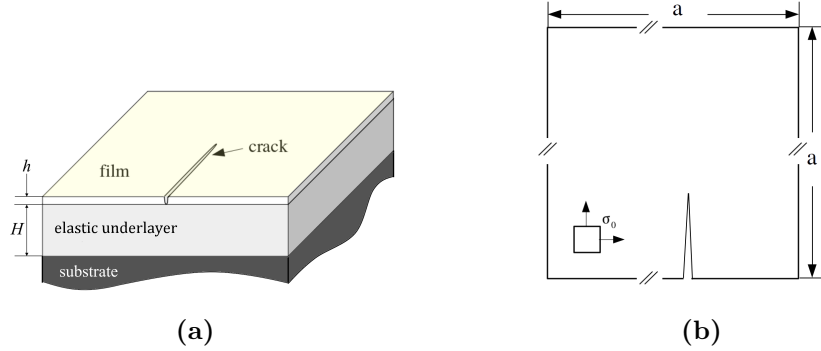


FIGURE 4.13. Description of a two-dimensional model for thin-film cracking. (a) Top view (highlighted in yellow) (b) schematic representation of the top view. A typical crack is shown to emphasize that fracture is only considered in the film.

tion (Section 4.4.1), two dimensionless parameters are extracted as

$$\mathcal{D}^* = \sqrt{\frac{(1 - \nu_1^2)h}{E_1 \underline{\mathcal{G}}_c}} \sigma_0, \quad l^* = \frac{\lambda}{h}, \quad \lambda \approx \sqrt{A}, \quad (4.65)$$

where the crack spacing λ is estimated from the fragment area A . Dimensionless curves are plotted in Figure 4.16.

As expected, it is seen that the PSE covariance model generates smoother realizations. As the normalized correlation length $L^* = L/p$ becomes larger, i.e. Figures 4.14c, 4.14i and 4.14o, a substantial amount of damage accumulates before localization occurs to form a “crack”. When the sample exhibits less spatial fluctuations, a non-negligible portion of the energy is dissipated into the matrix in the form of diffuse damage, resulting in fewer cracks and larger fragment sizes. As the normalized correlation gets even larger, i.e. Figures 4.14m to 4.14o, morphologically different crack networks are obtained.

On the other hand, the rougher samples generated using the PE covariance function, i.e. Figures 4.14d to 4.14f, 4.14j to 4.14l and 4.14p to 4.14r, have sufficient variations that serve as effective imperfections for damage localization. In terms of the mean size of fragments that form, the corresponding phase fields are seen to be

far less sensitive to the spatial correlation length. However, as the correlation length increases, the orientation of the phase fields begins to acquire a structure that aligns with the axes of the domain. This observation is in accordance with the tensor-product structure of the covariance model, and with the fact that larger correlation lengths allow more pronounced spatial structures to develop (sample-wise) for PE functions.

Samples obtained with the two covariance models (parameterized by the same correlation lengths), considering the same realization for the underlying Gaussian field (from one covariance model to another), are compared in Figure 4.15 to study the effect of smoothness. It is seen that rougher material properties provide more candidate locations for damage localization, hence resulting in more fragments per unit volume of the domain (in a statistical sense). More precisely, the probability density functions (PDFs) corresponding to the dimensionless crack spacing (Figure 4.17), estimated using approximately 2000 fragments and 10 independent realizations of the fields, show a substantial difference: the mean fragment size obtained with rough material properties (here, with the PE model) turns out to be much smaller than the mean fragment size generated by smoother samples of fracture properties (associated with the PSE model).

4.4.2.3 Parametric Analysis

The stochastic model constructed in this paper enables the introduction of point-wise correlation (that is, in the first-order marginal probability distribution) between the two fracture properties. With regard to fracture mechanics, one might wonder, for example, whether or not the fracture toughness \mathcal{G}_c and the critical fracture energy ψ_c are correlated (at a given location), and if so, to what extent. In this section, we perform a parametric analysis for different values of the correlation coefficient ρ , with the aim of understanding which field plays a dominant role in determining the

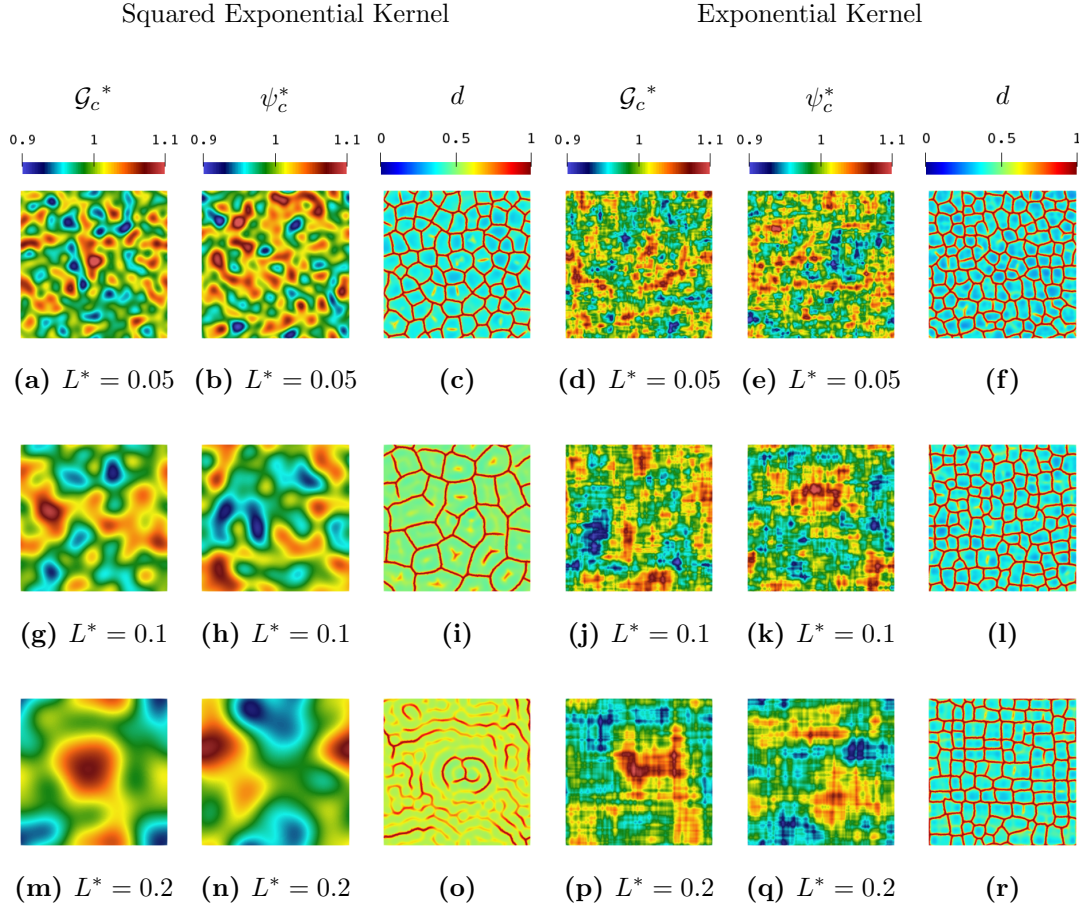


FIGURE 4.14. phase fields resulting from six pairs of realizations with different correlation models and normalized correlation lengths. The left three pairs (a-b, g-h, m-n) are realizations obtained with a PSE covariance function, while the right three pairs (d-e, j-k, p-q) are samples generated with a PE covariance function. Energy release rate \mathcal{G}_c and the critical fracture energy ψ_c have a coefficient of variation of 0.03, and normalized spatial correlation length L^* of (a-b, d-e) 0.05 (g-h, j-k) 0.1 (m-n, p-q) 0.2 The corresponding phase fields are shown in (c, f, i, l, o, r), respectively. In these results, independent realizations of the underlying Gaussian fields are used.

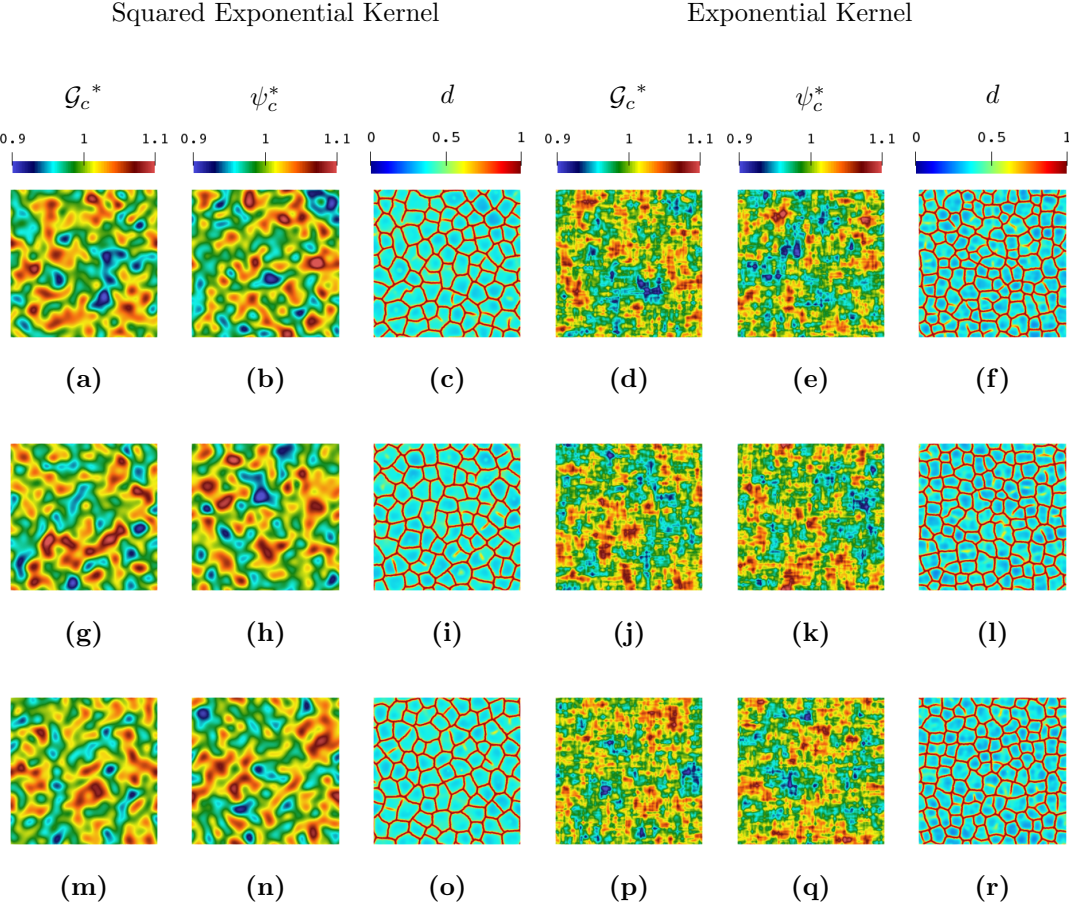


FIGURE 4.15. Three pairs of qualitative comparison of smoothness of the kernel function with the same normalized correlation length $L^* = 0.05$. (a-f) pair 1 (g-l) pair 2 (m-r) pair 3. Each row compares two kernel functions transformed from the same samples of the underlying Gaussian fields.

resulting fracture morphology in thin films.

In order to obtain meaningful statistical results, 10 independent realizations are considered, and the same samples (of the underlying Gaussian random fields) are used when ρ varies. The normalized correlation length is set to $L^* = 0.05$ for both fracture properties. Three pairs of fracture toughness and critical fracture energy samples, constructed using (4.27) and (4.28) with $\rho \in \{0, 0.5, 1\}$, are shown in Figure 4.18. Note that the special case of $\rho = 0$ recovers the case of independent material properties.

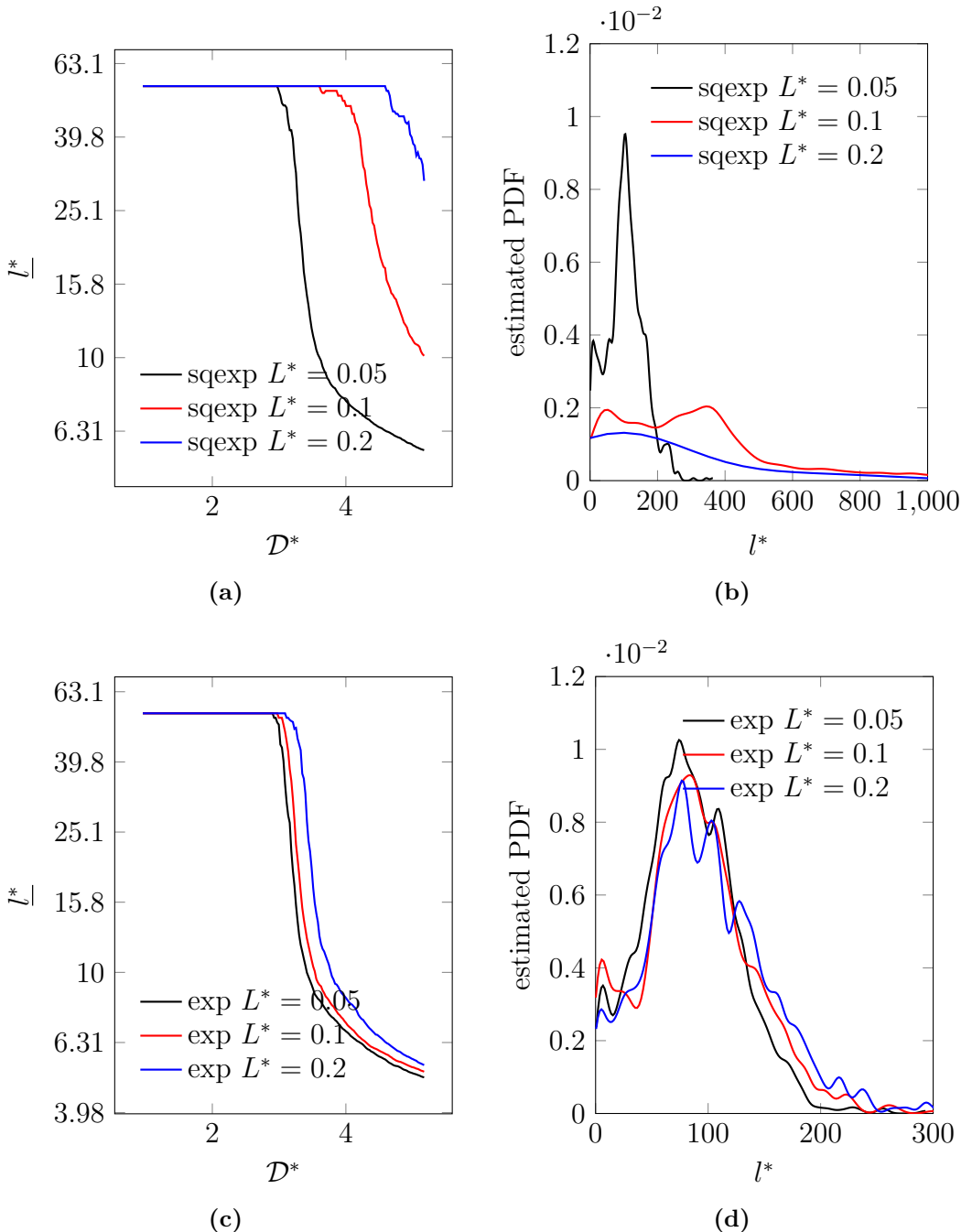


FIGURE 4.16. (a, c) Mean dimensionless crack spacing \bar{l}^* versus dimensionless crack driving force D^* (b, d) Estimated probability density of dimensionless crack spacing for different values of correlation length when $D^* = 5.17$ based on (a-b) a PSE kernel (c-d) a PE kernel

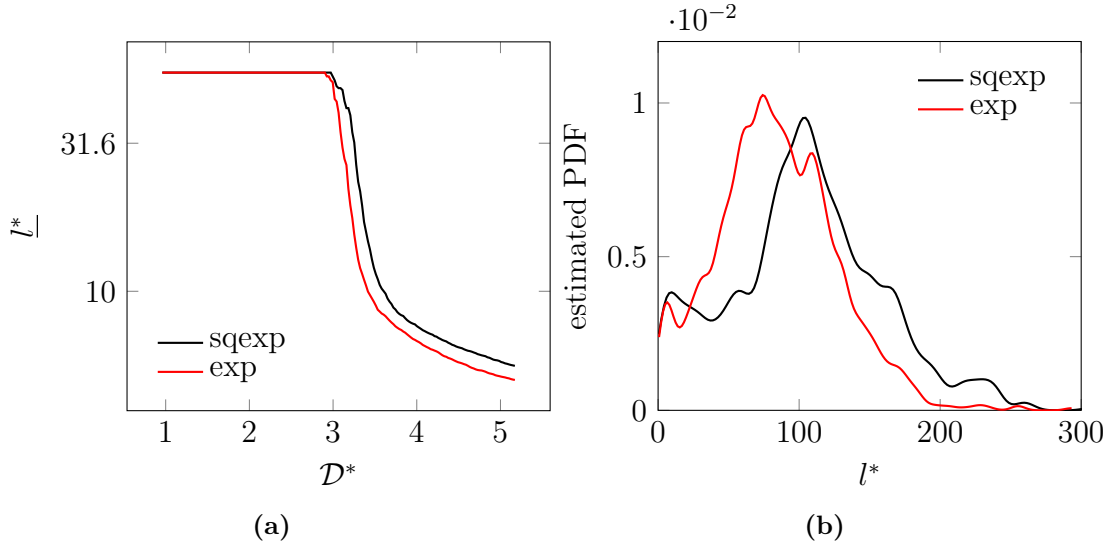


FIGURE 4.17. Comparisons of (a) mean dimensionless crack spacing \underline{l}^* versus dimensionless crack driving force D^* and (b) Estimated probability density of dimensionless crack spacing for different values of correlation length when $D^* = 5.17$ for results obtained using a PSE kernel and a PE kernel

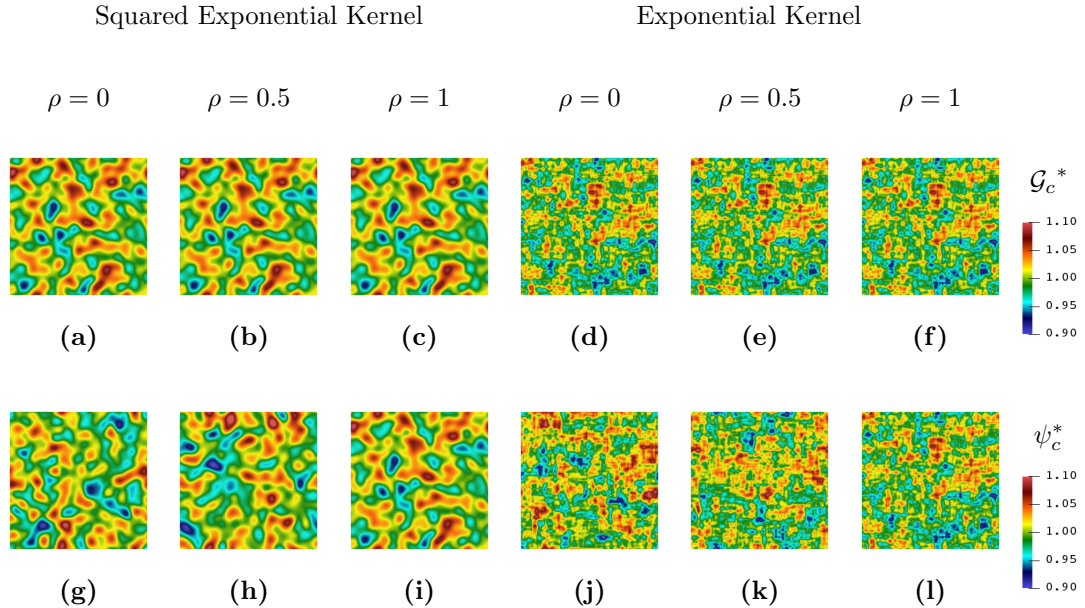


FIGURE 4.18. Point-wise correlated material properties: (a-f) normalized fracture toughness \mathcal{G}_c^* and (g-l) normalized critical fracture energy ψ_c^* with (left) PSE covariance function (right) PE covariance function

Statistics of the dimensionless crack spacing l^* are once again extracted at $\mathcal{D}^* = 5.17$. The resulting dimensionless curves and normalized probability density functions are shown in Figures 4.19 and 4.20. These results indicate that the distribution of fragment size is relatively insensitive to the coefficient of correlation, regardless of the smoothness of the covariance kernel.

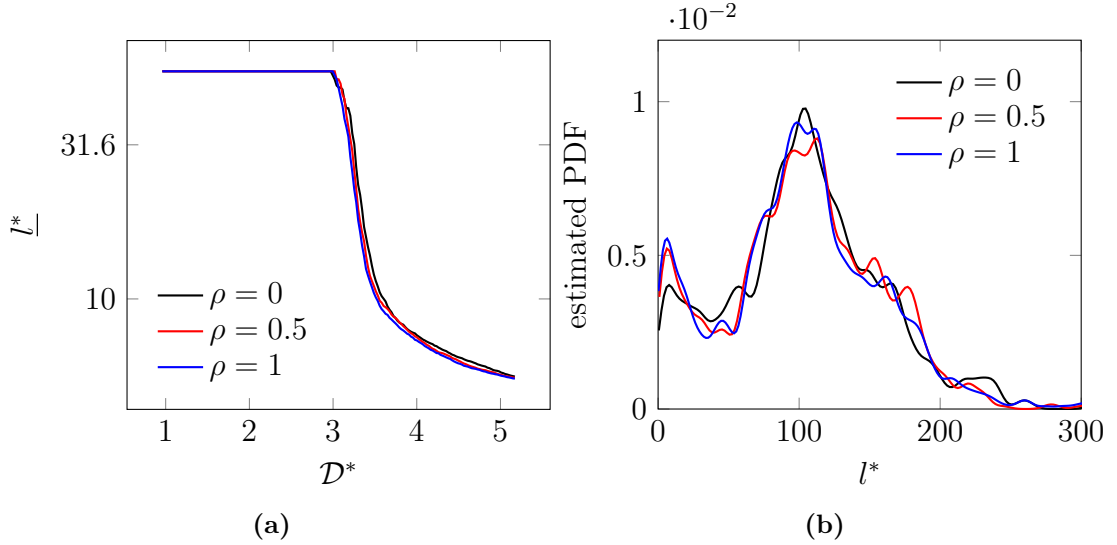


FIGURE 4.19. Comparisons of (a) mean dimensionless crack spacing as a function of dimensionless crack driving force and (b) estimated PDFs of dimensionless fragment size at loading $\mathcal{D}^* = 5.17$ for results with an underlying PSE kernel

In contrast, when we superimpose the fracture patterns, we observe that the fracture morphology does exhibit a sensitivity to variations in the fracture toughness (Figure 4.21a). The superimposed results are only shown for the PSE covariance function, but comparable results are obtained with the PE covariance function. By comparison, when the fracture toughness is held fixed while the critical fracture energy is varied, the superimposed fracture patterns are nearly indistinguishable (Figure 4.21b). The clear conclusion is that the energetics are primarily responsible for driving the fracture morphology, a result that is not surprising. This conclusion is also supported by the results shown in Figures 4.22 and 4.23, in which fracture pat-

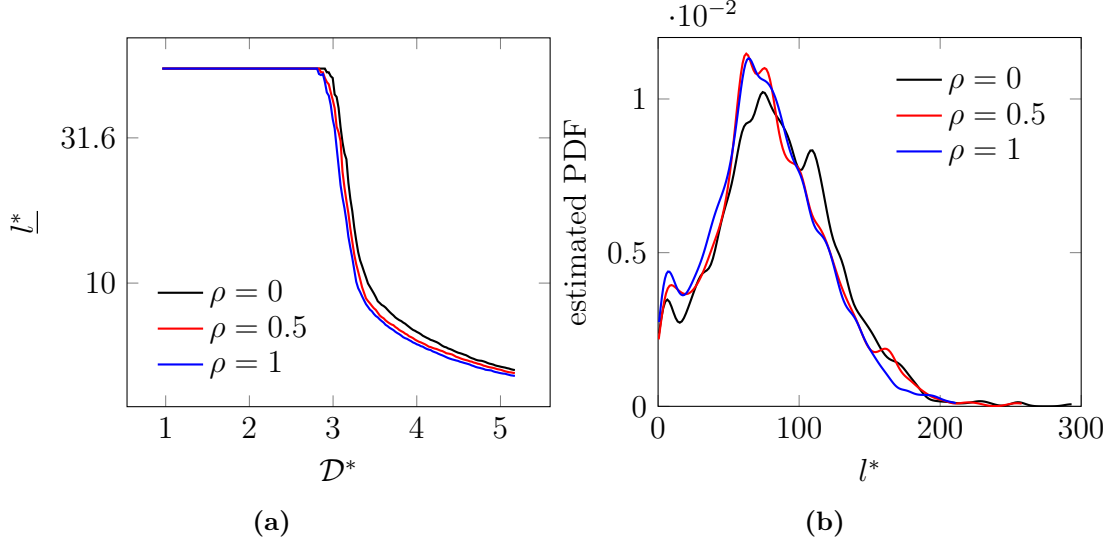


FIGURE 4.20. Comparisons of (a) mean dimensionless crack spacing and dimensionless crack driving force and (b) estimated PDFs of dimensionless fragment size at loading $D^* = 5.17$ for results with an underlying PE kernel

terns are plotted over contours of the fracture toughness and the critical energy. For both types of covariance functions, the fracture patterns are seen to follow contours of minimal fracture toughness while largely ignoring those of the critical fracture energy.

4.4.2.4 Discussion on Modeling Flexibility: Impact of the Covariance Structure

We now briefly examine how different structures of the covariance kernel can alter the fragment morphology. It has been demonstrated experimentally [91, 92, 93, 94, 95] how macro-scale processing conditions to construct samples may lead to morphologically different crack networks. For example, Kitsunezaki et al. [94] carried out a series of tests to study the effect of macroscopic disturbances on crack patterns. They poured calcium carbonate (CaCO_3) paste into a shallow circular container. Different modes of agitation were applied to the paste before it was dried, and the resulting crack patterns showed a strong correlation with the modes of agitation.

We hypothesize that the agitation gives rise to effective fracture properties at

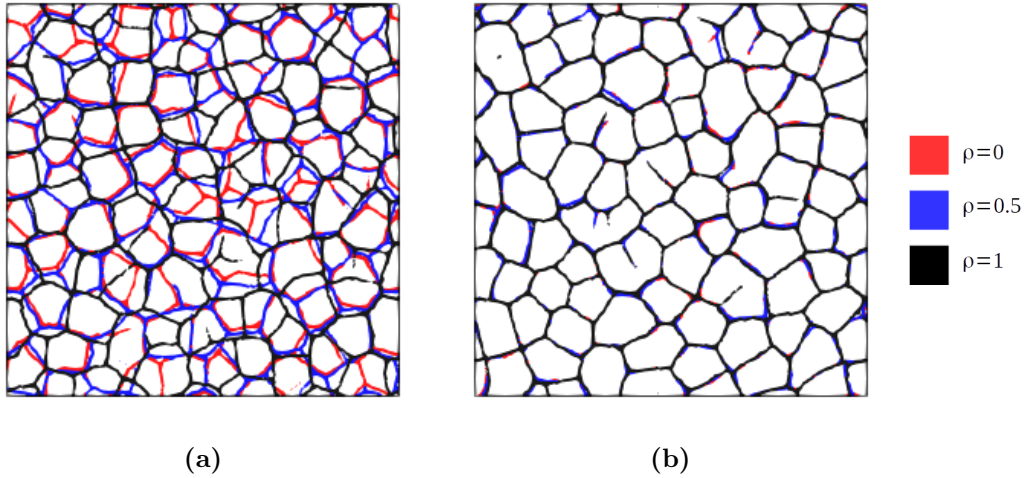


FIGURE 4.21. Superposition of fracture networks obtained by three samples of different coefficients of correlation, using the PSE kernel. Only the volume within the damage contour of $d = 0.9$ is shown to represent the resulting fracture network. Three samples are sampled (a) by holding \mathcal{G}_c constant and (b) by holding ψ_c constant.

the macro-scale that have a structure that is consistent with the agitation. We further assume a rougher spatial variation of properties in the direction parallel to the agitation than in the direction orthogonal to the agitation. Accordingly, we model the spatial variations in the fracture properties using composite covariance functions, defined on purpose by a tensor-product structure involving PSE and PE functions. In Figure 4.24, we compare the experimentally-observed crack patterns to our simulation results obtained using random fracture properties with the postulated anisotropic covariance functions. The comparison shows reasonable agreement (without specifically optimizing the hyperparameters in the stochastic model), indicating that the differing processing conditions may have resulted in different spatial variations in the effective fracture properties.

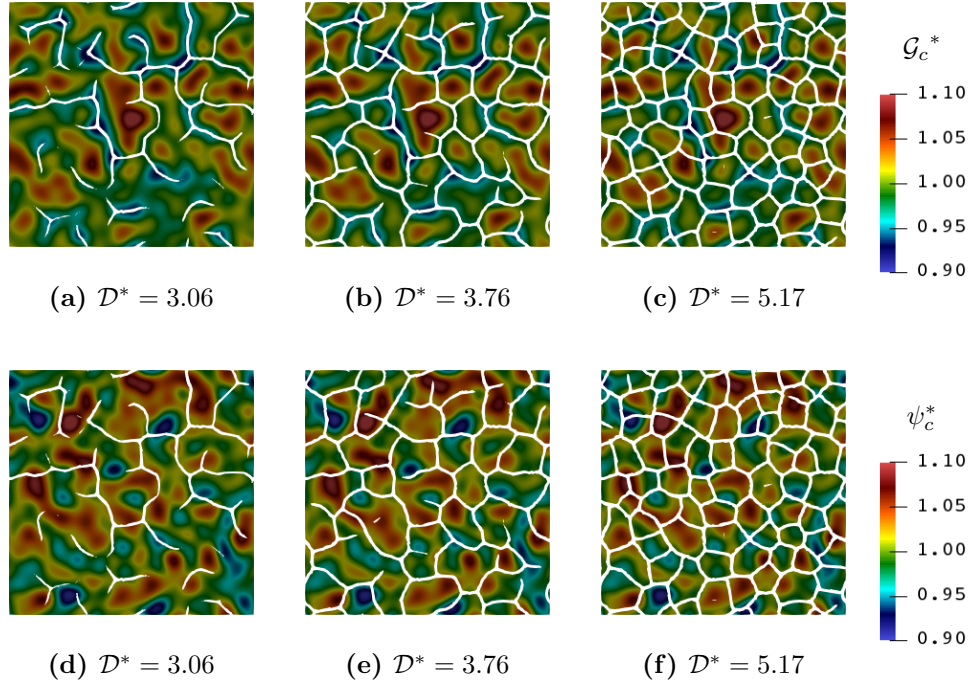


FIGURE 4.22. Snapshots of phase field at different loading levels with $d \geq 0.75$ plotted over (a-c) fracture toughness \mathcal{G}_c and (d-f) critical fracture energy ψ_c with an underlying PSE covariance function

4.4.3 Inverse Identification Based on Three-Dimensional Physical Experiments

In Rodriguez [1], a series of drying tests with mining waste placed on grooved circular plates (225 mm in diameter) was performed to observe crack evolution due to desiccation processes. Three tests were carried out with different film thicknesses $h \in \{4 \text{ mm}, 8 \text{ mm}, \text{ and } 16 \text{ mm}\}$.

To replicate this study using model-based simulations and our phase-field model (enhanced with the stochastic description of fracture properties), we adopt fully three-dimensional models. The material properties used for this study are listed in Table 4.2. Consistent with the experimental studies of [1], the film-substrate system is represented by a cylindrical domain. The substrate is modeled as a rigid body with an arbitrarily high fracture toughness. The substrate and film are discretized using tetrahedral elements with characteristic lengths of $h_0^e = 1.6 \text{ mm}$ and $h_1^e =$

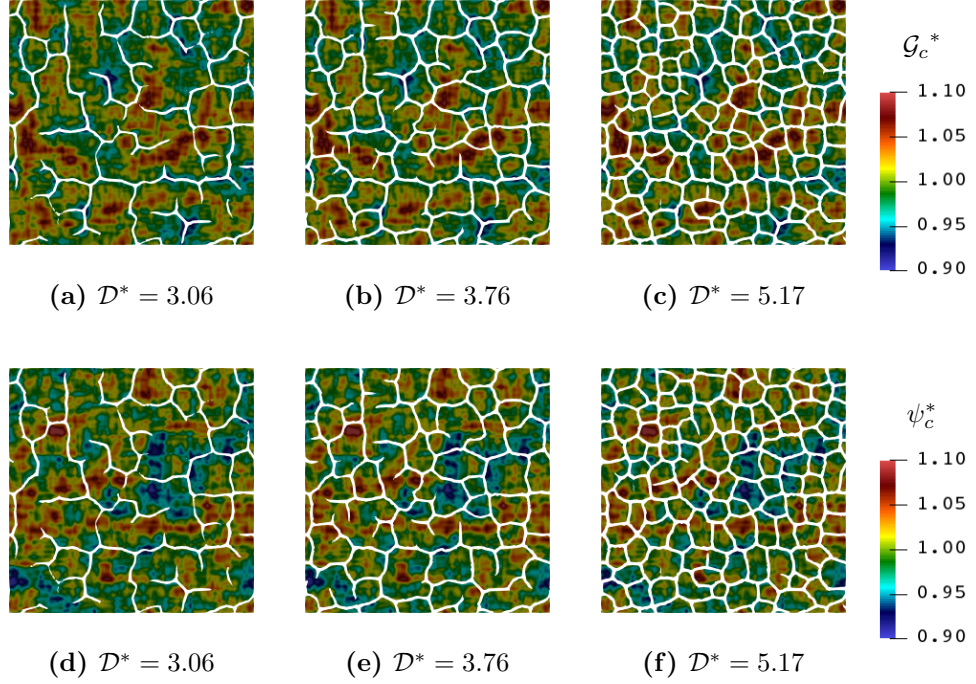


FIGURE 4.23. Snapshots of phase field at different loading levels with $d \geq 0.75$ plotted over (a-c) fracture toughness \mathcal{G}_c and (d-f) critical fracture energy ψ_c with an underlying PE covariance function

Table 4.2. Summary of material properties of mining waste and model parameters for all calculations in Section 4.4.3

Property/Parameter	Symbol	Value	Unit	Comment
Young's modulus	E	4	MPa	See [85]
Poisson's ratio	ν	0.2	nondim.	See [85]
Mean fracture toughness	$\underline{\mathcal{G}}_c$	27	kJ m^{-2}	See [113, 114]
Mean critical fracture energy	$\underline{\psi}_c$	30	J m^{-2}	See [113, 114]
Regularization length	l	0.8	mm	Such that $2l/h^e \approx 5$
Degradation shape parameter	p	1	nondim.	

0.36 mm, respectively. The solutions to the linear elasticity subproblem, the phase-field for fracture subproblem, and the generalized eigenvalue problem are once again approximated using the same mesh.

We first calibrate the spatial variability in our model against the experimental

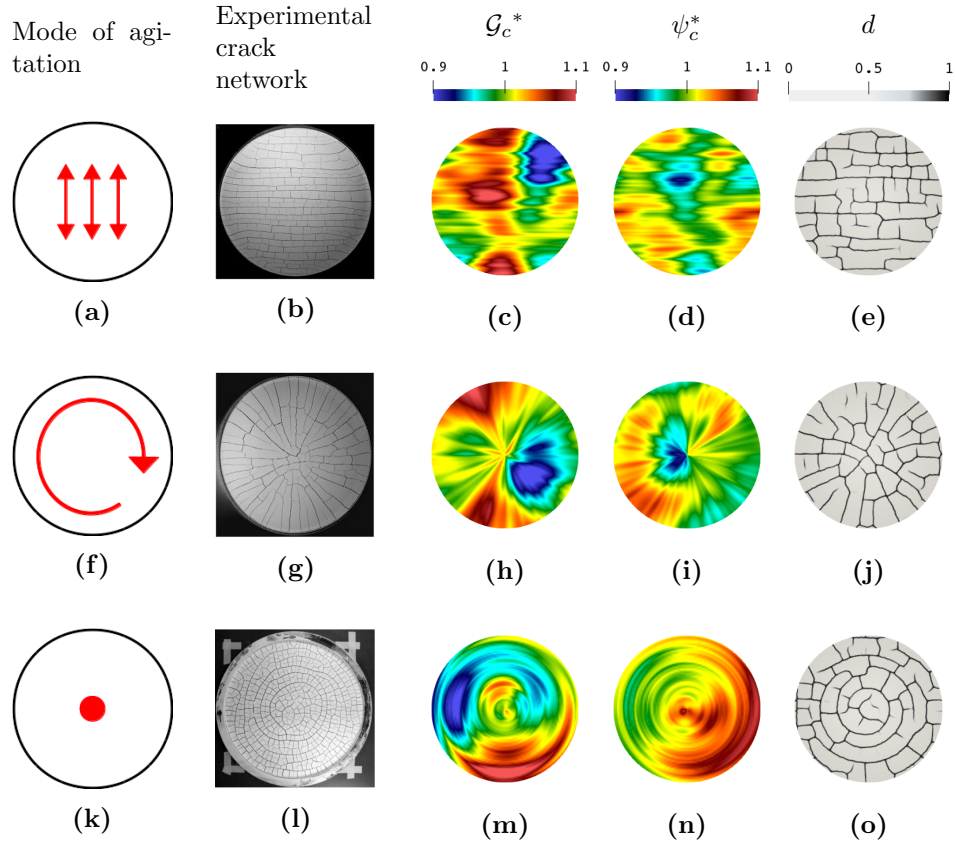


FIGURE 4.24. Three sets of experiments and calculations for (a-e) unilateral agitation (f-j) rotational agitation (k-o) point agitation. (b, g, l) snapshots of crack patterns from experiments. postulated spatially correlated (c, h, m) fracture toughness and (d, i, n) critical fracture energy to reproduce experimental observations. (e, j, o) phase fields obtained using corresponding spatially varying material properties.

observations of the fracture patterns for the thinnest ($h = 4\text{mm}$) specimen. To formulate the statistical inverse problem, we assume that (1) the fracture toughness and the critical fracture energy are uncorrelated (i.e., $\rho = 0$); and (2) both fracture properties have the same coefficient of variation (set to 0.03) and spatial correlation lengths, and that they can be defined using isotropic squared exponential kernels. In addition, the variations of the properties through the thickness of the film are assumed negligible compared to in-plane variations.

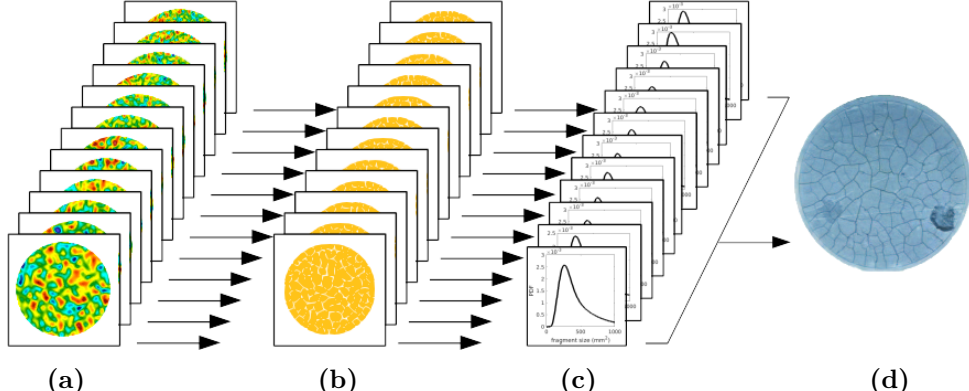


FIGURE 4.25. Procedures of finding the optimal hyperparameter to match the experiment: (a) 12 pairs of fracture properties are sampled to explore the space of admissible spatial correlation lengths; three dimensional energy minimization problems are solved to obtain (b) the resulting fracture morphology; (c) distributions of fragment sizes are extracted from the simulated results, and the log-likelihood values of these distributions at the samples extracted from (d) the experimental fracture morphology are computed.

Based on these assumptions, the spatial correlation length L is the only parameter to be determined, and a parametric search is performed in $\mathbb{L} = \{ 3 \text{ mm}, 3.5 \text{ mm}, 4 \text{ mm}, 4.5 \text{ mm}, 5 \text{ mm}, 5.5 \text{ mm}, 6 \text{ mm}, 6.5 \text{ mm}, 7 \text{ mm}, 7.5 \text{ mm}, 8 \text{ mm}, 8.5 \text{ mm} \}$. Energy minimization problems for the case of $h = 4 \text{ mm}$ are simulated for each pair of realizations and the corresponding fracture patterns are obtained. For a given value of $L \in \mathbb{L}$, the flooding algorithm is used to identify fragments on the top surface of the thin film, and a kernel density estimation of the probability density function associated with the fragment size, denoted by $f_{\text{fs}}^{\text{sim}}(\cdot; L)$, is obtained. The optimal value of L is then identified by maximizing the log-likelihood function \mathcal{L} defined as

$$\mathcal{L}(L) = \sum_{A_{\text{fs}}^{\text{exp}} \in \mathbb{A}^{\text{exp}}} \ln f_{\text{fs}}^{\text{sim}}(l^*(A_{\text{fs}}^{\text{exp}}); L) , \quad l^*(A) = \frac{\sqrt{A}}{h} , \quad (4.66)$$

where \mathbb{A}^{exp} denotes the collection of fragment size samples extracted by using the same flooding algorithm on the experimental result. The aforementioned workflow to calibrate the model is summarized in Figure 4.25. The fracture properties with spatial correlation $L = 4 \text{ mm}$ lead to the maximum log-likelihood among the span of

samples considered. Figure 4.26 compares the estimated PDF and the fracture morphology obtained using the calibrated stochastic model to those of the experimental specimen for $h = 4$ mm.

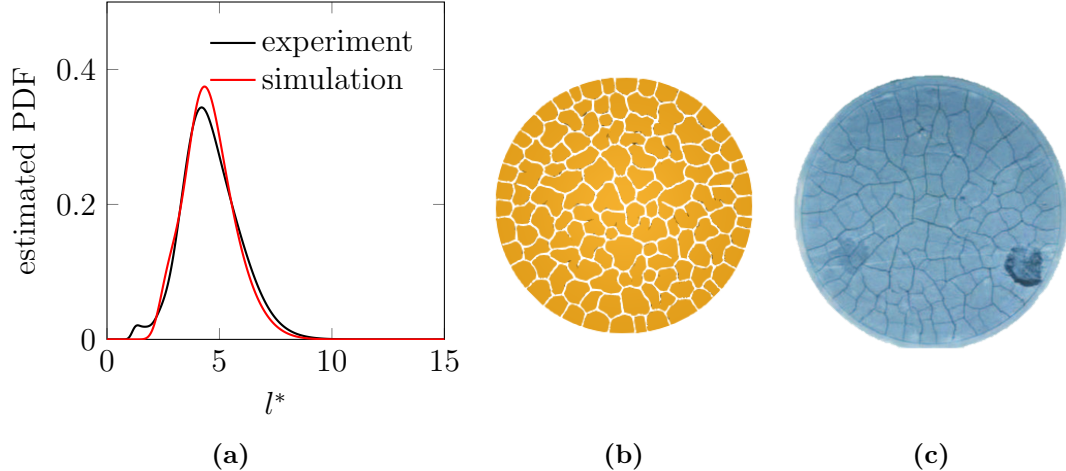


FIGURE 4.26. (a) Estimated PDFs of the dimensionless fragment sizes extracted from the experimental result and the calibrated stochastic model. (b) Fracture morphology obtained using the calibrated fracture properties. (c) Photograph of cracks in the mining waste.

To then benchmark our model against specimens with different thicknesses, three 3D calculations are carried out using the same realization of fracture properties with $L = 4$ mm. As shown in Figure 4.27, our results appear to agree reasonably well with the experimental observations. In general, the thicker films fracture into larger fragments, which also agrees with the simplified models presented in Sections 4.4.1 and 4.4.2.

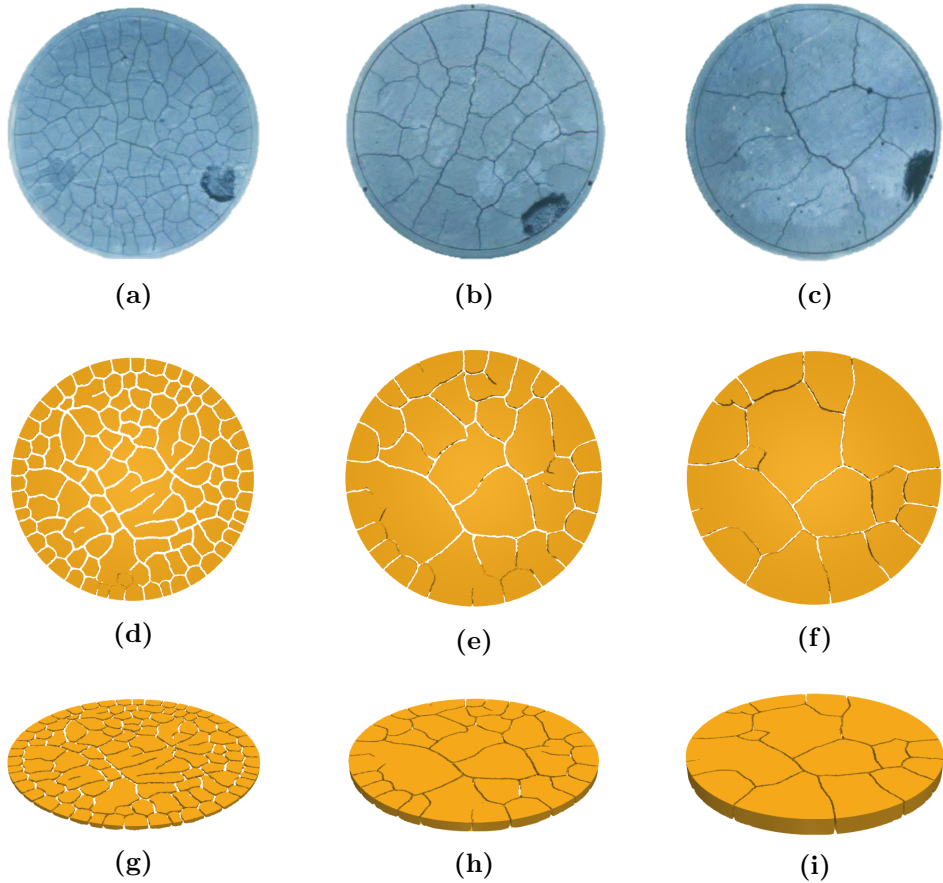


FIGURE 4.27. Qualitative comparison between the experiments and the simulations: (a-c) Photographs (modified from [1]) of cracks in mining waste due to desiccation at steady state for three test specimens with thickness (a) 4 mm, (b) 8 mm, and (c) 16 mm. (d-f) Top view and (g-i) panoramic view of corresponding numerical simulation results with different film thickness. Volumes of material with $d \geq 0.75$ were removed to improve the visualization of the crack geometry.

5

Towards Ductile Fracture

5.1 Introduction

The thermodynamic framework employed by the phase-field approach provides a convenient extension to incorporate plasticity by incorporating a plastic energy. However, how to best design the form of that plastic energy and its coupling with a phase field that regularizes a fracture surface remains an open question. There exist many approaches to modeling plasticity in the context of phase-field fracture [115, 116, 117, 118, 119, 120, 121, 122]. For a recent review of the various approaches that have been proposed, see Alessi et al. [123]. In this chapter, we explore possible extensions to ductile fracture within the proposed variational framework of Chapter 2. The proposed framework is flexible in the sense that a wide range of plastic flow rules and hardening behavior can be cast in a variational setting, as illustrated in [124]. The consistent variational approach does impart certain restrictions, such as the degradation of the yield surface with the phase field implying a corresponding plastic contribution to crack growth. While other models that break the variational structure may be of utility to effectively capture certain responses, they are beyond

the scope of the current work.

By adopting such a variational framework to model ductile fracture, the remaining major modeling choices are the form of the local term in the fracture energy (the crack geometric function)¹, the plastic degradation function (the functional dependence of the plastic energy on the phase-field variable), and the power expenditure. In this chapter, we extend the results to the regime of ductile fracture and demonstrate that an unperturbed elastic-plastic response can be obtained in certain cases, i.e. the yield stress and the plastic hardening law remain unmodified prior to crack initiation even when the plastic energy is degraded as a function of the phase-field variable.

In the case of brittle and quasi-brittle fracture, several studies have demonstrated that a regularization-length independent critical fracture strength and softening response can be obtained by a family of rational degradation functions in combination with the appropriate choice of the crack geometric function [125, 15, 100]. These are referred to as Lorentz-type degradation functions hereinafter. In another work [126], we showed that this decoupling of critical fracture strength and regularization length is crucial in elastic-plastic materials to ensure the crack growth resistance is convergent with respect to the regularization. This independence or lack of sensitivity is important both in the study of the Γ -convergence of the model behavior and in engineering applications where the specimen used for calibration and the actual structure of interest span vastly different spatial scales. In this chapter, we extend the use of these degradation functions to the coupling of the plastic energy so that the model response converges as the phase-field regularization length diminishes.

Although the phase-field regularization length can be divorced from the set of material properties by choosing the Lorentz-type degradation functions, an upper bound still exists, stemming from either polyconvexity requirements or physical con-

¹ Also sometimes referred to as the *local fracture dissipation function* in the phase-field for fracture related literature, despite its energetic nature in the thermodynamic framework.

straints (see e.g. [15, 100] for detailed analysis). With regard to phase-field models for ductile fracture, various choices of the coupling between damage and plasticity can result in the need for surprisingly small regularization lengths. In particular, some models require the need for smaller regularization lengths as the transition from plastic localization to the onset of damage is delayed. There have been several attempts to address this issue. Ambati et al. [118, 119] scaled the plastic degradation function by a critical plastic strain to be calibrated. Miehe et al. [127] introduced barrier functions related to critical values of the state variables. Most recently, Borden et al. [121] devised a threshold for the plastic work contributions to crack initiation. Although these are all valid, thermodynamically consistent approaches to introduce an arbitrary delay to crack initiation, the hybrid nature of these formulations makes it difficult to fit them into a variational framework.

Coupling the phase field to the plasticity tends to promote cracks in regions of extensive plasticity, which is often the case observed experimentally, but the observed damage process resulting from the model can be far more gradual than expected. On the other hand, when the phase field is coupled only to the elastic strain energy, the damage process is more abrupt, but the predicted crack growth directions tend not to agree with observations in ductile alloys. In particular, they tend to propagate orthogonally to the maximum tensile stress as in brittle materials, rather than in response to intense plastic straining. Here, we have identified a plausible micro-mechanical argument to reconcile these problems, and used this to formulate a model that fractures in regions with large plastic deformation even without the strong coupling between plasticity and fracture. Motivated by findings from several recent attempts to homogenize the fracture toughness, in this work we decouple the plastic dissipation from fracture degradation and propose a novel coalescence dissipation to model the coupling between plasticity and fracture. Rodriguez et al. [128], Chowdhury et al. [129], and Vo et al. [130] found that ligament length, shape, and

orientation of defects at the micro-scale influence the Mode-I fracture toughness. We postulate that the presence of plastic flow (or dislocations at the micro-scale) alters those properties related to defects, and at the continuum level, some configurational energy has been dissipated prior to crack initiation, effectively reducing the fracture toughness. We note that the idea of degrading the fracture toughness is not necessarily new, as a similar approach was recently proposed by Yin and Kaliske [131]. Importantly, by virtue of considering the coalescence dissipation in a variational framework, we show that fracture occurs in regions with large plastic deformation even without the strong coupling between plasticity and fracture. An upshot is a significant reduction in the fracture driving energy and a corresponding relaxation of the upper bound for the regularization length.

This chapter is organized as follows. Section 5.2.1 presents the constitutive choices, including the large deformation strain energy density, plastic energy density, fracture energy density, the Fourier potential, and their corresponding dual kinetic potentials. Section 5.3.1 motivates the choices of the crack geometric function and the degradation function by examining a homogeneous problem in detail. Section 5.3.2 demonstrates the regularization-length-independent softening behavior as well as the effect of the coalescence dissipation term. Section 5.4.1 applies the proposed model to simulate a three-point bending problem, Section 5.4.2 presents simulation results for a recent Sandia Fracture Challenge problem, and Section 5.4.3 shows how a creep fracture model instantiated from the variational framework can be used to model spallation of oxide scales.

5.2 Theory

5.2.1 Constitutive choices

Following the variational framework (Chapter 2), the Helmholtz free energy density is decomposed as

$$\psi = \psi^e + (1 - \mathcal{Q})\psi^p + \psi^f, \quad (5.1)$$

where ψ^e , ψ^p and ψ^f are the strain energy density, plastic energy density, and fracture energy density, respectively. The strain energy density for large deformation and the plastic energy density, along with the flow rule constraints and their thermodynamic conjugates, are presented in the following sections. The same Allen-Cahn type fracture energy density (as per Chapters 3 and 4) is used in this chapter.

The Taylor-Quinney factor $\mathcal{Q} \in [0, 1]$ is introduced to split the flow stress into an equilibrium (energetic) part and a viscous (dissipative) part. The dual kinetic potential characterizing dissipation mechanisms is decomposed as

$$\Delta^* = \psi^{e*} + \mathcal{Q}\psi^{p*} + \psi^{f*}, \quad (5.2)$$

where ψ^{e*} , ψ^{p*} and ψ^{f*} are viscous dissipations of their energetic counterparts. Again, the same superscripts are used only for convenience notation-wise, they are not to be confused with Legendre transformation of the Helmholtz free energy density. The Fourier potential is also included to account for heat conduction.

5.2.1.1 Strain energy density and Newtonian viscosity

Two types of strain energy density functions are considered in this chapter: one for compressible Neo-Hookean materials, and the other for Hencky-type materials.

Following [121, 119], the strain energy is defined as

$$\psi^e = g^e \psi_{\langle A \rangle}^e + \psi_{\langle I \rangle}^e, \quad (5.3a)$$

$$\psi_{\langle A \rangle}^e = \mathbb{H}_1(J) \left\{ \frac{1}{2} K \left[\frac{1}{2} (J^2 - 1) - \ln(J) \right] \right\} + \frac{1}{2} G (\bar{\mathbf{C}} : \mathbf{C}^{p-1} - 3), \quad (5.3b)$$

$$\psi_{\langle I \rangle}^e = (1 - \mathbb{H}_1(J)) \left\{ \frac{1}{2} K \left[\frac{1}{2} (J^2 - 1) - \ln(J) \right] \right\}, \quad (5.3c)$$

where K is the bulk modulus, G is the shear modulus, $\mathbb{H}_a(x)$ is the Heaviside function with the jump located at $x = a$, $\mathbf{C} = \mathbf{F}^T \mathbf{F}$ is the right Cauchy-Green strain tensor, $\bar{\mathbf{C}} = J^{-2/3} \mathbf{C}$ is the volume-preserving part of the right Cauchy-Green strain tensor, $\mathbf{C}^p = \mathbf{F}^{pT} \mathbf{F}^p$ is the plastic counterpart of the right Cauchy-Green strain, and g^e is the elastic degradation function (to be defined). We note that the kinematic state variable \mathbf{F} enters the potential through \mathbf{C} and \mathbf{C}^p only, according to the principle of frame indifference. The strain energy is split into an active part (with the subscript $\langle A \rangle$) and an inactive part (with the subscript $\langle I \rangle$) such that fracture is associated with only volumetric expansion and deviatoric deformation. The corresponding force conjugate per (2.25) is given as

$$\mathbf{P}^{\text{eq}} = \psi_{,\mathbf{F}}^e = \boldsymbol{\tau} \mathbf{F}^{-T}, \quad (5.4a)$$

$$\boldsymbol{\tau} = g^e(d) \boldsymbol{\tau}_{\langle A \rangle} + \boldsymbol{\tau}_{\langle I \rangle}, \quad (5.4b)$$

$$\boldsymbol{\tau}_{\langle A \rangle} = \frac{1}{2} \mathbb{H}_1(J) K (J^2 - 1) \mathbf{I} + G \text{dev}(\mathbf{b}^e), \quad (5.4c)$$

$$\boldsymbol{\tau}_{\langle I \rangle} = \frac{1}{2} (1 - \mathbb{H}_1(J)) K (J^2 - 1) \mathbf{I}. \quad (5.4d)$$

Another suitable hyperelastic material based on a volumetric-deviatoric decomposition is given in [126] as

$$\psi^e = g^e \psi_{\langle A \rangle}^e + \psi_{\langle I \rangle}^e, \quad (5.5a)$$

$$\psi_{\langle A \rangle}^e = \frac{1}{2} K \langle \text{tr}(\boldsymbol{\varepsilon}^e) \rangle_+^2 + G \text{dev} \boldsymbol{\varepsilon}^e : \text{dev} \boldsymbol{\varepsilon}^e, \quad (5.5b)$$

$$\psi_{\langle I \rangle}^e = \frac{1}{2} K \langle \text{tr}(\boldsymbol{\varepsilon}^e) \rangle_-^2, \quad (5.5c)$$

where $\boldsymbol{\varepsilon}^e = \frac{1}{2} \ln(\mathbf{C}^e)$ is the logarithmic elastic strain (also referred to as Hencky strain) based on the elastic right Cauchy-Green strain. The corresponding force conjugate is given as

$$\mathbf{P}^{\text{eq}} = \mathbf{F}^{e-T} \mathbf{M} \mathbf{F}^{p-T}, \quad (5.6)$$

$$\mathbf{M} = g^e \mathbf{M}_{\langle A \rangle} + \mathbf{M}_{\langle I \rangle}, \quad (5.7)$$

$$\mathbf{M}_{\langle A \rangle} = K \langle \text{tr}(\boldsymbol{\varepsilon}^e) \rangle_+ \mathbf{I} + 2G \text{dev} \boldsymbol{\varepsilon}^e, \quad (5.8)$$

$$\mathbf{M}_{\langle I \rangle} = K \langle \text{tr}(\boldsymbol{\varepsilon}^e) \rangle_- \mathbf{I}. \quad (5.9)$$

The dual kinetic potential ψ^{e*} is defined as

$$\psi^{e*} = g^e J \left[\frac{1}{2} \zeta \text{tr}(\mathbf{d})^2 + \eta \mathbf{d} : \mathbf{d} \right], \quad (5.10a)$$

$$\mathbf{d} = \text{sym} \left(\dot{\mathbf{F}} \mathbf{F}^{-1} \right), \quad (5.10b)$$

where ζ and η are damping coefficients for volume change and isochoric spin, respectively. Its thermodynamic conjugate can be written as

$$\mathbf{P}^{\text{vis}} = g^e J \boldsymbol{\sigma}^{\text{vis}} \mathbf{F}^{-T}, \quad (5.11a)$$

$$\boldsymbol{\sigma}^{\text{vis}} = \zeta \text{tr}(\mathbf{d}) \mathbf{I} + 2\eta \mathbf{d}. \quad (5.11b)$$

5.2.1.2 Flow rule constraints and the yield surface

The flow rule for J_2 -plasticity is defined as

$$\text{tr} \left(\dot{\mathbf{F}}^p \mathbf{F}^{p-1} \right) = 0, \quad (5.12a)$$

$$\left\| \dot{\mathbf{F}}^p \mathbf{F}^{p-1} \right\|^2 - \frac{3}{2} |\dot{\bar{\varepsilon}}^p|^2 = 0, \quad (5.12b)$$

where (5.12a) enforces the isochoric nature of plastic flow, and (5.12b) normalizes the effective plastic strain to be uniaxial.

Following the variational framework, minimizing the objective jointly with respect to $\dot{\mathbf{F}}^p$ and $\dot{\bar{\varepsilon}}^p$, subject to the constraints (2.5), (5.12a) and (5.12b), is equivalent to

minimizing the Lagrangian (point-wise)

$$\begin{aligned}\mathcal{L}^p(\dot{\mathbf{F}}^p, \dot{\bar{\varepsilon}}^p, \phi^p, \lambda_1, \lambda_2) &= \mathbf{T} : \dot{\mathbf{F}}^p + Y\dot{\bar{\varepsilon}}^p + \phi^p\dot{\bar{\varepsilon}}^p + \lambda_1 \operatorname{tr} \left(\dot{\mathbf{F}}^p \mathbf{F}^{p-1} \right) \\ &\quad + \lambda_2 \left(\left\| \dot{\mathbf{F}}^p \mathbf{F}^{p-1} \right\|^2 - \frac{3}{2} |\dot{\bar{\varepsilon}}^p|^2 \right),\end{aligned}\quad (5.13)$$

where $\phi^p \leq 0$, λ_1 , and λ_2 are Lagrange multipliers. The minimizer satisfies the following conditions (for any variations in the admissible space):

$$\mathcal{L}_{,\dot{\mathbf{F}}^p}^p : \delta \dot{\mathbf{F}}^p = \mathbf{T} : \delta \dot{\mathbf{F}}^p + \lambda_1 \mathbf{F}^{p-T} : \delta \dot{\mathbf{F}}^p + 2\lambda_2 \dot{\mathbf{F}}^p \mathbf{F}^{p-1} \mathbf{F}^{p-T} : \delta \dot{\mathbf{F}}^p = 0, \quad (5.14a)$$

$$\mathcal{L}_{,\dot{\bar{\varepsilon}}^p}^p \delta \dot{\bar{\varepsilon}}^p = \psi_{,\dot{\bar{\varepsilon}}^p}^p(\dot{\bar{\varepsilon}}^p, d) \delta \dot{\bar{\varepsilon}}^p + \phi^p \delta \dot{\bar{\varepsilon}}^p - 3\lambda_2 |\dot{\bar{\varepsilon}}^p| \delta \dot{\bar{\varepsilon}}^p = 0, \quad (5.14b)$$

$$\mathcal{L}_{,\phi^p}^p \delta \phi^p = \dot{\bar{\varepsilon}}^p \delta \phi^p = 0, \quad (5.14c)$$

$$\mathcal{L}_{,\lambda_1}^p \delta \lambda_1 = \operatorname{tr} \left(\dot{\mathbf{F}}^p \mathbf{F}^{p-1} \right) \delta \lambda_1 = 0, \quad (5.14d)$$

$$\mathcal{L}_{,\lambda_2}^p \delta \lambda_2 = \left(\left\| \dot{\mathbf{F}}^p \mathbf{F}^{p-1} \right\|^2 - \frac{3}{2} |\dot{\bar{\varepsilon}}^p|^2 \right) \delta \lambda_2 = 0. \quad (5.14e)$$

Solving (5.14a), (5.14d), and (5.14e) gives λ_1 and λ_2 as

$$\lambda_1 = -\frac{1}{3} \operatorname{tr}(\mathbf{M}), \quad \lambda_2 = \frac{1}{2} \sqrt{\frac{2}{3}} \frac{\|\operatorname{dev}(\mathbf{M})\|}{|\dot{\bar{\varepsilon}}^p|}, \quad (5.15)$$

where $\mathbf{M} = -\mathbf{T} \mathbf{P}^T$ is the Mandel stress, and the standard Prandtl-Reuss flow rule is recovered:

$$\dot{\mathbf{F}}^p \mathbf{F}^{p-1} = \dot{\bar{\varepsilon}}^p \mathbf{N}^p, \quad \mathbf{N}^p = \sqrt{\frac{3}{2}} \frac{\operatorname{dev}(\mathbf{M})}{\|\operatorname{dev}(\mathbf{M})\|}. \quad (5.16)$$

Next, the plastic loading/unloading conditions follow from (5.14b) & (5.14c) with the substitution of λ_2 :

$$\phi^p \leq 0, \quad \dot{\bar{\varepsilon}}^p \geq 0, \quad \phi^p \dot{\bar{\varepsilon}}^p = 0, \quad (5.17)$$

where ϕ^p is referred to as the yield function or the yield surface, i.e.

$$\phi^p = \|\operatorname{dev}(\mathbf{M})\| - \sqrt{\frac{2}{3}} Y = \|\operatorname{dev}(\mathbf{M})\| - \sqrt{\frac{2}{3}} (Y^{\text{eq}} + Y^{\text{vis}}). \quad (5.18)$$

It is convenient to define $\bar{\sigma} = \|\text{dev}(\boldsymbol{M})\|$ as the effective stress for the following discussions.

5.2.1.3 Plastic energy density and its rate sensitivity

Three commonly used plastic energy density functions and their viscous counterparts are considered in this chapter. The first plastic energy density resembles a simple linear hardening law:

$$\psi^p = g^p \left(\sigma_y \bar{\varepsilon}^p + \frac{1}{2} H \bar{\varepsilon}^{p2} \right), \quad (5.19a)$$

$$\psi^{p*} = g^p (\sigma_y + H \bar{\varepsilon}^p) \dot{\bar{\varepsilon}}^p, \quad (5.19b)$$

$$Y^{\text{eq}} = g^p (1 - \mathcal{Q}) (\sigma_y + H \bar{\varepsilon}^p), \quad (5.19c)$$

$$Y^{\text{vis}} = g^p \mathcal{Q} (\sigma_y + H \bar{\varepsilon}^p), \quad (5.19d)$$

where $g^p = \hat{g}^p(d)$ is the plastic degradation function, σ_y is the yield stress, and H is the hardening modulus.

The second plastic energy density recovers the commonly used power-law hardening:

$$\psi^p = g^p \frac{n}{n+1} \sigma_y \epsilon_0 \left[\left(1 + \frac{\bar{\varepsilon}^p}{\epsilon_0} \right)^{(n+1)/n} - 1 \right], \quad (5.20a)$$

$$\psi^{p*} = g^p \sigma_y \left(1 + \frac{\bar{\varepsilon}^p}{\epsilon_0} \right)^{1/n} \dot{\bar{\varepsilon}}^p, \quad (5.20b)$$

$$Y^{\text{eq}} = g^p (1 - \mathcal{Q}) \sigma_y \left(1 + \frac{\bar{\varepsilon}^p}{\epsilon_0} \right)^{1/n}, \quad (5.20c)$$

$$Y^{\text{vis}} = g^p \mathcal{Q} \sigma_y \left(1 + \frac{\bar{\varepsilon}^p}{\epsilon_0} \right)^{1/n}, \quad (5.20d)$$

where n is the power-law exponent and ϵ_0 is the characteristic plastic strain.

The third type of plastic energy density incorporates thermal softening according

to the Arrhenius law:

$$\psi^p = g^p \sigma_y^T \bar{\varepsilon}^p, \quad \psi^{p*} = g^p \sigma_y^T \dot{\bar{\varepsilon}}^p, \quad \sigma_y^T = \frac{\sigma_0}{\exp\left(-\frac{Q}{RT}\right)}, \quad (5.21a)$$

$$Y^{\text{eq}} = g^p(1 - \mathcal{Q})\sigma_y^T, \quad Y^{\text{vis}} = g^p \mathcal{Q} \sigma_y^T, \quad (5.21b)$$

where σ_0 is the reference yield stress, Q is the activation energy, R is the ideal gas constant. Note that since in this case Y^{eq} depends on T , it leads to cooling due to thermal softening (2.30), i.e.

$$\delta_T = TY_T^{\text{eq}} \dot{\bar{\varepsilon}}^p = Tg^p(1 - \mathcal{Q})\sigma_{y,T}^T \dot{\bar{\varepsilon}}^p, \quad \sigma_{y,T}^T = \frac{-Q}{RT^2} \sigma_y^T. \quad (5.22)$$

Remark 6. Consider plastic dissipation in the thermodynamic process resulting from the temperature dependent plastic energy, the dissipation can be written as

$$\delta + \delta_T = g^p \mathcal{Q} \sigma_y^T \dot{\bar{\varepsilon}}^p - g^p(1 - \mathcal{Q}) \frac{Q}{RT} \sigma_y^T \dot{\bar{\varepsilon}}^p \geq 0. \quad (5.23)$$

Rearranging the above equation yields the lower bound on the Taylor-Quinney factor:

$$\mathcal{Q} \geq \frac{Q}{Q + RT}. \quad (5.24)$$

In many engineering applications, large activation energy $Q \gg RT$ mandates the use of a Taylor-Quinney factor of $\mathcal{Q} \approx 1$, and several consequences follow from the variational framework, e.g. the contribution from plastic deformation in the fracture driving energy is negligible, and a large portion of the plastic deformation results in heat generation.

In addition, rate sensitivity of the yield surface can be introduced through the

plastic dual kinetic potential

$$\psi^{p*} = g^p \frac{m}{m+1} \sigma_y \dot{\epsilon}_0 \left(\frac{\dot{\bar{\varepsilon}}^p}{\dot{\epsilon}_0} \right)^{(m+1)/m}, \quad (5.25a)$$

$$Y^{\text{vis}} = g^p Q \sigma_y \left(\frac{\dot{\bar{\varepsilon}}^p}{\dot{\epsilon}_0} \right)^{1/m}, \quad (5.25b)$$

where m is the rate exponent, $\dot{\epsilon}_0$ is the characteristic plastic strain rate.

5.2.1.4 Viscous regularization of fracture propagation and the coalescence dissipation

The fracture dual kinetic potential is defined as

$$\psi^{f*} = \frac{1}{2} v d \dot{d}^2 - (1 - \beta) \frac{\mathcal{G}_c}{c_0 l} \alpha_{,d} (1 - e^{-\bar{\varepsilon}^p / \epsilon_0}) \dot{d} + (1 - C) \frac{\mathcal{G}_c}{c_0 l} \alpha_{,d} \dot{d}, \quad (5.26a)$$

$$f^{\text{vis}} = v d \dot{d} + [(1 - C) - (1 - \beta) (1 - e^{-\bar{\varepsilon}^p / \epsilon_0})] \frac{\mathcal{G}_c}{c_0 l} \alpha_{,d}, \quad (5.26b)$$

where the first term in (5.26a) describes the viscous dissipation of crack propagation and v is the kinetic viscosity for crack propagation. The second term introduces a novel representation of the dissipation (hereinafter referred to as the *coalescence dissipation*) associated with the development of the fracture process zone in ductile materials, such as through the evolution of voids, defects and dislocations. It models an exponential decay in the effective fracture toughness as defects increase, with the parameter $0 < \beta \leq 1$ controlling the ratio between the final fracture toughness and the initial fracture toughness.

It is assumed that the fracture process can be decomposed into an energetic part and a dissipative part, i.e.

$$\psi^f = \frac{\mathcal{G}_c}{c_0 l} (C \alpha(d) + l^2 \nabla d \cdot \nabla d), \quad (5.27)$$

$$(5.28)$$

where C denotes the fraction of the fracture process that is energetic. The dissipative part is the third term in (5.26a).

Remark 7. Consider the more strict form of the dissipation inequality where each of the thermodynamic processes is dissipative. For the process related to the fracture dissipation, that is

$$f^{\text{vis}}\dot{d} \geq 0$$

$$v\dot{d}^2 + [(1 - C) - (1 - \beta)(1 - e^{-\bar{\varepsilon}^p/\varepsilon_0})] \frac{\mathcal{G}_c}{c_0 l} \alpha_{,d}\dot{d} \geq 0.$$

Since $\dot{d} \geq 0$ and $\alpha_{,d} \geq 0, \forall d \in [0, 1]$, the inequality requires $v > 0$ and $\beta - C \geq 0$. In principle, C can be chosen to calibrate the energetic and dissipative portions of the fracture potential in a specific model given sufficient experimental data, which would in turn set the lower bound for β .

5.2.1.5 Fourier potential and heat conduction

To account for isotropic heat conduction, the Fourier potential is defined as

$$\chi = \frac{1}{2}\kappa\mathbf{g} \cdot \mathbf{g}, \quad (5.29)$$

where κ is the isotropic heat conduction coefficient. Recall that $\mathbf{g} = -\nabla T/T$ is the normalized thermal gradient. The resulting conductive heat flux is defined as

$$\mathbf{h} = -\chi_{,\mathbf{g}} = \kappa\nabla T. \quad (5.30)$$

5.2.1.6 The governing equations

Following the variational framework, substituting (5.1), (5.2) and (5.29) into the problem statement (2.40), the governing equations can be obtained as

$$\rho_0\mathbf{a} = \nabla \cdot \mathbf{P}, \quad (5.31)$$

$$v\dot{d} = \nabla \cdot \boldsymbol{\xi} - f, \quad (5.32)$$

$$\rho_0 c_v \dot{T} = \rho_0 q - \nabla \cdot \mathbf{h} + \delta + \delta_T \quad (5.33)$$

supplemented by the constitutive relations including the stress-strain relations presented in Section 5.2.1.1, the yield surface and loading/unloading conditions presented in Sections 5.2.1.2 and 5.2.1.3, the modified fracture thermodynamic conjugates Section 5.2.1.4, and the conductive heat flux (5.30). Substituting all of them into the governing equations, the fracture evolution equation can be expanded as

$$v\dot{d} = \nabla \cdot \frac{2\mathcal{G}_c l}{c_0} \nabla d - \left(\frac{\widehat{\mathcal{G}}_c}{c_0 l} \alpha_{,d} + \psi^d \right), \quad (5.34)$$

$$\psi^d = \psi_{,d}^e + (1 - \mathcal{Q})\psi_{,d}^p, \quad (5.35)$$

$$\widehat{\mathcal{G}}_c = g^c \mathcal{G}_c, \quad g^c = 1 - (1 - \beta) (1 - e^{-\bar{\varepsilon}^p/\varepsilon_0}), \quad (5.36)$$

where ψ^d is referred to as the fracture driving energy density. The heat conduction equation can be expanded as

$$\rho_0 c_v \dot{T} = \rho_0 q + \nabla \cdot \kappa \nabla T + \delta + \delta_T, \quad (5.37)$$

$$\delta = \mathbf{P}^{\text{vis}} : \dot{\mathbf{F}} + Y^{\text{vis}} \dot{\varepsilon}^p + f^{\text{vis}} \dot{d}, \quad (5.38)$$

$$\delta_T = -g^p(1 - \mathcal{Q}) \frac{Q}{RT} \sigma_y^T \dot{\varepsilon}^p. \quad (5.39)$$

Note that δ_T is only present if thermal softening in the flow stress is incorporated following the Arrhenius law, e.g. (5.21a).

5.2.2 A power-law approximation to the yield surface

A common task in engineering applications is to account for the dependence of yield surface on the strain-rate. To that end, consistent viscoplasticity models and Perzyna viscoplasticity models are proposed. The consistent viscoplasticity model has been presented in Section 5.2.1.3 by incorporating a plastic dual kinetic potential. The Perzyna viscoplasticity models typically employ a relation between the effective plastic strain rate and the effective stress of the following general form:

$$\dot{\varepsilon}^p = \mathcal{P}(\bar{\sigma}). \quad (5.40)$$

A commonly used temperature dependent Perzyna viscoplasticity model is

$$\dot{\bar{\varepsilon}}^p = A \left(\frac{\bar{\sigma}}{\sigma_0} \right)^n \exp \left(-\frac{Q}{RT} \right). \quad (5.41)$$

It is particularly difficult, if not impossible, to introduce a functional whose variation in $\dot{\bar{\varepsilon}}^p$ leads to this widely used model. However, it is straight-forward to show that the a form similar to (5.41) is an *approximation* to the consistent plasticity model with Arrhenius-law temperature dependence (5.21a). Consider the following power-law relation between $\dot{\bar{\varepsilon}}^p$ and $\bar{\sigma}$,

$$\dot{\bar{\varepsilon}}^p = A \left(\frac{\bar{\sigma}}{\sigma_y} \right)^n, \quad (5.42)$$

where A is the reference strain rate and σ_y is the yield stress. It can be shown that (5.42) is equivalent to the following KKT conditions

$$\phi^p = \bar{\sigma} - \sigma_y \leqslant 0, \quad \dot{\bar{\varepsilon}}^p \geqslant 0, \quad \phi^p \dot{\bar{\varepsilon}}^p = 0, \quad (5.43)$$

as $n \rightarrow \infty$. To sketch that, first introduce the semidiscrete form of the effective stress: Given the state at $t = t_1$, and the total deformation gradient at $t = t_2$, performing the point-wise plasticity update from t_1 to t_2 requires the following discretization of the effective stress (where the time discretization can be arbitrary):

$$\bar{\sigma} = \left\| \text{dev}(\widehat{\mathbf{M}}(\mathbf{F})) \right\| - \widehat{\mathbf{M}} \left(\int_{t_1}^{t_2} \dot{\bar{\varepsilon}}^p N^p \, dt \right) : \mathbf{N}^p, \quad (5.44)$$

where $\mathbf{M} = \widehat{\mathbf{M}}(\mathbf{F}^e)$ is the Mandel stress. Consider the following three cases:

- $\bar{\sigma} < \sigma_y$: it is immediate that $\lim_{n \rightarrow \infty} \dot{\bar{\varepsilon}}^p = 0$ assuming the relation (5.42);
- $\bar{\sigma} = \sigma_y$: $\dot{\bar{\varepsilon}}^p = A$ according to (5.42).

- Suppose $\bar{\sigma} > \sigma_y$, then $\dot{\bar{\varepsilon}}^p \rightarrow \infty$ as $n \rightarrow \infty$. Then, according to (5.44) (and recall the growth conditions on ψ^e), $\bar{\sigma} \rightarrow -\infty$, which contradicts with the assumption that $\bar{\sigma} > \sigma_y > 0$. Hence $\bar{\sigma} \leq \sigma_y$.

Summarizing the aforementioned cases recovers the KKT conditions (5.43) as $n \rightarrow \infty$. Next, substitute the flow stress with Arrhenius-law temperature dependence into (5.42), we arrive at the following Perzyna model:

$$\dot{\bar{\varepsilon}}^p = A \left(\frac{\bar{\sigma}}{g^p \sigma_0} \right)^n \exp \left(-\frac{nQ}{RT} \right). \quad (5.45)$$

Note that the only difference between (5.41) and (5.45) is in the numerator of the exponential term. Therefore, it only requires a straight-forward re-calibration to fit the existing materials with calibrated Perzyna models in the form of (5.41) into the current variational framework, knowing that the KKT conditions (5.43) are relaxed with a finite value of n .

5.2.3 Variational constitutive updates

In this section, we present the variational constitutive update using the Hencky-type elasticity model. A similar plasticity constitutive update for the compressible Neo-Hookean material can be found in [121].

Since \mathbf{F}^p and $\bar{\varepsilon}^p$ are local, i.e. confined to a material point, the variational constitutive updates can be performed point-wise considering the incremental form of the local energy density (2.38b): Given the state Λ_n at time t_n , the incremental local energy density can be expressed as

$$\begin{aligned} I_n(\Lambda_{n+1}, T_{n+1}; \Lambda_n, T_n) &= \psi^e(\boldsymbol{\varepsilon}_{n+1}^e, d_{n+1}) + \psi^p(\bar{\varepsilon}_{n+1}^p, d_{n+1}, T_{n+1}) \\ &\quad - (\psi^e(\boldsymbol{\varepsilon}_n^e, d_n) + \psi^p(\bar{\varepsilon}_n^p, d_n, T_n)) \\ &\quad + \Delta t \psi^{p*} \left(\frac{\Delta \bar{\varepsilon}^p}{\Delta t}, T_{n+1}; d_n \right). \end{aligned} \quad (5.46)$$

Note that only relevant terms are included. Using the exponential integration rule [132]

$$\mathbf{F}_{n+1}^p = \exp(\Delta\bar{\varepsilon}^p \mathbf{N}_{n+1}^p) \mathbf{F}_n^p, \quad (5.47)$$

the elastic deformation gradient can be written as

$$\mathbf{F}_{n+1}^e = \mathbf{F}^{e,\text{tr}} \exp(\Delta\bar{\varepsilon}^p \mathbf{N}_{n+1}^p), \quad \mathbf{F}^{e,\text{tr}} = \mathbf{F}_{n+1} \mathbf{F}_n^{p-1}, \quad (5.48)$$

where $\mathbf{F}^{e,\text{tr}}$ is the trial elastic deformation gradient assuming no plastic flow over the time step. Similarly, it can be shown that the elastic right Cauchy-Green strain can be defined as

$$\mathbf{C}_{n+1}^e = \mathbf{C}^{e,\text{tr}} \exp(-2\Delta\bar{\varepsilon}^p \mathbf{N}_{n+1}^p). \quad (5.49)$$

Then, the elastic Hencky strain can be written as

$$\boldsymbol{\varepsilon}_{n+1}^e = \boldsymbol{\varepsilon}^{e,\text{tr}} - \Delta\bar{\varepsilon}^p \mathbf{N}_{n+1}^p, \quad \boldsymbol{\varepsilon}^{e,\text{tr}} = \frac{1}{2} \ln(\mathbf{C}^{e,\text{tr}}), \quad (5.50)$$

and the trial conjugate stress can be derived as

$$\mathbf{M}^{\text{tr}} = \psi_{,\boldsymbol{\varepsilon}^{e,\text{tr}}}^e = \widehat{\mathbf{M}}(\boldsymbol{\varepsilon}^{e,\text{tr}}, d_{n+1}). \quad (5.51)$$

Next, minimizing the incremental local energy density subject the flow rule constraints (similar to the derivation in Section 5.2.1.2) yields

$$\begin{aligned} \phi^p(\Delta\bar{\varepsilon}^p) &= \mathbf{M}^{\text{tr}} : \mathbf{N}_{n+1}^p - \widehat{\mathbf{M}}(\Delta\bar{\varepsilon}^p \mathbf{N}_{n+1}^p) : \mathbf{N}_{n+1}^p \\ &\quad - Y^{\text{eq}}(\bar{\varepsilon}_n^p + \Delta\bar{\varepsilon}^p, d_{n+1}, T_{n+1}) - Y^{\text{vis}}\left(\frac{\Delta\bar{\varepsilon}^p}{\Delta t}; d_n\right), \end{aligned} \quad (5.52\text{a})$$

$$\mathbf{N}_{n+1}^p = \frac{3}{2} \frac{\text{dev}(\mathbf{M}^{\text{tr}})}{\bar{\sigma}^{\text{tr}}}, \quad \bar{\sigma}^{\text{tr}} = \sqrt{\frac{3}{2} \|\text{dev}(\mathbf{M}^{\text{tr}})\|}, \quad (5.52\text{b})$$

5.3 Verification

Unless otherwise stated, we choose $C = \beta$ for the modified fracture energy (5.27) and the fracture dual kinetic potential (5.26a) to satisfy the second law of thermodynamics. All other model parameters and material constants are provided separately for each of the problems in this section, below.

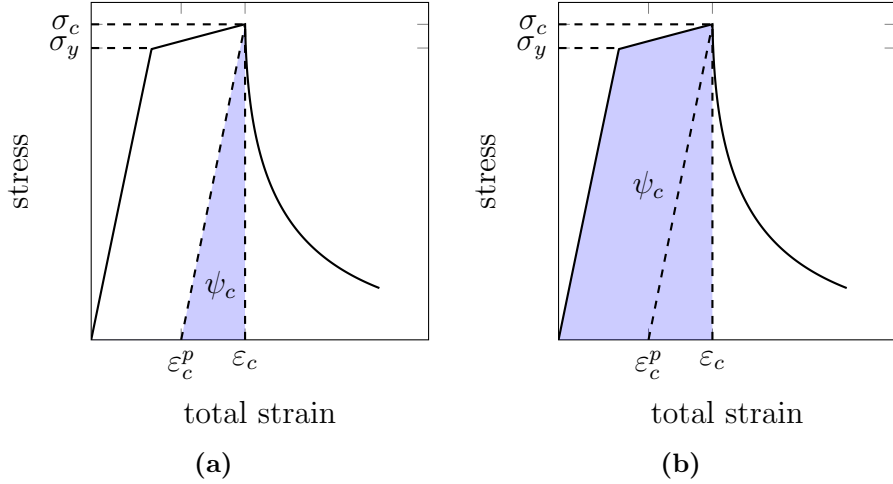


FIGURE 5.1. A prototypical stress-strain curve. The critical fracture energy ψ_c is represented by the shaded area. The compositions of the fracture driving energy are different for (a) an E-P-D model and (b) an E-P-PD model.

Prototypical stress-strain curves (Figure 5.1) obtained with the model presented in Section 5.2 serve to illustrate several terms that are used throughout this section. Following [117], the stress-strain response is categorized into E, P, D, and PD stages. First, during the *elastic* (E) loading stage, the stress increases with strain with a slope governed by the elastic moduli. Once the stress (in a measure defined by the plastic flow rule) reaches the yield stress σ_y , it enters the *plastic* (P) hardening stage, plastic flow occurs, and the plastic strain begins to accumulate. In this stage, the slope of the stress-strain curve is governed by the plastic flow rule and the plastic hardening law. Once the generalized fracture driving energy reaches the critical fracture energy ψ_c , a crack initiates and the stress-strain curve enters the softening stage. If the

plastic strain keeps increasing during the softening stage, it is referred to as *plastic-damaging* (PD), otherwise it is simply *damaging* (D). The stress, the total strain, and the equivalent plastic strain values attained just before the curve enters the softening stage are referred to as the critical fracture strength σ_c , the critical strain ε_c , and the critical plastic strain ε_c^p , respectively.

Although the variational framework allows the use of a variety of fracture models, here we focus on those obtained via particular choices for the crack geometric function α , the elastic degradation function g^e , and the plastic degradation function g^p . In particular, we propose a new model (hereinafter referred to as the E-P-D model) by selecting

$$\alpha = d, \quad g^e = g^{\text{Lorentz}}(d), \quad g^p = 1, \quad \beta \in (0, 1], \quad \varepsilon_0 > 0,$$

where plasticity and fracture are not strongly coupled, but the evolution of plastic deformation results in a “degraded” fracture toughness. For this E-P-D model, the corresponding generalized fracture driving energy consists of only the active strain energy $\psi_{\langle A \rangle}^e$, and the critical fracture energy ψ_c is pictorially depicted in Figure 5.1a.

In what follows, we will compare the behavior of the E-P-D model to an existing phase-field model for ductile fracture presented in [126]. The existing model, which we refer to as the E-P-PD model, is recovered by selecting

$$\alpha = d, \quad g^e = g^p = g^{\text{Lorentz}}(d), \quad \beta = 1.$$

These choices give rise to a model in which plasticity and fracture are strongly coupled, i.e. the yield surface is degraded by the phase field and the plastic energy contributes to fracture. For this E-P-PD model, the corresponding generalized fracture driving energy χ consists of both the active strain energy $\psi_{\langle A \rangle}^e$ and the plastic energy ψ^p . The corresponding critical fracture energy ψ_c is pictorially depicted in Figure 5.1b.

In this section, we demonstrate through numerical examples the motivations behind the various modeling choices. The naming of each model is explained Section 5.3.1.1 by investigating their characteristic loading and unloading behavior. Section 5.3.1.2 motivates the use of a linear crack geometric function, and Section 5.3.1.3 motivates the use of the Lorentz-type degradation functions. The effect of the coalescence dissipation in a homogenized setting is demonstrated in Section 5.3.1.4. Section 5.3.2 presents an example demonstrating that the nonhomogeneous model response is independent of the regularization length for different values of β .

5.3.1 A homogeneous example: uniaxial constitutive response

We begin by considering a problem in which the damage is spatially constant and so nonlocal features are effectively suppressed. This is effected by considering the response of a single element subjected to uniaxial tension. Examining this relatively simple system allows us to introduce the effect of different modeling choices.

For this study and the sake of comparison, the material parameters are largely taken in accordance with an analogous numerical example described in Borden et al. [121]. The domain is a one-element (HEX8) cube with side length a . The material and fracture parameters are: Young's modulus $E = 68.8$ GPa; Poisson's ratio $\nu = 0.33$; yield stress $\sigma_y = 320$ MPa; hardening modulus $H = 688$ MPa; fracture toughness $\mathcal{G}_c = 1.38 \times 10^5$ mJ mm $^{-2}$.

The single element is loaded in uniaxial tension with displacement control. Representative loading and unloading behaviors are illustrated using the E-P-D model and the E-P-PD model. In what follows, motivations for particular modeling choices of the crack geometric function α and the degradation functions g^e and g^p are provided.

5.3.1.1 Characteristic loading and unloading behavior

Consider $\beta = 1$, the proposed E-P-D model yields an E-P-D loading and unloading response (Figure 5.2a), and the E-P-PD model yields an E-P-PD loading and unloading response (Figure 5.2b).

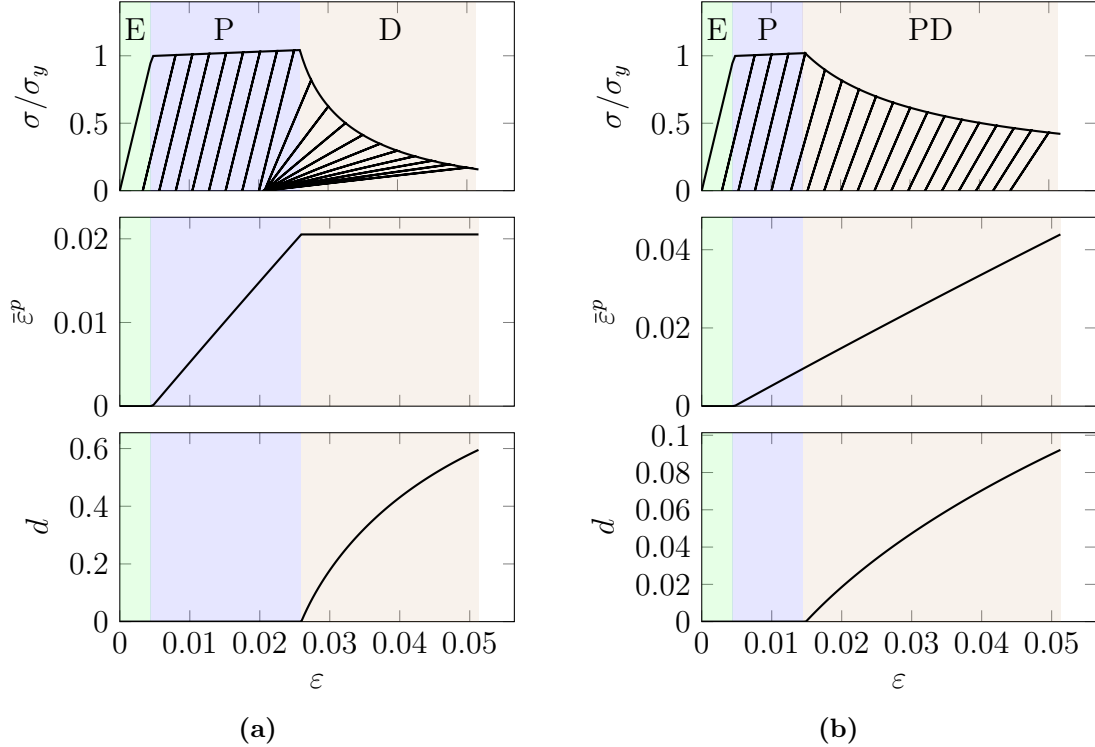


FIGURE 5.2. Characteristic loading and unloading curves of (a) the E-P-D model and (b) the E-P-PD model.

We note that if the critical fracture strength is chosen to be smaller than the yield stress, e.g. when the critical fracture energy is sufficiently small, the E-P-D response becomes an E-D response, and the E-P-PD response becomes an E-D-PD response, recovering the other two representative cases for the stress-strain response following Alessi et al. [117].

5.3.1.2 The crack geometric function

Next, two crack geometric functions, $\alpha = d^2$ and $\alpha = d$, are compared. The corresponding stress-strain curves are shown in Figure 5.3. In Figure 5.3a, we observe that the stress-strain response enters a damage softening stage *before* the stress reaches the yield stress. In essence, what happens is that a small amount of damage is accumulated during the elastic loading stage due to the nature of the specific crack geometric function $\alpha = d^2$. The yield surface is consequently shrunk according to (5.18), and a fair amount of plastic work contributes to the total fracture driving energy. As a result, the response enters the damage softening stage much earlier than expected.

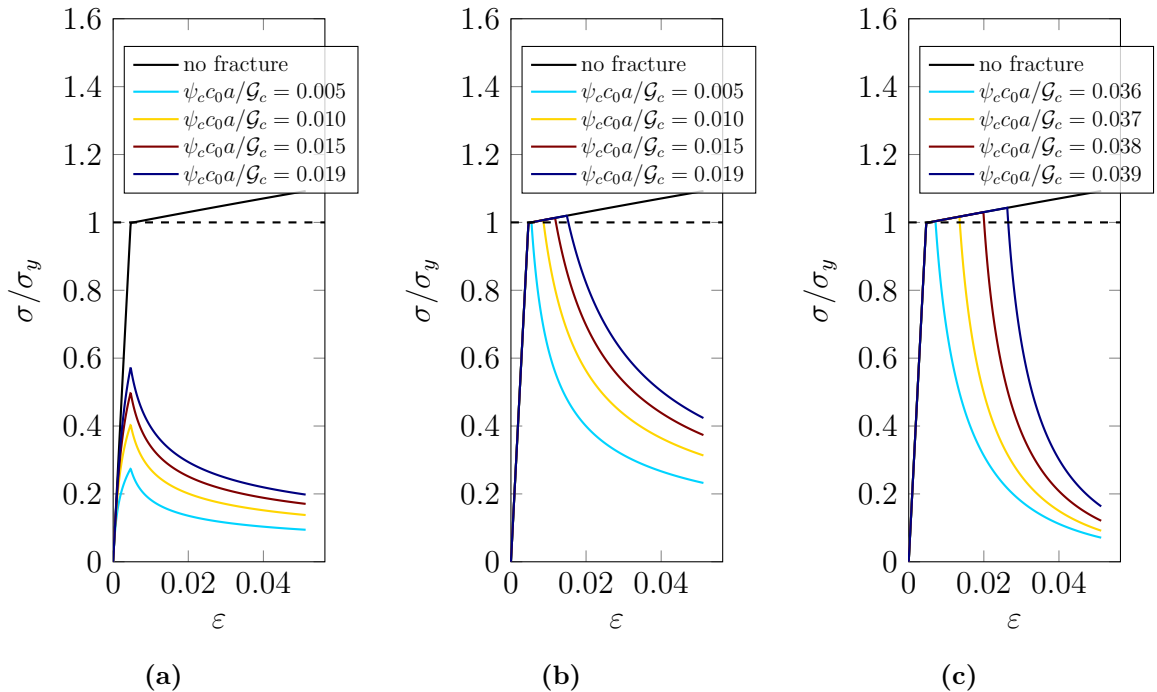


FIGURE 5.3. Stress-strain curves obtained with (a) the quadratic crack geometric function $\alpha = d^2$ and the Lorentz-type degradation function $g^e = g^p = g^{\text{Lorentz}}(d; m, p = 1)$, (b) the E-P-PD model with $\xi = 1$, and (c) the E-P-D model with $\xi = 1$.

By adopting a crack geometric potential with a linear term, e.g. $\xi > 0$, a finite

mobility is attained in the absence of damage, and an unperturbed elastic-plastic response can be recovered. The results shown correspond to the use of $\xi = 1$. The stress-strain curves for the E-P-PD model and the E-P-D model are shown in Figures 5.3b and 5.3c. Prior to crack initiation, the stress-strain curves with $\xi = 1$ align perfectly with the one where fracture is not considered. Such behavior is favorable in calibrations with experiments because it allows for decoupled hyperparameter tuning for plasticity and fracture: the elastic moduli, the yield stress, and the hardening parameters can be tuned without considering fracture. Accordingly, from this point forward we rely only on the use of a linear crack geometric function $\alpha(d; \xi = 1) = d$ for both the E-P-D model and the E-P-PD model.

5.3.1.3 The degradation functions

Next, we focus attention on the critical fracture strength σ_c . The Lorentz-type degradation is compared with the widely used quadratic degradation function $g^{\text{quad}} = (1 - d)^2$. As shown in Figure 5.4a, in conjunction with $\alpha = d$, the quadratic degradation function still relates the critical fracture energy (or equivalently the critical fracture strength) to the phase-field regularization length. As a result, as the regularization length is decreased, the stress at which the softening begins increases. By contrast, the use of a Lorentz-type degradation function removes this correlation between the critical fracture strength and the regularization length. As shown in Figures 5.4b and 5.4c, the use of a Lorentz-type degradation function thus gives rise to softening that begins at a stress that is insensitive to the regularization length, which confirms the observations of [126]. The influence of the regularization length is instead largely exhibited in the rate of decay in the stress during the softening portion of the response. Going forward, we therefore confine attention to models using only the Lorentz-type degradation functions.

We conclude this subsection by noting that while the observations regarding

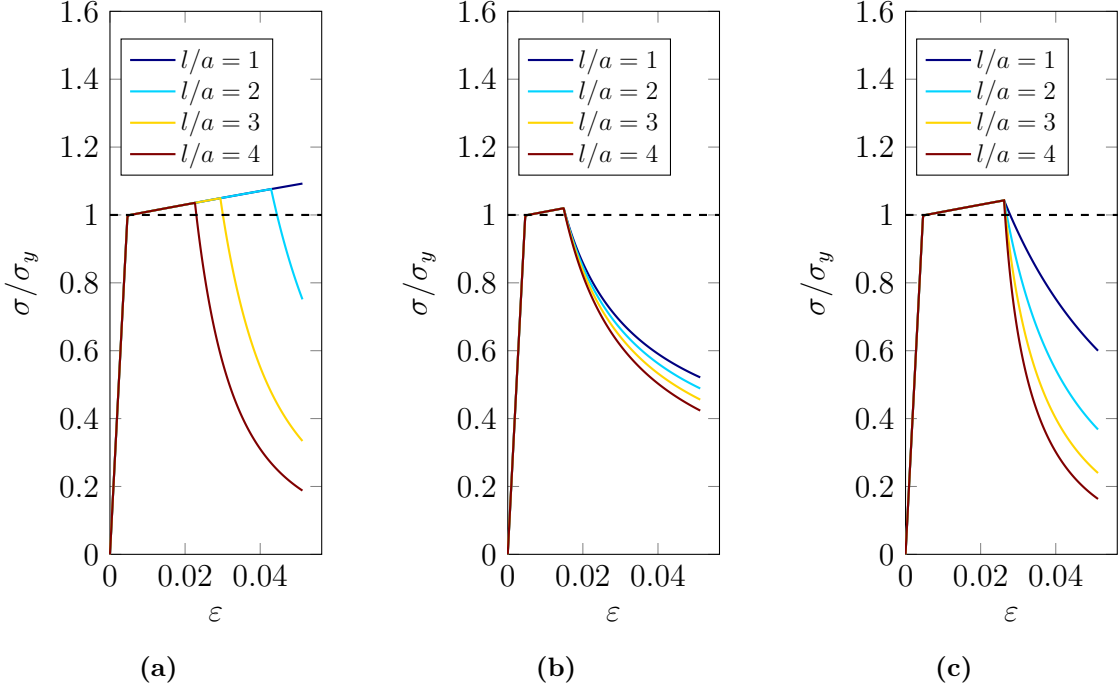


FIGURE 5.4. Stress-strain curves obtained with the linear crack geometric function $\alpha = d$ and (a) the quadratic degradation function (b-c) a Lorentz-type degradation function. Both (b) the E-P-PD model ($\psi_c c_0 a / G_c = 0.019$) and (c) the E-P-D model ($\psi_c c_0 a / G_c = 0.039$) show a regularization-length-independent critical fracture strength σ_c .

the critical fracture strength in this homogeneous setting can be generalized to a non-homogeneous setting, the softening response and its convergence have to be investigated separately in a non-homogeneous setting.

5.3.1.4 The coalescence dissipation

With clear justification for the modeling choices of the crack geometric function (Section 5.3.1.2) and the degradation functions (Section 5.3.1.3), we now examine the effect of the coalescence dissipation in this homogenized setting.

Without contributions from a fracture dual kinetic potential, i.e. when $C = \beta = 1$, the E-P-PD model and the E-P-D model have some shortcomings. First, the E-P-PD model introduces a strong coupling between plasticity and fracture, as both

the active part of the strain energy and the plastic energy contribute to damage evolution (according to (5.35), or see Figure 5.1b for a graphical illustration). As a result, the use of a large critical fracture energy ψ_c may be required to calibrate the E-P-PD model against experimental measurements. However, due to convexity concerns, the Lorentz-type degradation functions typically impose an upper-bound on the regularization length that scales inversely with the critical fracture energy:

$$l \leq l_u \propto \frac{1}{\psi_c}. \quad (5.53)$$

As a result, large values of ψ_c can give rise to a regularization length that is prohibitively small to resolve computationally.

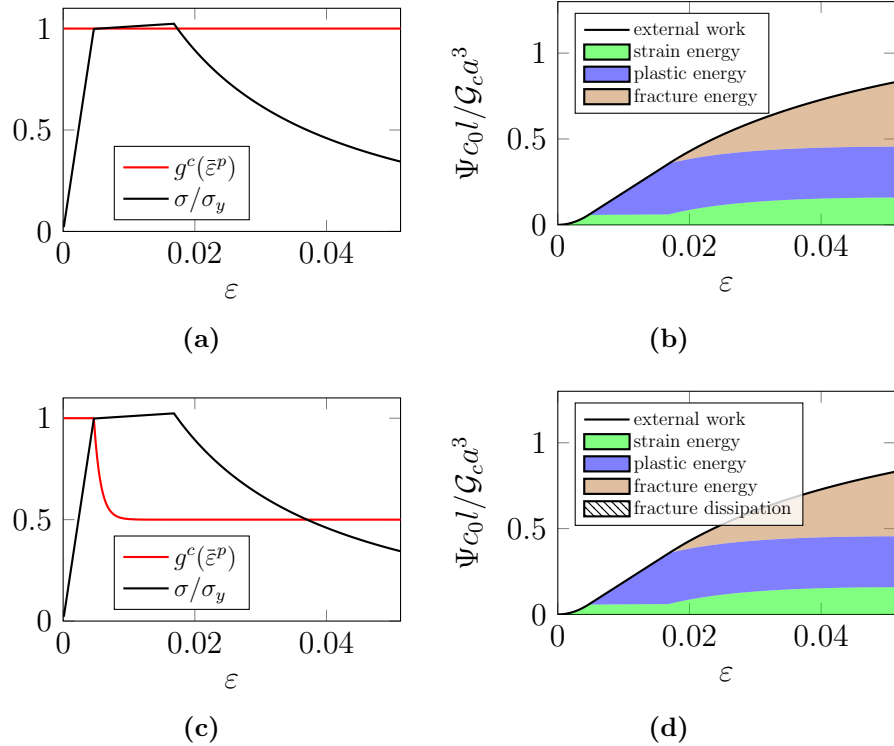


FIGURE 5.5. (a, c) the stress strain curve and the degradation for the fracture toughness and (b, d) the corresponding energy conservation. In (a-b), $C = \beta = 1$ and $\frac{\psi_c c_0 a}{\mathcal{G}_c} = 0.0021$. In (c-d), $C = \beta = 0.5$, $\varepsilon_0 = 0.001$, and $\frac{\psi_c c_0 a}{\mathcal{G}_c} = 0.0021$.

Second, the plastic energy contributes to the fracture driving energy in the E-P-PD model. Hence, by construction, the E-P-PD model results in fracture in regions with high plastic deformation, which agrees reasonably well with experimental observations. However, in many plasticity models, plastic flow occurs under both tension and compression. As a result the E-P-PD model can permit damage growth under compression. In contrast, with the E-P-D model, plastic energy does not contribute to the fracture driving energy. This both precludes crack growth in regions that are flowing plastically under compression and also tends to permit the use of larger regularization lengths compared to the E-P-PD model. The drawback is that, in tension, the E-P-D model tends to favor crack growth in regions with large elastic strains as opposed to large plastic strains.

In this work, the coalescence dissipation is proposed to address the aforementioned issues. According to (5.34), the coalescence dissipation introduces a dependency of the effective fracture toughness on the plastic strain. To demonstrate the influence, the stress-strain curve and the corresponding energy balance when $C = \beta = 1$ (i.e. no coalescence dissipation) are first shown in Figures 5.5a and 5.5b. Without any coalescence dissipation, there is no degradation of the fracture toughness. The sum of the strain energy, the plastic energy and the fracture energy equals the accumulated power expenditure due to external work.

Figures 5.5c and 5.5d show the stress strain curve and the corresponding energy balance when $C = \beta = 0.5$ and $\varepsilon_0 = 0.001 \ll \bar{\varepsilon}^p_c$. In this case, \mathcal{G}_c and ψ_c are scaled such that $\beta\mathcal{G}_c$ and $\beta\psi_c$ remains the same for comparison purposes. The degradation function $g^c(\bar{\varepsilon}^p)$ for the fracture toughness decreases as the plastic strain increases (Figure 5.5c), resulting in a final effective fracture toughness: $\lim_{\bar{\varepsilon}^p \rightarrow \infty} \hat{\mathcal{G}}_c = \beta\mathcal{G}_c$. The corresponding energy balance (Figure 5.5d) is virtually indistinguishable from the case *without* the fracture dual kinetic potential.

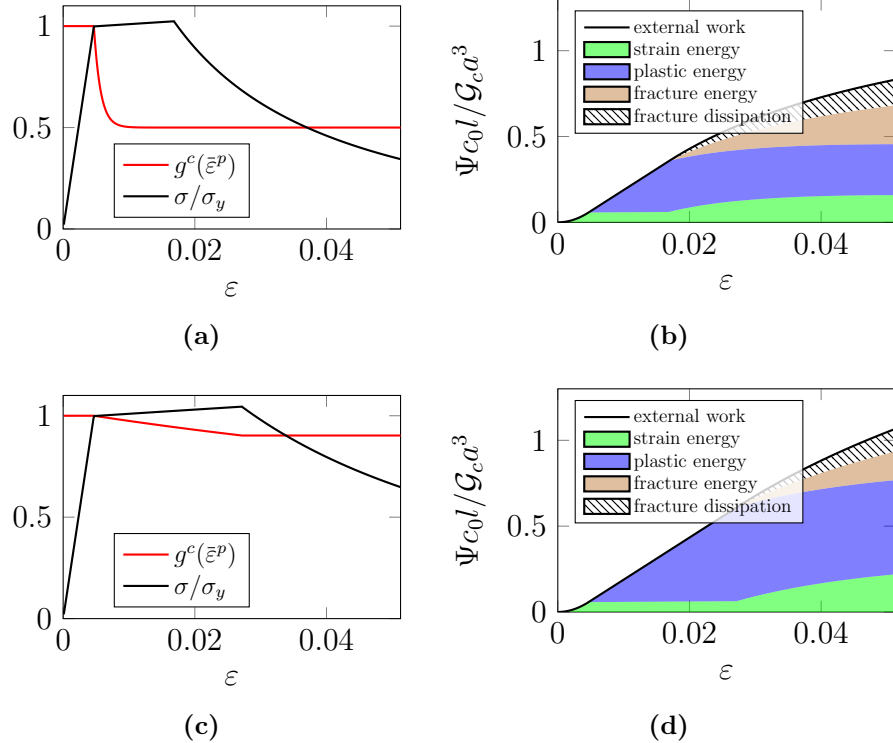


FIGURE 5.6. (a, c) the stress strain curve and the degradation for the fracture toughness and (b, d) the corresponding energy conservation. In (a-b), $C = 0.3$, $\beta = 0.5$, $\varepsilon_0 = 0.001$, and $\frac{\psi_c c_0 a}{\mathcal{G}_c} = 0.0021$. In (c-d), $C = \beta = 0.5$, $\varepsilon_0 = 0.1$ and $\frac{\psi_c c_0 a}{\mathcal{G}_c} = 0.0012$.

Remark 8. Recall from (5.26a) that the fracture dual kinetic potential consists of the coalescence dissipation as well as the dissipative portion of the fracture process:

$$\psi^{f^*} = \frac{1}{2}vd^2 - (1-\beta)\frac{\mathcal{G}_c}{c_0l}\alpha_{,d}\left(1-e^{-\bar{\varepsilon}^p/\varepsilon_0}\right)\dot{d} + (1-C)\frac{\mathcal{G}_c}{c_0l}\alpha_{,d}\dot{d}.$$

Before the onset of damage, i.e. $\dot{d} = 0$, the rate of the fracture dual kinetic potential is zero. After damage initiation, if $\bar{\varepsilon}_c^p \gg \varepsilon_0$, and hence $e^{-\bar{\varepsilon}_c^p/\varepsilon_0} \approx 0$, the fracture dual kinetic potential is approximately

$$\psi^f \approx (\beta - C) \frac{g_c}{c_0 l} \alpha_{,d}(d) d.$$

If $C = \beta$, the fracture dual kinetic potential density further reduces to

$$\psi^{f*} \approx 0,$$

and therefore the fracture dual kinetic potential shown in Figure 5.5d is negligible.

It follows immediately that a non-negligible amount of fracture dual kinetic potential will arise if $C < \beta$. In the other case, if the effective fracture toughness is not completely degraded by the plastic strain before damage initiation, i.e. $0 < e^{-\bar{\varepsilon}^p c / \varepsilon_0} < 1$ and $g^c(\bar{\varepsilon}^p c) > \beta$, it follows that

$$\begin{aligned}\psi^{f*} &= -(1 - \beta) \frac{\mathcal{G}_c}{c_0 l} \alpha_{,d}(d) (1 - e^{-\bar{\varepsilon}^p / \varepsilon_0}) \dot{d} + (1 - C) \frac{\mathcal{G}_c}{c_0 l} \alpha_{,d}(d) \dot{d} \\ &> -(1 - \beta) \frac{\mathcal{G}_c}{c_0 l} \alpha_{,d}(d) (1 - e^{-\bar{\varepsilon}^p / \varepsilon_0}) \dot{d} + (1 - \beta) \frac{\mathcal{G}_c}{c_0 l} \alpha_{,d}(d) \dot{d} \\ &= (1 - \beta) \frac{\mathcal{G}_c}{c_0 l} \alpha_{,d}(d) \dot{d} e^{-\bar{\varepsilon}^p / \varepsilon_0} > 0.\end{aligned}$$

Following the remark, in the case of $C = 0.3$ and $\beta = 0.5$, the fracture dual kinetic potential in the energy conservation is of the same order of magnitude as other contributions, and is indicated using dashed lines (Figure 5.6b). It bears emphasis that the presence of the fracture dual kinetic potential does not alter the stress-strain response in this homogeneous setting (Figure 5.6a). On the other hand, using a larger $\varepsilon_0 = 0.1$ (together with a smaller critical fracture energy) also results in a non-negligible fracture dual kinetic potential (Figure 5.6d).

5.3.2 A nonhomogeneous example: uniaxial load-displacement curves

In the homogenized example (Section 5.3.1), we have demonstrated that the use of a linear crack geometric function enables an unperturbed elastic-plastic behavior, and that the Lorentz-type degradation functions lead to a regularization-length-independent critical fracture strength. In this section, we demonstrate that as a consequence of these modeling choices the underlying softening response is also independent of the regularization-length. In particular, the force-displacement response

converges as the regularization-length is decreased.

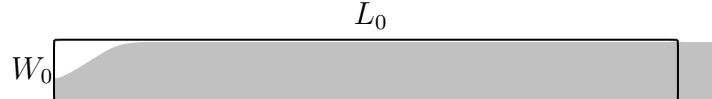


FIGURE 5.7. The geometry (black outline) and the final deformed configuration of the bar.

Consider a two-dimensional domain $\Omega = [0, L_0] \times [0, W_0]$ with $W_0/L_0 = 0.1$. The size of the bar is chosen such that no snap-back occurs in the force-displacement response for the values of regularization-length considered. The mesh is sufficiently refined such that the necking due to plastic flow is properly resolved. The domain is uniformly discretized with QUAD4 elements. Plane-strain conditions are assumed to hold.

With an estimate of the plastic zone size $r_p = E\mathcal{G}_c/(3\pi(1-\nu^2)\sigma_y^2)$, the dimensionless parameters are given as

$$\begin{aligned} \frac{W_0}{L_0} &= 0.1, & \frac{\sigma_y}{E} &= 0.00476, & \frac{H}{E} &= 0.02, \\ \frac{L_0}{r_p} &= 1.38, & \frac{\psi_c c_0 L_0}{\mathcal{G}_c} &= \begin{cases} 0.4, & \text{E-P-D} \\ 4, & \text{E-P-PD} \end{cases}. \end{aligned}$$

The critical fracture energy ψ_c is chosen to allow for plastic deformation prior to damage softening. A sequence of values of the phase-field regularization length are investigated to demonstrate convergence. The mesh is uniformly refined such that $l/h = 8$ remains constant and the phase-field bandwidth is always sufficiently resolved.

The bar is placed in tension through a prescribed horizontal displacement at the right end. Symmetry conditions are applied along the left and the bottom of the bar. To summarize, the boundary conditions on the displacement field are

$$u_x(x = 0) = 0, \quad u_x(x = L_0) = u_g, \quad u_y(y = 0) = 0.$$

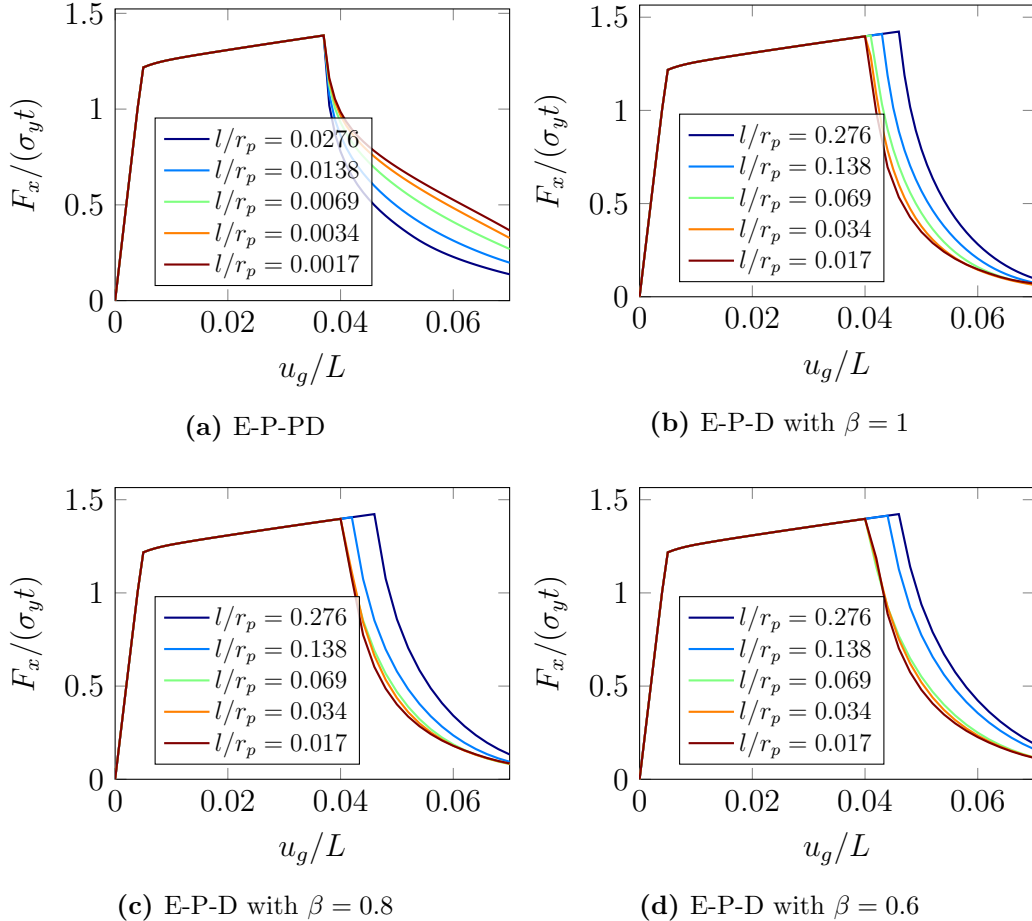


FIGURE 5.8. Normalized load-displacement curves obtained for (a) the E-P-PD model and (b-d) the E-P-D model with different values of β . Unit thickness is assumed.

The boundary conditions are illustrated in Figure 5.7 through the difference between the reference and final configurations. A numerical perturbation on the order of machine precision is introduced at $x = 0$ to ensure localization at the left end. The total reaction force F_x on the right edge is plotted as a function of the prescribed displacement u_g (Figure 5.8).

The convergence of the E-P-PD model and the E-P-D model are illustrated in Figures 5.8a and 5.8b. Two additional sets of load-displacement curves are generated for $\beta = 0.8$ and $\beta = 0.6$ in Figures 5.8c and 5.8d. Once the regularization length is

sufficiently small, the curves are virtually indistinguishable.

5.3.3 Crack growth resistance curves

In this section, we demonstrate that, with the appropriate modeling choices made in Section 5.3.1, crack growth resistance curves are insensitive to the phase-field regularization length. In order to compute the crack growth resistance and its sensitivity to the parameters of interest, a variation of the “surfing” problem devised by [133, 126] is used. The goal is to drive stable mode-I growth of a crack in a large (approximating infinite) domain. We fix a rectangular domain with width W_0 in the X_1 -direction and height H_0 in the X_2 -direction (see Figure 5.9). The adopted values

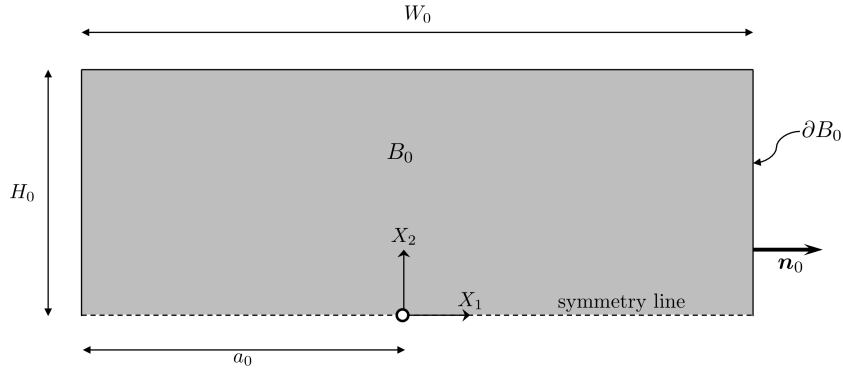


FIGURE 5.9. Schematic of domain for calculations. Actual dimensions are $W_0 = 150l$, $H_0 = 72l$, with pre-crack length $a_0 = 0.2W_0$. Symmetry boundary conditions are applied on the dashed line.

are

$$W_0/l = 150, \quad H_0/l = 72. \quad (5.54)$$

The origin is placed on the bottom edge, at a distance of a_0 from the left-hand side. The bottom edge is a symmetry plane, which is enforced with the boundary conditions

$$u_y = 0 \quad \text{on } X_1 > 0, X_2 = 0. \quad (5.55)$$

A pre-crack is represented with the boundary condition

$$d = 1 \quad \text{on } -a_0 \leq X_1 \leq 0, X_2 = 0, \quad (5.56)$$

thus a_0 represents the length of the pre-crack, which will be taken as

$$a_0 = 0.2W_0 \quad (5.57)$$

to keep the tip far from the boundary.

On the external boundary ∂B_0 (the left, top, and right edges in Figure 5.9), we drive crack growth by prescribing a displacement field that matches the asymptotic plane strain K_I field solution

$$\begin{Bmatrix} \bar{u}_x \\ \bar{u}_y \end{Bmatrix} = \frac{K_I(t)}{G} \sqrt{\frac{r(t)}{2\pi}} \begin{Bmatrix} \left[1 - 2\nu + \sin^2\left(\frac{\theta(t)}{2}\right) \right] \cos\left(\frac{\theta(t)}{2}\right) \\ \left[2 - 2\nu - \cos^2\left(\frac{\theta(t)}{2}\right) \right] \sin\left(\frac{\theta(t)}{2}\right) \end{Bmatrix}. \quad (5.58)$$

We apply the loading in two stages: in the first, for $0 \leq t \leq 1$, the origin of the K -field boundary condition is fixed at the coordinate system origin, where the crack tip sits, and the amplitude of $K_I(t)$ is ramped up linearly; in the second stage $t > 1$, the origin of the K -field boundary condition is translated at a constant velocity v , while the amplitude of $K_I(t)$ is held fixed, which drives stable crack propagation.

$$r(t) = \begin{cases} \sqrt{X_1^2 + X_2^2}, & t \leq 1, \\ \sqrt{(X_1 - v(t-1))^2 + X_2^2}, & t > 1, \end{cases} \quad (5.59)$$

$$\theta(t) = \begin{cases} \tan^{-1}\left(\frac{X_2}{X_1}\right), & t \leq 1, \\ \tan^{-1}\left(\frac{X_2}{X_1 - v(t-1)}\right), & t > 1. \end{cases} \quad (5.60)$$

$$K_I(t) = \begin{cases} t \sqrt{\frac{EG_0}{1-\nu^2}}, & t \leq 1, \\ K_I(t) = \sqrt{\frac{EG_0}{1-\nu^2}}, & t > 1. \end{cases} \quad (5.61)$$

To monitor the resistance as the crack propagates, the energy release rate \mathcal{G}_r is computed via the J -integral on the boundary [134]

$$J = \int_{\partial B_0} \mathbf{e} \cdot \boldsymbol{\Sigma} \mathbf{n} \, dA, \quad (5.62)$$

where \mathbf{e} is the unit vector in the direction of crack growth (in our case, the unit vector in the X_1 -direction), and \mathbf{n}_0 is the unit normal to the boundary. The symbol $\boldsymbol{\Sigma}$ stands for the energy-momentum tensor

$$\boldsymbol{\Sigma} \equiv \psi \mathbf{I} - \mathbf{H}^T \mathbf{P}, \quad \mathbf{H} \equiv \mathbf{F} - \mathbf{I}, \quad (5.63)$$

The system is always in equilibrium, so we assume $\mathcal{G}_r = J$, that is, that the resistance is always equal to the measured energy release rate.

To construct resistance curves, the other necessary output is the crack extension. The total crack length is computed as

$$a = \int_{B_0} \gamma_l \, dV, \quad (5.64)$$

which is consistent with the fracture energy density (5.27). The crack extension is given by $\Delta a = a - a_0$.

Using the E-P-D model with the following set of dimensionless parameters

$$\frac{\sigma_y}{E} = 0.005, \quad \frac{H}{E} = 0.5, \quad \nu = 0.3, \quad \frac{2E\psi_c}{\sigma_y^2} = 1, \quad (5.65)$$

the crack growth resistance curves with different values of l/r_p for are plotted in Figure 5.10, where $r_p \equiv \frac{1}{3\pi(1-\nu^2)\sigma_y^2} \frac{EG_c}{(1-\nu^2)\sigma_y^2}$ is the plastic zone size. The results suggest that the resistance curves are remarkably insensitive to l/r_p – the J-R curves for $l/r_p \leq 0.7$ are virtually indistinguishable. Similar results can be observed with

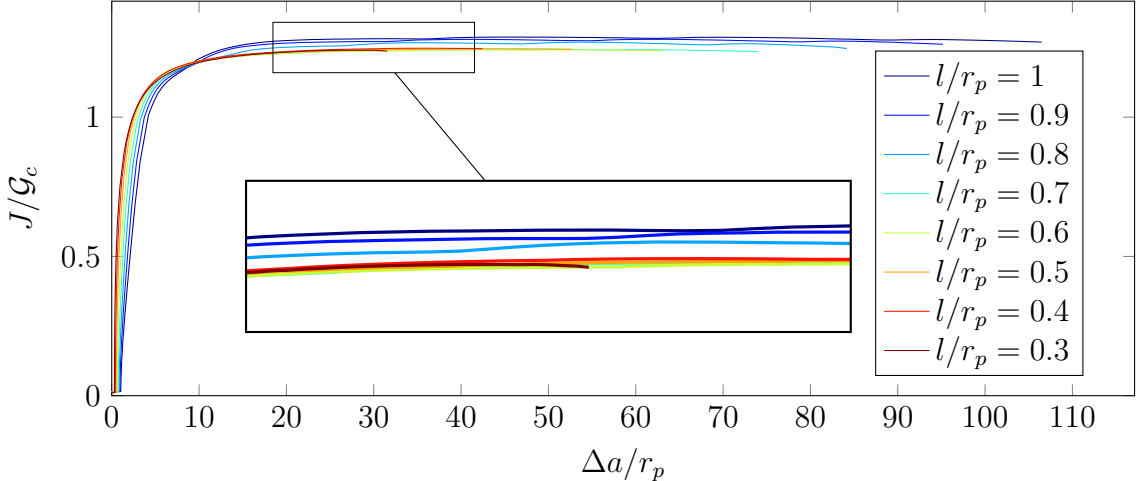


FIGURE 5.10. J-R curves for different values of l/r_p .

the E-P-PD model. Note that the use of a non-Lorentz-type degradation function, e.g. the quadratic degradation function, results in a strong dependence of the J-R response on the phase-field regularization l [126].

5.4 Numerical examples

Finally, both the proposed E-P-D model and the E-P-PD model are applied to simulate a three-point bending experiment in Section 5.4.1 and the experiment adopted for the Sandia Fracture Challenge in Section 5.4.2.

5.4.1 Three-point bending

With modeling choices motivated and demonstrated in Sections 5.3.1 and 5.3.2, the model is now applied to simulate a three-point bending experiment for a specimen composed of an aluminum alloy [3]. In particular, we focus attention on the comparison of the E-P-PD model and the proposed E-P-D model with coalescence dissipation.

First, material properties and model parameters are calibrated against a tension test of a notched cylindrical specimen (R13 notch). Details of the specimen geometry,

experimental setup and force-displacement data are provided in [2]. Our calculations employ a cylindrical coordinate system, and symmetry is assumed about both the centerline and the half-plane of the specimen. The finite element mesh for this problem is shown in Figure 5.11. QUAD4 elements are used to discretize the domain with a structured mesh. The maximum and the minimum element sizes are 1 mm and 0.0625 mm, respectively.

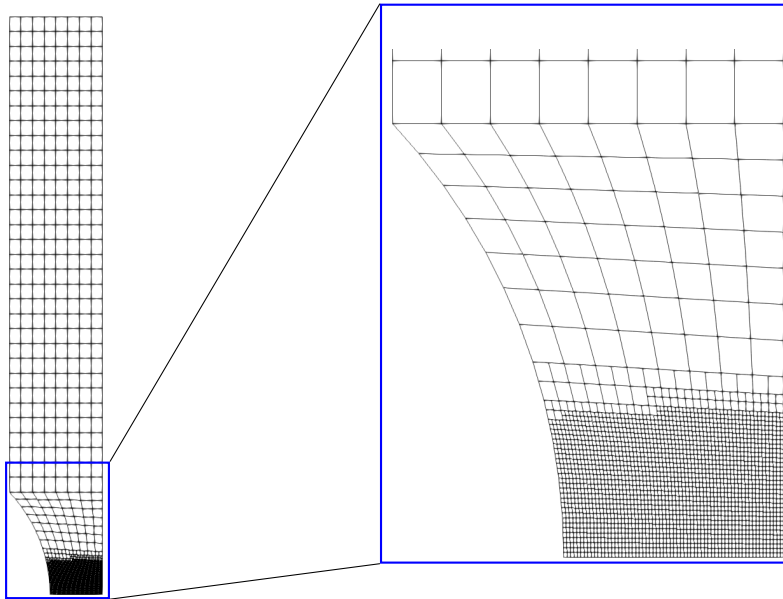


FIGURE 5.11. The mesh used for calibration and the zoomed-in view of the refined region.

Calibrated material properties and model parameters are summarized in Table 5.1. The E-P-D model is calibrated using a range of β and ε_0 values. The corresponding force-displacement curves are shown in Figure 5.12.

We note that a significantly larger critical fracture energy ψ_c is required for the E-P-PD model for the onset of damage to match the experiment. This is expected as the generalized fracture driving energy for the E-P-PD model includes contributions from plasticity, while only the active strain energy contributes to crack growth in the E-P-D model. According to (5.53), polyconvexity requires a phase-field regularization length $l \leq 0.01$ mm.

Table 5.1. Summary of the calibrated material properties and model parameters

Property/Parameter	Symbol	Value(E-P-D)	Value(E-P-PD)	Unit
Young's modulus	E	7.25×10^4	7.25×10^4	MPa
Poisson's ratio	ν	0.34	0.34	nondim.
Yield stress	σ_y	345	345	MPa
Hardening modulus	H	1000	1000	MPa
Fracture toughness	\widehat{G}_c	20	20	mJ mm^{-2}
Crack geometric coefficient	ξ	1	1	nondim.
Critical fracture energy	ψ_c	3.7	205	mJ mm^{-3}
Regularization length	l	0.1	0.01	mm
Interaction coefficient	β	{0.1, 0.2, 0.4, 0.6, 0.8, 1}	1	nondim.
Characteristic plastic strain	ε_0	{0.05, 0.1, 0.2, 0.4, 0.8}	-	nondim.
Elastic degradation function	g^e	$g^{\text{Lorentz}}(d; p = 1)$	$g^{\text{Lorentz}}(d; p = 1)$	nondim.
Plastic degradation function	g^p	1	$g^{\text{Lorentz}}(d; p = 1)$	nondim.

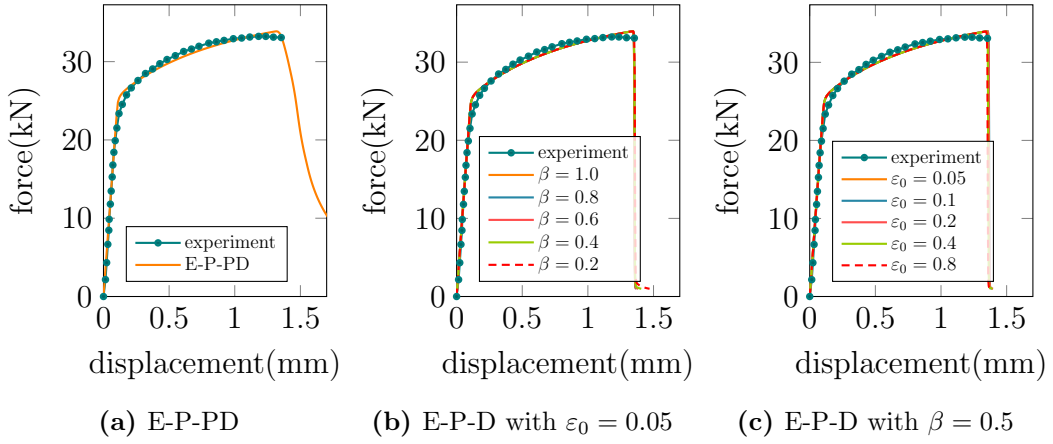


FIGURE 5.12. Experimental and calibrated force-displacement curves for the tension test. Experiment data are interpolated from [2]. The calibrated curves correspond to material properties and model parameters summarized in Table 5.1.

The calibrated E-P-D and E-P-PD models are now applied to simulate the three-point bending experiment with the same material. The specimen has a cylindrical notch on the bottom and two cylindrical holes around the middle of the specimen. The two holes are asymmetric about the mid-plane in terms of size and position. Details of the specimen geometry and experimental set up are available in [3]. Schematics of the boundary conditions and the mesh are shown in Figure 5.13. 19,182 TRI6 elements are used to discretize the domain. The maximum and the minimum element sizes are 5 mm and 0.01 mm, respectively. Second-order shape functions are

used for the mechanics subproblem, and first-order shape functions are used for the phase-field subproblem.

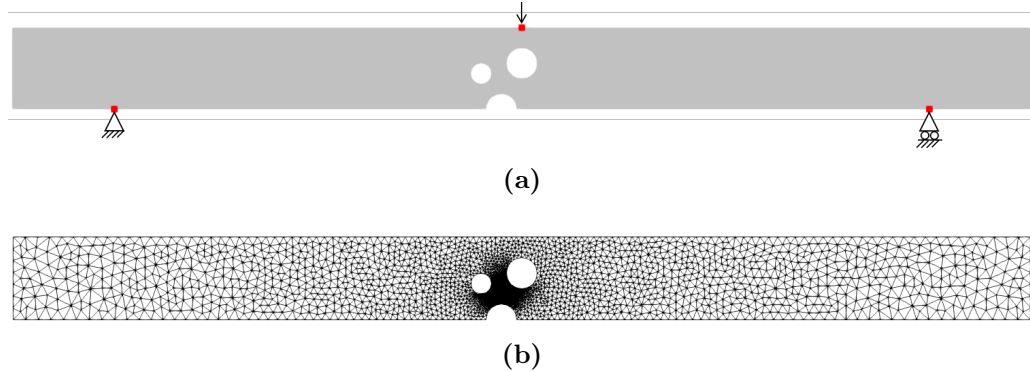


FIGURE 5.13. (a) schematics of the three-point bending experiment and (b) the mesh. See [3] for a detailed drawing with dimensions. The specimen is assumed to have a fixed support and a roller support on the bottom, and a downward displacement is applied at the location of the top punch.

In the experiment, the crack surface first originates from the half cylindrical notch on the bottom of the specimen, and then grows to connect the notch to the bottom of the left smaller cylindrical hole. After a while, the second crack surface originates from the top of the left smaller hole and grows towards the middle of the upper free surface.

5.4.1.1 Two-dimensional results

First, we focus attention on the initiation and propagation of the first crack, i.e. the crack connecting the notch to the left smaller hole. The calculations are performed in two dimensions under plane-strain assumptions. The experimental crack path and the contours of the equivalent plastic strain are shown in Section 5.4.1.1. Due to the nature of the linear crack geometric function, both the E-P-PD model and the E-P-D model has the same ductile response up to damage initiation: the equivalent plastic strain localizes around the middle of the bottom cylindrical notch, and two wakes of plastic deformation form at 45° angle towards the lower surfaces of the left smaller

cylindrical hole and the right larger cylindrical hole.

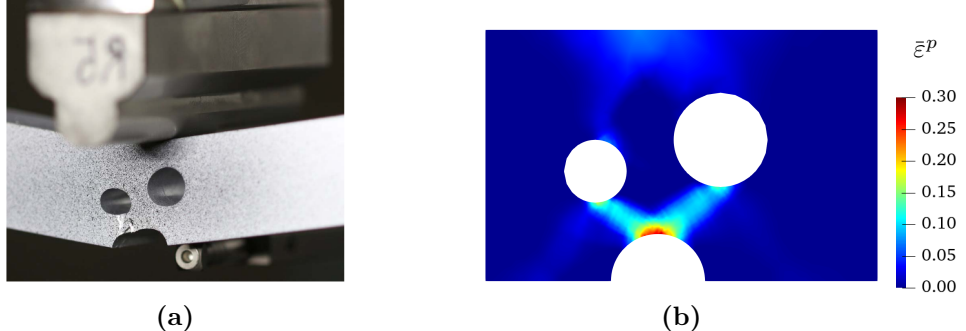


FIGURE 5.14. (a) a picture of the experiment setup [3] and (b) the effective plastic strain prior to crack initiation.

It bears emphasis that this three-point bending experiment is particularly challenging for most E-P-D models because the crack trajectories will be qualitatively different in a brittle material and in a ductile material, and it is of common concern that a loosely coupled E-P-D model may fail to predict the correct crack trajectory. In fact, we show that it is important to include the coalescence dissipation to predict the correct crack path.

After damage initiation, crack paths predicted by the E-P-D model and the E-P-PD model differ. For the E-P-D model, the crack paths depend on the parameters chosen for the coalescence dissipation. The effective fracture toughness $\hat{\mathcal{G}}_c(\bar{\varepsilon}^p; \beta, \varepsilon_0)$ decreases as the plastic strain $\bar{\varepsilon}^p$ increases following a decay characterized by β and ε_0 . In other words, the spatial variation of the effective fracture toughness conforms with the localization of the plastic strain. The effect of β and ε_0 are illustrated in Figures 5.15 and 5.16.

In Figure 5.15, β is kept constant and the sensitivity of the fracture path to ε_0 is examined. Smaller values of ε_0 result in faster decay of the fracture toughness as the plastic strain increases. As a result, given the same amount of plastic strain, a smaller ε_0 leads to a higher spatial variation or “contrast” in the effective fracture

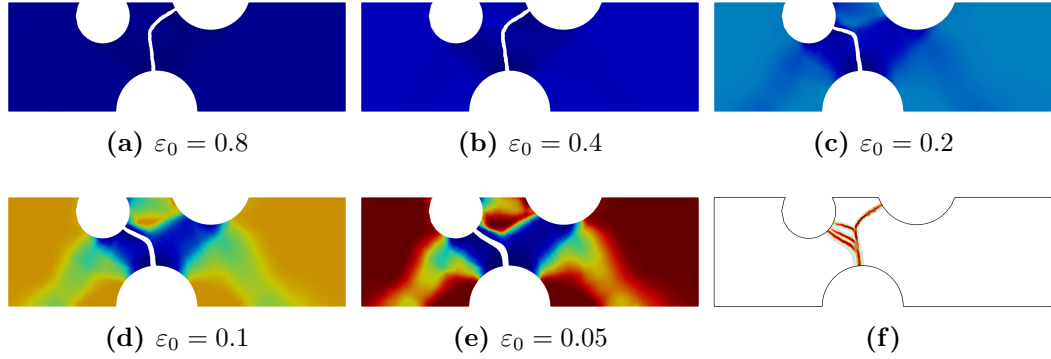


FIGURE 5.15. (a-e) Contour plots of the effective fracture toughness $\hat{\mathcal{G}}_c$ with $\beta = 0.1$ and different values of ε_0 , using the E-P-D model. The portion of the domain with $d > 0.8$ is removed to visualize the crack path. (f) Superposition of the damage contours. All contours are plotted on the reference configuration for the purpose of comparison.

toughness. When $\varepsilon_0 = 0.8$, the contrast is negligible, the effective fracture toughness is approximately homogeneous, and the crack propagates towards the right larger cylindrical hole. When $\varepsilon_0 = 0.05$, the contrast is high, the fracture toughness is degraded in regions with large plastic strain, and therefore the crack path largely follows the localization of the plastic strain.

Similar arguments hold in Figure 5.16 where ε_0 is kept constant and the sensitivity of the fracture path to changes in β is explored. When β is small, the spatial “contrast” of the effective fracture toughness is high, and the crack path is affected by the localization of the plastic strain.

For the E-P-PD model, due to the strong coupling between plasticity and fracture, the crack path follows the localization of the plastic strain, and the plastic strain keeps increasing around the crack surface. The resulting equivalent plastic strain and crack path in this case are shown in Figure 5.17.

Remark 9. In order to properly resolve the phase-field regularization length $l = 0.01$ mm for the E-P-PD model, a fairly small element size has to be used, resulting in a system with approximately 12 million degrees of freedom for this

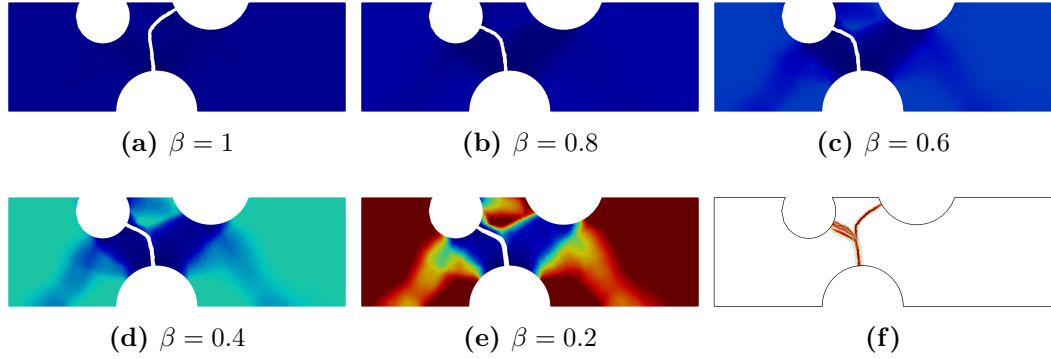


FIGURE 5.16. (a-e) Contour plots of the effective fracture toughness $\hat{\mathcal{G}}_c$ with $\varepsilon_0 = 0.05$ and different values of β . Domain with $d > 0.8$ is removed to visualize the crack path. (f) Superposition of the damage contours. All contours are plotted on the reference configuration for the purpose of comparison.

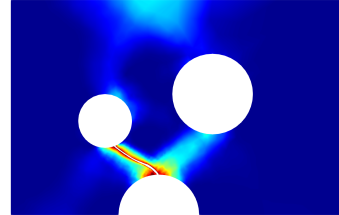


FIGURE 5.17. Contour of the equivalent plastic strain obtained using the E-P-PD model. Domain with $d > 0.8$ is removed to visualize the crack path.

two-dimensional problem. In contrast, only 147,772 degrees of freedom were used for the E-P-D model.

5.4.1.2 Three-dimensional results

With a qualitative understanding of the predicted trajectory of the first crack, a subset of the calibrated E-P-D models are now used in three-dimensional simulations of the three-point bending experiment. The calculated load-deflection curves are compared to experimental measurements.

In [3], experimental results are reported for two different trials of the three-point bending experiment, both using the same material, geometry, and etc. Both of the experimental load-deflection curves are shown in Figure 5.18 for the sake of

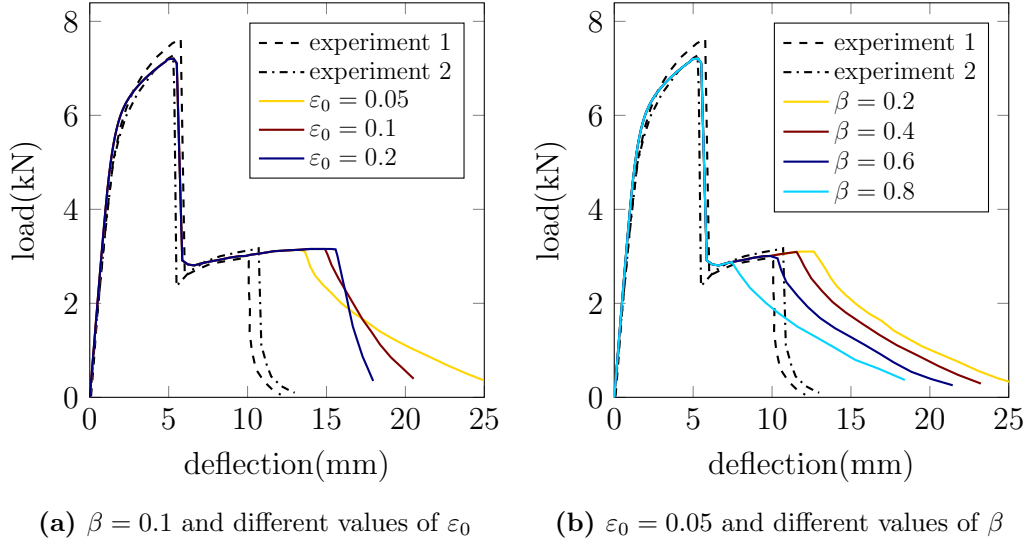


FIGURE 5.18. Comparison of load-deflection curves between simulations and experiments [3] for the 3D three-point bend experiment.

comparison to our simulation results. The experimental curves indicate an initial elastic-plastic response, followed by an abrupt drop in the load, subsequent force increase, and a final abrupt drop. The two drops in the force-displacement data (occurring for both experiments) correspond to the nucleation and propagation of the crack surfaces, first from the bottom notch to the hole, then from the hole to the upper free surface.

In the experiments, the first load drop occurs at a deflection around 5.8 mm (experiment 1) and 5.3 mm (experiment 2), and the second load drop occurs at a deflection around 10.1 mm (experiment 1) and 10.7 mm (experiment 2). In all load-deflection curves predicted by the model-based simulations, the first load drop occurs at a deflection of approximately 5.3 mm, which compares well to the experimental measurements. However, the prediction of the nucleation and propagation of the second crack is sensitive to model parameters β and ε_0 . While $\beta = 0.1$ is kept constant (Figure 5.18a), larger ε_0 delays the nucleation of the second crack and leads to a steeper load drop. While $\varepsilon_0 = 0.05$ is kept constant (Figure 5.18b),

larger β values accelerate the nucleation of the second crack, but the load drops at approximately the same rate.

The results shown in Figure 5.18 suggest that choosing $\varepsilon_0 = 0.2$ and $\beta = 0.6$ might result in a force-displacement curve that best matches the experimental data (the combination $\beta = 0.6$ and $\varepsilon_0 = 0.2$ yields a force-displacement response that is practically indistinguishable from those shown in Figures 5.12b and 5.12c). We performed an additional simulation using this choice of these parameters, and the results are shown in Figure 5.19. Indeed, the resulting simulation yields a force-displacement curve that is very close to the experimental result. Importantly, we find that our model-based simulations yield a better comparison to the experimental load-displacement curves than the various damage models explored in [3].

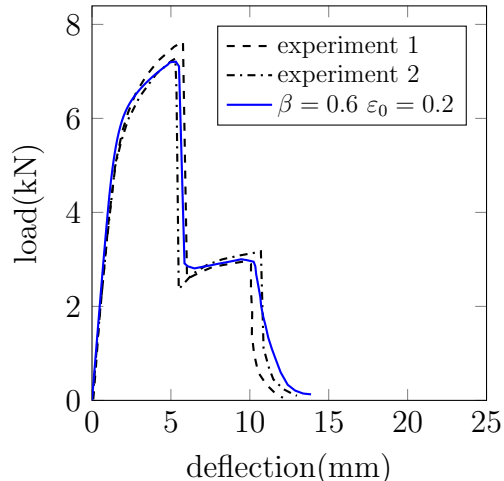


FIGURE 5.19. Comparison of load-deflection curves between simulations and experiments [3] with tuned β and ε_0 .

While the load-deflection curves differ based on different choices of model parameters, the crack trajectory predictions are relatively insensitive to the model parameters. In the experiments (Figure 5.20a), the crack nucleation and propagation can be divided into 4 stages. (I) The crack first nucleates around the center of the bottom notch and propagates through the thickness of the specimen. (II) Simultane-

ously the crack grows slant-wise towards the bottom of the smaller hole. (III) After a period of load increase, the second crack nucleates around the center of the top of the smaller hole and propagates through the thickness towards the free surfaces. (IV) Finally, the crack propagates towards the top free surface of the specimen. The corresponding stages in the simulation are shown in Figures 5.20b to 5.20e.

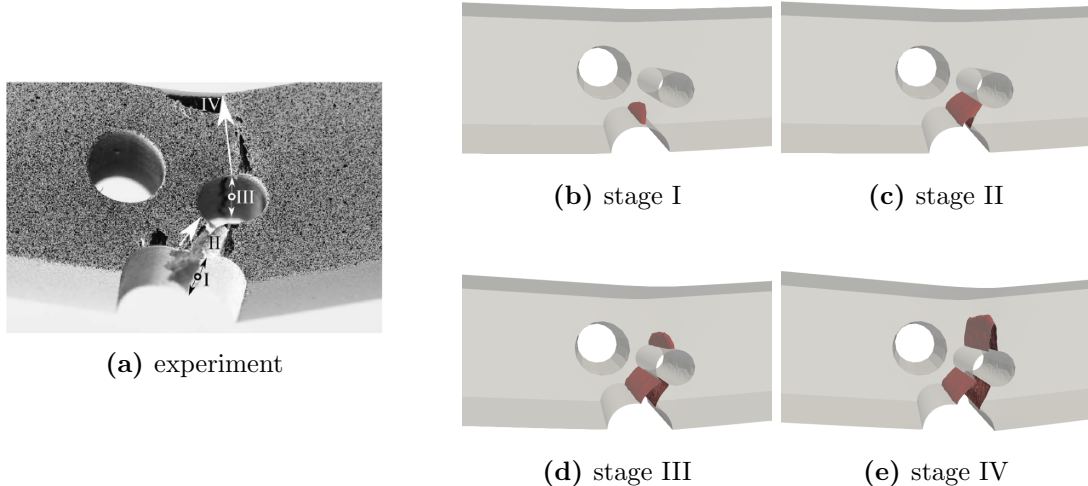


FIGURE 5.20. Comparison of crack paths between (a) the experiment [3] and (b-e) the simulation with $\beta = 0.1$ and $\varepsilon_0 = 0.2$. Iso-contours of $d = 0.8$ are highlighted in red.

The final crack surfaces obtained using $\beta = 0.1$ and $\varepsilon_0 = 0.2$ are shown in Figure 5.21. In the experiments, “shear lips” (circled in red) occur close to the free surfaces of the specimen due to high stress-triaxility. Although such “shear lips” are not predicted by the E-P-D model used in this work, the larger-scale crack trajectories agree reasonably well with the experimental observations.

5.4.2 The Sandia Fracture Challenge

Next, we examine the capabilities of the proposed E-P-D model by simulating an experiment from a Sandia Fracture Challenge [135]. The specimen is composed of Al-5052 H34. The hardening model is first calibrated against tensile test data for a

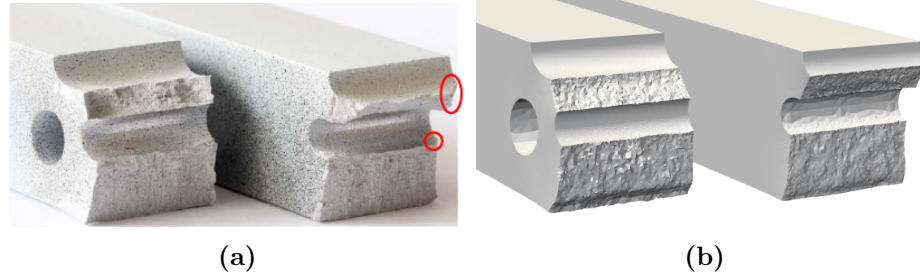


FIGURE 5.21. Comparison of the final crack surfaces between (a) the experiment [3] and (b) the simulation ($\beta = 0.1$ and $\varepsilon_0 = 0.2$). “Shear lips” are circled in red. For comparison purposes, the computational domain is separated into two pieces by removing the domain within the $d \geq 0.8$ contour after complete failure.

smooth round bar [136]. The calibrated material properties and model constants are summarized in Table 5.2. Based on the calibrated tensile test results, the crack should initiate at a critical equivalent plastic strain of $\varepsilon_c^p = 0.8$. The fracture toughness \mathcal{G}_c is then scaled accordingly, such that $\hat{\mathcal{G}}_c$ matches experimental measurements.

Table 5.2. Summary of the calibrated material properties and model parameters for the Sandia Fracture Challenge specimen

Property/Parameter	Symbol	Value	Unit
Bulk modulus	K	6.495×10^4	MPa
Shear modulus	G	2.4906×10^4	MPa
Yield stress	σ_y	225	MPa
Hardening modulus	H	250	MPa
Fracture toughness	$\hat{\mathcal{G}}_c$	13.6	mJ mm^{-2}
Fracture dissipation coefficient	ξ	1	nondim.
Critical fracture energy	ψ_c	1	mJ mm^{-3}
Regularization length	l	0.3	mm
Interaction coefficient	β	0.5	nondim.
Characteristic plastic strain	ε_0	0.1	nondim.

The calibrated model is then applied to simulate crack initiation and growth in the specimen adopted for the Sandia Fracture Challenge. Drawings of the specimen with detailed dimensions are available in [136, 119]. The geometry and the mesh of the specimen is shown in Figure 5.22. The three-dimensional geometry is discretized

using tetrahedral elements (TET10). The mesh is locally refined near the round notch to sufficiently capture plastic and fracture localizations. It is assumed that the extension of the second crack is known a priori, and the region to the right of the middle hole is also refined to properly resolve the phase field. The resulting mesh consists of 10831 tetrahedra.

The specimen is loaded in tension via two pins that connect to the specimen through the circular holes whose centers coincide with nodes *A* and *B* in Figure 5.22. Rather than apply the loads to the boundaries of the holes or employ a contact algorithm with the pins, here we simplify the model by explicitly meshing the pins and assuming they are perfectly bonded to the specimen at the hole locations. The material of the pins is assumed to be elastic with moduli that match the specimen.

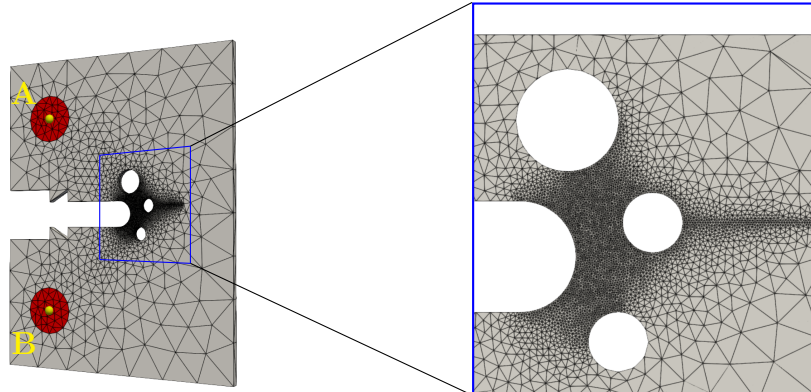


FIGURE 5.22. Sandia Fracture Challenge problem geometry and mesh, with zoomed-in view of the refined region. The specimen is loaded vertically with displacement control at lines of nodes *A* and *B* marked as yellow spheres.

The resulting force-displacement curves are shown in Figure 5.23. The response predicted by our proposed E-P-D model indicates an excellent agreement with the experimental measurements. Force-displacement curves from [119] are also included for comparison. The proposed E-P-D model clearly provides the best quantitative and qualitative match with the experiment.

Contour plots of the phase field d are shown in Figures 5.24a to 5.24c. The first

crack nucleates on the left side of the middle hole, and then connects with the round notch. After a while, the second crack nucleates on the right side of the middle hole and propagates to the right, with a nearly horizontal orientation. The active part of the strain energy is shown in Figures 5.24d to 5.24f, where the stress concentration at the crack tips and a stress release after the first crack can be clearly observed. The plastic energy is shown in Figures 5.24g to 5.24i, and the coalescence degradation is shown in Figures 5.24j to 5.24l. The fracture toughness is substantially degraded in the regions with high plastic localization.

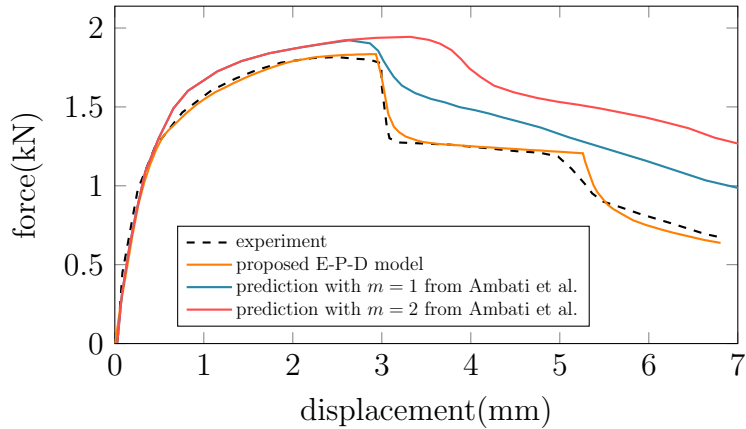


FIGURE 5.23. The force displacement curves from the experiment and the numerical simulations for the Sandia Fracture Challenge.

5.4.3 Spallation of oxidation scale

Next, we extend the ductile fracture model within the variational framework to construct a coupled thermo-elasto-creep model to simulate the spallation of oxide scale on high temperature heat exchangers.

High temperature heat exchangers (HTHXs) are key components of many power conversion systems, including advanced nuclear power generation systems. HTHXs typically operate in the inlet temperature range of 750-1100 °C and are subject to unique operating challenges including oxidation, corrosion, creep and fracture. We

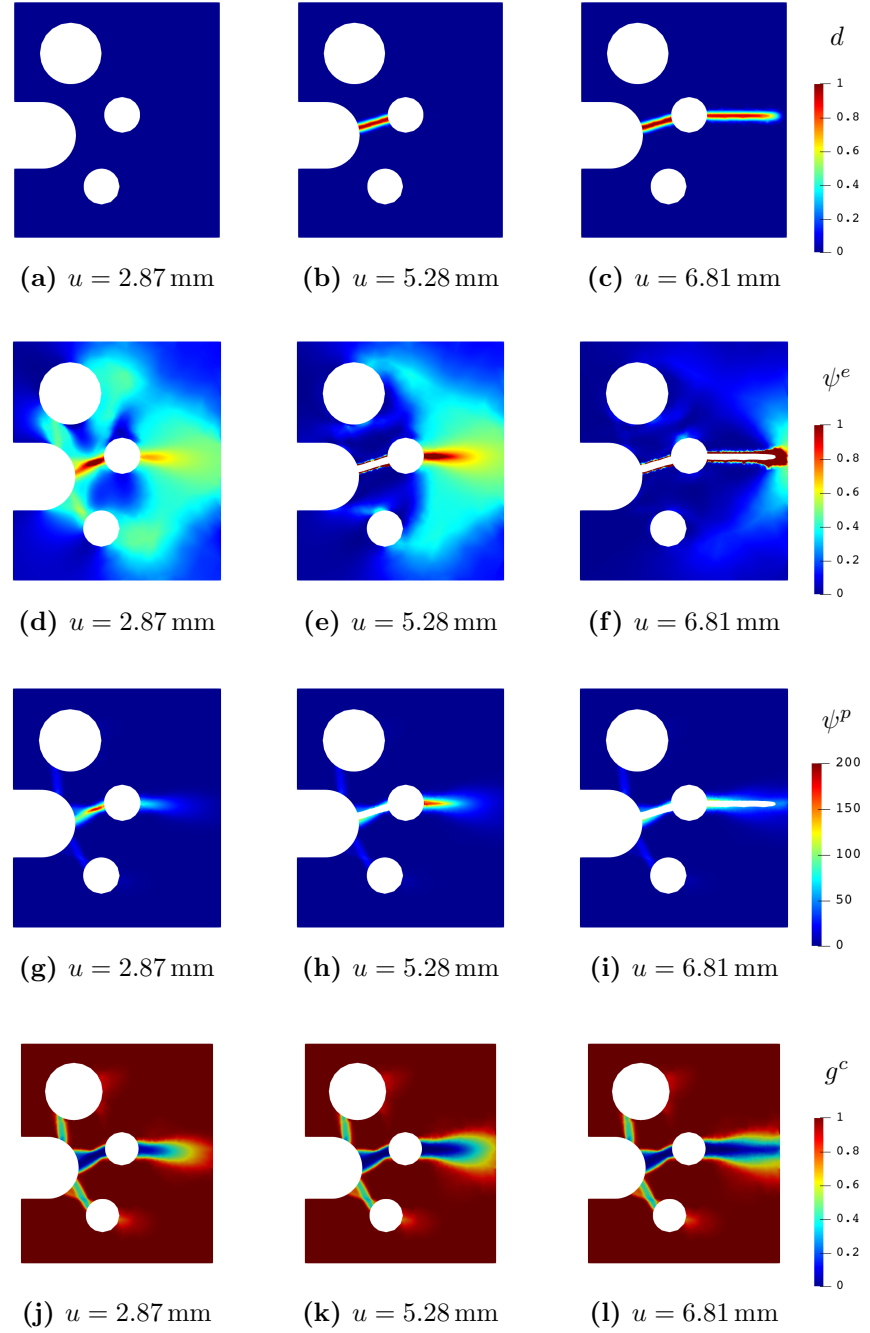


FIGURE 5.24. The Sandia Fracture Challenge. Contour plots of (a-c) the phase field d , (d-f) the active part of the strain energy $\psi_{\langle A \rangle}^e$, (g-i) the plastic energy ψ^p , and (j-l) the coalescence degradation function g^c at three different loads. In subfigures (d-i) the domain within the contour of $d > 0.8$ is removed to facilitate crack path visualization.

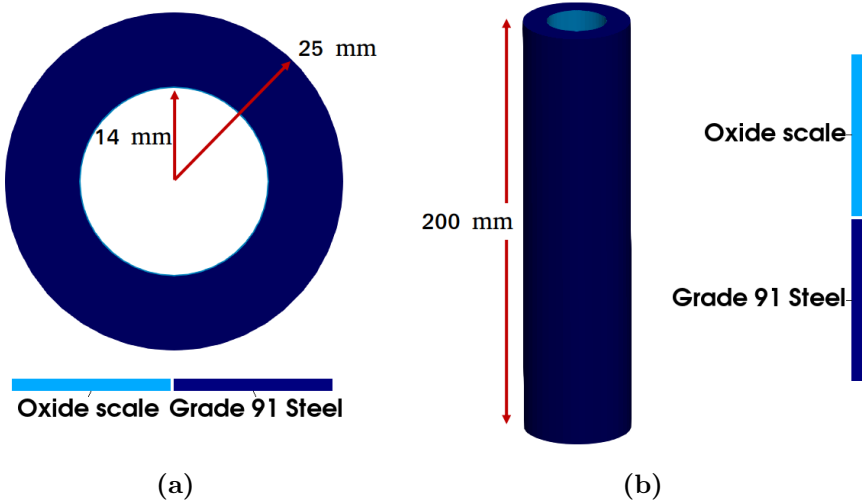


FIGURE 5.25. (a) Top view and (b) side view of the section of the heat exchanger.

focus on modeling the mechanical response of the metal operating at high temperatures, with the objective of developing physics-based models for predicting fracture and spallation of the scale, which will provide insight into the lifetime performance of the heat exchanger.

Consider a 200 mm-long section of a metal tube with inner radius 14 mm and outer radius 25 mm (Figure 5.25). Steam flows through the tube, and the tube is surrounded by flue gas. Both the steam and the flue gas are assumed to have a homogeneous temperature and pressure within the control volume at a given instant. Oxide growth on the inner surface of the metal tube is of particular interest. In this section, oxide is assumed to grow following the relation

$$\tau = \sqrt{2A_{\text{ox}} \exp\left(-\frac{Q_{\text{ox}}}{RT}\right) t}, \quad (5.66)$$

where τ is the thickness of the oxide layer, A_{ox} is the growth coefficient, Q_{ox} is the oxidation activation energy, R is the ideal gas constant, and T is the temperature on the inner surface of the tube.

5.4.3.1 Incorporating debonding

The power-law creep model presented in Section 5.2 is used to model the mechanical response of the metal. In particular, no viscous effects are incorporated, i.e. $\psi^{e*} = \psi^{p*} = \psi^{f*} = 0$. It is assumed that the metal does not fracture during the spallation process, therefore $\psi^f = 0$. The interface between the oxide and the metal is modeled together with the oxide, and they are represented as a lower-dimensional manifold attached on the inner surface of the metal tube. Under the assumption that the thickness of the oxide is much smaller than that of the metal tube, both in-plane transverse cracks and out-of-plane debonding at the oxide-metal interface could be represented on the same lower-dimensional manifold, with proper enrichment to the constitutive model.

The modified fracture energy density of the oxide is extended to consider debonding at the oxide-metal interface. Debonding at the interface is associated with the release of energy, i.e. $\int_D \mathcal{G} dA$, where D is the debonded region, and \mathcal{G} is the energy release rate per unit debonded area. Under the assumption that the oxide layer is sufficiently thin, the interface energy can be smeared by an auxiliary field c and distributed throughout the thickness of the oxide, i.e.

$$\psi^f = \frac{\mathcal{G}_c}{c_0 l} (C\alpha(d) + l^2 \nabla d \cdot \nabla d) + \frac{1}{\tau} \mathcal{G}\omega(c), \quad (5.67)$$

where $\omega(c)$ is a characteristic function for the debonding area, and $\omega(0) = 0$, $\omega(1) = 1$.

The strain energy density of the oxide is defined in the local coordinate system attached to each material point. The global coordinate system is transformed such that the local z -axis aligns with the exterior normal of the oxide. The transformation

tensor \mathbf{T} is computed using the Rodrigues formula:

$$T_{ij}(\hat{\mathbf{n}}, \theta) = \cos(\theta)\delta_{ij} + [1 - \cos(\theta)] n_i n_j + \sin(\theta)\epsilon_{ijk}n_k, \quad (5.68)$$

where $\hat{\mathbf{n}}$ is the axis of rotation, θ is the rotation angle, and ϵ is the permutation tensor. The Hencky-type logarithmic strain measure is used for the oxide. The strain is first transformed into the local coordinate system by $\boldsymbol{\varepsilon}^{e'} = \mathbf{T}\boldsymbol{\varepsilon}^e\mathbf{T}^T$ and decomposed into in-plane and out-of-plane components

$$\boldsymbol{\varepsilon}_{\text{ip}}^{e'} = \mathbf{E}_{\text{ip}}\boldsymbol{\varepsilon}'\mathbf{E}_{\text{ip}}^T, \quad (5.69a)$$

$$\boldsymbol{\varepsilon}_{\text{op}}^{e'} = \boldsymbol{\varepsilon}' - \mathbf{E}_{\text{ip}}^T\boldsymbol{\varepsilon}_{\text{ip}}^{e'}\mathbf{E}_{\text{ip}}, \quad (5.69b)$$

where \mathbf{E}_{ip} is the embedding matrix for the in-plane components, defined as

$$\mathbf{E}_{\text{ip}} = \begin{bmatrix} 1 & 0 & 0 \\ 0 & 1 & 0 \end{bmatrix}. \quad (5.70)$$

The modified strain energy density is then defined as

$$\psi^e = g_{\text{ip}}^e \psi_{\text{ip},\langle A \rangle}^e + \psi_{\text{ip},\langle I \rangle}^e + g_{\text{op}}^e \psi_{\text{op},\langle A \rangle}^e + \psi_{\text{op},\langle I \rangle}^e, \quad (5.71a)$$

$$\psi_{\text{ip},\langle A \rangle}^e = \frac{1}{2}K \langle \text{tr}(\boldsymbol{\varepsilon}_{\text{ip}}^{e'}) \rangle_+^2 + G \text{dev } \boldsymbol{\varepsilon}_{\text{ip}}^{e'} : \text{dev } \boldsymbol{\varepsilon}_{\text{ip}}^{e'}, \quad (5.71b)$$

$$\psi_{\text{ip},\langle I \rangle}^e = \frac{1}{2}K \langle \text{tr}(\boldsymbol{\varepsilon}_{\text{ip}}^{e'}) \rangle_-^2, \quad (5.71c)$$

$$\psi_{\text{op},\langle A \rangle}^e = \frac{1}{2}K \langle \boldsymbol{\varepsilon}_{\text{op}}^{e'} \rangle_+^2 + G (\boldsymbol{\varepsilon}_{\text{op}}^{e'} - \boldsymbol{\varepsilon}_{\text{op}}^{e'} \mathbf{e}_3 \otimes \mathbf{e}_3) : (\boldsymbol{\varepsilon}_{\text{op}}^{e'} - \boldsymbol{\varepsilon}_{\text{op}}^{e'} \mathbf{e}_3 \otimes \mathbf{e}_3), \quad (5.71d)$$

$$\psi_{\text{op},\langle I \rangle}^e = \frac{1}{2}K \langle \boldsymbol{\varepsilon}_{\text{op}}^{e'} \rangle_-^2, \quad (5.71e)$$

$$\boldsymbol{\varepsilon}_{\text{op}}^{e'} = \mathbf{e}_3 \cdot \boldsymbol{\varepsilon}_{\text{op}}^{e'} \mathbf{e}_3, \quad (5.71f)$$

where g_{ip}^e and g_{op}^e are the in-plane and the out-of-plane degradation functions, respectively.

The modified Piola stress \mathbf{P}^{eq} follow from the constitutive restrictions (2.25). Furthermore, minimizing with respect to c (together with the irreversibility condition

$\dot{c} \geq 0$) leads to the following KKT conditions:

$$\phi^i = -\frac{1}{\tau} \mathcal{G} \omega_c - \psi_c^e \leq 0, \quad \dot{c} \geq 0, \quad \phi^i \dot{c} = 0. \quad (5.72)$$

The following constitutive functions are chosen in this section, such that both the in-plane transverse fracture and the out-of-plane debonding are characterized by a linear traction-separation law:

$$\alpha = d, \quad \omega = c, \quad g^p = 1, \quad (5.73a)$$

$$g^e = g_{ip}^e = \frac{(1-d)^2}{(1-d)^2 + m_{ip}d(1-0.5d)}, \quad (5.73b)$$

$$g_{op}^e = \frac{(1-c)^2}{(1-c)^2 + m_{op}c(1-0.5c)}, \quad (5.73c)$$

$$m_{ip} = \frac{3}{8l} \frac{\mathcal{G}_c}{\psi_c}, \quad m_{op} = \frac{\mathcal{G}}{\tau \psi_c^i}, \quad (5.73d)$$

where ψ^e is the (in-plane) critical fracture energy density, and ψ_c^i is the (out-of-plane) critical fracture energy density.

5.4.3.2 Boundary conditions

For convenience, boundaries of the section of the heat exchanger under consideration are marked in Figure 5.26. Utilizing symmetry, only a quarter of the domain is modeled. Symmetry conditions, i.e. $\mathbf{u} \cdot \mathbf{n}_0 = 0$ and $\nabla T \cdot \mathbf{n}_0 = 0$, are enforced on the sides. The bottom of the section is fixed in the z -direction, i.e. $u_z = 0$. The inner and outer surfaces are subjected to pressure and heat convection. The Pressure and temperature of the steam and the flue gas are summarized in Table 5.3 for different operating conditions. The operation of the heat exchanger cycles between the full and the partial schedule. The heat exchanger shuts down every 6 months, during which the temperature of the steam and the flue gas drops to room temperature, and the pressure becomes negligible. Since the actual heat exchanger is longer than

the section under consideration, generalized plane strain conditions are assumed to hold on the top surface of the tube, i.e. $\int_{\partial\Omega_0} \mathbf{n}_0 \cdot \boldsymbol{\varepsilon} \mathbf{n}_0 \, dA = 0$.

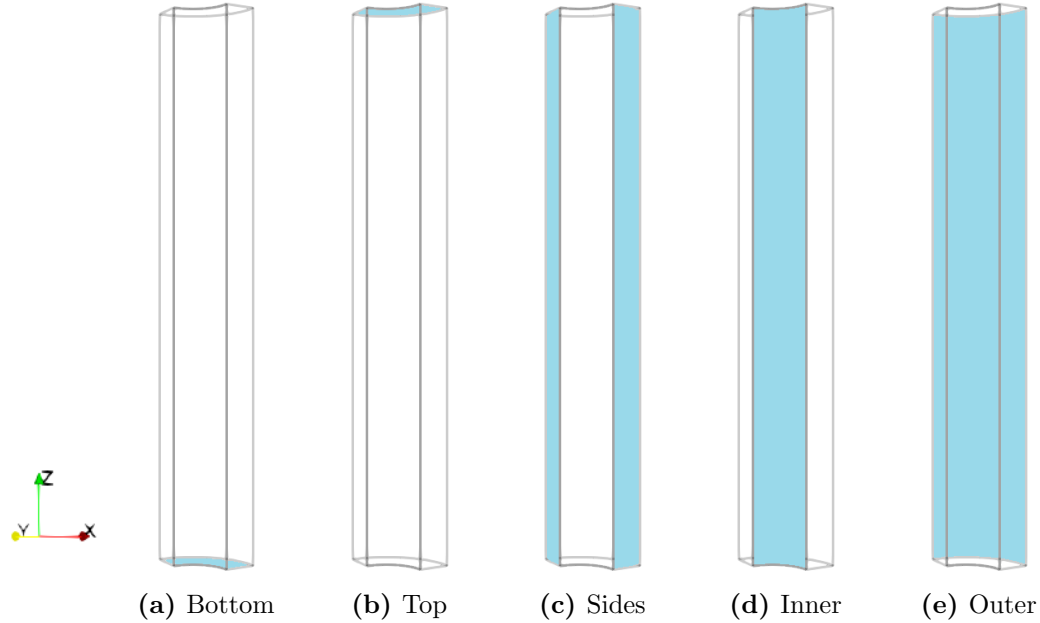


FIGURE 5.26. Boundaries of the heat exchanger.

Table 5.3. Summary of operation schedule

Load	Duration (h)	T_s (°C)	T_g (°C)	p_s (MPa)	p_g (MPa)	Transition (h)
Full	14	530	1100	17	0.2	Full to Partial: 1
Partial	8	525	845	10	0.1	Partial to Full: 1
Shutdown	25	25	25	0.1	0.1	Full to Shutdown: 6 Shutdown to Full: 3

5.4.3.3 Model parameters and material properties

Model parameters and material properties for the oxide and the metal are summarized in Tables 5.4 and 5.5, respectively. Most material properties are taken in accordance with [137] for comparison purposes. Following Remark 6, since the creep activation energy for both the oxide and the metal are much larger than the product of the ideal gas constant and the temperature, i.e. $Q \gg RT$, we take $\mathcal{Q} = 1$ to

satisfy the second law of thermodynamics. The fracture toughness \mathcal{G}_c of the oxide layer is taken in the ballpark of that of Cr_2O_3 . Due to the lack of experimental measurements, both the in-plane and the out-of-plane critical fracture energy density are chosen such that the transverse fracture energy and the debonding energy are of the same order of magnitude during the spallation process. To introduce coupling between plasticity and fracture, the coalescence dissipation (see Section 5.2.1.4) is included with $\beta = 0.3$ and $\varepsilon_0 = 1 \times 10^{-6}$.

Table 5.4. Summary of material properties and model parameters for the oxide

Property/Parameter	Symbol	Value	Unit
Young's modulus	E	120	GPa
Poisson's ratio	ν	0.24	nondim.
Thermal conductivity	κ	3	$\text{W m}^{-1} \text{K}^{-1}$
Convection coefficient (steam-oxide)	h	2800	$\text{W m}^{-2} \text{K}^{-1}$
Creep coefficient	A	8.5875×10^7	s^{-1}
Creep exponent	n	3	nondim.
Creep activation energy	Q	421.62	kJ mol^{-1}
Taylor-Quinney factor	Q	1	nondim.
Fracture toughness	\mathcal{G}_c	0.125	mJ mm^{-2}
Critical fracture energy density	ψ_c	0.013	mJ mm^{-3}
Regularization length	l	0.4	mm
Interaction coefficient	β	0.3	nondim.
Characteristic creep strain	ε_0	1×10^{-6}	nondim.
Oxidation coefficient	A_{ox}	6.22×10^8	$\text{m}^2 \text{h}^{-1}$
Oxidation activation energy	Q_{ox}	326	kJ mol^{-1}

Table 5.5. Summary of material properties and model parameters for the metal

Property/Parameter	Symbol	Value	Unit
Young's modulus	E	190	GPa
Poisson's ratio	ν	0.3	nondim.
Thermal conductivity	κ	30	$\text{W m}^{-1} \text{K}^{-1}$
Convection coefficient (metal-gas)	h	100	$\text{W m}^{-2} \text{K}^{-1}$
Creep coefficient	A	2.3×10^6	s^{-1}
Creep exponent	n	5.06	nondim.
Creep activation energy	Q	400	kJ mol^{-1}
Taylor-Quinney factor	Q	1	nondim.

The thermal expansion is accounted for by the thermal deformation gradient \mathbf{F}^g defined in terms of the measured instantaneous isotropic coefficient of thermal expansion $\bar{\alpha}$:

$$\mathbf{F}^g = \left(1 + \int_{T_0}^T \alpha \, dT' \right) \mathbf{I}, \quad (5.74)$$

where T_0 is the reference stress-free temperature. Since the oxide mainly forms at high temperature, the temperature profile obtained with the full operating conditions is considered to be the reference temperature. The instantaneous coefficients of thermal expansion are taken in accordance with [137] and are shown in Figure 5.27.

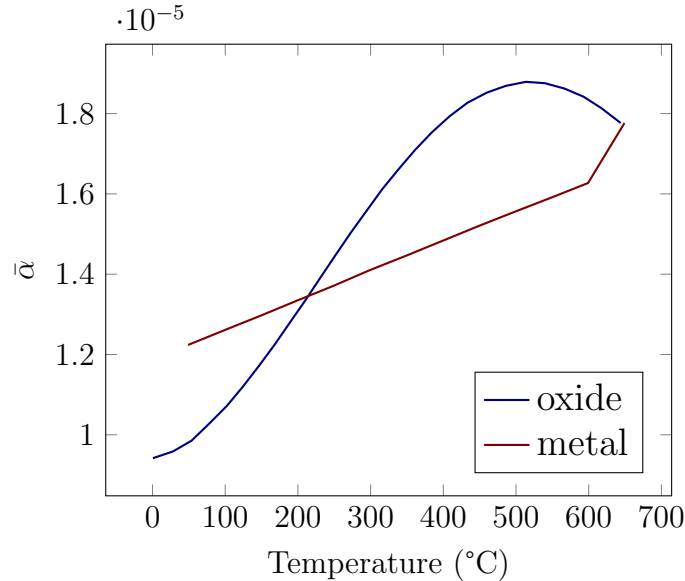


FIGURE 5.27. Instantaneous thermal expansion coefficients.

5.4.3.4 Debonding around a single crack

The model for spallation is first verified by simulating debonding around a pre-existing crack. During normal operation conditions at high temperature, debonding is expected to occur in the vicinity of a crack. A small pre-existing crack is introduced as the initial condition of the phase-field. The crack set is defined by $\Gamma = \{\mathbf{X} \mid \frac{\pi}{6} \leqslant$

$\theta \leq \frac{\pi}{3}$, $X_3 = 100\text{ mm}\}$, where $\theta = \tan(\frac{X_2}{X_1})$. All nodes within the crack set are initialized to have $d = 1$. The response of the heat exchanger is simulated for 140 days under normal operation conditions. The evolution of the phase field d , the debonding indicator c , and the effective creep strain $\bar{\varepsilon}^p$ are shown in Figure 5.28. Only a section of the tube near the crack is shown. Debonding first occurs in the vicinity of crack tips due to localization of the out-of-plane strain energy density, followed by the debonding of a continuous region around the crack.

The effective creep strain localizes around the crack tips along their horizontal extensions. As a result, the prescribed crack is expected to propagate along the horizontal direction during the following shut-down events.

5.4.3.5 Incorporating spatially-varying properties

The response of the heat exchanger is then simulated for 5 years. Boundary conditions are generated following the operation schedule indicated in Table 5.3. Shut-down events are scheduled to happen every half year, resulting in 10 shut-down events in total. The Young's modulus and the fracture toughness are modeled as marginal-Gamma random fields with mean values shown in the table ?? and coefficient of variance of 0.03. The evolution of the effective creep strain $\bar{\varepsilon}^p$, the coalescence degradation function g_c , the active strain energy density $\psi_{(A)}^e$, the active interface energy density $\psi_{(A)}^i$, and the debonding indicator c are shown in Figures 5.29 to 5.33, respectively.

During daily operations, the heat exchanger is surrounded by steam and flue gas with high temperatures, therefore the effective creep strain (Figure 5.29) and the oxide thickness increase at a relatively high rate. Newly formed oxide is assumed to be in a stress-free state, therefore the response of the oxide and the metal is driven by the high radial stress due to pressurized surfaces. The active strain energy density does not exceed the in-plane critical fracture energy density ψ_c in this stage.

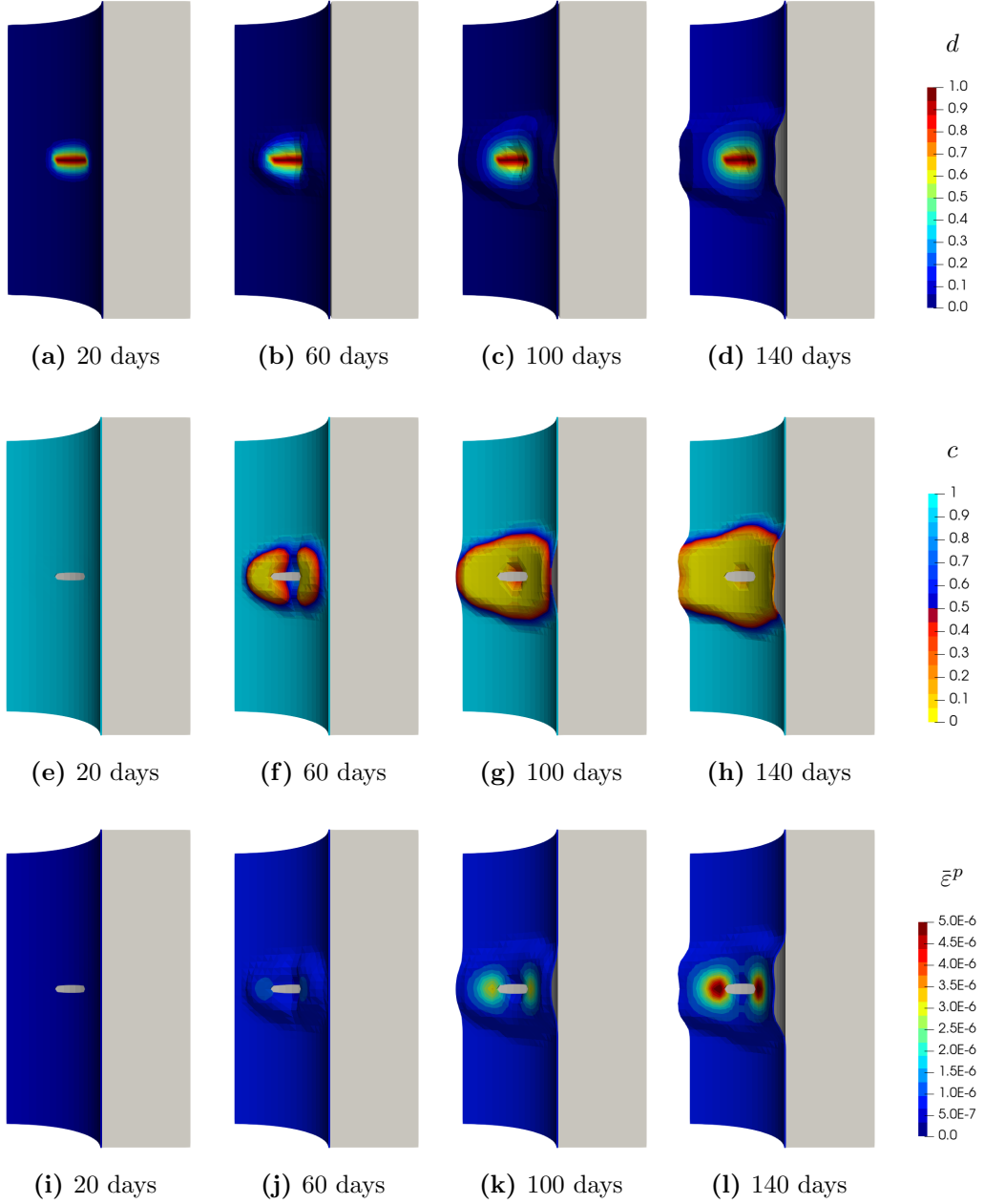


FIGURE 5.28. Contour plots of (a-d) the phase field, (e-h) the debonding indicator, and (i-l) the effective creep strain. In the contour plots of the debonding indicator and the effective creep strain, elements within the contour of $d \leq 0.75$ are removed to visualize the pre-existing crack. In all contour plots, the oxide layer is warped according to the debonding indicator to visualize debonding.

However, the active interface energy density exceeds the out-of-plane critical fracture energy density ψ_c^i (Figure 5.30), and debonding develops in this stage.

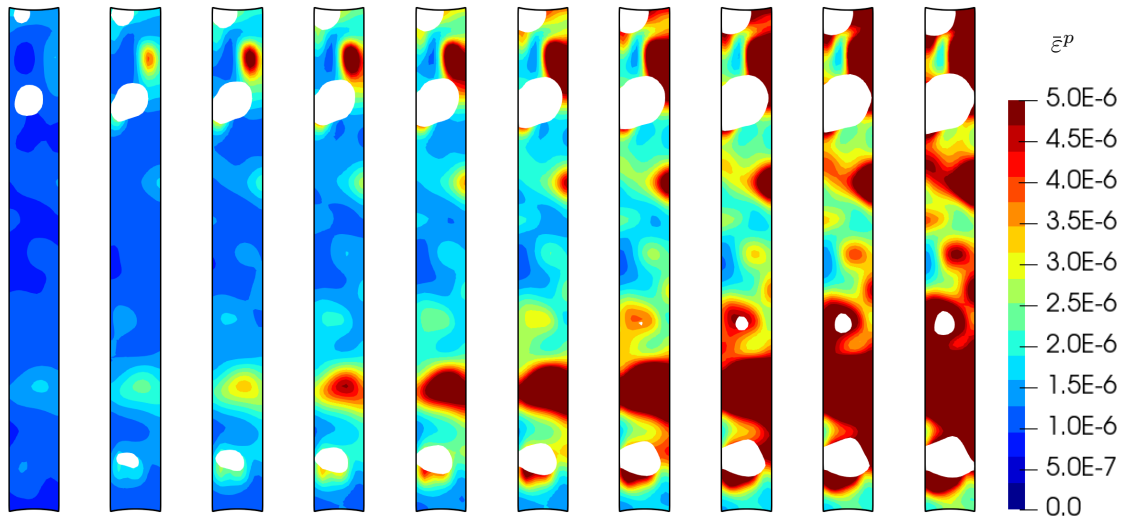


FIGURE 5.29. The effective plastic strain right after each shut-down event. The region within the contour of $d \leq 0.75$ is removed to visualize in-plane fracture.

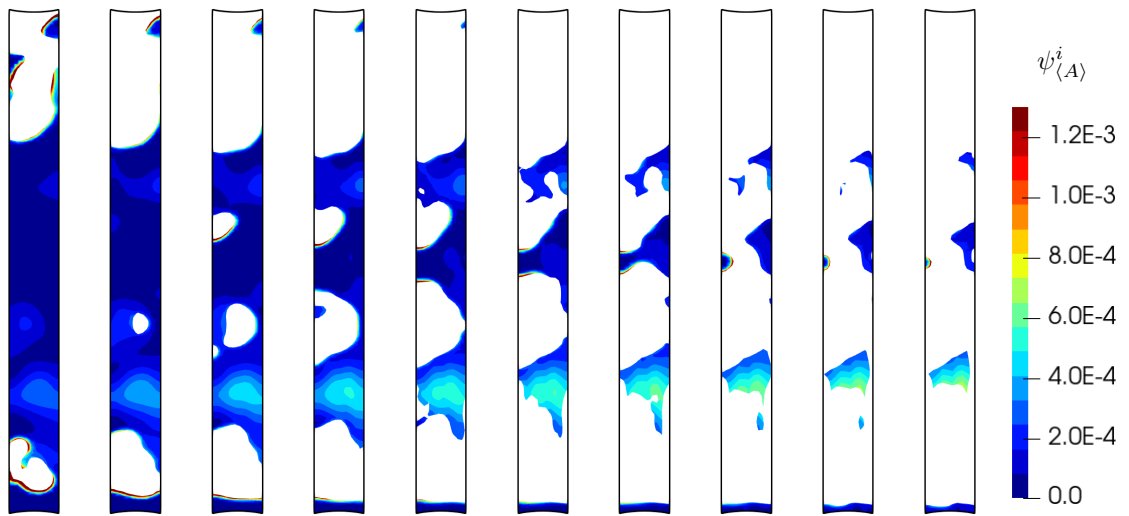


FIGURE 5.30. The active interface energy density right after each shut-down event. The region within the contour of $c \leq 0.75$ is removed to visualize out-of-plane debonding.

During the shut-down event, the temperatures of the steam and the flue gas drop to room temperature, and the pressure from the surrounding fluid and the oxidation rate become negligible. The response of the oxide and the metal is driven by the high thermal eigenstrain. Due to the difference in the instantaneous CTE of the

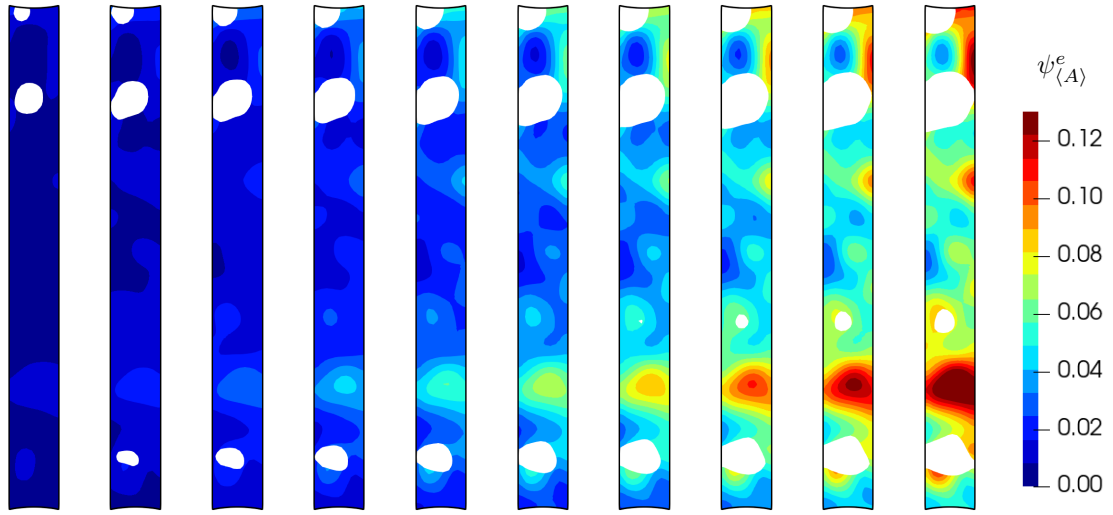


FIGURE 5.31. The active strain energy density right after each shut-down event. The region within the contour of $d \leq 0.75$ is removed to visualize in-plane fracture.

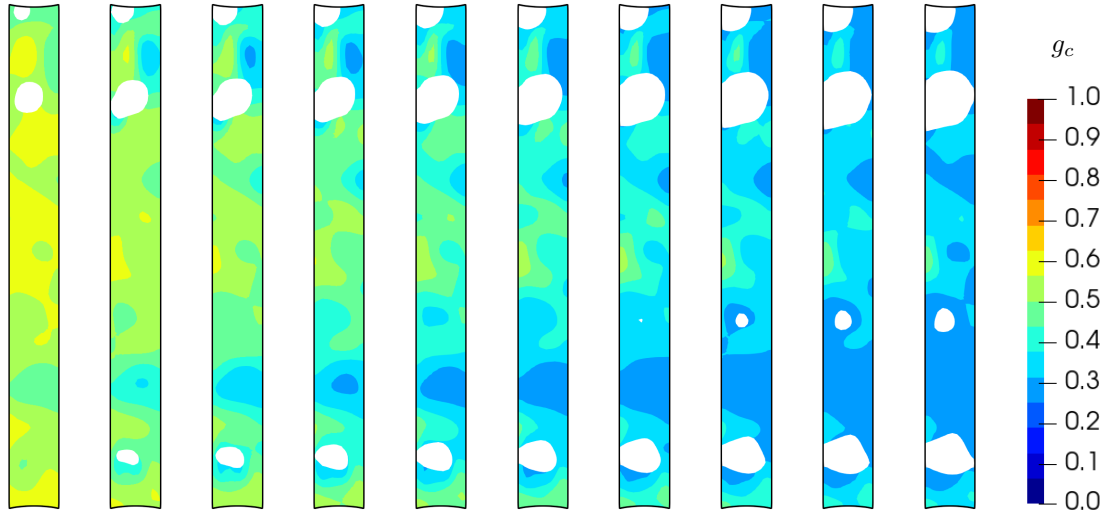


FIGURE 5.32. The coalescence degradation function right after each shut-down event. The region within the contour of $d \leq 0.75$ is removed to visualize in-plane fracture.

oxide and the metal, the oxide is put in tension in the longitudinal direction and the circumferential direction. The active strain energy density in the oxide exceeds the in-plane critical fracture energy density (Figure 5.31), therefore in-plane fracture propagates in this stage. The in-plane fracture localizes in regions with high creep

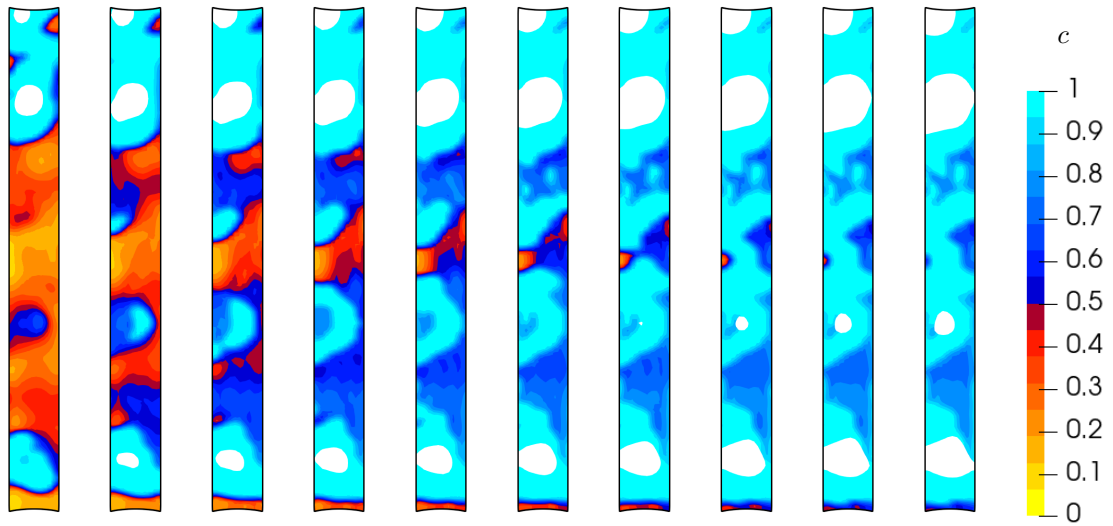


FIGURE 5.33. The debonding indicator right after each shut-down event. The region within the contour of $d \leq 0.75$ is removed to visualize in-plane fracture.

strain due to the coupling introduced by the coalescence dissipation, i.e. g_c is small in regions with high effective creep strain (Figure 5.32). With the presence of some in-plane fracture, when the heat exchanger goes back to normal operation conditions, debonding happens in the vicinity of transverse cracks (Figure 5.33).

6

Conclusions

In this dissertation, the variational approach to fracture is extended to account for general dissipative solids and different types of fracture. Several models are constructed within the proposed variational framework to study practical engineering problems.

In Chapter 3, a model for brittle/quasi-brittle fracture is developed to investigate fracture evolution at the microscale. 3D numerical studies are performed to investigate the effect of bubble geometry, porosity and loading conditions on the critical fracture strength. The bubble geometry affects the fracture stress by changing the stress concentration near the bubble and grain boundary interface. Loading conditions also make an important impact on the critical fracture strength – with multiple loading directions, the critical fracture strength appears to be lower. Intergranular crack propagation simulations have been performed considering different porosity levels. The variation of the critical fracture strength with porosity has then been compared with experimental measurements. 3D simulation results show a better agreement with the experiment data than the previous 2D results. The model is then extended to account for pressurized cracks. The model is proven to be capable

of reflecting fine fragmentation phenomena and providing insights into the mechanisms of HBS fine fragmentation. Simulations show that fracture occurs along the grain boundaries surrounding the large fission gas bubbles, which agrees with the hypothesized mechanism of fine fragmentation during LOCA transients. Bubble size and the amount of external pressure will change the critical pressure for crack initiation. Crack propagation at different recrystallization stages on a partial HBS is also investigated using this model. The recrystallization changes the grain structure, thus altering crack propagation paths and directions.

In Chapter 4, a model for cohesive fracture is used to study soil desiccation. A novel split of the elastic potential is proposed to account for the external work done by contact forces on regularized crack surfaces. Such a split results in a constitutive relation that naturally enforces traction-free boundary conditions and contact conditions in the vicinity of the cracks. The advantage of the contact split in systems subject to shear loading or even purely tensile loading is demonstrated in Section 4.3. We then develop a stochastic model for the random field of fracture properties in Section 4.2.3. The representation enables the integration of pointwise correlation between the fracture toughness and the critical fracture energy, and two prototypical covariance models are specifically considered to offer modeling flexibility. The variational phase-field fracture model with the proposed contact split is then applied to study thin-film fracture. A qualitative agreement with an analytical solution is established using a quasi one-dimensional simplification. A two-dimensional plane-stress model is subsequently used to explore the effect of random fracture properties on crack morphology. Forward propagation problems are first considered to study the effect of kernel smoothness, correlation length, and pointwise correlation between the fracture properties. In particular, it is observed that (1) smooth fracture properties result in larger fragment sizes (in mean); (2) the crack path is mainly influenced by the spatial variations of the fracture toughness, rather than fluctuations in the

critical fracture energy; and (3) different compositions of covariance functions can result in dramatically different crack patterns. Finally, the versatility offered by the probabilistic framework is highlighted by solving a statistical inverse problem based on physical experiments. Despite the apparent simplicity of the identification methodology, it is seen that the stochastic phase-field formulation allows key characteristics of observed crack patterns to be reproduced with reasonable accuracy, hence paving the way for future developments coupling fracture simulations with experimental results exhibiting substantial variability.

In Chapter 5, several models for ductile fracture are constructed within the variational framework. The framework provides two mechanisms for coupling plasticity and fracture, either using the plastic degradation function (E-P-PD) or through the coalescence dissipation (E-P-D). The proposed E-P-D model using this novel coalescence dissipation was compared with the E-P-PD model from [126]. Several important modeling choices are discussed in Section 5.3.1 in a “homogenized” setting: A crack geometric function $\alpha(d; \xi > 0)$ allows for an unperturbed elastic-plastic response prior to damage initiation (Section 5.3.1.2); a Lorentz-type degradation function separates out the critical fracture energy as an independent material property such that a regularization-length independent finite critical fracture strength can be obtained (Section 5.3.1.3); the decrease in the fracture toughness as a function of the increasing plastic strain can be modeled using the proposed coalescence dissipation (Section 5.3.1.4). Convergence of the softening response is numerically demonstrated in Section 5.3.2. The force-displacement responses obtained using both the proposed E-P-D model and the E-P-PD model presented in [126] become insensitive to the regularization length as the regularization length is sufficiently small, regardless of the amount of coalescence dissipation. The performance of the proposed E-P-D model is evaluated by simulating a three-point bending experiment in Section 5.4.1. The model is first calibrated against a standard tension test of a notched specimen, and

then applied to predict the crack path and load-deflection response of the aluminum alloy specimen in the three-point bending experiment. The predicted load-deflection curves and crack trajectories are found to be in good agreement with experimental measurements. The capabilities of the proposed E-P-PD model are examined by simulating an experiment from a recent Sandia Fracture Challenge. Both the predicted force-displacement response and the crack path indicate an excellent agreement with the experimental observations. Finally, debonding is incorporated into the E-P-D model to spallation of the oxide layer due to creep fracture. Debonding are observed to happen in the vicinity of the crack during normal operation conditions, and cracks propagate during the shut-down events.

Besides the advantages from theoretical aspects mentioned in Chapter 1, several other advantages of the variational framework from a modeling perspective can be summarized from the research presented in Chapters 3 to 5: the framework is flexible enough to describe a wide range of coupled field phenomena and many common fracture mechanisms; the definitions of specific stress-strain relations, micro- and macro-force balances, plastic flow, yield surface, heat generation and boundary conditions all follow directly from physically motivated constitutive energies and potentials; and the restrictions imposed on the constitutive choices to ensure existence and uniqueness of the solution also lead to numerically well-behaved models.

There are other coupled field phenomena that have not been incorporated into the proposed variational framework in its current form. What follows are some future research directions.

- Fatigue effects are important in structures subject to cyclic loading. There has been a number of attempts to incorporate fatigue effects in the phase-field model for fracture [138, 139, 140, 141], all of which introduce fatigue effects by “degrading” the fracture toughness as a function of certain fatigue measure.

Casting these models into the proposed variational framework requires the construction of a dual kinetic potential representing configurational changes of the material (similar to the coalescence dissipation introduced in Chapter 5).

- The proposed variational framework is suitable for modeling fracture propagation which is mainly driven by energetics. The fracture driving energies are often decomposed to provide some ad-hoc strength envelope for fracture nucleation. However, several authors have found that the existing decompositions of the strain energy density are not sufficiently flexible to model general strength envelopes, e.g. the Drucker-Prager criterion [142, 143]. Kumar et al. [143] introduced a micro body force blended with the crack geometric function to model general strength envelopes for nucleation. Recently, De Lorenzis and Maurini [144] proposed a variational formulation for nucleation which can be fit within our proposed variational framework. How best to extend such formulation to model the transition from nucleation to propagation remains to be an open question.
- As a direct extension of the work presented in Chapter 5, the ductile fracture model can be applied to simulate ductile failure with dynamic effects, e.g. subject to impact loading. For example, the Kalthoff-Winkler experiment [145] shows two qualitatively different failure mode at low and high loading rates. At low impact loading rates, brittle fracture is observed, which has become a standard benchmark problem for phase-field models of brittle fracture. At high impact loading rates, a shear band is formed due to large plastic deformation. There has been few attempts to simulate the ductile failure at high loading rates. [146] is a notable exception, where two different sets of parameters are calibrated for the two failure modes. A model which can simulate the two failure modes with the same set of parameters is yet to be discovered.

- Stress triaxiality effects are important in ductile failure. “Shear lips” are often observed in regions with high stress triaxiality, e.g. Figure 5.21. Borden et al. [121] proposed a means of incorporating stress triaxiality effects by scaling the plastic work. Ambati et al. [118, 119] scaled the plastic degradation function by a critical plastic strain to be calibrated. Although not variational, these approaches are shown to be capable of capturing shear lips. It would be of interest to incorporate stress triaxiality effects within the variational framework.

Appendix A

Code availability

Most calculations in this dissertation are carried out using RACCOON [147, 148], a software package specialized in phase-field for fracture. RACCOON is developed based on the MOOSE framework [149]. MOOSE stands for Multiphysics Object-Oriented Simulation Environment and is being actively developed and maintained by the Idaho National Laboratory. Both RACCOON and MOOSE are open-source projects.

Reproducibility crisis is a common issue in many communities, and the computational mechanics community is of no exception. As an attempt to address such issue, both RACCOON and MOOSE are being continuously tested using CIVET [150]. Most, if not all, models, verifications and numerical examples are available in the format of input files in the RACCOON GitHub repository.

Appendix B

The flooding algorithm for counting fragments

We describe the algorithm for clustering various elements in a mesh to individual fragments, as delineated by a phase field. The algorithm assigns each element a cluster order parameter, and different clusters are separated by a band of “broken” elements where the damage is above a threshold, i.e. $d > d_{\text{th}}$. Figure B.1 provides an example of this algorithm for a representative phase field.

The algorithm has a fundamental “flooding” structure. In particular, a seeding element broadcasts its information to all of its geometric neighbors, and each neighbor becomes a new seed for the next round of information propagation. In the context of counting fragments, the information of an element includes its state and the cluster it belongs to. An element is considered to be “intact” if all of its nodal damage values are below d_{th} , otherwise it is considered to be “broken”.

Three lists are managed by the algorithm. The first list **ALL** includes all elements that need to be classified. The second list **CANDIDATE**, optionally a first-in-first-out (FIFO) queue, includes all candidate elements for the current cluster. The third list **BROKEN** includes all “broken” elements. Each cluster CLUSTER^i is essentially a list of

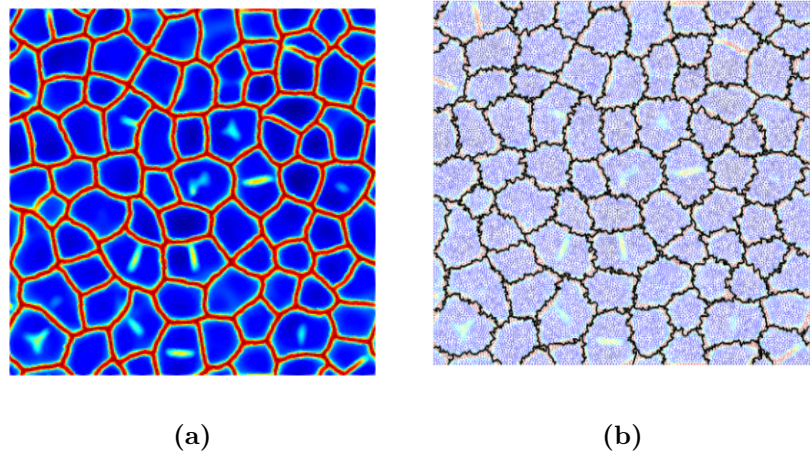


FIGURE B.1. (a) Final phase field obtained using a spatially correlated random \mathcal{G}_c and ψ_c . (b) Corresponding clusters labeled by the flooding algorithm. Cluster boundaries are marked in black.

elements that belong to the same parent cluster.

The algorithm consists of three stages. In the first stage, we update the damage values of all nodes and states of all elements. All elements that have a status change require reclassification. Therefore, any cluster that contains elements pending reclassification is pushed into **ALL** for future reclassification.

In the second stage, all “intact” elements in **ALL** are pushed into **CANDIDATE** one at a time until **ALL** has no more “intact” elements. Each new cluster is constructed by dequeuing **CANDIDATE**. The first element in **CANDIDATE** is dequeued after all of its connecting “intact” elements from **ALL** are pushed into **CANDIDATE**.

During the third stage, “broken” elements are grouped into their nearest cluster to preserve the total volume of the mesh. In our implementation, “broken” elements are assigned to clusters based on the solution to a minimization problem of weighted Euclidean distance between the elements and cluster centroids.

The skeleton of the flooding algorithm is outlined in Algorithm 2.

Algorithm 2 An iterative flooding algorithm for fragmentation count

```
1: Set  $d_0 \leftarrow 0$ 
2: Set cluster count  $c \leftarrow 0$ 
3: Group all elements into  $\text{CLUSTER}^c$ 
4: for time step  $n \in \{0, 1, 2, \dots\}$  do
5:   for each cluster  $\text{CLUSTER}^i$  do
6:     Move all “broken” elements into  $\text{BROKEN}$ 
7:     if  $\text{CLUSTER}^i$  contains any element that has a state change, i.e. from “intact” to “broken” then
8:       Move all remaining elements into  $\text{ALL}$ 
9:     end if
10:    end for
11:    while  $\text{ALL}$  is not empty do
12:      if All elements in  $\text{ALL}$  are “broken” then
13:        Move all elements in  $\text{ALL}$  into  $\text{BROKEN}$ 
14:        Break while loop
15:      else
16:        Move one “intact” element from  $\text{ALL}$  to  $\text{CANDIDATE}$ 
17:        Increment cluster count  $c \leftarrow c + 1$ 
18:        while  $\text{ALL}$  is not empty do
19:          for each element  $e$  that shares a common edge with the first element
in the queue  $\text{CANDIDATE}$  do
20:            if  $e$  is “intact” then
21:              Enqueue  $e$  into  $\text{CANDIDATE}$ 
22:            else
23:              Move  $e$  into  $\text{BROKEN}$ 
24:            end if
25:          end for
26:          Dequeue first element in  $\text{CANDIDATE}$  into  $\text{CLUSTER}^c$ 
27:        end while
28:      end if
29:    end while
30:    Move all elements in  $\text{BROKEN}$  into their nearest cluster
31: end for
```

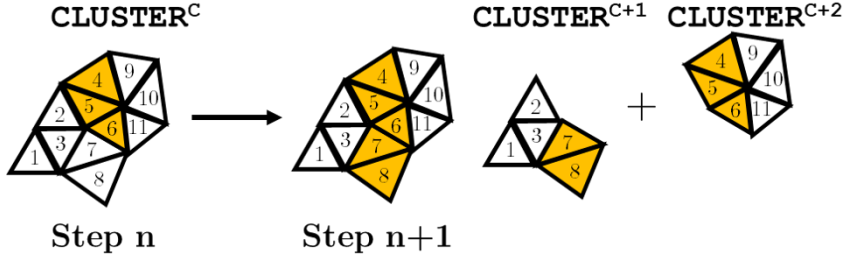


FIGURE B.2. Status change from step n to step $n+1$. “Broken” elements are labeled in yellow, and “intact” elements are white. The step-by-step reclassification procedure is shown in Table B.1.

Table B.1. Demonstration of classification after the update from time step n to time step $n+1$. Broken elements are denoted with an underscore.

Step	Stage	ALL	CANDIDATE	BROKEN	Comments
n		\emptyset	\emptyset	\emptyset	$CLUSTER^c = \{1, 2, 3, \underline{4}, \underline{5}, \underline{6}, 7, 8, 9, 10, 11\}$
$n+1$		\emptyset	\emptyset	\emptyset	$CLUSTER^c = \{1, 2, 3, \underline{4}, \underline{5}, \underline{6}, \underline{7}, \underline{8}, 9, 10, 11\}$
$n+1$	1	$\{1, 2, 3, 9, 10, 11\}$	\emptyset	$\{\underline{4}, \underline{5}, \underline{6}, \underline{7}, \underline{8}\}$	Declassify $CLUSTER^c$
$n+1$	2	$\{2, 3, 9, 10, 11\}$	$\{1\}$	$\{\underline{4}, \underline{5}, \underline{6}, \underline{7}, \underline{8}\}$	Enqueue element 1 to CANDIDATE
$n+1$	2	$\{9, 10, 11\}$	$\{1, 2, 3\}$	$\{\underline{4}, \underline{5}, \underline{6}, \underline{7}, \underline{8}\}$	Enqueue connected elements 2, 3
$n+1$	2	$\{9, 10, 11\}$	$\{2, 3\}$	$\{\underline{4}, \underline{5}, \underline{6}, \underline{7}, \underline{8}\}$	Dequeue element 1
$n+1$	2	$\{9, 10, 11\}$	$\{3\}$	$\{\underline{4}, \underline{5}, \underline{6}, \underline{7}, \underline{8}\}$	Dequeue element 2
$n+1$	2	$\{9, 10, 11\}$	\emptyset	$\{\underline{4}, \underline{5}, \underline{6}, \underline{7}, \underline{8}\}$	Dequeue element 3
$n+1$	2	$\{10, 11\}$	$\{9\}$	$\{\underline{4}, \underline{5}, \underline{6}, \underline{7}, \underline{8}\}$	$CLUSTER^{c+1} = \{1, 2, 3\}$
$n+1$	2	\emptyset	$\{9, 10, 11\}$	$\{\underline{4}, \underline{5}, \underline{6}, \underline{7}, \underline{8}\}$	Enqueue element 9 to CANDIDATE
$n+1$	2	\emptyset	$\{10, 11\}$	$\{\underline{4}, \underline{5}, \underline{6}, \underline{7}, \underline{8}\}$	Enqueue connected elements 10, 11
$n+1$	2	\emptyset	$\{11\}$	$\{\underline{4}, \underline{5}, \underline{6}, \underline{7}, \underline{8}\}$	Dequeue element 9
$n+1$	2	\emptyset	\emptyset	$\{\underline{4}, \underline{5}, \underline{6}, \underline{7}, \underline{8}\}$	Dequeue element 10
$n+1$	2	\emptyset	\emptyset	$\{\underline{4}, \underline{5}, \underline{6}, \underline{7}, \underline{8}\}$	Dequeue element 11
$n+1$	3	\emptyset	\emptyset	$\{\underline{4}, \underline{5}, \underline{6}\}$	Group elements 7, 8 into $CLUSTER^{c+1}$
$n+1$	3	\emptyset	\emptyset	\emptyset	Group elements 4, 5, 6 into $CLUSTER^{c+2}$

Bibliography

- [1] R Rodriguez. Hydrogeotechnical characterization of a metallurgical waste. *Canadian Geotechnical Journal*, 43(10):1042–1060, 2006.
- [2] Petr Kubík, František Šebek, and Jindřich Petruška. Notched specimen under compression for ductile failure criteria. *Mechanics of Materials*, 125:94–109, 2018.
- [3] Petr Kubík, František Šebek, Josef Zapletal, Jindřich Petruška, and Tomáš Návrat. Ductile failure predictions for the three-point bending test of a complex geometry made from aluminum alloy. *Journal of Engineering Materials and Technology*, 141(4), 2019.
- [4] I. BABUŠKA and J. M. MELENK. The partition of unity method. *International Journal for Numerical Methods in Engineering*, 40(4):727–758, 1997.
- [5] Nicolas Moës, John Dolbow, and Ted Belytschko. A finite element method for crack growth without remeshing. *International Journal for Numerical Methods in Engineering*, 46(1):131–150, 1999. ISSN 1097-0207.
- [6] A. Needleman. Micromechanical modelling of interfacial decohesion. *Ultramicroscopy*, 40:203–214, 1992.
- [7] M. Ortiz and A. Pandolfi. Finite-deformation irreversible cohesive element for three-dimensional crack-propagation analysis. *International Journal for Numerical Methods in Engineering*, 44:1267–1282, 1999.
- [8] Masayuki Kamaya, Yoshihiro Kawamura, and Takayuki Kitamura. Three-dimensional local stress analysis on grain boundaries in polycrystalline material. *International Journal of Solids and Structures*, 44(10):3267 – 3277, 2007. ISSN 0020-7683.
- [9] Masayuki Kamaya and Mitsuhiro Itakura. Simulation for intergranular stress corrosion cracking based on a three-dimensional polycrystalline model. *Engineering Fracture Mechanics*, 76(3):386 – 401, 2009. ISSN 0013-7944.

- [10] G.A. Francfort and J.J. Marigo. Revisiting brittle fracture as an energy minimization problem. *Journal of the Mechanics and Physics of Solids*, 46(8):1319–1342, 1998.
- [11] B. Bourdin, G.A. Francfort, and J.J. Marigo. Numerical experiments in revisited brittle fracture. *Journal of the Mechanics and Physics of Solids*, 48(4):797–826, 2000.
- [12] Blaise Bourdin, Gilles A Francfort, and Jean-Jacques Marigo. The variational approach to fracture. *Journal of elasticity*, 91(1-3):5–148, 2008.
- [13] Kim Pham and Jean-Jacques Marigo. From the onset of damage to rupture: construction of responses with damage localization for a general class of gradient damage models. *Continuum Mechanics and Thermodynamics*, 25(2-4):147–171, 2013.
- [14] Luigi Ambrosio and Vincenzo Maria Tortorelli. Approximation of functional depending on jumps by elliptic functional via t-convergence. *Communications on Pure and Applied Mathematics*, 43(8):999–1036, 1990.
- [15] Jian-Ying Wu. A unified phase-field theory for the mechanics of damage and quasi-brittle failure. *Journal of the Mechanics and Physics of Solids*, 103:72–99, 2017.
- [16] A. Karma, D. A. Kessler, and H. Levine. Phase-field model of mode III dynamic fracture. *Physical Review Letters*, 87(4):045501–1–4, 2001.
- [17] A. Karma and A. E. Lobkovsky. Unsteady crack motion and branching in a phase-field model of brittle fracture. *Physical Review Letters*, 93(10):245510, 2004.
- [18] H. Henry and H. Levine. Dynamic instabilities of fracture under biaxial strain using a phase field model. *Physical Review Letters*, 93(10):105504, 2004.
- [19] R. Spatschek, C. M. Gugenberger, and E. Brener. Phase field modeling of fracture and stress-induced phase transitions. *Physical Review E*, 75:066111, 2007.
- [20] H. Amor, J. J. Marigo, and C. Maurini. Regularized formulation of the variational brittle fracture with unilateral contact: Numerical experiments. *Journal of the Mechanics and Physics of Solids*, 57(8):1209–1229, 2009.
- [21] Maurice Anthony Biot. Thermoelasticity and irreversible thermodynamics. *Journal of applied physics*, 27(3):240–253, 1956.
- [22] George Herrmann. On variational principles in thermoelasticity and heat conduction. *Quarterly of Applied Mathematics*, 21(2):151–155, 1963.

- [23] M Ben-Amoz. On a variational theorem in coupled thermoelasticity. 1965.
- [24] John Tinsley Oden and Junuthula Narasimha Reddy. *Variational methods in theoretical mechanics*. Springer Science Business Media, 2012.
- [25] A Molinari and M Ortiz. Global viscoelastic behavior of heterogeneous thermoelastic materials. *International journal of solids and structures*, 23(9):1285–1300, 1987.
- [26] Gautam Batra. On a principle of virtual work for thermo-elastic bodies. *Journal of elasticity*, 21(2):131–146, 1989.
- [27] Seishiro Matsubara and Kenjiro Terada. A variationally consistent formulation of the thermo-mechanically coupled problem with non-associative viscoplasticity for glassy amorphous polymers. *International Journal of Solids and Structures*, 212:152–168, 2021.
- [28] Qiang Yang, Laurent Stainier, and Michael Ortiz. A variational formulation of the coupled thermo-mechanical boundary-value problem for general dissipative solids. *Journal of the Mechanics and Physics of Solids*, 54(2):401–424, 2006.
- [29] Gianni Dal Maso. *An introduction to Γ -convergence*, volume 8. Springer Science Business Media, 2012.
- [30] Andrea Braides et al. *Approximation of free-discontinuity problems*. Number 1694. Springer Science & Business Media, 1998.
- [31] Ronald F Gariepy. Functions of bounded variation and free discontinuity problems (oxford mathematical monographs) by luigi ambrosio, nicolo fucso and diego pallara: 434 pp., £ 55.00, isbn 0-19-850254-1 (clarendon press, oxford, 2000). *Bulletin of the London Mathematical Society*, 33(4):492–512, 2001.
- [32] Satish Balay, Shrirang Abhyankar, Mark F. Adams, Jed Brown, Peter Brune, Kris Buschelman, Lisandro Dalcin, Alp Dener, Victor Eijkhout, William D. Gropp, Dmitry Karpeyev, Dinesh Kaushik, Matthew G. Knepley, Dave A. May, Lois Curfman McInnes, Richard Tran Mills, Todd Munson, Karl Rupp, Patrick Sanan, Barry F. Smith, Stefano Zampini, Hong Zhang, and Hong Zhang. PETSc Web page. <https://www.mcs.anl.gov/petsc>, 2019. URL <https://www.mcs.anl.gov/petsc>.
- [33] Steve Benson, Lois Curfman McInnes, Jorge J More, and Jason Sarich. Tao users manual. Technical report, Argonne National Lab., IL (US), 2003.
- [34] Michael A Heroux, Roscoe A Bartlett, Vicki E Howle, Robert J Hoekstra, Jonathan J Hu, Tamara G Kolda, Richard B Lehoucq, Kevin R Long, Roger P Pawłowski, Eric T Phipps, et al. An overview of the trilinos project. *ACM Transactions on Mathematical Software (TOMS)*, 31(3):397–423, 2005.

- [35] Desmond J Higham and Nicholas J Higham. *MATLAB guide*. SIAM, 2016.
- [36] Timo Heister, Mary F Wheeler, and Thomas Wick. A primal-dual active set method and predictor-corrector mesh adaptivity for computing fracture propagation using a phase-field approach. *Computer Methods in Applied Mechanics and Engineering*, 290:466–495, 2015.
- [37] Tianchen Hu, Johann Guilleminot, and John E Dolbow. A phase-field model of fracture with frictionless contact and random fracture properties: Application to thin-film fracture and soil dessication. *Computer Methods in Applied Mechanics and Engineering*, 368:113106, 2020.
- [38] Nathan Capps, Colby Jensen, Fabiola Cappia, Jason Harp, Kurt Terrani, Nicolas Woolstenhulme, and Daniel Wachs. A critical review of high burnup fuel fragmentation, relocation, and dispersal under loss-of-coolant accident conditions. *Journal of Nuclear Materials*, 546:152750, 2021.
- [39] Vincenzo V. Rondinella and Thierry Wiss. The high burn-up structure in nuclear fuel. *Materials Today*, 13(12):24–32, 2010.
- [40] J. A. Turnbull, S. K. Yagnik, M. Hirai, D. M. Staicu, and C. T. Walker. An assessment of the fuel pulverization threshold during loca-type temperature transients. *Nuclear Science and Engineering*, 179(4):477–485, 2015.
- [41] Wen Jiang, Benjamin W. Spencer, and John E. Dolbow. Ceramic nuclear fuel fracture modeling with the extended finite element method. *Engineering Fracture Mechanics*, 223:106713, 2020. ISSN 0013-7944.
- [42] Katalin Kulacsy. Mechanistic model for the fragmentation of the high-burnup structure during loca. *Journal of Nuclear Materials*, 466:409 – 416, 2015.
- [43] Lars O. Jernkvist. A review of analytical criteria for fission gas induced fragmentation of oxide fuel in accident conditions. *Progress in Nuclear Energy*, 119:103188, 2020. ISSN 0149-1970.
- [44] Pritam Chakraborty, Yongfeng Zhang, and Michael R. Tonks. Multi-scale modeling of microstructure dependent intergranular brittle fracture using a quantitative phase-field based method. *Computational Materials Science*, 113: 38 – 52, 2016. ISSN 0927-0256.
- [45] Martin Diehl, Marcel Wicke, Pratheek Shanthraj, Franz Roters, Angelika Brueckner-Foit, and Dierk Raabe. Coupled crystal plasticity–phase field fracture simulation study on damage evolution around a void: Pore shape versus crystallographic orientation. *JOM*, 69(5):872–878, May 2017.

- [46] Chukwudi Chukwudzie, Blaise Bourdin, and Keita Yoshioka. A variational phase-field model for hydraulic fracturing in porous media. *Computer Methods in Applied Mechanics and Engineering*, 347:957 – 982, 2019.
- [47] Andro Mikelić, Mary F Wheeler, and Thomas Wick. A quasi-static phase-field approach to pressurized fractures. *Nonlinearity*, 28(5):1371–1399, apr 2015.
- [48] C. Miehe, F. Welschinger, and M. Hofacker. Thermodynamically consistent phase-field models of fracture: Variational principles and multi-field FE implementations. *International Journal for Numerical Methods in Engineering*, 83: 1273–1311, 2010.
- [49] C. Miehe, M. Hofacker, and F. Welschinger. A phase field model for rate-independent crack propagation: Robust algorithmic implementation based on operator splits. *Computer Methods in Applied Mechanics and Engineering*, 199: 2765–2778, 2010.
- [50] Jian-Ying Wu. A unified phase-field theory for the mechanics of damage and quasi-brittle failure. *Journal of the Mechanics and Physics of Solids*, 103:72 – 99, 2017.
- [51] Zachary A. Wilson and Chad M. Landis. Phase-field modeling of hydraulic fracture. *Journal of the Mechanics and Physics of Solids*, 96:264 – 290, 2016. ISSN 0022-5096.
- [52] Keita Yoshioka, Dmitri Naumov, and Olaf Kolditz. On crack opening computation in variational phase-field models for fracture. *Computer Methods in Applied Mechanics and Engineering*, 369:113210, 2020.
- [53] B. Bourdin, G.A. Francfort, and JJ Marigo. The variational approach to fracture. *Journal of Elasticity*, 91:5 – 148, 2008.
- [54] K. Govers. Comparison of interatomic potentials for UO₂. *Journal of Nuclear Materials*, 366:161–177, 2007.
- [55] N. Moelans, B. Blanpain, and P. Wollants. Quantitative analysis of grain boundary properties in a generalized phase field model for grain growth in anisotropic systems. *Phys. Rev. B*, 78:024113, Jul 2008.
- [56] E.N. Hodkin. The ratio of grain boundary energy to surface energy of nuclear ceramics as determined from pore geometries. *Journal of Nuclear Materials*, 88(1):7 – 14, 1980. ISSN 0022-3115.
- [57] G.L. Reynolds, W.B. Beeré, and P.T. Sawbridge. The effect of fission products on the ratio of grain-boundary energy to surface energy in irradiated uranium dioxide. *Journal of Nuclear Materials*, 41(1):112 – 114, 1971. ISSN 0022-3115.

- [58] Mohamed S. Ebeida, Scott A. Mitchell, Anjul Patney, Andrew A. Davidson, and John D. Owens. A simple algorithm for maximal poisson-disk sampling in high dimensions. *Computer Graphics Forum*, 31(2pt4):785–794, 2012.
- [59] M. Oguma. Microstructure effects on fracture strength of UO₂ fuel pellets. *Journal of Nuclear Science and Technology*, 19(12):1005–1014, 1982.
- [60] A. G. Evans and R. W. Davidge. The strength and fracture of stoichiometric polycrystalline UO₂. *Journal of Nuclear Materials*, 33:249–260, 1969.
- [61] Anders Puranen. Post test examinations on loca tested rods. Studsvik Report STUDSVIK/N-13/198, Studsvik, 2013.
- [62] R. L. Williamson, J. D. Hales, S. R. Novascone, G. Pastore, K. A. Gamble, B. W. Spencer, W. Jiang, S. A. Pitts, A. Casagrande, D. Schwen, A. X. Zabriskie, A. Toptan, R. Gardner, C. Matthews, W. Liu, , and H. Chen. Bison: A flexible code for advanced simulation of the performance of multiple nuclear fuel forms. *Nuclear Technology*, 2020.
- [63] L. K. Aagesen, S. Biswas, W. Jiang, A. M. Jokisaari, D. Andersson, M. W. D. Cooper, and C. Matthews. Determine fragmentation criteria in high-burnup uo₂ fuel during accident conditions. Technical Report INL/EXT-20-00558, Idaho National Laboratory, 2020.
- [64] Hanen Amor, Jean-Jacques Marigo, and Corrado Maurini. Regularized formulation of the variational brittle fracture with unilateral contact: Numerical experiments. *Journal of the Mechanics and Physics of Solids*, 57(8):1209 – 1229, 2009. ISSN 0022-5096.
- [65] Michael Strobl and Thomas Seelig. A novel treatment of crack boundary conditions in phase field models of fracture. *Pamm*, 15(1):155–156, 2015.
- [66] Michael Strobl and Thomas Seelig. On constitutive assumptions in phase field approaches to brittle fracture. *Procedia Structural Integrity*, 2:3705–3712, 2016.
- [67] Fan Fei and Jinhyun Choo. A phase-field method for modeling cracks with frictional contact. *arXiv preprint arXiv:1905.10547*, 2019.
- [68] Fan Fei and Jinhyun Choo. A phase-field model of geologic shear fracture, 2020.
- [69] Yu-Sheng Lo, Michael Borden, K. Ravi-Chandar, and Chad M. Landis. A phase-field model for fatigue crack growth. *Journal of the Mechanics and Physics of Solids*, 132(103684), 2019.
- [70] JTA Roberts, E Smith, N Fuhrman, and D Cubicciotti. On the pellet-cladding interaction phenomenon. *Nuclear Technology*, 35(1):131–144, 1977.

- [71] Bruno Michel, Jérôme Sercombe, Gilles Thouvenin, and Rémy Chatelet. 3d fuel cracking modelling in pellet cladding mechanical interaction. *Engineering fracture mechanics*, 75(11):3581–3598, 2008.
- [72] Lars Olof Jernkvist. A model for predicting pellet-cladding interaction-induced fuel rod failure. *Nuclear engineering and design*, 156(3):393–399, 1995.
- [73] Fumihsisa Nagase and Toyoshi Fuketa. Effect of pre-hydriding on thermal shock resistance of zircaloy-4 cladding under simulated loss-of-coolant accident conditions. *Journal of nuclear science and technology*, 41(7):723–730, 2004.
- [74] Michael Billone, Yong Yan, Tatiana Burtseva, Robert Daum, et al. Cladding embrittlement during postulated loss-of-coolant accidents. Technical report, Argonne National Lab.(ANL), Argonne, IL (United States), 2008.
- [75] Mohamed M El-Basyouny and Matthew Witczak. Calibration of alligator fatigue cracking model for 2002 design guide. *Transportation research record*, 1919(1):76–86, 2005.
- [76] Sherif M El-Badawy, Myung Goo Jeong, and Mohamed El-Basyouny. Methodology to predict alligator fatigue cracking distress based on asphalt concrete dynamic modulus. *Transportation Research Record*, 2095(1):115–124, 2009.
- [77] T Saar and O Talvik. Automatic asphalt pavement crack detection and classification using neural networks. In *2010 12th Biennial Baltic Electronics Conference*, pages 345–348. IEEE, 2010.
- [78] Joe W Button and Robert L Lytton. Guidelines for using geosynthetics with hot-mix asphalt overlays to reduce reflective cracking. *Transportation Research Record*, 2004(1):111–119, 2007.
- [79] Yetkin Yildirim, Ahmed Qatan, Jorge Prozzi, et al. *Field manual for crack sealing in asphalt pavements.*, 2006.
- [80] John W Hutchinson and Zhigang Suo. Mixed mode cracking in layered materials. In *Advances in applied mechanics*, volume 29, pages 63–191. Elsevier, 1991.
- [81] Kevin M Crosby and R Mark Bradley. Fragmentation of thin films bonded to solid substrates: Simulations and a mean-field theory. *Physical Review E*, 55(5):6084, 1997.
- [82] Kwan-tai Leung and Zoltan Néda. Pattern formation and selection in quasistatic fracture. *Physical review letters*, 85(3):662, 2000.

- [83] Supti Sadhukhan, Tapati Dutta, and Sujata Tarafdar. Crack formation in composites through a spring model. *Physica A: Statistical Mechanics and its Applications*, 390(4):731–740, 2011.
- [84] Jingwen Zhang, Yuyang Lu, Linghui He, Lizhong Yang, and Yong Ni. Modeling progressive interfacial debonding of a mud-crack film on elastic substrates. *Engineering Fracture Mechanics*, 177:123–132, 2017.
- [85] Marcelo Sánchez, Osvaldo L Manzoli, and Leonardo JN Guimar˜aes. Modeling 3-d desiccation soil crack networks using a mesh fragmentation technique. *Computers and Geotechnics*, 62:27–39, 2014.
- [86] J Liang, R Huang, Jean-Herve Prevost, and Z Suo. Evolving crack patterns in thin films with the extended finite element method. *International Journal of Solids and Structures*, 40(10):2343–2354, 2003.
- [87] N Sukumar and J-H Prévost. Modeling quasi-static crack growth with the extended finite element method part i: Computer implementation. *International journal of solids and structures*, 40(26):7513–7537, 2003.
- [88] Rui Huang, N Sukumar, and J-H Prévost. Modeling quasi-static crack growth with the extended finite element method part ii: Numerical applications. *International Journal of Solids and Structures*, 40(26):7539–7552, 2003.
- [89] Z Cedric Xia and John W Hutchinson. Crack patterns in thin films. *Journal of the Mechanics and Physics of Solids*, 48(6-7):1107–1131, 2000.
- [90] HM Yin, GH Paulino, and William G Buttlar. An explicit elastic solution for a brittle film with periodic cracks. *International Journal of Fracture*, 153(1):39, 2008.
- [91] So Kitsunezaki, Akio Nakahara, and Yousuke Matsuo. Shaking-induced stress anisotropy in the memory effect of paste. *EPL (Europhysics Letters)*, 114(6):64002, 2016.
- [92] So Kitsunezaki, Yousuke Matsuo, and Akio Nakahara. Stress development up to crack formation in drying paste. *Journal of Chemical Engineering of Japan*, 50(10):775–779, 2017.
- [93] Zoltán Halász, Akio Nakahara, So Kitsunezaki, and Ferenc Kun. Effect of disorder on shrinkage-induced fragmentation of a thin brittle layer. *Physical Review E*, 96(3):033006, 2017.
- [94] So Kitsunezaki, Arina Sasaki, Akihiro Nishimoto, Tsuyoshi Mizuguchi, Yousuke Matsuo, and Akio Nakahara. Memory effect and anisotropy of particle arrangements in granular paste. *The European Physical Journal E*, 40(10):88, 2017.

- [95] Akio Nakahara, Tomoki Hiraoka, Rokuya Hayashi, Yousuke Matsuo, and So Kitsunezaki. Mechanism of memory effect of paste which dominates desiccation crack patterns. *Philosophical Transactions of the Royal Society A*, 377(2136):20170395, 2018.
- [96] Katherine A. Acton, Sarah C. Baxter, Bahador Bahmani, Philip L. Clarke, and Reza Abedi. Voronoi tessellation based statistical volume element characterization for use in fracture modeling. *Computer Methods in Applied Mechanics and Engineering*, 336:135 – 155, 2018.
- [97] Darith-Anthony Hun, Johann Guilleminot, Julien Yvonnet, and Michel Bornert. Stochastic multiscale modeling of crack propagation in random heterogeneous media. *International Journal for Numerical Methods in Engineering*, 119(13):1325–1344, 2019.
- [98] C. Peco, Y. Liu, C. Rhea, and J.E. Dolbow. Models and simulations of surfactant-driven fracture in particle rafts. *International Journal of Solids and Structures*, 156:194–209, 2019.
- [99] Jian-Ying Wu and Miguel Cervera. A thermodynamically consistent plastic-damage framework for localized failure in quasi-brittle solids: Material model and strain localization analysis. *International Journal of Solids and Structures*, 88:227–247, 2016.
- [100] Rudy JM Geelen, Yingjie Liu, Tianchen Hu, Michael R Tupek, and John E Dolbow. A phase-field formulation for dynamic cohesive fracture. *Computer Methods in Applied Mechanics and Engineering*, 348:680–711, 2019.
- [101] Mircea Grigoriu. Existence and construction of translation models for stationary non-gaussian processes. *Probabilistic Engineering Mechanics*, 24:545–551, 2009.
- [102] E.T. Jaynes. Information theory and statistical mechanics i. *Physical Review*, 106(4):620–630, 1957.
- [103] E.T. Jaynes. Information theory and statistical mechanics ii. *Physical Review*, 108(2):171–190, 1957.
- [104] C.E. Shannon. A mathematical theory of communication. *Bell System Technical Journal*, 27(3):379–423, 1948.
- [105] C.E. Shannon. A mathematical theory of communication. *Bell System Technical Journal*, 27(4):623–656, 1948.
- [106] N. Balakrishnan and C.-D. Lai. *Continuous Bivariate Distributions*. Springer-Verlag New York, 2009.

- [107] Patrick Moran. Statistical inference with bivariate gamma distributions. *Biometrika Trust*, 56:627–634, 1969.
- [108] R. G. Ghanem and P. D. Spanos. *Stochastic Finite Elements: A Spectral Approach (Revised Edition)*. Dover, 2003.
- [109] O. Le Maitre and O. Knio. *Spectral Methods for Uncertainty Quantification*. Springer Netherlands, 2010.
- [110] J.L. Beuth. Cracking of thin bonded films in residual tension. *International Journal of Solids and Structures*, 29(13):1657 – 1675, 1992. ISSN 0020-7683.
- [111] R Obrzud. *The hardening soil model: A practical guidebook*. Zace Services, 2010.
- [112] A Ramsaroop, K Kanny, and TP Mohan. Fracture toughness studies of polypropylene-clay nanocomposites and glass fibre reinforced polypropylene composites. *Materials Sciences and Applications*, 1(05):301, 2010.
- [113] R Rodríguez, Marcelo Sanchez, A Ledesma, and A Lloret. Experimental and numerical analysis of desiccation of a mining waste. *Canadian Geotechnical Journal*, 44(6):644–658, 2007.
- [114] MR Lakshmikantha, PC Prat, and A Ledesma. Image analysis for the quantification of a developing crack network on a drying soil. *Geotechnical Testing Journal*, 32(6):505–515, 2009.
- [115] Roberto Alessi, Jean-Jacques Marigo, and Stefano Vidoli. Gradient Damage Models Coupled with Plasticity and Nucleation of Cohesive Cracks. *Archive for Rational Mechanics and Analysis*, 214(2):575–615, November 2014. ISSN 0003-9527, 1432-0673.
- [116] Roberto Alessi, Jean-Jacques Marigo, and Stefano Vidoli. Gradient damage models coupled with plasticity: Variational formulation and main properties. *Mechanics of Materials*, pages 351–367, 2015.
- [117] Roberto Alessi, Jean-Jacques Marigo, Corrado Maurini, and Stefano Vidoli. Coupling damage and plasticity for a phase-field regularisation of brittle, cohesive and ductile fracture: One-dimensional examples. *International Journal of Mechanical Sciences*, 149:559–576, December 2018. ISSN 0020-7403.
- [118] M. Ambati, T. Gerasimov, and L. De Lorenzis. Phase-field modeling of ductile fracture. *Computational Mechanics*, 55(5):1017–1040, May 2015. ISSN 0178-7675, 1432-0924.

- [119] Marreddy Ambati, Roland Kruse, and Laura De Lorenzis. A phase-field model for ductile fracture at finite strains and its experimental verification. *Computational Mechanics*, 57(1):149–167, 2016.
- [120] Christian Miehe, Fadi Aldakheel, and Arun Raina. Phase field modeling of ductile fracture at finite strains: A variational gradient-extended plasticity-damage theory. *International Journal of Plasticity*, 84:1–32, September 2016. ISSN 0749-6419.
- [121] Michael J Borden, Thomas JR Hughes, Chad M Landis, Amin Anvari, and Isaac J Lee. A phase-field formulation for fracture in ductile materials: Finite deformation balance law derivation, plastic degradation, and stress triaxiality effects. *Computer Methods in Applied Mechanics and Engineering*, 312:130–166, 2016.
- [122] Michael J. Borden, Thomas J. R. Hughes, Chad M. Landis, Amin Anvari, and Isaac J. Lee. Phase-Field Formulation for Ductile Fracture. In *Advances in Computational Plasticity: A Book in Honour of D. Roger J. Owen*, volume 46, page 443. Springer International Publishing, September 2017. ISBN 978-3-319-60885-3.
- [123] R. Alessi, M. Ambati, T. Gerasimov, S. Vidoli, and L. De Lorenzis. Comparison of Phase-Field Models of Fracture Coupled with Plasticity. In *Advances in Computational Plasticity: A Book in Honour of D. Roger J. Owen*, volume 46, page 443. Springer International Publishing, September 2017. ISBN 978-3-319-60885-3.
- [124] M. Ortiz and L. Stainier. The variational formulation of viscoplastic constitutive updates. *Computer Methods in Applied Mechanics and Engineering*, 171(3):419–444, April 1999. ISSN 0045-7825.
- [125] Eric Lorentz, Sam Cuvilliez, and Kyrylo Kazymyrenko. Convergence of a gradient damage model toward a cohesive zone model. *Comptes Rendus Mécanique*, 339(1):20–26, 2011.
- [126] Brandon Talamini, Michael R. Tupek, Andrew J. Stershic, Tianchen Hu, James W. Foulk III, Jakob T. Ostien, and John E. Dolbow. Attaining regularization length insensitivity in ductile failure with a variational phase-field model of cohesive fracture. *Computer Methods in Applied Mechanics and Engineering*, 2021.
- [127] Christian Miehe, M Hofacker, L-M Schänzel, and Fadi Aldakheel. Phase field modeling of fracture in multi-physics problems. part ii. coupled brittle-to-ductile failure criteria and crack propagation in thermo-elastic-plastic solids. *Computer Methods in Applied Mechanics and Engineering*, 294:486–522, 2015.

- [128] Omar Rodriguez, Ali Matinmanesh, Sunjeev Phull, Emil H Schemitsch, Paul Zalzal, Owen M Clarkin, Marcello Papini, and Mark R Towler. Silica-based and borate-based, titania-containing bioactive coatings characterization: critical strain energy release rate, residual stresses, hardness, and thermal expansion. *Journal of functional biomaterials*, 7(4):32, 2016.
- [129] Sanjib C Chowdhury, Ethan A Wise, Raja Ganesh, and John W Gillespie Jr. Effects of surface crack on the mechanical properties of silica: A molecular dynamics simulation study. *Engineering Fracture Mechanics*, 207:99–108, 2019.
- [130] Truong Vo, Bang He, Michael Blum, Angelo Damone, and Pania Newell. Molecular scale insight of pore morphology relation with mechanical properties of amorphous silica using reaxff. *Computational Materials Science*, 183:109881, 2020.
- [131] Bo Yin and Michael Kaliske. A ductile phase-field model based on degrading the fracture toughness: Theory and implementation at small strain. *Computer Methods in Applied Mechanics and Engineering*, 366:113068, 2020.
- [132] Gustavo Weber and Lallit Anand. Finite deformation constitutive equations and a time integration procedure for isotropic, hyperelastic-viscoplastic solids. *Computer Methods in Applied Mechanics and Engineering*, 79(2):173–202, 1990.
- [133] M.Z. Hossain, C.-J. Hsueh, B. Bourdin, and K. Bhattacharya. Effective toughness of heterogeneous media. *Journal of the Mechanics and Physics of Solids*, 71:15–32, November 2014. ISSN 0022-5096. doi: 10.1016/j.jmps.2014.06.002. URL <http://www.sciencedirect.com/science/article/pii/S0022509614001215>.
- [134] J. R. Rice. A Path Independent Integral and the Approximate Analysis of Strain Concentration by Notches and Cracks. *Journal of Applied Mechanics*, 35(2):379–386, June 1968. ISSN 0021-8936. doi: 10.1115/1.3601206. URL <http://dx.doi.org/10.1115/1.3601206>.
- [135] Brad L Boyce, Sharlotte LB Kramer, H Eliot Fang, Theresa E Cordova, Michael K Neilsen, K Dion, Amy K Kaczmarowski, Erin Karasz, Liang Xue, Andrew J Gross, et al. The sandia fracture challenge: blind round robin predictions of ductile tearing. *International Journal of Fracture*, 186(1-2):5–68, 2014.
- [136] Junhang Guo. *An experimental and numerical investigation on damage evolution and ductile fracture mechanism of aluminum alloy*. PhD thesis, PhD dissertation, The University of Tokushima, 2013.

- [137] Fei Xue, Tian-Le Cheng, and You-Hai Wen. Stress analysis of the steam-side oxide of boiler tubes: Contributions from thermal strain, interface roughness, creep, and oxide growth. *Oxidation of Metals*, 93(5):515–543, 2020.
- [138] Martha Seiler, Thomas Linse, Peter Hantschke, and Markus Kästner. An efficient phase-field model for fatigue fracture in ductile materials. *Engineering Fracture Mechanics*, 224:106807, 2020.
- [139] Ataollah Mesgarnejad, Anahita Imanian, and Alain Karma. Phase-field models for fatigue crack growth. *Theoretical and Applied Fracture Mechanics*, 103:102282, 2019.
- [140] Roberto Alessi, Stefano Vidoli, and Laura De Lorenzis. A phenomenological approach to fatigue with a variational phase-field model: The one-dimensional case. *Engineering fracture mechanics*, 190:53–73, 2018.
- [141] Yu-Sheng Lo, Michael J Borden, K Ravi-Chandar, and Chad M Landis. A phase-field model for fatigue crack growth. *Journal of the Mechanics and Physics of Solids*, 132:103684, 2019.
- [142] Erwan Tanné, Tianyi Li, Blaise Bourdin, J-J Marigo, and Corrado Maurini. Crack nucleation in variational phase-field models of brittle fracture. *Journal of the Mechanics and Physics of Solids*, 110:80–99, 2018.
- [143] Aditya Kumar, Blaise Bourdin, Gilles A Francfort, and Oscar Lopez-Pamies. Revisiting nucleation in the phase-field approach to brittle fracture. *Journal of the Mechanics and Physics of Solids*, page 104027, 2020.
- [144] Laura De Lorenzis and Corrado Maurini. Nucleation under multi-axial loading in variational phase-field models of brittle fracture. *International Journal of Fracture*, pages 1–21, 2021.
- [145] JF Kalthoff and S Winkler. Failure mode transition at high rates of shear loading. *DGM Informationsgesellschaft mbH, Impact Loading and Dynamic Behavior of Materials*, 1:185–195, 1988.
- [146] Heike Ulmer, Martina Hofacker, and Christian Miehe. Phase field modeling of brittle and ductile fracture. *PAMM*, 13(1):533–536, 2013.
- [147] Tianchen Hu. RACCOON, 2020. URL <https://github.com/hugary1995/raccoon>.
- [148] Tianchen Hu. RACCOON documentation, 2020. URL <https://hugary1995.github.io/raccoon>.
- [149] MOOSE: Multiphysics Object Oriented Simulation Environment. Idaho National Lab., USA, URL: <http://mooseframework.org/>, 2014.

- [150] Andrew E Slaughter, Cody J Permann, Jason M Miller, Brian K Alger, and Stephen R Novascone. Continuous integration, in-code documentation, and automation for nuclear quality assurance conformance. *Nuclear Technology*, pages 1–8, 2021.

Biography

Tianchen (Gary) Hu earned his B.S. degree in Mechanical Engineering from Washington University in Saint Louis. He joined the Department of Mechanical Engineering and Materials Science at Duke University in 2017 as a graduate research assistant. He received his Ph.D. degree in 2021. He will be working as a postdoctoral fellow at the Idaho National Laboratory.